Stimuli-induced structural switchability in the pillared-layer metal-organic framework DUT-8

DISSERTATION

Zur Erlangung des akademischen Grades

Doctor rerum naturalium
(Dr. rer. nat.)

Vorgelegt

dem Bereich Mathematik und Naturwissenschaften
der Technischen Universität Dresden

von

M. Sc. Leila Abylgazina

Eingereicht am 03.04.2023

Die Dissertation wurde in der Zeit von 10/2018 bis 12/2022
im Institut für Anorganische Chemie I angefertigt.

Erstgutachter: Herr Prof. Dr. rer. nat. habil. Stefan Kaskel

Zweitgutachter: Herr Prof. Dr. rer. nat. habil. Eike Brunner

Acknowledgements

My Ph.D. work would not have been possible without a great deal of support in various ways. I would like to take the opportunity to acknowledge people supporting and helping me in the period of my studies.

The most profound gratitude is addressed to my supervisor Prof. Dr. Stefan Kaskel for the interesting research project, inspiring scientific guidance, great encouragement, fascinating ideas, and the tremendous efforts for accepting me for doctoral studies in TU Dresden. Beyond that, I am also grateful for the possibility to participate in international conferences and for the numerous internal and external cooperation in the frame of my research.

Prof. Dr. Eike Brunner is sincerely acknowledged for reviewing my thesis, as well as for fruitful collaboration with his group. Thanks a lot for NMR measurements and data interpretation.

I would like to express my sincerest gratitude to my co-supervisor Dr. Irena Senkovska whose invaluable knowledge and wealth of experience have always inspired and motivated me. I am very thankful for the constant support, practical guidance, immediate solutions of any puzzling problems, training on the adsorption measurements, as well as for the wonderful working environment in MOF group. Through working with Irena, I have acquired the invaluable scientific skills in designing and planning of experiments, interpretation of my findings, writing of papers, presenting the results. Irena, thank you very much for kindness and friendship.

My sincere thanks are directed to Dr. Volodymyr Bon for X-ray diffraction measurements, data processing, analysis and continuous trainings.

I would like to give special thanks to Dr. Sebastian Ehrling for the introduction in a new laboratory culture, as well as the world of DUT-8, the tutorial in Origin, measurements, data processing and fruitful discussions.

There must be an extraordinary thanks to lab mates (lab 490) and colleagues who became my friends during 4 years of PhD journey: Dr. Andreas Schneemann, Leonid Shupletsov, Dr. Eunji Jin, Dr. Kartik Maity, Nadine Bönisch, Dr. Adrian Guiterrez Serpa, Dr. Kornel Roztocki, Mariia Maliuta, Richard Engemann and former colleagues: Dr. Khoa Dang Nguyen, Dr. En Zhang, Friedrich Schwotzer, Francesco Walenszus.

Many thanks, guys, for a great time together, working, teaching, socializing, helping, as well as supporting me intellectually and emotionally.

I would like to acknowledge all members of AK Kaskel for friendly working atmosphere and technical staff for assistance, especially Kerstin Zechel, Dr. Ilka Kunert, Rüdiger Kunschke. I am also very thankful to Linda Peterson and Kristin Rausch for help with documentations.

Furthermore, I value the love and support of my family. My deepest gratitude is expressed to my mother Olga Imambaeva, cousin Dmitriy Imambaev, niece Nelli Imambaeva and nephew Arslan Imambaev, uncle Serik Zhamanbalin. Their belief and encouragement helped me to keep my spirit high and overcome the barriers on the way to my goal.

Special thanks are addressed to my teachers from Kazakhstan: Prof. Dr. Bolat Yermagambet, Dr. Gulnar Nurgazina, Dr. Zhanar Kassenova, Dr. Raisa Zhakparova, Dr. Maira Kazankapova. Thanks for the knowledge, experience and anticipation of my visit.

My friends Evgeniy Zinko, Saniya Kartay, Almagul Zhakienova, Dr. Arash Kermani, Aliya Sarina, Svetlana Heinrich, Corinna Roberts, Emma Hermann, Nikolaj Lopatik, Natalia Lyubaykina are greatly appreciated for kindness, warmth and support.

“Keep your face always toward the sunshine and shadows will fall behind you”

- Walt Whitman

Abstract

Keywords: pillared-layer MOF, switchability, crystal size, morphology, surface, adsorption

Metal-Organic Frameworks (MOFs) are highly porous materials built from inorganic nodes joined by organic linkers forming extended crystalline networks. One of the distinguishing features of metal-organic frameworks is the ability to adaptively change their crystal structure in response to external stimuli with significant porosity switching. Such structural switchability of MOFs offers new opportunities in gas separation, selective recognition, sensing, and energy storage. However, there are still open questions in understanding factors affecting switchability. The electronic structure of the metal in the building blocks, host-guest interactions, but also particle size, morphology, surface, desolvation conditions are involved into the responsiveness of the system.

One of the representative of switchable metal-organic frameworks is pillared-layer DUT-8 (M_2(2,6-ndc)$_2$(dabco), M = Ni, Co, Cu, Zn, 2,6-ndc = 2,6-naphthalenedicarboxylate, dabco = 1,4-diazabicyclo[2.2.2]octane). Depending on the metal node and particle size, it is possible to synthesize either switchable or rigid materials differing in physisorption isotherm profiles.

In order to understand switching behaviour of DUT-8, the important parameters influencing structural switchability are addressed in my work. For this purpose, the impact of crystal size and morphology, as well as crystal surface on adsorption-induced structural transformations of DUT-8(Ni) were investigated. DUT-8(Ni) shows reversible structural transition between open (*op*) and closed pore phase (*cp*) upon adsorption/removal of guest molecules. To understand which particular crystal surfaces dominate the phenomena observed, crystals similar in size and differing in morphology were involved in a systematic study. The analysis of the data shows that the width of the rods (corresponding to the crystallographic directions along the layer) represents a critical parameter governing the dynamic properties upon adsorption of nitrogen at 77 K. This observation is related to the anisotropy of the channel-like pore system and the nucleation mechanism of the solid-solid phase transition triggered by gas adsorption.

To investigate the influence of external surface on adsorption-induced switchability, DUT-8(Ni) samples were exposed to different treatment techniques. By means of analytical methods, it was revealed that the surface of samples was modified leading to a significant increase of the gate-opening pressure, reflecting the increase of activation barrier for phase switching form *cp* to *op* upon adsorption of nitrogen at 77 K.

Furthermore, the properties of DUT-8(Zn) were studied precisely, focusing on the variation of particle size and morphology, host-guest interactions, desolvation conditions, selectivity and thermoresponsivity.

Depending on the synthesis conditions, DUT-8(Zn) can be synthesised in macro-sized regime (150 µm) and micron-sized regime (0.5 µm). The solvent removal process (pore desolvation stress contracting the framework) significantly controls the *cp/op* ratio after desolvation and, subsequently, the adsorption induced switchability characteristics of the system. Among the applied desolvation techniques, the solvent exchange with subsequent heating causes phase transition from open (*op*) to closed pore phase (*cp*). After desolvation, the dense *cp* phase of DUT-8(Zn) shows no adsorption-induced reopening and therefore is non-porous for N_2 at 77 K and CO_2 at 195 K. However, polar molecules with a higher adsorption enthalpy, such as chloromethane at 249 K and dichloromethane (DCM) at 298 K can reopen the macro-sized crystals upon adsorption, while micron-sized crystals retain the *cp* phase. For macro-sized particles (160 µm), the outer surface energy is negligible and only the type of metal (Zn, Co, Ni) controls the DCM-induced gate opening pressure. The node hinge stiffness increases from Zn to Ni as confirmed by DFT calculations, X-ray crystal structural analysis, and low frequency Raman spectroscopy. This softer Zn-based node hinges and overall increased stabilization of *cp vs. op* phase shift the critical particle size at which switchability starts to become suppressed to even lower values. Hence, the three factors affecting switchability (energetics of the empty host, (E_{op}–E_{cp}) (i), particle size (ii), and desolvation stress (iii)) appear to be of the same order of magnitude and should be considered collectively, not individually.

Crystal downsizing (0.5 µm) facilitates the responsivity of DUT-8(Zn) towards different guest molecules, not opening for macro-sized crystals. Among investigated adsorptives, the alcohols are in the center of attention due to ability to induce so called shape-memory effect in micron-sized crystals. The adsorption of alcohols stimulates the change of initial shape of pores (*cp*) into a temporary shape (*op*) which is maintained even after desorption.

To brighten the crystal size range and to study the dependence of gate opening pressure from crystal size and morphology, differently shaped crystals in micron-sized regime were produced by face-selective coordination modulation. Morphology modification allowed to determine the critical parameter controlling switchable transformations in DUT-8(Zn).

Thus, the crystal size engineering and morphology modification provide an opportunity not only to control the structural dynamics of MOFs, but also to tailor responsivity towards guest molecules, influencing the selective adsorption behaviour.

Table of Contents

Preface

Parts of this dissertation have been published as follows:

L. Abylgazina**,** I. Senkovska, S. Ehrling, V. Bon, P. Petkov, J. D. Evans, S. Krylova, A. Krylov and S. Kaskel, “Tailoring adsorption induced switchability of a pillared layer MOF by crystal size engineering”, *CrystEngComm,* 23, (2020) 538-549.

L. Abylgazina, I. Senkovska, R. Engemann, S. Ehrling, T. E. Gorelik, N. Kavoosi, U. Kaiser, S. Kaskel, “Impact of Crystal Size and Morphology on Switchability Characteristics in Pillared-Layer Metal-Organic Framework DUT-8(Ni)”, *Fronties in Chemistry,* 21, (2021) 1-10.

Abbreviations

MOF	Metal-organic Framework
DUT	Dresden University of Technology
PCP	Porous Coordination Polymer
SPC	Soft Porous Crystal
MIL	Materiaux l'Institut Lavoisier
ELM	Elastic Layer Material
ZIF	Zeolitic Imidazol Framework
HKUST	Hong-Kong University of Science and Technology
SBU	Secondary Building Unit
TGA	Thermogravimetric Analysis
DSC	Differential Scanning Calorimetry
DFT	Density Functional Theory
PXRD	Powder X-ray Diffraction
FT-IR	Fourier Transform Infrared Spectroscopy
ATR	Attenuated Total Reflection
NMR	Nuclear Magnetic Resonance Spectroscopy
XPS	X-ray Photoelectron Spectroscopy
ED	Electron Diffraction
IUPAC	International Union of Pure and Applied Chemistry
BET	BRUNAUER-EMMETT-TELLER
APHM	Adsorption maximum at half maximum uptake
CAS	Chemical Abstracts Service
DMF	N,N-Dimethylformamide
DCM	Dichloromethane
EtOH	Ethanol
PrOH	Propanol
BuOH	Butanol
THF	Tetrahydrofuran
PDMS	Polydimethylsiloxane
3D	Three-dimentional
2D	Two-dimentional
cp	Closed Pore
op	Open Pore
ccp	Confined Closed Pore
np	Narrow Pore
fu	Formula Unit

Chapter 1 Motivation

Motivation

Metal-organic frameworks (MOFs) are a class of porous materials, built from inorganic nodes joined by organic linkers forming extended crystalline networks.[1, 2] The discovery of MOFs greatly contributed to the development of advanced porous materials for adsorption-based technologies.[3, 4] A special subclass of MOFs are so called soft porous crystals or switchable MOFs, which undergo structural transformations under external stimuli.[5] Such unique feature makes them promising materials for gas storage, gas separation, or sensing.[6]

However, applications of MOFs, often require material downsizing, especially for integration into the operating systems.[7-9] The confined submicron dimensions and morphology affect the structural transformations of MOFs, consequently changing the gas adsorption properties with significant implications for separation efficiency.[10-12] Hence, an understanding of the impact of the crystal size and morphology on the switchability of MOFs is of utmost importance.[13] Moreover, defects, internal and external surface are decisive for tuning the material properties.[9]

Among famous representatives of particle-size dependent switchable MOFs is the pillared-layer DUT-8 system (DUT – Dresden University of Technology). DUT-8 (M_2(2.6-ndc)$_2$(dabco), M = Ni, Co, Cu, Zn, 2,6-ndc = 2,6-naphthalenedicarboxylate, dabco = 1,4-diazabicyclo[2.2.2]octane) with nickel in the metal cluster was first reported in 2010 by Klein *et al*.[14] The three other compounds containing Co, Zn, Cu were published in 2012.[15] The electronic structure of the metal significantly influence the stiffness of the paddle wheel unit and its tendency to deformation.[16] The macro-sized (>1 µm) crystals of DUT-8(M), (M = Ni, Co, Zn) transform from the open pore structure (*op*) to the closed pore structure (*cp*) upon the guest-molecule removal, while DUT-8(Cu) remains in the *op* phase.[15] Adsorption of guest species induces the reverse transition and opening of the DUT-8(Ni) crystal structure. Both macro-sized crystals DUT-8(Co) and DUT-8(Zn) retains the *cp* phase upon adsorption of different gases (N_2 at 77 K, CO_2 195 K, C_4H_{10} at 273 K). However, for DUT-8(Co) framework reopening can be triggered by adsorption of dichloromethane at 298 K.[16]

The remarkable influence of crystal size on switchable behaviour was revealed in DUT-8(Ni).[17] Crystal downsizing to the submicron range (<0.5 µm) enables the trapping of the material in a metastable, solvent free phase which is still open and behaves as a microporous rigid framework.[17] Previous studies have shown that the

crystal size of DUT-8(Ni) can be tuned by micromixer synthesis, controlling the nucleation process and crystal growth by contact time of starting materials and aging time.[18] The variation of the crystal size in the micrometer range leads to changes in the slope of nitrogen adsorption isotherms. In the size regime (0.5-1 µm) crystals become unresponsive to nitrogen at 77 K. Similar to DUT-8(Ni), the particle downsizing (<0.2 µm) in DUT-8(Co) induces framework rigidification.[16]

Since the framework crystalizes as rod-like shaped crystals, it remains unclear (i) *size of which faces of the anisotropic crystals influences switchability*; (ii) *why the systematic variation of size influences switchable behaviour;* (iii) *what is the possible mechanism controlling the phase transition.*

Finding answers to these questions is the core of Chapter 4. The crystal size and morphology modulation of DUT-8(Ni) was performed by different synthetic procedures. To correlate the gate opening characteristics of the isotherms with the size and morphology of the DUT-8(Ni) crystals, the materials were analysed using scanning electron microscopy (SEM), electron diffraction, and nitrogen physisorption at 77 K. To understand the effects on the isotherm and the relationship between the size, morphology, and isotherm shape, characteristic quantities, which can be extracted from the isotherm and related to the sample characteristics, thermodynamics, and kinetics of the switching process were identified.

Concerning DUT-8(Zn), it is a system with open questions regarding *the switchable behaviour, depending on (i) the nature of the guest, (ii) crystal size and morphology, (iv) stress acting on the framework upon desolvation, as well as (v) thermal behaviour.*

Finding answers to these questions is the core of Chapter 5. The crystal size and morphology modulation was performed by differences in synthetic procedures. Various analytical methods are used in order to gain an insight into phase transformation of samples with modulated crystal size and shape, caused by adsorption of guest molecules. Powder X-ray diffraction experiments, various adsorption experiments, *in situ* X-ray diffraction measurements, solid and liquid state nuclear magnetic resonance spectroscopy are particularly noteworthy. The thermoresponsivity is investigated by dynamic differential scanning calorimetry, thermogravimetric analysis, and powder diffraction at variable temperatures.

The influence of surface exterior on switchable properties of DUT-8 system was not investigated in the past. In this regard, the influence of surface modification/deformation on adsorption-induced phase transitions of DUT-8(Ni) is

addressed in Chapter 6. The protic polar solvents (alcohols) are not able to induce *cp*-to-*op* transition,[19] pointing on possible surface modification by these species. The influence of surface treatment procedures by alcohols and polymers on framework closing upon desolvation and framework opening upon N_2 (77 K) adsorption is investigated. In order to prove, surface chemistry modification of DUT-8(Ni) crystals, surface characterization techniques are used such as SEM, XPS, and contact angle measurements. By combination of different analytical methods, it is possible to get insight into the surface modification and associated surface barriers that may affect the stimuli-induced transfomations.

Chapter 2 State of the art

2.1 From discovery to functions of metal-organic frameworks

Metal-organic frameworks (MOFs) are a class of porous materials, built from inorganic nodes joined by organic linkers forming extended crystalline networks.[1, 2] The history of MOFs dates back 30 years when Robson reported an “infinite polymeric framework”,[20] after which, Yaghi,[21] Kitagawa,[22] and Férey[23] primed the investigation of such hybrid materials.[24] According to the IUPAC definition “A Metal-organic framework is a Coordination Polymer (or alternatively Coordination Network) with an open framework containing potential voids.[25]

One of the first representatives of MOFs (Figure 2-1) with permanent porosity are MOF-5 ($Zn_4O(bdc)_3$) formed by octahedral Zn(II) clusters and 1,4-benzenedicarboxylate linker (bdc),[26] and HKUST-1 ($Cu_3(btc)_2$) containing Cu(II) paddle-wheel nodes and benzene-1,3,5-tricarboxylate (btc) linkers.[27]

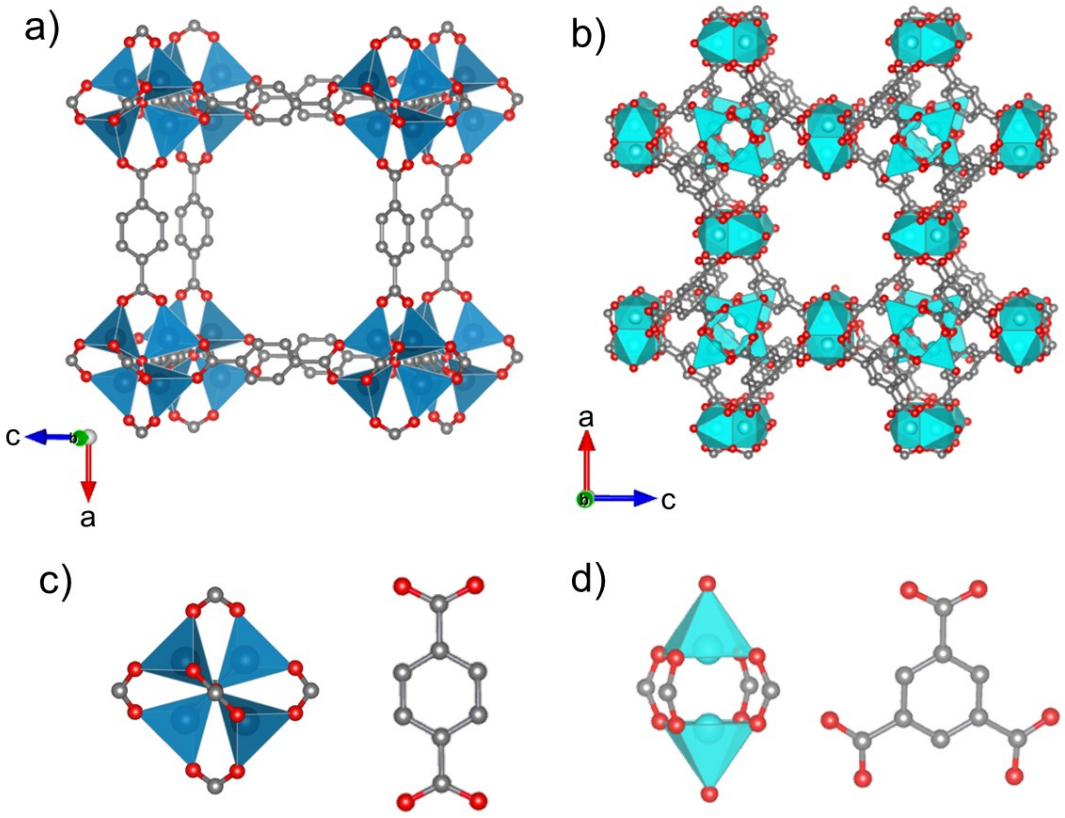

Figure 2-1. Depiction of the crystal structure of a) MOF-5, b) HKUST-1; metal cluster and linker of c) MOF-5 and d) HKUST-1 (carbon is represented in grey, oxygens in red, blue polyhedra represent coordination environment around zinc, cyan polyhedra represent coordination environment around copper, hydrogens have been omitted for the sake of clarity.

Yaghi's group created a series of MOFs called isoreticular MOFs (IRMOFs) based on the before mentioned Zn_4O nodes that can also be found in MOF-5, which act as joints, while the linear dicarboxylate linker can be varied in length (i.e. number of aromatic rings) and can be substituted with functional groups, controlling the pore size and pore function. The series of IRMOFs are representatives of the concept of reticular design.[26, 28, 29]

One of the reported MOF-5 syntheses was conducted in a closed vessel at elevated temperature (85° to 105° C) using *N,N*-diethylformamide or *N,N*-dimetylformamide as a solvent.[30, 31] It allows for slow decomposition of solvent which leads to steady delivery of the deprotonation agent (diethylamide or dimethylamide), which in turn deprotonates the bdc linker. The thermodynamic equilibrium of reversible coordination of the linkers to the clusters proceeds via self-assembly, which results in the formation of large crystals suitable for single crystal X-ray diffraction analysis. Since that time the community developed many different methods for the synthesis of MOFs such as solvothermal, electrochemical, microwave-assisted, mechanochemical, microfluidic methods.[32, 33]

The tunable pore structures, high pore volumes, large surface areas and multifunctional properties of the metal-organic frameworks allow to develop the application pathway in the fields of gas storage, separation, catalysis, sensing and drug delivery.[3, 34-39]

2.2 Switchable Metal-Organic Frameworks

A unique feature of Metal-Organic Frameworks is switchability: A subset of MOFs can adaptively change their crystal structure without bond breaking in response to a stimulus. The stimuli-responsive characteristic of MOFs was already predicted in 1998,[22] when Kitagawa classified them into three generations (Figure 2-2). The first generation (1st) compounds irreversibly loose structural integrity and disintegrate upon loss of the included guest species caused by the weak metal–ligand binding energy.[40] The structural stability of frameworks can be achieved by utilizing polynuclear clusters, so called secondary building units (SBUs) and multidentate linkers (carboxylates).[26]

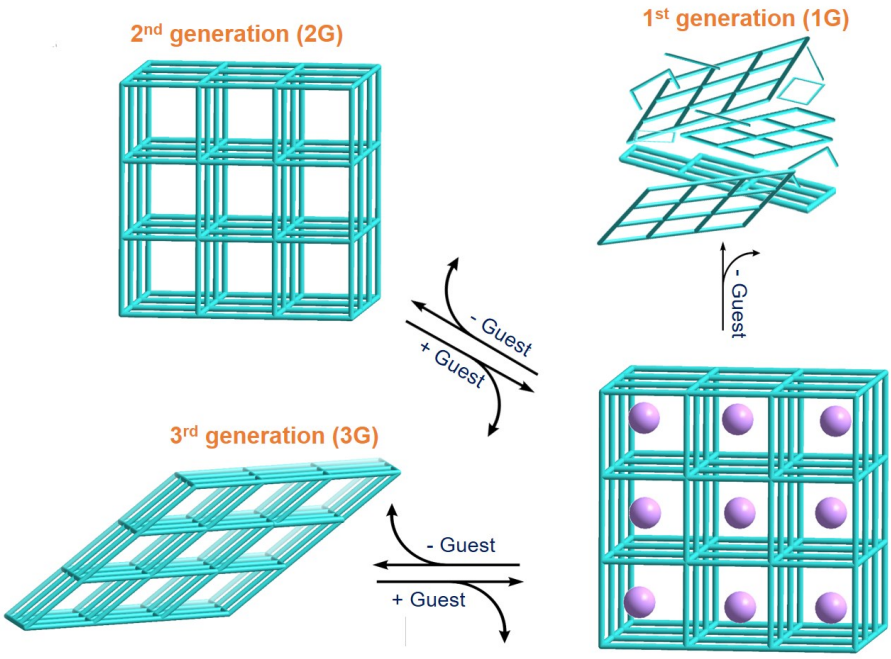

Figure 2-2. Classification of different generations of MOFs. Adapted from ref.[5] (Copyright © 2009, Nature Publishing Group)

These second-generation (2nd) compounds are able to maintain the original porous structure upon guest removal/reintroduction and possess in contrast to the 1st permanent porosity. The third generation (3rd) compounds are defined as flexible porous frameworks and characterized by the ability to switch between different phases initiated by an external stimulus, for example by guest inclusion upon adsorption.[5]

According to S. Horike et al. *"Soft porous crystals are porous solids that possess both a highly ordered network and structural transformability. They are bistable or multistable crystalline materials with long range structural ordering, a reversible transformability between states, and permanent porosity. The term porosity means that at least one crystal phase possesses space that can be occupied by guest molecules, so that the framework exhibits reproducible guest adsorption".*[5]

Figure 2-3 demonstrates the timeline of discovery of representative flexible frameworks, the important flexibility modes and effects.[41]

Structural flexibility has been initially recognized by Li and Kaneko in a framework today termed ELM-11.[42] From 2002 onwards the groups of Kitagawa and Ferey intensively investigated the 3rd generation of MOFs,[43-47] which are also termed as "flexible",[48] "switchable",[9] "soft porous crystals (SPCs)",[5] "dymanic MOFs" or "sponge-like MOFs"[49] (Figure 2-2). A more rigorous definition is discussed in the work by Evans.[50]

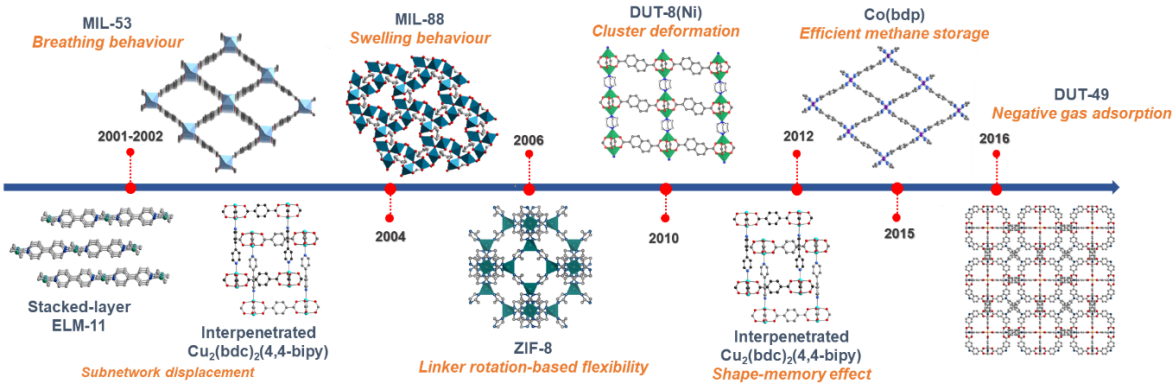

Figure 2-3. Timeline discovery of flexible MOFs. Adapted from ref.[51]

In order to trigger the dynamic behaviour of the 3rd generation MOFs, certain external stimuli such as light, temperature, pressure or guest molecules insertion/release is necessary.[24, 48, 52-54]

The structure-property correlation of the frameworks depends on the judicious selection of the components, as well as the type of linkage.[55] The presence of weak interactions such as hydrogen bonds, π-interactions have the ability to control the inherent flexibility in switchable MOFs.[56] These kind of MOFs are designed by the rigorous selection of metal ions/clusters and organic linkers with different geometry, length, functionality.[57]

In principle, the connection of flexible organic linker by coordination bonds results in the *linker based flexibility*. Meanwhile, the linkage of rigid organic linker by dynamic coordination bonds ensures the *cluster based flexibility*.[41]

The main origin for structural transformation phenomena are associated with the changed coordination environment of metal ions,[58, 59] the deformed configuration of SBUs in response to the removal or binding of coordinating guest molecules[60] and breaking/reforming of coordination bonds.[55]

Several reviews have presented the impact of flexible linkers on the MOF properties either by exploiting linker local dynamics (e.g., twisting, rotation, and bending) or functionalization of the organic linker.[6, 47, 61] The organic linker can be functionalized by non-coordinative side groups, which are able to induce framework flexibility due to steric (repulsive), attractive and/or electronic effects.[62]

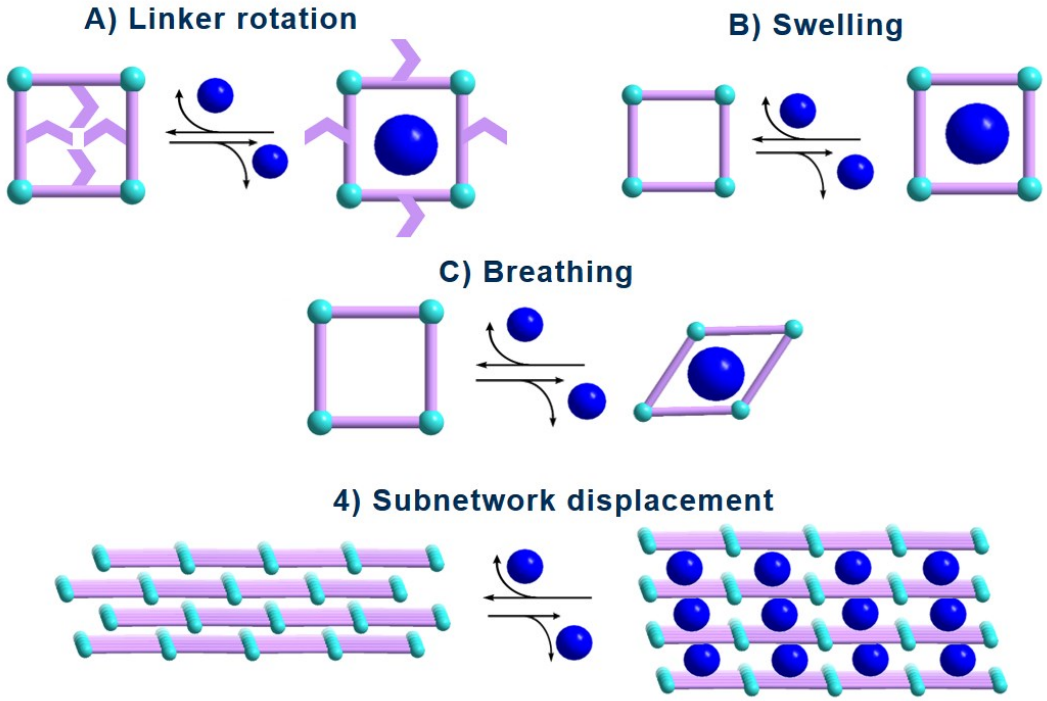

Figure 2-4. Classification of different flexibility modes. Adapted from ref.[6] with permission from the Royal Society of Chemistry.

Thus, the structural response towards external stimuli can proceed by different mechanisms such as *linker rotation, mobility of functional groups or metal-cluster deformation*.[6]

The stimulus-responsive cooperative transformations of MOFs could be realized through *gate opening, swelling, breathing* (change in the cell parameters)*, subnetwork displacement* (Figure 2-4).

In the following, the framework motions and underlying mechanisms will be explained on the basis of representative examples of stimuli responsive MOFs (Figure 2-5).

ELM-11. The flexible phenomena are often observed in metal-organic frameworks consisting of stacked two-dimensional (2D) layers, which are connected through weak (dispersive, dipolar, H-bonds) interactions.[6] The displacement of the layers can be initiated by external stimuli.[6] Among these materials, ELM-11 $[Cu(bpy)_2(BF_4)_2]$ – a switchable layered 2D MOF, is a representative example. The structure is built from copper ions, connected by 4,4'-bipyridine (bpy) molecules forming $[Cu(bpy)_2]$ square-grids, which are axially connected to charge-balancing BF_4^- anions (Figure 2-5).[51] The stacking of adjacent sheets leads to the stabilization of the closed pore (*cp*) form. The phase transformation of ELM-11 upon induced by adsorption of CO_2, N_2, Ar and

hydrocarbons leads to gate adsorption isotherms.[63, 64] The discovery of ELM-11 was the first example of a “gate pressure” isotherm (Figure 2-6a). *Gating* represents the collective phenomenon accompanying porosity increase via a cooperative phase transition of the entire crystalline lattice.[52] Gating characterizes a MOF which has no porosity in the guest-free phase (*cp* = closed pore) but opens the pores for a specific guest (*op* = open pore) at a characteristic “gate pressure” of the guest molecule.[65] This behavior results in a characteristic adsorption isotherm which is basically a combination of two characteristic IUPAC defined isotherm shapes typical for a non-porous (type II) and microporous (type I) material which are connected by a steep, almost vertical increase in uptake at the gate pressure characterizing a 1st order transformation of the framework from closed to open pore.[65] As typical for 1st order phase transitions (discontinuous, step-wise), it shows a hysteresis loop and closing occurs at much lower pressures close to the equilibrium transition pressure. The characteristic switchable porosity of MOFs is accompanied by huge volume change.[65] For MOFs which demonstrate a gating profile, the Helmholtz free energy of the *cp* phase is considered to be lower than for the *op* ($F_{cp} < F_{op}$) (F - Helmholtz free energy of empty host).[66] Gate opening is initiated if the *op* form can be stabilized by the guest after approaching a system-specific condition (gate pressure, p_{go}): $F(guest)_{op} < F_{cp}$ for $p > p_{go}$ ($F(guest)_{op}$ – guest loaded framework).[50] Moreover it should be emphasized that p_{go} typically does not represent the equilibrium pressure (p_e) for the *cp*-*op* transition but the chemical potential needed for overcoming the activation energy barrier for pore expansion ($p_{go} > p_e$, $p_{go} - p_e = \Delta p$).[50]

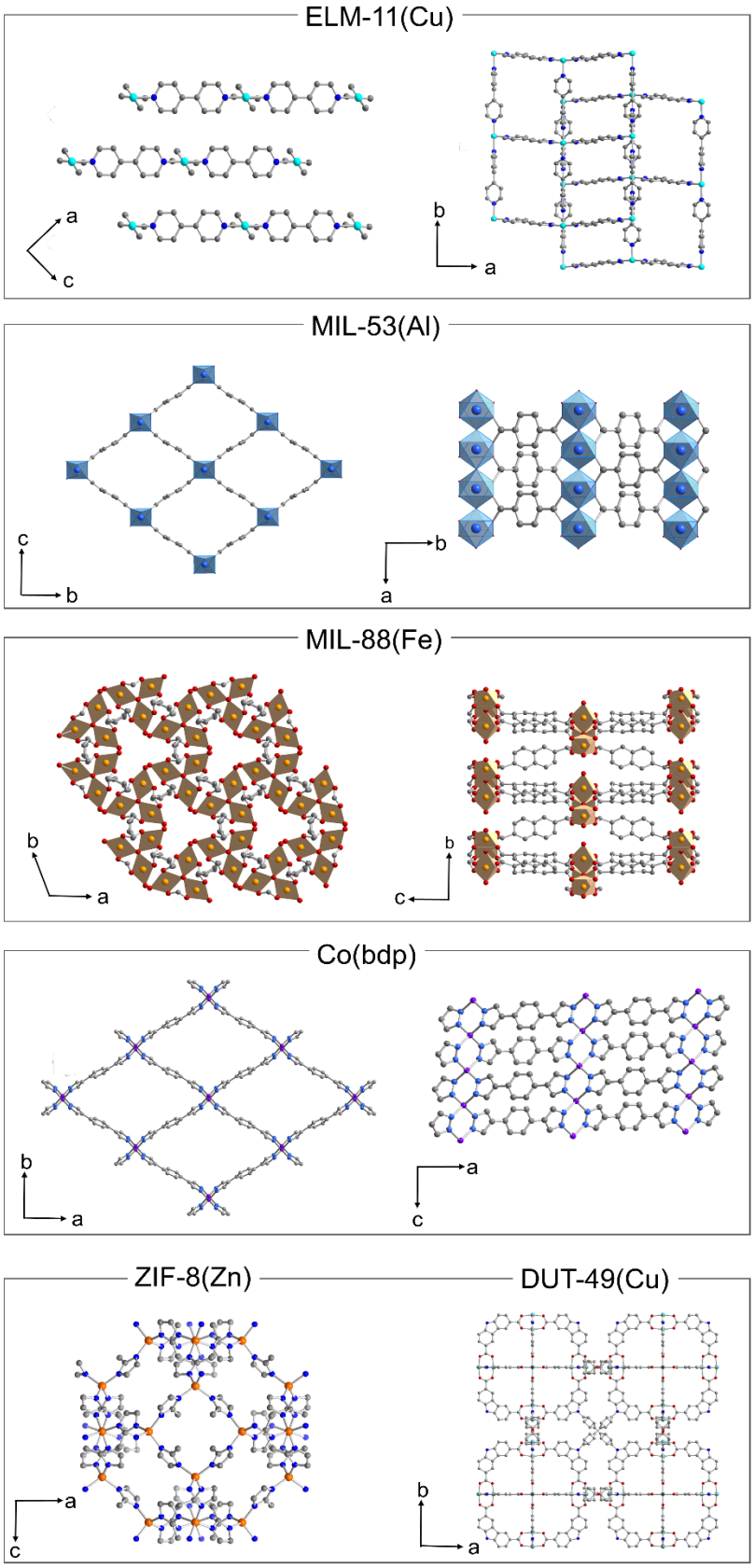

Figure 2-5. Crystal structures of switchable MOFs: ELM-11(Cu), MIL-53(Al), MIL-88(Fe), Co(bdp), ZIF-8(Zn), DUT-49(Cu).

MIL-53. The group of Ferey in 2002 developed the synthesis of the most famous breathing metal-organic framework - MIL-53(Cr) (Cr(OH)bdc).[67] So-called breathing MOFs show a change in unit cell volume (pore volume) upon external stimuli (e.g. guest molecule adsorption/desorption). *Breathing* is characterized by 2-step process and it is possible if $F_{np} > F_{op}$.[44, 66, 68-70] The guest free MOF has its minimum in the *op* form. Upon adsorption at intermediate loading, host-guest interactions lead to framework contraction – stabilization of a narrow pore phase *(np)*, with reduced porosity, at intermediate relative pressure driven by the enhanced adsorption enthalpy $\Delta_{ads}H$ of the guest for the *np* host ($\Delta_{ads}H_{np} > \Delta_{ads}H_{op}$). At higher pressure, the *op* host is able to accommodate more guest molecules ($n_{ads,\,op} > n_{ads,\,np}$) and the stabilisation of the *op* host framework is caused by guest-guest interaction (since $|\Delta_{ads}H_{op} * n_{ads,op}| > |\Delta_{ads}H_{np} * n_{ads,\,np}|$).[50] After reaching such a critical concentration of the guest fluid, the pore volume expands again due to the relaxation of the framework to the initial geometry. The consequence is an *op-cp-op* structural transition trajectory following increasing relative pressure along the adsorption isotherm (Figure 2-6c).[51]

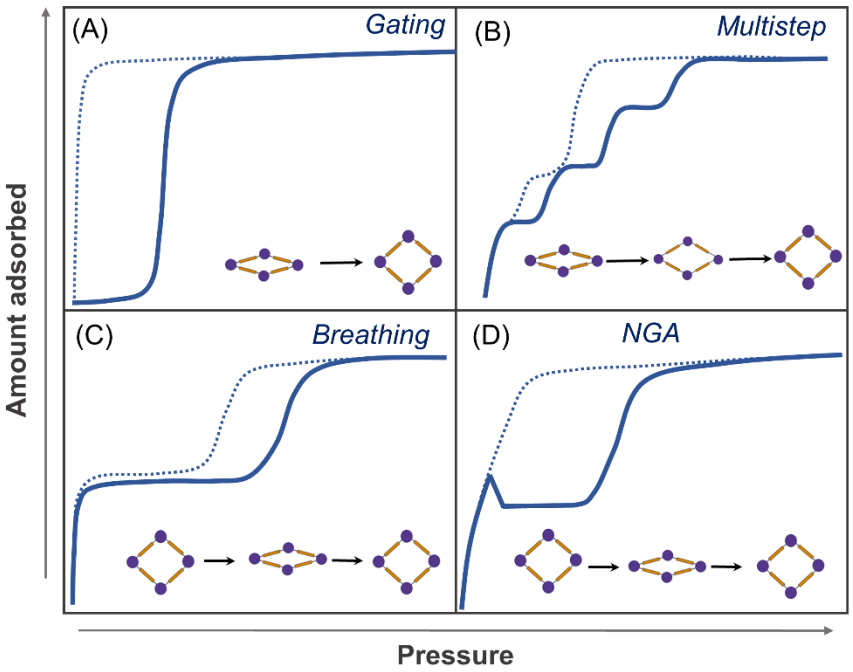

Figure 2-6. Adsorption isotherms for switchable MOFs: a) Gating processes are characterized by a one-step opening (adsorption) and closing (desorption) step; b) Stepwise adsorption isotherm characterized by gradual pore reopening; c) Breathing traverses in two steps from empty *op* by increasing guest pressure via partially filled *np* to a completely filled *op* phase; d) Negative gas adsorption isotherm characterized by spontaneous release of guest molecules. Adapted from ref.[50] (CC BY 4.0).

MIL-53 is formed by corner-sharing octahedral SBUs linked by bdc ligands to form a 3D framework with 1D lozenge-line channels (Figure 2-5). The octahedral unit MO_6 is composed of oxygen atoms provided by four carboxylate groups and two oxygen atoms originate from the bridging hydroxyl groups (μ_2-OH). The "breathing" movement of MIL-53 is associated with linker rotation around the O-O axis of carboxylate group in the so-called kneecap manner.[68]

In MIL-53(Al) and MIL-53(Cr), breathing behaviour can be triggered by moisture adsorption.[47] The contraction of the pores is assigned to hydrogen-bonding interactions between the hydrogen atoms of water molecules and the oxygen atoms of the carboxylates and the μ_2-hydroxyl groups in the hydrated state. The dehydration of material under heating transforms the structure into the original large pore form. Upon adsorption of CO_2 molecules, adsorption initially takes place near the hydroxyl groups in MIL-53(Al), which is followed by shrinkage/contraction of the host framework.[71] In the course of pressure increase, the framework expands. Therefore, depending on the conditions, the three common phases are distinguished: as synthesized - MIL-53-*as*, activated high-temperature phase - MIL-53-*ht*, low-temperature MIL-53-*lt* resulted after guest molecules adsorption (H_2O, CO_2).

Framework contraction in MIL-53(Al) can be provoked by host–host and host–guest interactions.[52] The *cp* phase is stabilized due to enhanced host–host interactions via π-π type interactions, meanwhile stabilisation of *op* phase is caused by guest-guest interactions.[52]

MIL-88. Another representative of switchable MOFs is MIL-88,[72, 73] which is characterized by a gradual enlargement of the unit cell volume without any change in geometry as well as connectivity of SBUs, known as *swelling*.[6] The framework structure of the MIL-88 family is based on combination of trigonal prismatic units $M_3O(H_2O)_2X^{6+}$ (M = Fe^{3+}, Cr^{3+}; X = F^-, OH^-) and dicarboxylates such as fumarate in MIL-88A, 1,4-bdc in MIL-88B, 2,6-naphthalene dicarboxylate (2,6-ndc) in MIL-88C (Figure 2-5) or 4,4′-biphenyldicarboxylate (4,4′-bpdc) in MIL-88D, generating "honeycomb" system.[73-76] Interestingly, the expansion of unit cell volume of MIL-88 is caused by the rotation of metal cluster around the [001] axis in the course of transformation. The angular orientations of metal clusters and the phenyl rings can be altered around the O-O axis of carboxylate groups, which can be considered as "knee cap".[51] The degree of swelling depends also on the nature of the guest molecules,

therefore reaching a change of the unit cell volume from 85% to 230% during solvation.[55]

ZIF-8. The different fragments of host framework are able to rotate around single bonds within an organic ligand (internal flexible bonds) or between metal ion and organic ligand (flexible metal-linker bonding). Such rotation leads to modification of the pore geometry. A reversible linker reorientation in the prototypical example ZIF-8 ($Zn(mIM)_2$ with mIM = 2-methylimidazolate; Zeolitic imidazolate framework), results in the expansion of the pore windows. ZIF-8 is based on tetrahedrally coordinated Zn ions and the mIM linker (Figure 2-5).[77] The metal bond angle (145°) is similar to Si-O-Si angle of zeolites leading to topological isomorphism. The swing effect (gate-opening) in ZIF-8 was revealed in 2009 by single crystal XRD performed under high pressure (1.47 GPa).[78] Initially, due to the small pore-aperture ZIF-8 (3.4 Å) was expected to separate H_2 (kinetic diameter of 2.9 Å) from a mixture of H_2, CO_2, O_2, N_2, and CH_4. However, an experimental-theoretical study revealed that the reorientation of mIM in ZIF-8 increases the pore window size to 3.6 Å.[78-80]

Co(bdp). An outstanding representative of the gate-opening effect is Co(bdp) framework (bpd = 1,4-benzenedipyrazolate).[81] The 3D framework is formed by 1D chains of tetrahedrally coordinated Co ions connected by μ_2-pyrazolates, resulting in square channels (Figure 2-5). The remarkable feature of this MOF is that during methane adsorption at 298 K, working capacity reaches 155 $cm^3\ cm^{-3}$ at 5–35 bar at 298 K with typical gating isotherm.[82] However, the material undergoes a stepwise phase transition from *cp* to *op* upon N_2 adsorption (Figure 2-6b).[83] In the course of five steps the phase transition is accomplished, which is revealed by a combination of in situ synchrotron powder XRD and molecular simulations. The structural flexibility is related to a coordination geometry change from square planar (*cp*-host) to tetrahedral (*op*-host). Upon framework expansion, the coordination angle of Co-clusters and organic building blocks changes from 152° to 108°, which is assigned to the reorientation of benzene rings.[83]

DUT-49. An exceptional case of breathing transition was revealed in DUT-49(Cu), which is named negative gas adsorption phenomena (NGA).[84] DUT-49 is an assembly of cuboctahedral metal–organic polyhedra (MOPs) formed by Cu_2 paddle-wheel units and 9,9´-([1,10-biphenyl]-4,4´-diyl)bis(9H-carbazole-3,6-dicarboxylate) (BBCDC) units resulting in face-centred cubic analogue arrangement of MOPs (Figure 2-5).[84] Upon adsorption of methane at 111 K, reaching certain pressure range (10 kPa) the

structure releases a significant amount of gas (Δn_{NGA}=8.62 mmol g^{-1}), which is caused by framework contraction. This results in a negative step in uptake with increasing gas pressure in the adsorption isotherm (Figure 2-6d).[51] The structural switchability originates from buckling of (bbcdc) struts upon modest stress according to DFT simulations.[53]

2.3 Switchable pillared-layer metal-organic frameworks

Despite the combination of metal nodes and organic ligands produces a wide variety of structures with specific functionality, the addition of a third neutral building unit leads to a new subclass of porous coordination polymers – pillared-layer frameworks, which is of great interest.[85]

In general, the pillaring strategy is an effective and straightforward approach for the construction of three-dimensional (3D) porous frameworks from two-dimensional (2D) layers (Figure 2-7).[85] By coordinating metal nodes with pillar linkers, more stable structures were obtained.[86]

Pillared-layer MOFs can be related to a subclass of Hofmann clathrates (1977), which represent the first coordination networks consisting of 2D cyanide-containing layers, were bonded to each other through axial ligands.[87] Kitagawa et al. firstly performed the introduction of pillars in MOFs (1996), where the guest molecules were inserted between the layers, just like pillars, supported by hydrogen bonds.[88]

To form 2D layer motifs, most frequently oxygen donor ligands are used for pillared-layer MOFs construction. Such ligands contain two carboxylate groups coordinating in the equatorial site of the metal. Multi-donor linkers such as tri, tetra, penta, hexa and octatopic are also widely used in pillared-layer MOFs.[85, 89] Pillaring of MOFs can be achieved by using oxygen, sulphur, or nitrogen donors, coordinating axially to two metals. Dabco and bipyiridine were firstly used as N-coordinated pillars for mixed-ligand systems.[85] Such systems can be constructed by carboxylate-based ligands coordinated to paddle-wheel metal units which are connected by axially coordinated neutral ligands, forming a 3D coordination network (Figure 2-7).[85, 89]

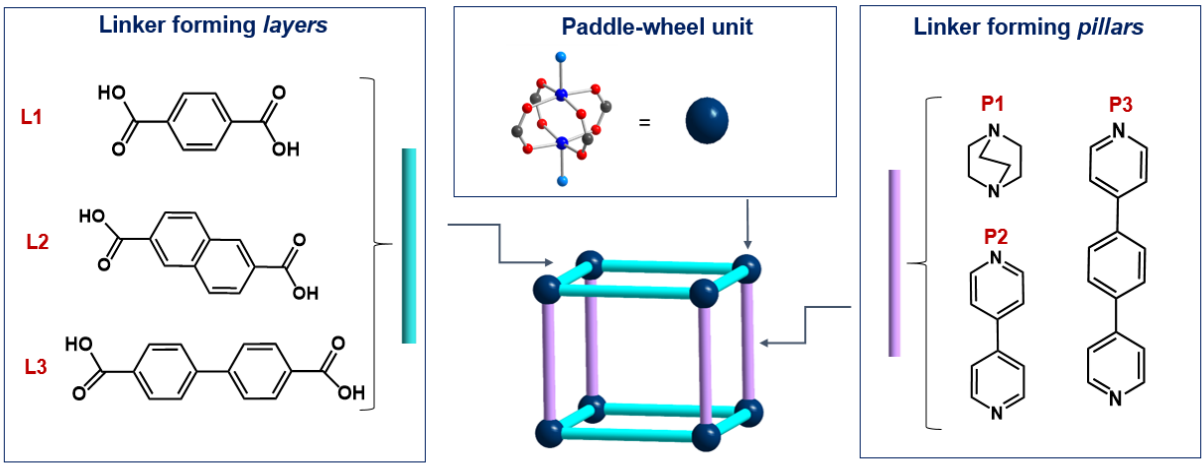

Figure 2-7. Schematic representation of pillared-layer MOFs construction by dicarboxylates linkers: (L1) benzene-1,4-dicarboxylic acid, (L2) 2,6-naphthalenedicarboxylic acid, (L3) biphenyl-4,4′- dicarboxylic acid, and N-donor pillars: (P1) 1,4-diazabicyclo[2.2.2]octane, (P2) 4,4′-bipyridine, (P3) 1,4-bis(4-pyridyl)benzene.

The first reported flexible pillar-layered MOF was reported by Kitagawa in 2002.[43] The framework of compound $[Cu_2(pzdc)_2(dpyg)\cdot 8H_2O]_n$ was constructed by $Cu_2(\mu\text{-}O)_2$ units linked by the pyrazine-2,3-dicarboxylate (pzdc) ligands forming two-dimensional layers, which are connected by 1,2-dipyridylglycol (dpyg) ligands acting as pillars. The gating isotherm was recorded upon MeOH adsorption at 298 K, indicating a framework transformation, allowing the inclusion of guest molecules.

Later on, the typical representative of the pillared-layer frameworks - DMOF with the formula $[Zn_2(1,4\text{-bdc})_2(dabco)]_n$ (bdc = benzene-1,4-dicarboxylic acid, dabco = 1,4-diazabicyclo[2.2.2]octane) was reported by Dybtsev in 2004.[90] The 3D architecture is constructed by connection of Zn_2 paddle wheel SBUs with bdc into 2D square grids, which in turn are linked by neutral dabco pillars. The guest-induced structural changes are observed upon benzene inclusion, resulting in pore shrinkage and smaller pore volume in comparison with solvent-free state. These reversible structural transformations point to the dynamic nature of paddle-wheel SBUs.

The functionalization of pillared layered DMOF, $[Zn_2(bdc)_2(dabco)]_n$, by alkoxy groups results in different degree of structural responsivity.[91-93] The parent DMOF undergoes only minor stimuli-induced transformations.[90] Meanwhile the substituted frameworks $[Zn_2(fu\text{-}bdc)_2(dabco)]_n$ are able to reversibly contract/expand upon guest release/adsorption (DMF, CO_2).[94] Structural response depends on the nature of the chain length and polarity of incorporated groups. By means of XRD, the extent of framework contraction was revealed. After solvent removal, the frameworks shrink due

to attractive interactions between the alkyl chains. However, it was shown that the frameworks with longer alkyl chains are more rigid, which is caused by steric hindrance.

The decoration of the 1,4-bdc ligand with the dynamic aromatic substitutes may lead to cooperative flexibility via intra-framework π-π interactions.[95] In particular, for Zn-based pillared-layer frameworks 2,5-bis[(2-nitrobenzyl)oxy]-1,4-benzenedicarboxylic acid (H_2bdc-NO_2) and 2,5-bis(benzyloxy)-1,4-benzene-dicarboxylic acid (H_2bdc-H) and bpy were used. The integrated mobile fragments significantly influence framework switchability. Both frameworks undergo phase transition upon thermal activation in vacuum. However, structural responsivity towards CO_2 incorporation was revealed only in the framework with nitro-substituted arenes. Such distinctive sorption behaviours are related to intra-framework π-π interactions. It was revealed that π-π interactions are absent in the framework with benzyl substituent, leading to disruption of 2D grid layers upon activation. On the contrary, π-π interactive dimers, formed by the central benzene of 1,4-bdc and nitro-substituted arenes, are preserved even after thermal activation. These interactions maintain the integrity of the 2D-layers. Moreover, the π-π interaction-controlled structural transformations result in a responsive guest-free framework that can distinguish between C_6 alkane isomers by different gate-opening pressure.

The pillared-layer MOF crystallites can be grown onto substrates forming thin films with different dimensions and orientation. Fischer and co-workers investigated the structural flexibility of Cu-based alkylether-functionalized $[Cu_2(DE\text{-}bdc)_2(dabco)]_n$ (DE-bdc = 2,5-diethoxy-1,4-benzenedicarboxylic acid) crystallites anchored onto the differently terminated surfaces.[96] The bulk material shows breathing behaviour, reversibly transforming from *op* (square grids) to narrow pore *np* form (rhombic grids) upon guest removal/incorporation. The fabrication of thin films was achieved by liquid phase epitaxy with varying deposition cycles (40, 60, 80, 120) and therefore controlling the thickness of thin films (430-1000 nm). The structural responsivity of the deposited materials was investigated upon methanol removal and adsorption by in-situ synchrotron grazing incidence X-ray diffraction (GIXRD). It was shown that the crystallites remain structurally intact in very thin films (40 deposition cycles), which is attributed to the strong interactions between the crystallites and substrate leading to a higher activation barrier for structural transformation. On the contrary, thick films (60–120 deposition cycles) change from *op* form to a mixture of *op* and *np* after activation.

Importantly, the breathing transformation is observed only in the crystallite domains at higher distance (60–120 deposition cycles) to the substrate, as the influence of the surface interaction gets less pronounced. Moreover, the pressure needed to induce phase transformation is higher for the crystallites deposited onto the surface in comparison with bulk sample. Particle-size dependent flexibility will be introduced and extensively discussed in section 2.4.

Interpenetrated frameworks

The extension of the ligand length ensures the void, which allows accommodating a second or more nets.[97] The elongation of the pillar in the 1,4-bdc or 2,6-ndc (2,6-naphthalenedicarboxylate) based MOFs from dabco to 4,4′-bipyridine (bpy) often leads to interpenetration due to weaker metal–pillar bond promoting M-N bond cleavage.[98, 99]

For examples, the copper paddle wheel units connected by 1,4-bdc ligands in equatorial plane, forming layers which are pillared by dabco forms a non-interpenetrated, rigid framework $[Cu_2(1,4\text{-bdc})_2(dabco)]_n$.[100] Meanwhile, the pillaring by bpy leads to flexible 2-fold interpenetrated framework $[Cu_2(1,4\text{-bdc})_2(bpy)]_n$.[101] The interpenetrated framework switches reversibly between guest-included open and guest-free closed states upon methanol removal/incorporation due to the bending of the pillar.

In Zn-based MOF, the combination of longer carboxylate linker bpdc with bpy leads to a 2-fold interpenetrated structure $[Zn_2(4,4'\text{-bpdc})_2(bpy)]_n$, which contracts upon solvent removal due to π–π stacking of 4,4′-bpdc linker (4,4′-biphenyldicarboxylate). However, the framework retains the contracted phase during adsorption of N_2 (77 K) and CO_2 (195 K).[102] Further elongation of pillar length results in 3-fold interpenetrated pcu network $[Zn_2(4,4'\text{-bpdc})_2(bpb)]_n$, (bpb = 1,4-bis(4-pyridyl)benzene).[103] This compound undergoes phase transition from *op* phase to denser desolvated phase, which is responsive towards different gases such as N_2 (77 K), CO (82 K), and CO_2 (195, 298 K).

The interpenetration can be controlled by employing bulky linkers. The use of long bulky pillar bp4va (9,10-bis((E)-2-(pyridine-4-yl)vinyl)anthracene) instead of bpb leads to 2-fold interpenetrated $[Zn_2(4,4'\text{-bpdc})_2(bp4va)]_n$.[104]

In some cases, the interpenetration is prevented by introduction of bulky substituents in the linker. For instance, $[Zn_2(1,4\text{-bdc})_2(bpy)]_n$ is 2-fold interpenetrated system.[99]

However, after decoration of linker with bulky substituents, the framework is formed as non-interpenetrated structure.[95] The degree of interpenetration can be also controlled by synthetic conditions, which in turn impacts on the structural flexibility. Kitagawa et al. showed that depending on solvent used for synthesis 2-fold and 3-fold interpenetrated structures $[Zn_2(5,5'\text{-btdc})_2(bpy)]_n$, (5,5′-btdc = 2,2′-bithiophene-5,5′-dicarboxylic acid).[105] It was revealed that 2-fold interpenetrated framework experiences structural transformations upon guest removal/adsorption, while 3-fold interpenetrated framework is rigid.

The interpenetrated pillared-layer systems can be also constructed by using photo-sensitive ligands. Photo-responsive azobenzene groups can be anchored either on pillars[106] or on layers[107] forming ligands.

In the photo-responsive framework $[Zn_2(2,6\text{-ndc})_2(azo\text{-bipy})]_n$ (azo-bipy = 3-azo-phenyl-4,4´-bipyridine), the square grid nets of the $Zn_2(ndc)_2$ were connected by the azo-bipy linkers forming 2-fold interpenetrated structure. The azo-groups are oriented towards the pores. When the “as-synthesized” material is exposed to light (λ = 365 nm), azo-groups being in the stable *trans*-form reconfigure to the *cis*-form, providing the pore access.[106]

Non-interpenetrated frameworks

While the combination of 2,6-ndc and 1,4-bdc linkers with bpy results in interpenetrated frameworks, there are several examples showing that use of longer carboxylic acid linkers in combination with dabco prevent interpenetration.[108]

One of the representative non-interpenetrated frameworks is DUT-8(Ni) $[Ni_2(ndc)_2dabco]_n$ (DUT – Dresden University of Technology), consisting of Ni-paddle wheel units connected by 2,6-ndc linkers forming 2D layers, which are bridged by dabco pillars.[15] The framework is able reversibly to switch the structure from *op* to *cp* upon guest molecule removal/incorporation. The desolvation of framework leads to transformation to the *cp* phase due to deformation mode of the paddle wheel unit. The structural responsivity significantly depends on the nature of guest molecules in both the liquid and gas phase.[19, 109] The PXRD data revealed that single-step gating isotherms recorded during adsorption of N_2 at 77 K, CO_2 at 195 K, and *n*-butane 272.5 K accompanied by phase transition from *cp* to *op* phase. The unit cell volume difference of *cp* and *op* phases is 254%.[109]

The longer carboxylic linkers 4,4′-biphenyldicarboxylate (4,4′-bpdc) and 4,4′-stilbenedicarboxylate (4,4′-sdc) were used for construction of frameworks isoreticular to the highly flexible pillared layer structure DUT-8(Ni), $[Ni_2(2,6\text{-ndc})_2dabco]_n$ compounds DUT-128(Ni) and DUT-131(Ni). The linker elongation resulted in different structural response towards desolvation and guest adsorption, which is discussed more in detail in section 2.4.

Similarly to $[Ni_2(4,4'\text{-bpdc})_2(dabco)]_n$ DUT-128(Ni), the solvent removal triggers framework contraction in isomorphous $[Zn_2(4,4'\text{-bpdc})_2(dabco)]_n$.[102] However, low N_2 uptake at 77 K (< 50 cm^3/g), and low CO_2 uptake (<100 cm^3/g) at 195 K indicates non-responsive behavior of the compound under these conditions. To alter structural flexibility, the linker was mono-functionalized with nitro groups, leading to 2-nitro-[1,1′-biphenyl]-4,4′-dicarboxylic acid (4,4′-bpdc-NO_2). The incorporation of nitro-groups $[Zn_2(4,4'\text{-bpdc-}NO_2)_2(dabco)]_n$ resulted in almost 4 times higher N_2 uptake (77 K) than that of the non-functionalized analogue.[110]

Further elongation of the carboxylic linker along with functionalization by bulky substituents allowed to produce $[Zn_2(dpt)_2(dabco)]_n$ (dpt = 2,5-diphenylbenzene-1,4-dicarboxylate).[111] This compound undergoes a phase transformation from open pore to the closed pore state. The framework is selectively responsive to CO_2 over N_2 and CH_4 at 298 K, generating a gating isotherm with pronounced hysteresis.

2.4 Parameters influencing switchability

For the technological development of switchable MOFs for applications, a fundamental understanding of the role of critical factors influencing and controlling framework switchability is of utmost importance and will provide a platform for tuning the switching characteristics.[13]

Whether a framework is responsive to a specific stimulus or not depends not only on the crystal structure but on many determining factors (Figure 2-8).[41] The idealized crystal structure, in particular the topology and deformability of the nodes, their hinges and the linkers defines the basis for switchable solids. However, a crystal also has a real structure, finite size, domain architecture, defects etc. presumably also impacting responsivity. The most critical factors severely influencing switchability are structural composition, particle size, surface deformation, domain formation, defects, etc. and these superimpose on network topology and framework composition. Not all of these

factors are easily quantifiable by analytical methods. However, these secondary factors are imprinted into the material by synthesis conditions, desolvation procedures, handling, exposure to atmosphere or defined gases, repeated switching etc. In other words: these secondary factors contain information on the history of the material.[65]
In the following, the main factors influencing switchable characteristics will be considered.

Metal node

One of the crucial factors affecting the switchability of MOFs is their structural composition as the metal clusters, organic linker and their connections can form softer or stiffer hinges. The impact of the metal nodes on the switchability of MOFs has been previously discussed in the literature.[6, 48]
In general metal-dependent switchability is influenced by electronic configuration of the metal, which in turn determines the metal-ligand interaction strength.[55] Consequently, the structural changes are caused by coordination geometry change, deformation of the cluster or linker rotation.[55]
Switchability in the breathing MIL-53 series ($[M(OH)(bdc)_2]_n$ (M = Cr,[67] Al,[68] Fe,[112] Sc,[113] In,[114] Ga[115]) strongly depends on the metal centre. The Cr-, Al- and Ga-analogues of MIL-53 reversibly transform from large pore form (17 x 13 Å) to narrow pore form (19 x 7 Å) in one-step upon hydration/dehydration. Meanwhile, dehydration at elevated temperature triggers two-step transformation via the intermediate and narrow pore forms in Fe- and Sc-counterparts.[24].
Pillared layer MOFs represent the class of porous coordination frameworks with representative switching transitions. DMOFs with the composition $[M_2(bdc)_2(dabco)]_n$ (M = Zn,[90] Co,[116] Cu,[100] Ni[117]) demonstrate contractive/expansive behaviour during desolvation/resolvation.

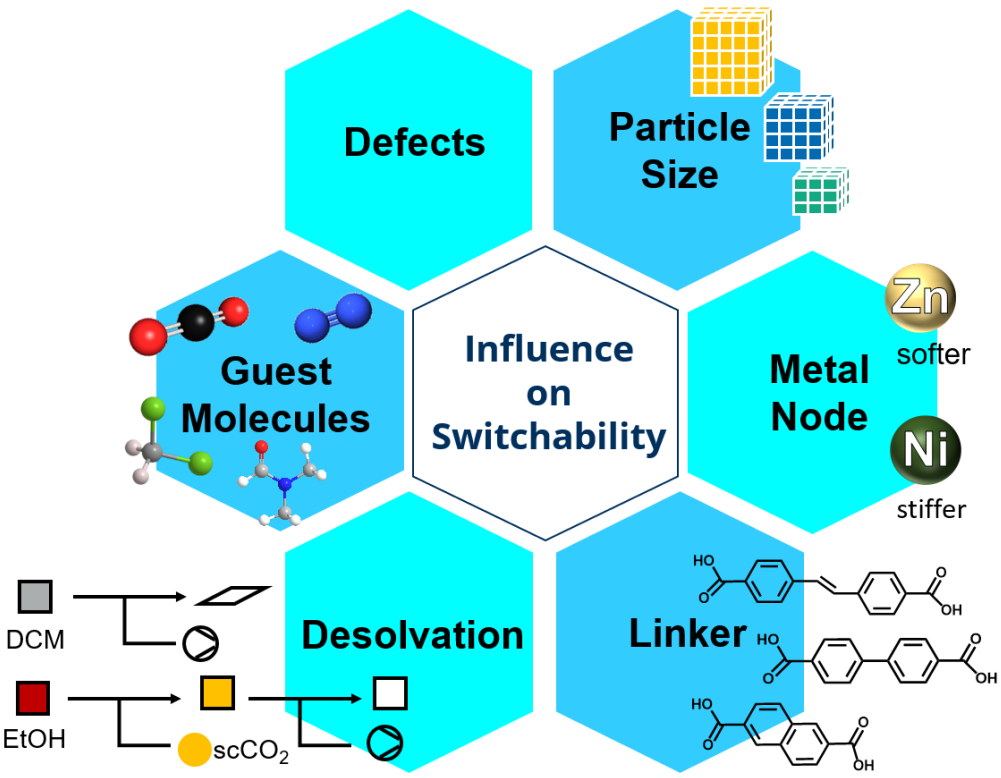

Figure 2-8. The factors influencing the switchable behavior of MOFs.

Similarly to DMOFs, pillared-layer DUT-8 system $[M_2(2,6\text{-ndc})_2(dabco)]_n$ be synthesized using Ni^{2+}, Co^{2+}, Zn^{2+} and Cu^{2+}.[15] The electronic structure of the metal significantly influence the stiffness of the paddle wheel unit and its tendency to deformation.[16] The macro-sized (>1 μm) crystals of DUT-8(M), (M = Ni, Co, Zn) transform from the open pore structure (*op*) to the closed pore structure (*cp*) upon the guest-molecule removal, while DUT-8(Cu) remains in the *op* phase.[15] Adsorption of gases with low adsorption enthalpy induces the reverse transition and opening of the DUT-8(Ni) crystal structure. Both DUT-8(Co) and DUT-8(Zn) retains *cp* phase upon adsorption of different gases (N_2 at 77 K, CO_2 195 K, C_4H_{10} at 273 K). The main reason for significant differences in the framework responsivity is the difference in the deformation mode of paddle wheel unit as was shown by Ehrling et al.[16] A very strong distortion from the square-pyramidal coordination geometry of Ni leads to the O–Ni–O angles between 61° and 110° in DUT-8(Ni)_*cp*. Concerning DUT-8(Co)_*cp*, only minor changes were revealed in the coordination geometry of the Co cluster with corresponding O–Co–O angles between 91° and 97°. However, the shear deformation the $Co_2(COO)_4$ unit alters remarkably the angle between he N···N (dabco) and M···M (PW) axes. The corresponding M–M–N angle in DUT-8(Co)_*cp* is smaller (141.5°) in

comparison with DUT-8(Ni)_*cp* (153.9°), pointing on a softer paddle wheel cluster. The theoretical calculations explain the metal-dependent switchability of DUT-8(M) based on energetic contributions, such as strain energy (energy required for cluster deformation upon framework closing) and dispersion energy (energy gain caused by attractive interactions between the 2,6-ndc linkers).[16, 118] These energetic contributions determine the total energy change $\Delta E_{(cp\text{-}op)}$, which constitutes -86 and -91 kJ mol^{-1} for DUT-8(Ni) and DUT-8(Co), respectively. As a result, the *cp* phase of DUT-8(Co) is more stabilized in comparison with DUT-8(Ni). Therefore, more energy is required to induce phase switching in DUT-8(Co) compared to DUT-8(Ni). Among the investigated adsorptives, only dichloromethane triggers framework reopening of DUT-8(Co).[16]

The flexible Co(bdp) and Fe(bdp) frameworks exhibit gating isotherms upon methane adsorption.[82] In the Co-based framework, methane-induced *cp*-to-*op* phase transition occurs at 16 bar, generating hysteresis loop with gate-closing at 7 bar. For the Fe analogue, framework opening and closing are observed at 24 bar and 10 bar, respectively. The higher gate-opening pressure is associated with a higher energetic barrier for phase transition. Co(bdp) was shown to be the adsorbent with the highest values of usable CH_4 capacity, reaching working capacity of 155 cm^3 at 25°C for CH_4 storage at 5-35 bar, while Fe(bdp) achieves 150 cm^3 at the same conditions.

Another example of the impact of metal identity on switchable behavior was shown in a series of isonicotinate-based flexible MOFs [$M(4\text{-}PyC)_2$] (M=Mg, Mn, and Cu; 4-PyC = 4-pyridine carboxylic acid), where the strength of the metal−nitrogen bonds decreases from $Mg^{2+} < Mn^{2+} < Cu^{2+}$.[108] The isomorphous $Mg(4\text{-}PyC)_2$ and $Mn(4\text{-}PyC)_2$ compounds crystallize in the monoclinic space group $P2_1$ with structure based on an octahedral coordination geometry of the metal node, which is coordinated by four oxygen atoms of carboxylates and two nitrogen atoms from pyridine. In case of $Cu(4\text{-}PyC)_2$ (monoclinic space group $P2_1/c$), the coordination geometry of Cu is tetragonal pyramidal formed by three oxygen atoms of monodentate carboxylate groups and two nitrogen atoms from two pyridine units. As a result, the Cu-based compound has open metal sites (OMS). The three flexible MOFs are characterized by different guest-responsive nature (C_2H_4, C_2H_6, Xe, Kr, and SO_2). The altered structural response was shown to be related to chemical hardness of transition metal ions and the strength of the coordination bond. The gating behaviour induced by C_2H_4 and C_2H_6 are observed for $Mg(4\text{-}PyC)_2$ and $Mn(4\text{-}PyC)_2$, whereas $Cu(4\text{-}PyC)_2$ is responsive only to C_2H_4. It

was assumed that the structural changes in the Cu-MOF, is driven by the rotation of pyridine units and can be triggered by strong π interactions of C_2H_4 with OMSs. Meanwhile, only a partial pore opening is observed upon adsorption of C_2H_6 with weak van der Waals interactions. It was also shown that gate-opening pressures vary depending on the metal node. In particular, the gate-opening pressures for C_2H_6 and C_2H_4 of Mg-MOF were 52 and 132 mbar, respectively, while those for Mn-MOF were 186 and 266 mbar, respectively. The structural response of Mg-based MOFs occurs at lower gate-opening pressure, therefore the structure is more flexible, which in turn depends on chemical hardness of the metal ion. In this case, the chemical hardness of Mg^{2+} is stronger than that of Mn^{2+}, resulting in the weaker Mg−N bond, contributing to easier structural transformation in $Mg(4\text{-}PyC)_2$.

The impact of linker

In principal, the linker-based switchability involves dispersion interactions, including π–π interactions and hydrogen bonding, which may contribute to the stabilization of the contracted phases. The framework switchability can be tuned by variation of linker functionalization or organic linker length.[6]

- Linker functionalization

The chemical functionality of linker remarkably influences the framework switchability in MIL-53(Fe). In particular, the incorporation of the following functional groups –Cl, –Br, $–CH_3$, $–NH_2$, $–(OH)_2$, $–(COOH)_2$ and$–(CF_3)_2$ into 1,4-bdc linker allows to tune framework contraction/expansion.[6] Upon desolvation the guest filled *op* phase of MIL-53(Fe) transforms into *cp* phase. The degree of framework contraction depends on the nature of functional group, which results in the specific host-guest interactions. Most of the functionalized MIL-53(Fe) undergo framework expansion upon solvation in water, ethanol, pyridine, tetrachloroethane. However, some of the functional groups such as $–NH_2$, $–(OH)_2$, $–(COOH)_2$ may contribute to the intra-framework H-bonding interactions the bridging μ^2-OH groups of the framework. For instance, MIL-53(Fe) $–(COOH)_2$ remains unresponsive upon exposure to different solvent, pointing on the strong H-bonding interactions, which prevent pore opening.[6]

The functionalization of bpb (1,4-benzenedipyrazolate) linker in Co(bpb) allows to tune gate-opening pressure upon methane adsorption from 1 to 70 bar at 25°C.[119] The desolvation of framework leads to the phase transition from *op* to *cp* phase due to edge-to-face π–π interactions with neighboring benzene rings of linker. It was shown

that fluorination of bdp linker leads to the disruption of the edge-to-face π–π interactions in Co(F-bpb). As a result, adsorption-induced reopening occurs at lower pressure (8 bar) in comparison with non-functionalized Co(bpd) (18 bar) pointing on the destabilization of *cp* phase. Moreover, deuteration of the linker does not influence significantly on the structural transformations upon adsorption, resulting in the almost identical adsorption profiles. On the contrary, the functionalization of the linker with methyl groups enhances π–π interactions, stabilizing *cp* phase. However, upon methane adsorption no phase transition was observed below 70 bar, instead exhibiting type I isotherm. On the contrary, stepwise nitrogen adsorption isotherm at 77 K was recorded, pointing on the phase transition. Therefore, it was hypothesized that CH_4-induced phase transformation is not detectable at measurement conditions (1-70 bar at 25°C) and may occur at higher pressure.

- Linker elongation

The integration of an elongated carboxylic ligand (L) into the $[M_2(L)_2(dabco)]_n$ system allows to tailor switchable behaviour for Ni-based frameworks.[120] The longer carboxylic linkers 4,4′-bpdc and 4,4′-sdc were used for construction of $[Ni_2(4,4'\text{-bpdc})_2dabco]_n$ DUT-128(Ni) and $[Ni_2(4,4'sdc)_2dabco]_n$ DUT-131(Ni) frameworks isoreticular to the highly switchable pillared layer structure DUT-8(Ni) $[Ni_2(ndc)_2dabco]_n$. The linker elongation resulted in different structural response towards desolvation and guest adsorption. Similar to DUT-8(Ni), the solvent removal under vacuum leads to a structural transformation from *op* to *cp* state. However, the structural changes in DUT-128(Ni) are irreversible, which is attributed to paddle wheel disintegration due to optimum linker stacking and maximal dispersion energy gain. The phase transition in DUT-131(Ni) is accompanied by change in the coordination geometry of Ni atoms, change of angles Ni-Ni-N and O-Ni-O, and an increase of the distance between the two nickel atoms within the paddle wheel. Despite of these changes, the integrity of the paddle-wheel is preserved. The framework is structurally responsive to DCM and a few aprotic polar solvents. Independent on activation conditions, DUT-131(Ni) transforms to a dense closed pore phase due to the strong dispersive interactions between the linkers. Upon the supercritical desolvation, the reduced stress acting on DUT-128(Ni) leads to the trapping of a metastable open pore state, which is attributed to the smaller energy difference $\Delta E_{(op-cp)}$. Depending on the nature of adsorptive (weakly or strongly adsorbing), the metastable *op* phase of DUT-128 behaves as rigid

material resulting in type I isotherm or as switchable framework exhibiting a breathing-like (*op−cp−op*) behaviour.

Host-guest interactions

As discussed above, the switchability of metal-organic frameworks originates from the dynamics of the organic linker, paddle wheel or other secondary building unit. These structural transformations can be induced by the incorporation or removal of guest molecules. Thus, depending on the nature of guest molecules, different structural response can be observed.

In the review of Krause et al,[52] it is highlighted that in soft systems, guest adsorption occurs only when the structural deformation energy (E_{def}) is lower than the interaction energy (E_{int}) of the MOF and guest molecules, and also that between the adsorbed guest molecules. The energy difference between the empty *op* and *cp* frameworks is defined as deformation energy (E_{def}).[52] The guest–guest, host–guest interaction as well as E_{def} significantly influence the pressure range of phase transition. When there is no transition, E_{def} is positive upon guest-free conditions, while E_{int} is negative due to guest–host and guest–guest interactions. The adsorption of guest molecules leads to the increase of E_{int}, therefore energy gain overrides E_{def}, stimulating the structural transformation. As a result, the phase transition is possible when $E_{tot} < 0$ (the total energy of the system defined as sum $E_{def} + E_{int}$).[52] E_{def} can be modulated in order to change the adsorption-energy profile of guests for molecular recognition as was shown in the two-fold interpenetrated network $[Zn_2(1,4\text{-bdc})_2(bpy)]_n$.[121] The framework transforms reversibly from guest-containing open phase to a dense guest-free phase. The coexistence of subnetwork distortion and displacement in framework $[Zn_2(1,4\text{-bdc})_2(bpy)]_n$, allows to encode hydrogen-bonding interactions by means of amino-functionalization of the bdc linker, resulting in $[Zn_2(NH_2\text{-bdc})_2(bpy)]_n$ (NH_2-bdc = 2-aminoterephthalic acid). The hydrogen bonding between amino groups and oxygen atom on paddle wheel increases the E_{def} during transition from the dense to the open framework in comparison with the pristine compound. A dense-to-open transformation is induced by N_2 and CO_2 only in $[Zn_2(bdc)_2(bpy)]_n$, meanwhile the amino-functionalized analogue is structurally not responsive. Such behaviour indicates a higher E_{def}, therefore flexibility is supressed. However, the hydrogen bond lock can be selectively broken by $CHCl_3$ adsorption in $[Zn_2(NH_2\text{-bdc})_2(bpy)]_n$, producing a typical gating isotherm. Meanwhile, adsorption of CH_2Cl_2 leads to typical type I isotherm,

pointing on the enhanced host-guest interactions, which in turn do not lead to open pore structure, due to the increased E_{def} for the $[Zn_2(NH_2\text{-bdc})_2(bpy)]_n$.[121]

Considering, the structural transformations caused by solvent removal, depending on the guest molecules present in the pore and desolvation technique applied, the forces acting on the framework can be varied[122, 123] and indirect information of the relative robustness of the network can be extracted.

Activation-dependent structural responsivity was investigated in the non-interpenetrated pillared-layer framework $[Zn_2(dpt)_2(bpy)]_n$ constructed by zinc paddle-wheel units, dpt (2,5-diphenylbenzene-1,4-dicarboxylates) and bpy.[111] The different activation conditions significantly influenced the structural response upon solvent removal. The conventional thermal evacuation resulted in a mixture of crystalline phases. A common approach to reduce the stress upon activation, the exchange with a volatile solvent prior to vacuum activation, yielded the pure contracted phase, which is selectively responsive towards CO_2 over N_2 and CH_4. The gentle supercritical drying technique yielded the guest-accessible open pore phase.

Crystal size and morphology

The influence of the crystal downsizing on the structural transition characteristics in classical materials (alloys, organic compounds) stimulated by temperature or mechanical pressure was intensively studied in the past, showing pronounced particle size dependence.[124, 125] The postulated observations could be rationalized, considering the internal pressure and surface energy differences between polymorphs, confinement effects, and nucleation theory.[124-127]

The impact of the crystal size on functional properties of MOFs has also received considerable attention.[101, 128-131] It was recognized that, by changing the particle size, the intermolecular interactions between the adsorbent and adsorbate, the catalytic performance of the MOF, and the magnetic properties can be tuned.[9, 132, 133]

Downsizing of switchable MOF crystallites to the nanoscale regime not only alters their adsorption profiles, but also generates new intrinsic features differing from the bulk MOFs.[18, 101]

Previous experimental and computational approaches revealed the effects of the crystal size on the structural switchability in several representative MOFs.

The particle size dependent switchability was firstly reported by Kitagawa et al. for compound [Zn(ip)(bpy)]·DMF (H_2ip = isophthalic acid), which represents interdigitated

structure of 2D layers.[10, 134] The bulk crystals (5 μm wide × 20 μm long) and nano-sized crystals (5 nm wide × 320 nm long) show different degree of framework contraction upon desolvation under vacuum at 130˚C (decrease of unit cell volume of 3.2% and 2.1%).[134]

The group of Kitagawa also reported that crystal size modulation leads to the new properties, which are absent in bulk crystals. As was already mentioned in Section 1.2.1, macrocrystals of the pillared layer framework $[Cu_2(bdc)_2(bpy)]_n$ show an open pore (*op*) to closed pore (*cp*) structural transition upon guest desorption.[101] The main feature of this compound is that crystal downsizing induces a so-called sorbate-induced shape-memory effect. Upon adsorption of methanol (303 K), crystals in a certain size regime (1 μm) can adopt a metastable phase open pore state, which is maintained even after desorption, and only by thermal treatment the closed pore phase can be recovered. Meanwhile, the bulk crystals undergo reversible adsorption-induced phase transition.

A similar effect was reported for 3-fold interpenetrated framework $Zn_2(bpdc)_2(bpb)]_n$.[103] The sorbate-induced shape-memory effect was promoted by several gases N_2 (77 K), CO (82 K), and CO_2 (195, 298 K). The denser activated phase β is transformed to an intermediated phase γ upon adsorption of guests, which is retained after desorption. The resulting γ phase is a kinetically stable form, retaining the structure over multiple adsorption/desorption cycles with type I isotherms. The transformation from γ to β phase is a temperature driven process at >400 K under vacuum.

Sakata et al. proposed two possible explanations of the particle-size dependent phase transitions, which are based either on solid-phase thermodynamics or on kinetic effects.[81, 101] The decrease of particle size leads to the increase of surface-to-volume ratio. As a result, the increased surface enthalpy contributes to the stability of the guest-free *op* phase over the *cp* phase and reduces the thermodynamic driving force for the transition.[81, 101]

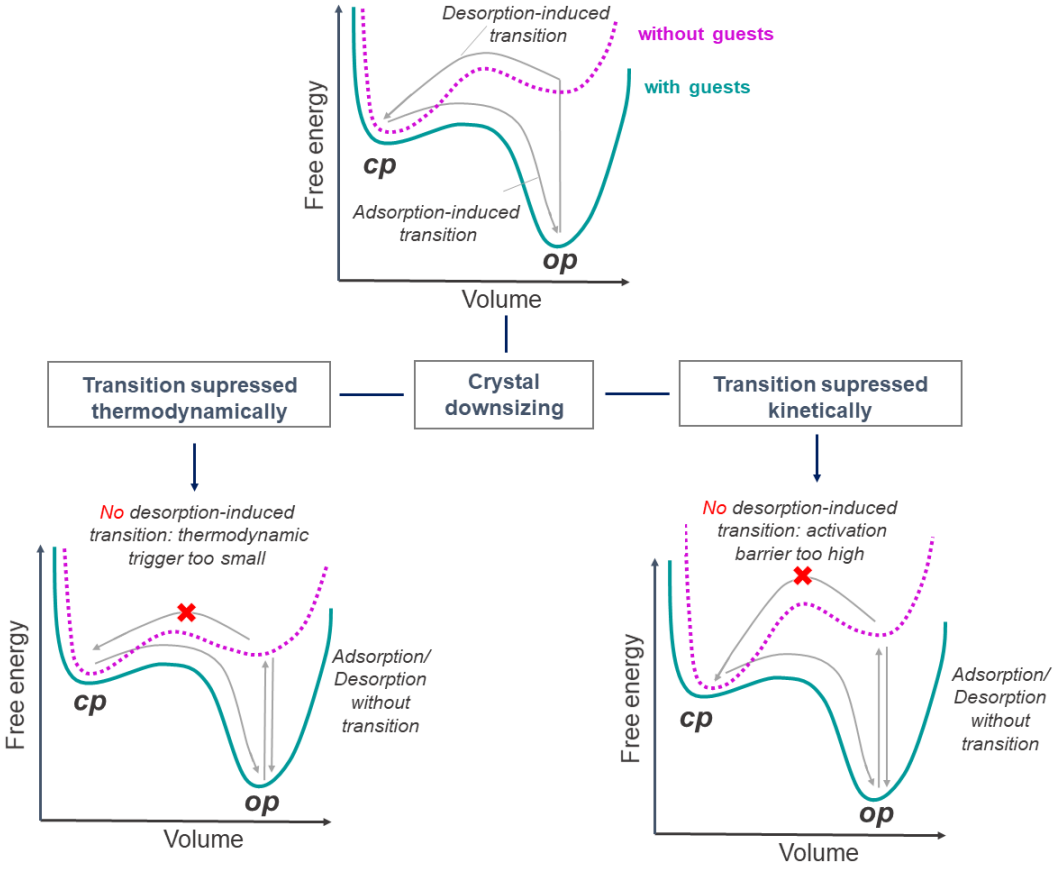

Figure 2-9. Schematic representation of the free energy profiles with (cyan) and without (pink) guests in MOF. Top: guest adsorption/desorption triggers a phase transition between *op* and *cp* state. Bottom: upon crystal downsizing, the *op*-to-*cp* transition is suppressed, either thermodynamically due to too small a free energy difference between the *op* and the *cp* state (left), or kinetically due to too high activation barrier between the *op* and *cp* state (right). Adapted from ref.[81](CC BY 4.0).

Furthermore, the suppressed switchability of MOFs can be considered from a kinetic point of view. In this regard, defects are considered to serve as preferential nucleation sites, facilitating the nucleation of new phase. The presence of defects is supposed to lower the barrier height, which reflects the activation energy for transition. Smaller crystals contain fewer defect sites, causing the increase of the activation barrier between both phases (Figure 2-9).[81, 101]

Several studies are devoted to crystal size engineering of ZIF-8 influencing adsorption-induced transitions. In ZIF-8 the phase transition is accompanied by a reorientation of the linkers, which leads to a stepwise nitrogen adsorption isotherm with a hysteresis loop at elevated relative pressure.[135] Commonly in ZIF-8, the gas pressure of nitrogen required to provoke gate opening is shifted towards higher pressures and the hysteresis loop becomes broader upon crystal downsizing.[128, 131, 135] By reaching the nano-sized regime the framework becomes rigid. The theoretical investigations

revealed the contribution of crystal interior, crystal surface, as well as interfacial region. The increased surface-to-volume ratio of the nanoparticles leads to reduced loading of guest molecules in the surface region and hence an insufficient thermodynamic driving force for guest-induced transition.[131] Another explanation of the supressed flexibility in smaller crystals is based on the influence of the surface barrier on the overall mass transfer resistance and increased surface resistence.[135]

Similarly, to the work of Tanaka et al, a series of ZIF-8 materials with different particle size were investigated.[128] In ZIF-8 particle downsizing (from 98 to 0.14 μm) leads to a shift of the gate pressure to higher values and a wider hysteresis, suggesting a higher energy barrier for phase transition, therefore higher kinetic hindering. Watanabe et al., using GCMC simulation showed that the width of the hysteresis loop was inversely proportional to the energy barrier.[136] Since the particle size decrease contributes to different adsorption behaviour at thermodynamic equilibrium conditions, the adsorption kinetics can also vary significantly. The adsorption kinetics can be studied by the measurement of equilibration time of each point of the adsorption isotherm. It was shown in ZIF-8 materials that for smaller particles longer equilibration times are needed in the low-pressure region before the phase transition occurs in comparison to larger crystals. However, the slower kinetics at the gating pressure region is associated with reorientation of mIM rings, increasing the access for guest molecules into the cavities, and therefore the phase transition. After reconfiguration of the pore shape, the equilibration times were shortened irrespective of particle size.

The crystal size-dependent switchability is characteristic for pillared-layered MOF DUT-8(Ni). The macro-sized (>1 μm) crystals of DUT-8(Ni) reversible transform from *op* to *cp* phase upon the guest-molecule removal/adsorption. However, cycled adsorption of *n*-butane (298 K) leads to the reduction of the crystal size which is accompanied by a shift of the “gate pressure” to higher values in the nitrogen (77 K) and *n*-butane (298 K) adsorption isotherms.[137] The crystal size of DUT-8(Ni) can be tuned by micromixer synthesis, controlling the nucleation process and crystal growth by the contact time of starting materials and aging time.[18] The variation of the crystal size in the micrometer range leads to changes in the slope of the nitrogen adsorption isotherms. Crystal downsizing to the submicron range enables the trapping of the material in a metastable, open, solvent-free phase and transforming it to a microporous rigid adsorbent.[17]

The modulation of crystal size and associated changes in structural responsivity was revealed in Zr-based MOF, termed as DUT-98 with composition $[Zr_6O_4(OH)_4(cpcdc)_4(H_2O)_4]_n$, where cpcdc = (9-(4-carboxyphenyl)-9H-carbazole-3,6-dicarboxylate).[138] Its structure contains 1D channels with a diameter of 9.8 Å, representing a wine-rack framework topology. The solvent removal process is accompanied by a framework contraction with massive cell volume shrinkage of 40%. The framework contraction is accompanied by a rearrangement of all hydrogen bonds between the non-coordinated carboxylate oxygen atoms, the water molecules, and hydroxyl groups, coordinated to the cluster with subsequent change of the coordination mode of two carboxylates.[51] It was also revealed that upon transition, the linker bends slightly, the carboxylates twist out of the carbazole plane, as well as the knee-cap angles between the carbazole carboxylate and corresponding Zr atoms increase.[51] Various guest molecules, including N_2 (at 77 K), CO_2 (at 195 K), *n*-butane (at 273 K), and various alcohols (at 298 K) are able to induce the pore expansion generating an isotherm with distinct steps that are typical for gate-opening MOFs.[138] However, the characteristic feature of this framework is the structural expansion with pronounced pressure reduction which is known as “negative gas pressure”. The artificial pressure drop upon framework reopening is related to metastable adsorption state, as previously described by Kitagawa and co-workers.[139] Interestingly, the cyclic adsorption of nitrogen leads to gradual shift of the gate pressure to lower pressures, which is on the contrary to all reported cases, where the repeated adsorption stress leads to crystal fractionation and higher gate opening pressure. The structural features of DUT-98(Zr) are drastically altered by particle downsizing similarly to ZIF-8 and DUT-8 systems. The ability to transform from open to closed pore phase was supressed. The adsorption profiles exhibits type I and IV, depending on size regime.

The comparison of adsorption behaviour of bulk crystals and nanosheets (NSs) of the 2D framework ELM-11 $[Cu(bpy)_2(BF_4)_2]_n$ reveals a significant difference in the gate-opening pressures in N_2 and CO_2 adsorption.[140] Nanosheets of ELM-11 shows a shift of gate-opening pressure upon adsorption, which is attributed to the decrease of layer spacing due to lattice relaxation, in which lattice constants gradually decrease at the surface of crystals, because NSs have a large specific surface area.

In the examples discussed above, downsizing of the crystals leads to suppression of the swicthability. However, in some limited examples, the structural transformations can be induced by decreasing the crystal size.[9, 81]

Such particle size-dependent structural switchabiliy greatly influenced the water intrusion performance in ZIF-7 ($Zn(PhIm)_2$, PhIm: benzimidazolate), a typical representative of ZIF family.[141] The framework is composed of Zn clusters and benzimidazolate linkers. Several phases of ZIF-7 are known, namely as-synthesized rhombohedral unit cell ($R\bar{3}$ space group) - ZIF-7 (I), guest free ZIF-7-II with a triclinic unit cell ($P\bar{1}$ space group) and two-dimensional (2D) layered architecture ZIF-7-III with monoclinic unit cell (C2/c space group). All three phases can be obtained in micron-sized and nano-sized regime. The pressure-induced water infiltration effect was detected only for nano-sized ZIF-7-II phase associated with a structural deformation. The inaccessibility of the bigger crystals was related to the suppressed flexibility, meanwhile the enhanced interaction of nanosized crystals with water, as a result of the pore window opening effect, was assumed to be driven by the increased surface area.

The enhanced flexibility induced by particle size decrease was found in the breathing system amino-functionalized MIL-53(Al).[12] The modulation of particle size simply was achieved by controlling the solvent ratio (DMF/water). The particle downsizing facilitated the phase transition, therefore increasing the deliverable capacity of methane by 33%.

Another examples of the emerged switchability upon particle downsizing was revealed in $Fe(py)_2[Pt(CN)_4]$ compound.[142, 143] The bulk crystals are not responsive towards EtOH due to the strong interlayer π–π interactions of pyridine ligands. Meanwhile, the π–π interactions between layers are decreased in nano-sized crystals (16 nm). As a result, the structural transformations are observed upon adsorption of EtOH, leading to typical gating isotherm.

Based on the considered examples, the modulation of crystal size of MOFs can either enhance or supress the stimulus-induced structural responsivity, resulting in different type of isotherm (Figure 2-10). In particular, gating (Figure 2-10a) or breathing (Figure 2-10b) behaviour of macro-sized crystals is suppressed by downsizing which leads to a type I isotherm in rigid crystals. Most frequently, gate-shift and hysteresis widening (Figure 2-10c) is observed upon particle size decrease. In some systems, switchability is promoted by nanosizing (Figure 2-10d).[9]

In addition to experimentally revealed particle-size dependent switchable behaviour of MOFs, theoretical calculations demonstrated the contribution of crystal surface and phase coexistence.[81] Keupp et al. investigated DMOF-1 nanocrystallites showing that

phase transitions preferentially initiated at the crystal surface.[144] In the work of Rogge et al,[145] the investigation of mesosized crystals allowed to hypothesize that the transition barrier decreases with increasing crystal size due to the occurrence of phase coexistence.[81,145]

A few studies dedicated to the crystal shape and its role on the characteristics of structural transition have been published so far.[146, 147]. In flexible MOFs, where the transitions are often adsorption driven, the transition characteristics may be influenced not only by the particle size but also by the crystal habit. The pore structure and pore connectivity, as well as associated pore accessibility, may determine the adsorption-induced phase transitions in porous materials. An important aspect, in particular for gate opening systems, is that the activation barrier for gate opening is mechanistically connected to the pore entry of the adsorptive into the framework. In this sense, nucleation is expected to begin on the outer surface of the crystal, and the morphology is expected to affect nucleation barriers significantly for a given adsorptive.

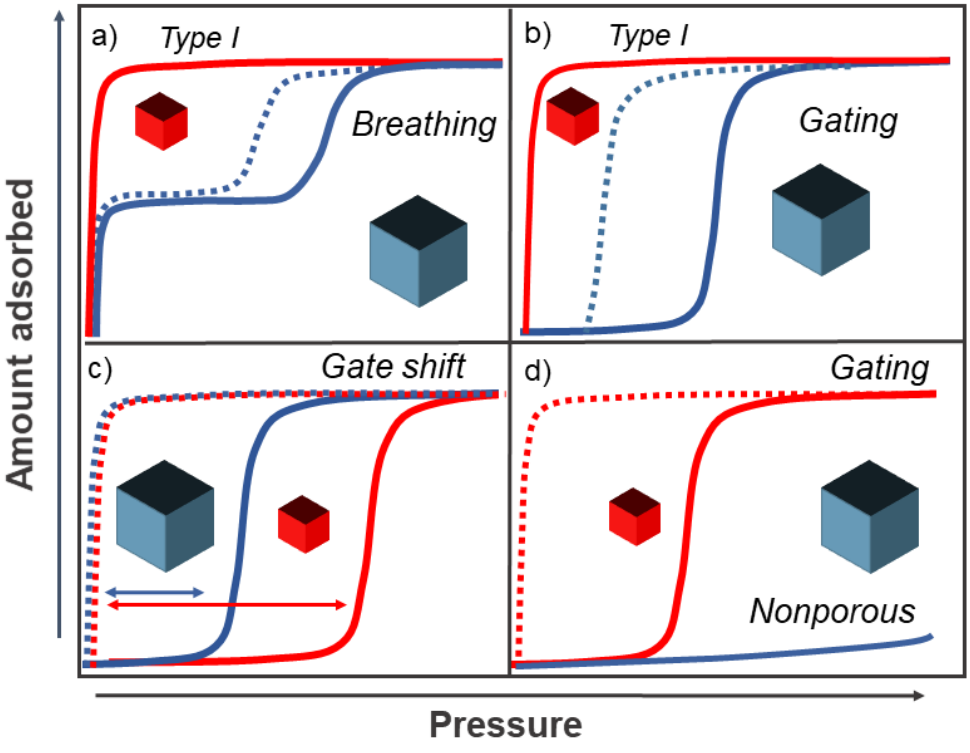

Figure 2-10. The influence of crystal downsizing on adsorption profiles.
Adapted from ref.[9] (CC BY 4.0)

In the ZIF-8 system not only particle size influences adsorption behaviour, but also crystal shape affects significantly phase transition process upon adsorption. Watanabe et al. produced a series of ZIF-8 with different particle sizes ranging from 50 nm to 1.8 µm and different morphologies, including cube, chamfered cube and rhombic dodecahedron using a microreactor.[146] Remarkably, differently shaped crystals need different energy input gained by adsorption in order to increase the pore space by linker reorientation. In particular, the phase transition pressure for the cubic shaped particles is lower than that of the rhombic dodecahedron shaped particles, whereas the gate closing pressure is almost the same. The gate closing can be described as an equilibrium process because the equilibrium transition pressure is close to the gate closing pressure. The difference in gate-opening pressure was ascribed to the surface energy of the present faces. The crystals with cubic-like morphology are formed by {100} faces, rhombic dodecahedral particles composed of only {110} face. The calculation of surface energy revealed that the surface energy of the {100} face is higher than that of {110} face, which in turn leads to higher stability of {110} faces. As a result, the energy barrier for phase transition is increased.
The mentioned studies provide an indication for a mechanism associated with interior and exterior defects, crystal surface, phase coexistence which may be involved in adsorption induced transformation. However, there are still open questions, which are addressed in the following chapters.

Defects and disorder

As reported by Bennett *et al.* flexibility, defects and disorder in MOFs are certainly interdependent.[148] The defects can generated by defect engineering approach particularly in mixed metal MOFs,[149] multivariate linker MOFs,[150] post synthetic linker/metal exchanged systems[151]. However, there are also classical defects[152], such as cluster or linker vacancies, dislocations, cracks, or inclusions, which may exist in MOFs, influencing the switchability of the crystals.[153]
For the explanation of particle-size dependent switchability it was assumed that defects to serve as preferential nucleation sites, facilitating the nucleation of a new phase.[81, 101] The presence of defects is supposed to lower the barrier height, which reflects the activation energy for phase transition.[81, 101]

The presence and amount of defects significantly influence mechanical properties of MOFs.[154] Concerning, the defect-dependent switchable behaviour, it was investigated in DUT-8(Ni) compound $[Ni_2(ndc)_2dabco]_n$, which can be synthesized as macro-sized (switchable) and submicron-sized (rigid) crystals. By means of electron paramagnetic resonance (EPR) spectroscopy, it was revealed that submicron-sized (rigid) crystals may contain high defect concentrations (defective paddle wheel units with only one Ni^{2+} ion, missing ndc, dabco).[155] However, the presence of defects did not contribute to softening, since submicron-sized DUT-8(Ni) maintain the *op* phase upon solvent removal. As stated in review,[9] defect-induced softening seems not to be effective in this case. The presence of defects may contribute to reduced dispersive interactions which are considered to be the driving force for transition from *op* to *cp* phas.[9]

The compositional or orientation disorder may also influence the structure/property relationship of MOFs.[152] In particular, the orientational disorder was found in DUT-8(Ni), which originates from nonlinear 2,6-ndc linkers.[156] The arrangement of linkers can be either up or down in the positions of the neighbouring paddlewheel pillars. It was shown that different solvents induce the switching between disordered frameworks by overcoming the ~20 kJ mol^{-1} barrier to ndc 'flips'.

Chapter 3 Characterization methods and Experimental section

3.1 Adsorption methodology

3.1.1 Terms and definitions

Porous materials, containing empty space, which can be easily occupied by guest molecules, are typically characterized by gas adsorption methodology, evaluating textural characteristics, such as specific surface area, total pore volume, pore size distribution.[157]

Among traditional porous materials such as zeolites, activated carbons, porous glasses and aerogels, MOFs stands out in terms of porosity and surface area.[122] Since the 3rd generation of MOFs demonstrates stimuli-responsive behaviour, most frequently adsorption-driven,[52] it is important to consider the terminology and basic principles of adsorption process.

In principal, the different levels of solid surface are distinguished.[158] The surface atoms with specific van der Waals radii can be considered as fused spheres (Figure 3-1). The outer part of the fused spheres is considered as *van der Waals surface*. The second surface is accessed by physisorption is called *probe-accessible*. This surface can be defined by rolling a probe sphere over the van der Waals surface (mapped out by the center of the probe sphere). The surface mapped out by the inward-facing surface of the probe sphere is known as *Connolly surface* (contact surface), which is typically used in molecular simulations for geometric structure analysis.[159] The crystalline nature of MOFs provides the opportunity to determine textural parameters by Monte-Carlo integration technique.[160]

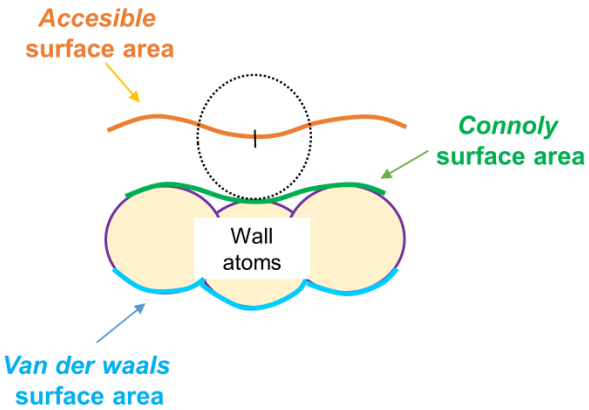

Figure 3-1. Schematic representation of possible surface of adsorbents. Adapted from ref.[158]

When gas molecules are brought in contact with the solid, adhesion (adsorption) of atoms or molecules in an interfacial layer occurs. The reversed process to adsorption is called desorption. The term adsorbent is used for the adsorbing material, meanwhile adsorbate and adsorptive are gases or liquids in the adsorbed state and fluid phase, respectively. The interactions between adsorbent and adsorbate are accompanied by attractive van der Waals forces (physisorption) or chemical bond formation (chemisorption). The former involves chemical bonding of the gas or vapour with the surface, therefore is limited to a monolayer coverage. Moreover, the equilibrium rate is often found to be slow due to insufficient thermal energy for overcoming activation barrier at critical temperature of adsorbate.[158]

Physisortion involves the attractive dispersion forces and the short range repulsive forces, specific molecular interactions (e.g., polarisation, field-dipole, field gradient-quadrupole). Unlike chemisorption, physical adsorption is reversible and may lead to multilayers formation. The equilibrium in physisorption systems can be achieved rapidly since no activation energy is required.[158]

In the context of physisorption, according to International Union of Pure and Applied Chemistry (IUPAC), the porous materials are classified in three groups depending on internal pore width. The pores of microporous materials are not exceeding 2 nm. The pore sizes of mesoporous materials are in the range between 2 and 5 nm. The last group refers to macroporous materials with pore size larger than 50 nm. The pore size of MOFs typically ranges from ultramicro- up to mesoporous.[158]

The sorption process in micropores differs from that of mesopores and macropores. Since macropores are so wide, it is possible to consider them as nearly flat surfaces. The interactions between fluid molecules and the pore walls in micropores leads to overlapping of adsorption potential of the opposite pores. As a result, micropore filling occurs, which is not the case in mesopores and macropores, where surface coverage takes place. In mesopores, several stages of adsorption can be distinguished. Firstly, one layer of adsorbed molecules on the surface is formed, which is then followed by multilayer adsorption. The pore potential is not prevailing anymore in the core of the pores. Hence, adsorption behavior is governed by adsorptive-adsorbent interaction and attractive interactions between adsorbate molecules, which promotes capillary (pore) condensation. In the course of this stage, condensation of gas to a liquid-like phase is possible at the pressure less than saturation pressure p_0 of the bulk fluid.[157]

3.1.2 Physisorption isotherms

The amount gas adsorbed by a solid at constant temperature as a function of equilibrium pressure represents the adsorption isotherm.[158] It is recommended to plot the isotherm with molar quantity of adsorbate (mmol g^{-1}) against the relative pressure (p/p_0), which is the absolute pressure divided by saturation pressure of adsorptive at operational temperature.[158]

The form of adsorption isotherm is related to the pore structure and provides an information about surface area, *porosity* of adsorbent, type of interactions.

Based on physical adsorption, the isotherms were grouped into six types by IUPAC (Figure 3-2). The reversible type I isotherm is characteristic for microporous materials (activated carbons, silicagels, zeolites) having relatively small external surface areas. The micropores width does not exceed several molecular dimensions, consequently the force fields of neighboring pore walls overlap, resulting in the enhanced energy interaction of adsorbent with gas molecules. Such interactions are strong enough to ensure the pore filling at very low relative pressure region, leading to steep uptake.

Type II, III and VI physisorption isotherms are observed for non-porous and macroporous adsorbents. The shape of type II isotherm is dictated by unrestricted monolayer-multilayer adsorption. The isotherm is concave to p/p_0 axis showing a rather steep curve. The start of the linear central section of isotherm is shown by point B, which is an indicator of relative pressure at which a monolayer is formed. The weak adsorbent-adsorbate interactions lead to undefined monolayer coverage in type III isotherms. The amount of gas adsorbed is quite low at low pressure region. Once the molecule is adsorbed, adsorbate-adsorbate interaction forces promote the process and isotherm become convex to p/p_0 axis over its entire range. This type of isotherm is typical for the adsorption of water vapour on nonporous carbons. The type VI isotherm is represented by multistep adsorption profile.

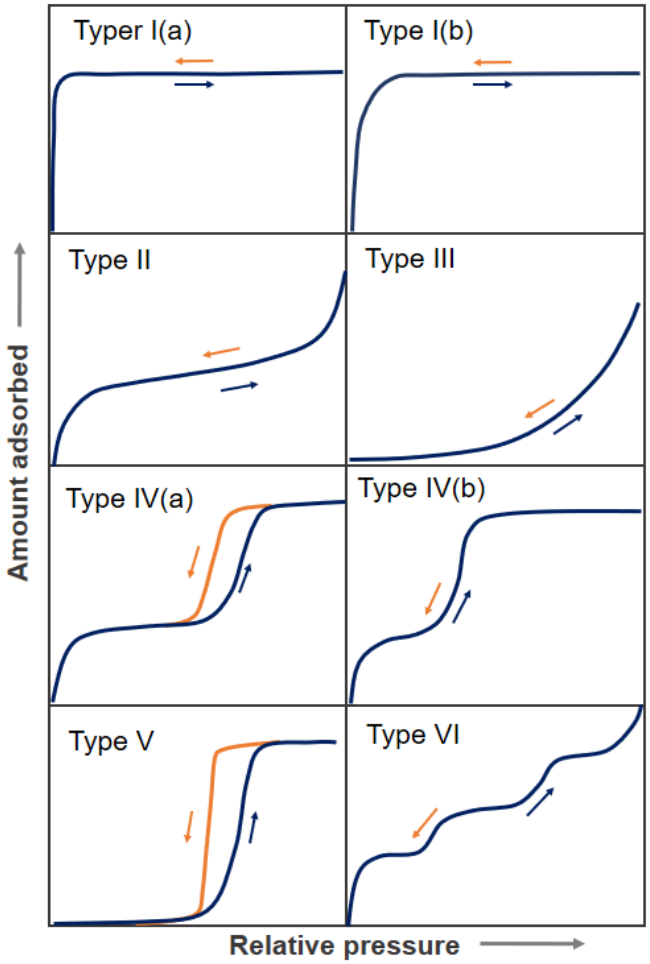

Figure 3-2. The types of isotherms are characteristic for microporous (Type I), nonporous or macroporous (Types II, III, VI) and mesoporous/microporous (Types IV, V) materials. Adapted from ref.[158]

The characteristic feature of mesoporous adsorbents with type IV and V isotherms is a hysteresis loop, which is attributed to capillary condensation in mesopores. In type IV isotherm, the initial part is similar to the type II, reaching the limiting uptake at high p/p_0. The plateau of isotherm points on complete pore filling.

In the low relative pressure range, the initial part of Type V isotherm is similar to Type III, pointing out relatively weak adsorbent–adsorbate interactions. Upon pressure increase, molecular clustering is followed by pore filling.

In both isotherms, the desoption branch does not follow adsorption one, demonstrating hysteresis loop. The correlation between the shape of hysteresis loop and textural properties (pore size distribution, pore geometry, connectivity) can be established. According to IUPAC classification of 1985,[161] which is based on classification by de Boer, four types of hysteresis in the multilayer range of physisorption isotherms were

defined. The porous materials with well-defined cylindrical pores have hysteresis type H1. The wide distribution of pore size results in type H2 hysteresis, which can be attributed bottleneck constrictions. Hysteresis loops H3 (adsorption branch resembles isotherm type II) and H4 (adsorption branch resembles isotherm type I) are observed in nonrigid aggregates of plate-shaped particles with wide and narrow slit pores. The sharp step-down region in the desorption curve referred to the closure of hysteresis loop directed by tensile strength effect (at p/p_0 0.42 for nitrogen at 77 K).

The switchability of the porous solid adds new degrees of freedom in the system resulting in novel adsorption isotherms in which multiple solid-phase transformations are highly coupled to the adsorption process and fluid-phase transitions leading to characteristic hysteresis even for microporous materials.[50] Such archetypical coupled adsorption processes are called gating (closed-to-open pore transition), breathing (open-narrow-open), NGA (open-contracted-open with gas pushout) and multi-step transformations (Figure 3-3).

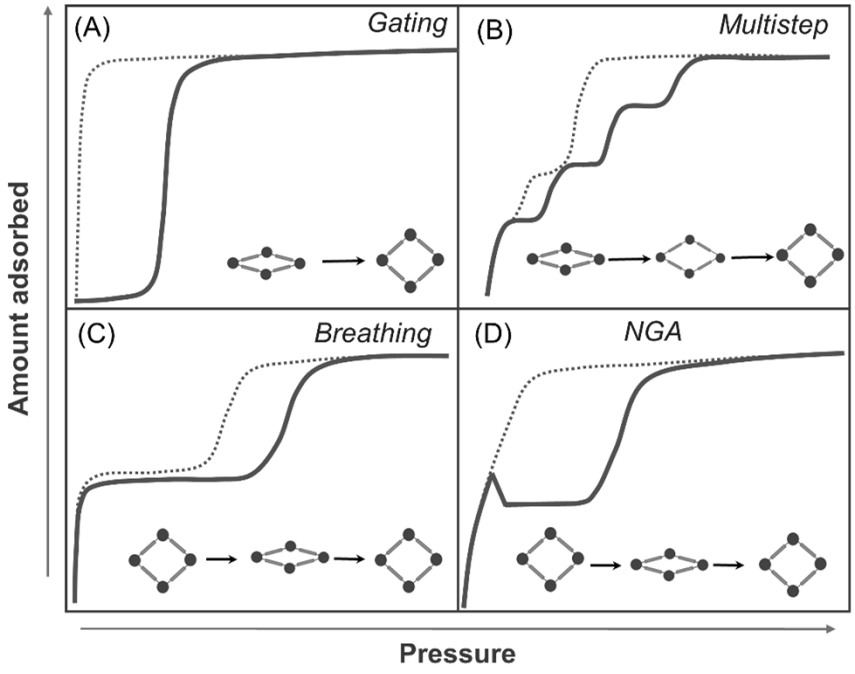

Figure 3-3. The typical adsorption isotherms of switchable MOFs. Adapted from ref.[50] (CC BY 4.0).

3.1.3 Adsorptives

The micropore and mesopore size analysis was mainly based on use of N_2 at 77 K and Ar at 87 K as adsorptive. However, problems arise when it comes to characterization of adsorbents containing surface functional groups. The quadrupole moment of nitrogen influences the specific interaction and therefore molecule orientation on the adsorbent surface, as well as micropore filling pressure. Argon can be used as adsorptive for pore size and surface area determination, due to the lack of quadrupole moment. The experimental benefit of argon adsorption at 87 K is related to micropore filling at higher relative pressure in comparison with nitrogen, therefore enhancing adsorption kinetics.[158]

Nitrogen and argon at cryogenic conditions (77 K, 87 K) have kinetic restrictions accessing the narrow micropores (width <0.45 nm). In order to address these limitations, carbon dioxide (kinetic diameter 0.33 nm) can be used as adsorptive at 273 K.[157, 162, 163] The saturation pressure of CO_2 at 273 K constitutes 34.85 bar, which allows performing the measurement in the range of moderate absolute pressures (0.001-1 bar). Owing to higher temperature and pressure compared with nitrogen and argon (77 K, 87 K), the kinetic of adsorption process is accelerated in ultramicropores.

3.1.4 Specific surface area, pore volume and pore size distribution

Surface area

Two models were developed to describe adsorption phenomena in porous materials. The American Nobel Prize winner Irving Langmuir (1881 - 1957) developed his adsorption theory in the years 1916-1918. The Langmuir model is based on the following assumptions: (I) the solid surface is homogeneous, i.e. there are only energetically the same adsorption sites; (ii) each adsorption site can be occupied only by one molecule; (iii) adsorbates form a monolayer; (iv) adsorption of gas molecules at one site occurs independently of adsorption at neighboring sites.[164]

Langmuir used a kinetic approach to describe type I isotherms and formulated the equation (1), where n/n_m, is the amount adsorbed relative to the amount adsorbed in a completed monolayer, the Langmuir constant k (k^{ads} / k^{des}) describes the ratio of the adsorption and desorption rates and depends on the temperature. Rearrangement of equation (1) gives (2).

$$\frac{n}{n_m} = \frac{kp}{1+kp} \quad (1) \qquad \frac{p}{n} = \frac{1}{kn_m} + \frac{p}{n_m} \quad (2)$$

A plot of *p/n* versus p will give a straight line of slope $1/n_m$ and intercept $1/kn_m$ from which monolayer capacity n_m can be calculated. Afterwards, multiplication of adsorbate cross-sectional area with monolayer capacity and Avagadro´s constant divided by the mass and molar weight of adsorbent result in *specific surface area*.

Since Langmuir model is restricted to the formation of a monolayer, the equation is often only applicable to chemisorption. However, adsorbate molecules bind to specific adsorption sites, making cross-sectional area uncertain, because of spacing between adsorbed molecules.

Nowadays the BET theory is widely used for evaluating surface area of porous materials.[157, 163] The BET model is an extension of the Langmuir model with additional assumptions, which do not restrict physisorption to monolayer coverage. According to BET model, the adsorption mechanism follows the formation of infinite number of adsorbed layers, which can serve as adsorption sites at any pressure $p<p_0$, where p_0 is a saturation pressure of adsorptive at the operational temperature.

The standard protocol of surface area determination includes several stages. Firstly, the physisorption isotherm is transformed into the “BET plot” (Figure 3-4), which is derived from BET equation (3).[165]

$$\frac{p}{(p_0-p)n_{ads}} = \frac{1}{Cn_m} + \frac{C-1}{Cn_m}\frac{p}{p_0} \quad (3)$$

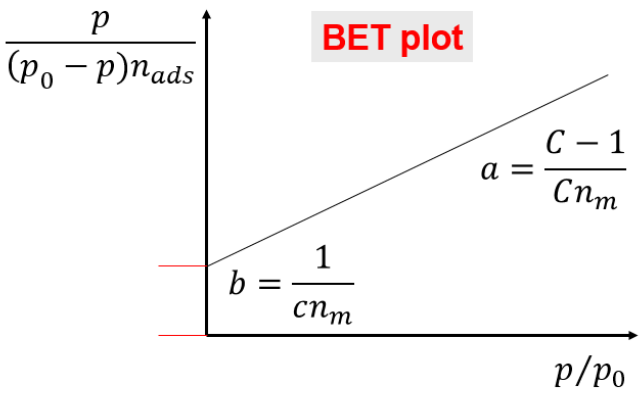

Figure 3-4. Schematic representation of BET plot.

The parameter *C* (4) is associated with the energy of monolayer adsorption and the shape of isotherm. Larger values of *C* (~80) ensure sharp knee on type II and IV isotherms, therefore well-defined point B of monolayer formation and the beginning of multilayer adsorption. If C value is <2, indicative point B disappears, leading to type III and IV isotherms. When C value reaches ~150, the narrow micropore filling occurs.

$$C = \frac{a}{b} + 1 \quad (4) \qquad n_m = \frac{1}{a+b} \quad (5)$$

The linear plot $p/(p_0-p)n_{ads}$ vs. p/p_0 is restricted to a limited part of isotherm within the relative pressure range of 0.05-0.3. From the slope and intercept of BET plot, monolayer capacity can be derived (5). The BET specific surface area of adsorbent (6) can be calculated from the monolayer capacity (n_m), molar weight (M_r) and cross-sectional area of adsorbate (σ for N_2 0.162 nm^2), Avagadro´s number (N_a), mass of sample (m).

$$S_m = \frac{n_m \sigma N_a}{M_r m} \quad (6)$$

The BET equation (3) is applicable to the surface area analysis of nonporous materials, meso- and macroporous materials under controlled conditions (Type II, IV isotherms). In this case, BET area may be compared to the “probe-accessible” area (i.e., the effective area available for the adsorption of the specified adsorptive). In the presence of micropores and narrow mesopores (<ca. 4 nm), the BET theory is not strictly applied, because it is quite difficult to distinguish between the process of mono- and multilayer adsorption from pore filling. For choosing the appropriate range for analysis, Rouquerol and Llewellyn suggested a set of rules (consistency criteria) which the chosen pressure range should comply with.[166]

(i) The analysis should be limited to the range in which the term $n(1-p/p_0)$ increases continuously as a function of the relative pressure p/p_0.

(ii) The value of the BET constant *C* resulting from the linear fit should be positive. To give meaningful results the *C* constant should have a value of at least 10.

(iii) The BET monolayer capacity n_m calculated from the linear fit corresponds to a certain relative pressure, which must be located within the linear region chosen for the area calculation.

This procedure is useful for determination of linear BET range, but it does not ensure the validation of the BET monolayer capacity. BET area of microporous materials

represents apparent surface area reflecting the number of molecules with the strongest interaction (first monolayer), which is not identical to the calculated accessible geometric surface area.[158, 162, 163]

It is known that BET model is based on multilayer adsorption on flat surfaces. However, the inner surface of MOFs is typically not flat, this is why the validity of this method for the evaluation of surface area was under question.[167] However, the theoretical calculations confirmed the meaningful data obtained by BET method.[167, 168]

The crystalline nature of MOFs allows to determine textural parameters by geometric structure analysis and compare with experimental data.[169] There are several methods based on geometric analysis for the calculation of the pore volume, surface area, and pore size distribution in model porous crystalline materials (zeolites, MOFs, ZIFs, etc.).[170-173]

Pore volume

The most widely accepted method for pore volume (V_p) estimation is the adsorption of nitrogen or argon at their respective boiling point. The total pore volume is derived from the amount of gas adsorbed, assuming that pores are filled with the condensed adsorptive in the normal liquid state (Gurvich rule).[158] In the isotherms with a virtually horizontal plateau, the limiting uptake can be a simple measure of the total pore volume with respect to adsorption of particular gas at the operational conditions. For instance, from nitrogen adsorption isotherm, knowing volume of gas adsorbed, total pore volume can be calculated by using formula (7)

$$V_p = V_{max} M_r(N_2) \frac{1}{V_m \rho} \quad (7)$$

where V_{max} - volume of gas adsorbed, M_r - molar weight of N_2, ρ – density of liquid N_2, V_m – molar volume.

Several approaches were developed for micropore analysis including classical macroscopic procedures (t-, alpha-s methods, Dubnin´s pore-volume filling).[158]

Pore size distribution (PSD)

There are several classical, macroscopic thermodynamic methods for calculating PSD from physisorption isotherm including Dubinin–Radushkevich, Horvath–Kawazoe (HK), Saito–Foley (SF), and Kelvin equation-based methods (e.g., Barrett-Joyner-Halenda (BJH)). However, these methods are based on the assumption that pore contains the adsorbed phase being in a liquid-like state, which is irrelevant for a fluid

confined to micro- and narrow mesopores. In order to address this and other problems associated with the classical methods, the modern approaches based on density functional theory (DFT) and molecular simulation were developed. These advanced methods derived from the statistical mechanics of nanophases, describing the configuration of the adsorbate on a molecular level.[174]

PSD can be obtained using a particular kernel of reference adsorption isotherms in model pores of different sizes.[158] However, the prerequisite of characterization methods (BET, BJH, nonlocal density functional theory NLDFT, quenched solid density functional theory QSDFT, etc.) is an assumption of pore geometry (cylindrical, spherical, or slit-shaped pores). Using these methods for pore size analysis, neglecting complex pore architecture of MOF crystals, may lead, in some cases, to PSDs inconsistent with the crystallographic parameters.[175]

Recently Neimark et al. reported a new approach characterization of hierarchical and multimodal pore architecture.[175] Since MOFs pore structure are formed by different types of pore counterpart (cages, channels), it is worth to consider the contribution of each pore type into the adsorption profile, therefore to calculate the pore type distribution (PTD). The proposed method is based on generation of *in silico* fingerprint isotherms which can be calculated for individual pore compartment of MOF crystallographic structures. Afterwards, experimental adsorption isotherms are matched with the theoretical isotherms of adsorption in order to distinguish the contributions from different types of pores and determine the PTD.[175]

3.1.5 Sample preparation and measurements

Prior to any measurements the sample must be degassed to remove all physisorbed species. Samples are typically degassed in vacuum at elevated temperature. According to IUPAC recommendations, samples should be degassed for at least 16 hours.[158]

MOF pores contain guest molecules such as guest molecules such as solvent, excess of linkers, or other species, which should be removed in order to access the porosity and to obtain the reproducible isotherms.[174]

There two main factors causing the discrepancies in porosity values for the same MOF: (i) the instability of many compounds under humid conditions, especially after activation, consequently the decomposition during the sample handling under ambient

conditions and (ii) the insufficient activation conditions prior adsorption measurements.[174]

The stress acting on the framework during desolvation depends on surface tension and capillary forces imposed on the structure by the liquid- to gas-phase transformation of included solvent molecules, which is high especially when the solvent has a high boiling point and/or high surface tension.[176] A common approach to reduce the stress is to exchange the solvent with a low-boiling point/low-surface-tension solvent (these parameters tend to be correlated) prior to heating the sample under vacuum.[177] The most gentle desolvation approach is supercritical drying (SCD) using carbon dioxide as a working fluid.[178] SCD avoids the liquid–gas phase transition and thus any capillary forces.[13]

As described in the IUPAC report,[158] the measurement of physisorption isotherms can be carried out by (a) measurement of pressure change (i.e., manometric method) and (b) measurement of the change in mass of the adsorbent (i.e., (gravimetric method). The manometric method is based on the measurement of pressure change in calibrated gas volumes. Firstly, a certain amount of gas is dosed to a confined calibrated volume, which contain the adsorbent at constant temperature. Upon adsorption, the pressure in the confined volume decreases until equilibrium is reached. The amount of gas adsorbed at the equilibrium pressure is determined as the difference between the amount of gas confined and the amount of gas required to fill the space around the adsorbent, i.e., the dead volume.[158] The gradual dosing of gas to adsorbent and application of the appropriate gas laws result in the adsorption isotherm. The dead volume can be determined in the following ways: pre-calibration of the confined volume and subtracting the volume of the adsorbent (calculated from its density) or by the dosing of a gas with a negligible adsorption ability.[158]

3.2 Instruments and parameters

Physisorption

Volumetric physisorption experiments, nitrogen adsorption at 77 K, carbon dioxide at 195 K were performed on Autosorb IQ apparatus, using liquid nitrogen or a mixture of dry ice with isopropanol, respectively, to reach the temperatures of measurements. Helium, nitrogen, carbon dioxide with purity of 99.999% were used for all the experiments. Chloromethane adsorption at 249 K was measured on BELSORP-max apparatus equipped with cryostat.

Vapour adsorption of different solvents were performed on samples using BELSORP-max apparatus at 298 K. Prior the adsorption measurement the samples were evacuated at room temperature for 16 h, besides samples desolvated by means of supercritical carbon dioxide.

Powder X-ray diffraction (PXRD)

PXRD patterns were obtained at room temperature on a STOE STADI P diffractometer using Cu-Kα1 radiation (λ = 1.5406 Å) and a 2D detector (Mythen, Dectris). All measurements were performed in transmission geometry using a rotating flatbed sample holder, 2θ resolution of 3.12° and exposition time of 120 s per step.

VT-PXRD

Powder diffraction patterns at variable temperatures (VT) were measured using PANALYTICAL Empyrean powder diffractometer (alpha-1 system, 3rd generation), equipped with X-ray tube with copper anode (linear focus), Johannson monochromator (λ = 1.54058 Å), motorized anti-scatter and receiving slits. The intensities were registered using Pixcel 1D detector, performing in 1D modus. HTK-1200N high temperature chamber (ANTON PAAR) was used to control the sample temperature. All measurements were conducted in the nitrogen flow. PXRD patterns were collected in reflection geometry using scanning mode in the 2θ range from 50 to 50° with 0.0131° steps and 97 s per step. The sample was conditioned for 10 min before each scan. The sample height correction program for the measurements in the inert atmosphere was applied to correct the thermal expansion of the sample holder. Because of the low absorption of the sample, corundum reflections, originating from the sample holder are observed in all PXRD patterns.

Scanning electron microscopy (SEM)

SEM measurements were carried out by recording a secondary electrons using 2–5 kV acceleration voltage and a working distance of 4–14 mm on a SU8020 from Hitachi. Before the measurement, the samples were sputtered with Au to enhance surface conductivity. SEM images of the crystals obtained were analyzed by ImageJ software and the corresponding crystal size distributions were calculated.[179] Polydispersity index (PDI) was calculated as follows: $PDI = SD^2 / mean^2$ [SD, standard deviation; mean, the averaged value of the crystal size (µm)].

Thermogravimetric analysis (TGA)

TGA was performed in synthetic air flow in a temperature range from 298 K to 873 K with a heating rate of 5 K min^{-1} using a STA 409 PC from NETZSCH Company.

Infrared spectroscopy (IR)

Fourier transform (FT-IR) ATR spectra were collected were collected at 2 cm^{-1} resolution ranging from 4000 to 400 cm^{-1} using a Bruker Vertex 70 alpha instrument equipped with an ATR accessory (diamond crystal) and placed inside the device.

Nuclear magnetic resonance spectroscopy

^1H NMR experiments in solution were performed using a Bruker AVANCE 300 MHz (300 MHz, 282 MHz) spectrometer. The chemical shifts were specified in ppm and correlate to the visible solvent peak. Coupling constants were presented in hertz (Hz). For specification of multiplicities following abbreviations were used: s – singlet, d – doublet, dd – dual doublet, t – triplet, q – quartet, m – multiplet. The samples were dissolved in DCl/D_2O in DMSO-d^6.

Solid state NMR spectroscopy

The solid-state NMR experiments (cross polarization, CP) were carried out on a 300 MHz Bruker Avance spectrometer with a commercial 2.5 mm double-resonance magic angle spinning (MAS) probe with a mixing time of 4 ms. Spectra were referenced relative to TMS using adamantane as a secondary reference for ^{13}C, resonating at 29.5 ppm.

Raman spectroscopy

Raman spectra in the 180° geometry were recorded at room temperature on a Horiba Jobin Yvon T64000 spectrometer equipped with a liquid nitrogen cooled charge

coupled device detection system in subtractive dispersion mode. Ar^+ ion laser (Stabilite®2017, Spectra-Physics) with λ = 514.5 nm and Kr^+ ion laser (Lexel 95 K) with λ = 647.1 nm were used. The spectra were measured with the excitation power on the sample of 0.7 mW. The experiments were carried out using the incident laser beam focused on the sample by a 50×Olympus objective lens with a numerical aperture of 0.75. The scattered light was collected by the same objective lens and analysed through a polarizer and λ-plate. Spectroscopic measurements were performed in the subtractive dispersion mode, which attained a low-frequency limit of 10 cm^{-1} in the present setup, to investigate the low-frequency spectra. The deformation of the low-frequency spectral edge by an optical slit, which sometimes smears the true features of low-frequency spectra, was carefully eliminated by rigorous optical alignment.

Single crystal X-ray diffraction

A single crystal of as synthesized DUT-8(Zn) was prepared in a borosilicate glass capillary (*d* = 0.3 mm) with small amount of DMF. The dataset was collected at MX BL14.2 beamline of BESSY II synchrotron, operated by Helmholtz-Zentrum Berlin for Materials and Energy.[180] Four images from different crystal orientations were collected in order to determine the crystal symmetry and scan range using iMosflm program.[181] The *φ*-scan with oscillation step of Δ*φ* = 1° was used for collection of 180 frames, which were processed automatically using XDSAPP 2.0 software.[182] The crystal structure was solved by direct methods and refined by full matrix least-squares on F^2 using SHELX-2018/3 program package.[183] All non-hydrogen atoms were refined in anisotropic approximation. Hydrogen atoms were refined in geometrically calculated positions using “riding model” with $U_{iso}(H)$=1.2$U_{iso}(C)$. Disordered guest molecules could not be refined unambiguously from the difference Fourier map, hence, SQUEEZE routine in PLATON was used to generate the reflection intensities with subtracted solvent contribution.[184] As a result, 679 electrons were squeezed from the volume of 2235 $Å^3$.

Structure solution and refinement of cp phase from powder X-ray diffraction data

PXRD patterns of DUT-8(Zn)_160 µm_*cp* were collected on Empyrean-2 diffractometer (Panalytical) equipped with Parallel linear Cu-$Kα_1$ beam (hybrid 2xGe(220) monochromator). 10 mm mask and primary divergence and secondary

antiscatter slits with ¼° opening were used upon data collection. Pixcel-3D Detector in 1D scanning mode (255 active channels) was used. The data collection was performed in transmission geometry using capillary spinner setup and the sample was sealed in the borosilicate capillary under argon. The measured PXRD was indexed using DICVOL91. The obtained unit cell parameters were similar to the *cp* phase of DUT-8(Ni)[185], therefore, the initial model for the Rietveld refinement was obtained by geometry optimization of the DUT-8(Ni)_*cp* phase with unit cell parameters, derived from the *ab initio* indexing procedure. The Rietveld refinement with energy option (energy contribution 1%) was performed using reflex tool of Materials Studio 5.0 software package (Accelrys Software Inc, San Diego, California, USA, 2009). Zinc atoms, naphthalene cores, dabco ligands and carboxylates were treated as rigid bodies. The Rietveld plot is shown in Figure 5-4. CCDC-2020030 contains the supplementary crystallographic data for DUT-8(Zn)_*cp*.

In situ experiments

In situ PXRD patterns upon physisorption of CH_3Cl at 249 K were measured at KMC-2 beamline of BESSY II synchrotron, operated by Helmholtz-Zentrum Berlin for Materials and Energy.[186] The automated instrumentation was developed there, based on the volumetric adsorption instrument and closed-cycle Helium cryostat, equipped with adsorption chamber with beryllium domes was used in all experiments. PXRD patterns were measured at constant wavelength λ = 1.3332 Å (E = 9300 eV) in transmission geometry. Diffraction images were collected using 2θ scans and Vantec 2000 detector (Bruker). Each 2D image was measured with 31 s exposure. 1b sample was used in experiment. In order to cut off reflections coming from the crystalline Be-dome, tungsten slits with 5 mm aperture were mounted on the detector cone. The obtained diffraction images were integrated using DATASQUEEZE 2.2.9 with further processing in FITYK 0.9 software.[187] Adsorption equilibrium setting was defined as pressure change of 0.1% within 300 s. In situ PXRD experiments on 3c in parallel to CO_2 adsorption at 195 K were performed on a specialized Empyrean powder X-ray diffractometer (ω–2θ goniometer, $K\alpha_1$ system) using a customized setup based on ARS DE-102 closed cycle helium cryostat, which assured isothermal conditions in the temperature range of 30–300 ± 0.1 K. The adsorption cell is based on 1.33″ CF-flange and covered with a Beryllium dome. The cell was connected to the low pressure port of the BELSORP-max volumetric adsorption instrument. The TTL-trigger was used for

establishing the communication between BELSORP-max and Empyrean software and ensure the measurement of adsorption isotherm and PXRD pattern data collection in fully automated mode. The diffraction experiments were performed using ω–2θ scans in transmission geometry in the range of 2θ = 2–50°. Parallel linear Cu-Kα1 beam, generated by hybrid 2xGe(220) monochromator, 4 mm mask, and primary divergence and secondary antiscatter slits with ¼° opening were used upon data collection. Pixcel-3D detector in 1D scanning mode (255 active channels) was used. A complete adsorption–desorption physisorption isotherm of carbon dioxide at 195 K was measured on 8.9 mg of sample, statically fixed in the X-ray beam, and PXRD patterns were recorded after equilibration (0.1% of pressure change within 300 s) at selected points of the isotherm in situ by means of an automated dosing procedure of BELSORP-max.

Density functional theory modelling (DFT)

The periodic DFT calculations of DUT-8(Zn) were carried out using the QUICKSTEP module of CP2K[188] with a mixed Gaussian and plane waves basis set.[189] Periodic boundary conditions were applied in all three dimensions. The PBE exchange-correlation functional was used[190] with Goedecker–Teter–Hutter (GTH) pseudo-potentials.[191-193] The orbital transformation method was employed for efficient wave function optimization. Basis sets of DZVP quality were used with a grid cutoff 360 Ry for the geometry optimization and 300 Ry for the molecular dynamic simulations.[194] In all calculations, Grimme's DFT-D3 dispersion correction was applied.[195]

Molecular DFT was used to investigate the stability of the paddlewheel unit. Constraining geometry optimisations were performed using the NWchem 6.3 software package[196] with the PBE0 functional[197] and a polarized triple-zeta basis set (def2-TZVP).[198] Tight convergence criteria were employed. Input files can be found in the data repository of J. D. Evans (https://github.com/jackevansadl/supp-data).

3D Electron Diffraction (ED)

3D ED data were collected using a Termofisher TITAN TEM, equipped with a 2 k Gatan MSC camera, in nanodiffraction geometry with the C2 condenser aperture of 50 μm, and the effective beam diameter on the sample of 1 μm. Acceleration voltage was 300 kV.

Contact angle measurements

The contact angle measurements were performed on an OCA 35xl (Drop Shape Analysis) instrument from DataPhysics GmbH. The contact angles were calculated by the tangent method using conventional software. For each material, liquid droplets (diiodomethane, water) are generated at suitable locations on the sample surface and advancing and receding angles are measured by enlarging and reducing the droplets, respectively. As the droplet progresses or recedes, ~20 angles are determined every second. From these many advancing or receding angles, an average advancing or receding angle is calculated per droplet. After the advancing angle was formed, the needle was pulled out of the droplet to determine the static angle. For the measurements, the powdered material (50 mg) was pressed by 10 tons under hydraulic pressure.

X-ray photoelectron spectroscopy (XPS)

XPS measurements were performed using a ThermoScientific K-Alpha$^+$ X-ray Photoelectron Spectrometer. All samples were analyzed using a microfocused, monochromated Al K α X-ray source (1486.68 eV; 400 µm spot size). The analyser had a pass energy of 200 eV (survey), and 50 eV (high resolution spectra), respectively. To prevent any localized charge buildup during analysis the K-Alpha$^+$ charge compensation system was employed at all measurements. The samples were mounted on conductive carbon tape the resulting spectra analyzed using the Avantage software from ThermoScientific.

Elemental analysis

CHN analysis was performed on a EuroEA elemental Analyser.

Differential scanning calorimetry (DSC)

The DSC experiments were carried out with a DSC device from Mettler Toledo with a working temperature range from -90 °C to 600 °C. All experiments were performed in sealed aluminum crucibles (100 µL) with a hole to remove any leaking solvent vapours. The heating rates of 5 $K \cdot min^{-1}$ and argon flow of 20 $mL \cdot min^{-1}$ were used. The characteristic temperatures were determined at the onset (ϑ_{onset}) of the thermal effect. All samples were prepared under inert atmosphere of argon.

3.3 List of chemicals and gases

Table 3-1. List of chemicals

Name	CAS-number	Purity, %	Manufacturer
Nickel (II) nitrate hexahydrate	13478-00-7	≥98.5	Sigma Aldrich
Zinc (II) nitrate hexahydrate	10196-18-6	≥99	Sigma Aldrich
Zinc (II) acetate dihydrate	5970-45-6	≥99	Riedel-de Haën
1,4-diazabicyclo-[2.2.2]octane	280-57-9	≥99.7	Sigma Aldrich
2,6-naphthalenedicarboxylic acid	1141-38-4	99	Sigma Aldrich
Acetic acid	64-19-7	100	Carl Roth
Pyridine	110-86-1	99	Acros Organic
Polyacrylic acid (M_w = 1800)	9003-01-4		Sigma Aldrich
Polydimethylsiloxane	63148		Sigma Aldrich

Table 3-2. List of solvents

Name	CAS	Purity, %	Manufacturer
N,N-Dimethylformamide (DMF)	109-72-8	99.5	Fisher Scientific
Methanol	67-56-1	N/A	VWR
Tetrahydrofuran (THF)	109-99-9	≥99	Sigma Aldrich
Acetonitrile (ACN)			
Acetone	67-64-1	≥99.5	ALFA AESAR
Dichloromethane (technical) (DCM)	75-09-2	N/A	BIESTERFELD
Chloroform	67-66-3	99.9	Sigma Aldrich
Chloroform-d	865-49-6	99.8	Sigma Aldrich
Tetrachloromethane	56-23-5	99.9	Sigma Aldrich
Dimethylsulfoxide-d6	2206-27-1	99.9	Sigma Aldrich
n-Hexane		99	VWR
n-Heptane	142-82-5	97	Sigma Aldrich
Ethanol absolute	64-17-5		Fisher Scientific
1-Propanol	71-23-8	99.5	VWR
2-Propanol	67-63-0	100	VWR
1-Butanol	71-36-3	100	GRUSSING
1-Pentanol	71-41-0	99	Sigma Aldrich

3.4 The synthesis and treatment of metal-organic frameworks

3.4.1 DUT-8(Ni) synthesis, desolvation, treatment

Samples A, B, and C

In a typical synthesis, $Ni(NO_3)_2 \cdot 6H_2O$ (0.407 g, 1.4 mmol) was dissolved in 6 ml DMF, 2,6-H_2ndc (0.303 g, 1.4 mmol) was dissolved in 15 ml DMF, and dabco (0.1 g, 0.9 mmol) was dissolved in 9 ml methanol (MeOH) using ultrasonic bath and mixed.[17] Samples A, B, and C were synthesized using the same composition of the reaction mixture but utilizing different crystallization conditions. The reaction mixture for sample A was heated in a Teflon-lined autoclave under static conditions for 48 h at 393 K. Afterwards, the mother liquor was removed by centrifugation, and crystals were washed several times with DMF. For the preparation of sample B, the autoclave was rotated for 48 h using a BINDER oven at 393 K. The reaction mixture of sample C was heated by microwave irradiation of 150 W for 30 s.

Sample D

All chemicals were dissolved separately: $Ni(NO_3)_2 \cdot 6H_2O$ (0.145 g, 0.5 mmol) in 1.5 ml DMF, 2,6-H_2ndc (0.096 g, 0.44 mmol) in 7 ml DMF, and dabco (0.112 g, 1 mmol) in 1.5 ml DMF using an ultrasound bath for 10 min before mixing. To synthesize plates, solutions of 2,6-H_2ndc and dabco were mixed with the subsequent addition of 0.05 ml pyridine (modulator 2). Afterward, nickel nitrate solution was added to the reaction mixture. A cloudy suspension was obtained after mixing all the chemicals, which was transferred to a Teflon vessel (50 ml) and heated at 393 K in autoclave for 24 h. After synthesis, the mother liquor was removed by centrifugation, and the resulting particles were washed several times with DMF.

Sample E

All the chemicals were dissolved separately: $Ni(NO_3)_2 \cdot 6H_2O$ (0.145 g, 0.5 mmol) in 1.5 ml DMF, 2,6-H_2ndc (0.096 g, 0.44 mmol) in 7 ml DMF, and dabco (0.112 g, 1 mmol) in 1.5 ml DMF, using an ultrasound bath before mixing for 10 min. The solutions of 2,6-H_2ndc and dabco were combined with the subsequent addition of 0.05 ml pyridine (modulator 2). Afterward, a nickel nitrate solution, containing 0.05 ml of acetic acid (modulator 1), was added to the reaction mixture. A cloudy suspension was obtained

after mixing all the chemicals, which was transferred to a Teflon vessel (50 ml) and heated at 393 K in autoclave for 24 h. After synthesis, the mother liquor was removed by centrifugation, and the resulting particles were washed several times with fresh DMF.

Samples PAA_1, PAA_2, and PAA_3

Synthesis of flexible DUT-8(Ni), reported by Kavoosi et al. (2017),[17] was adopted for morphology modification of crystals, using PAA (modulator 3). Typically, $Ni(NO_3)_2 \cdot 6H_2O$ (0.204 g, 0.7 mmol) was dissolved in 3 ml DMF, 2,6-H_2ndc (0.152 g, 0.7 mmol) was dissolved in 7.5 ml DMF, and dabco (0.05 mg, 0.45 mmol) was dissolved in 4.5 ml methanol. The three resulting solutions were combined prior to the addition of PAA (0.001 g). The mixture was sonicated for 10 min, transferred into a Teflon vessel (50 ml in volume), and heated in an autoclave at 393 K for 48 h. The resulting crystals were washed with DMF several times. The sample is termed PAA_1. In the following syntheses, the amount of PAA was varied: sample PAA_2 was synthesized under the addition of 0.005 g, and sample PAA_3 was synthesized under the addition of 0.01 g of modulator 3.

DUT-8(Ni)_rigid

The synthesis of rigid DUT-8(Ni) was adopted from Kavosi et al.[17] All the chemicals were dissolved in 30 ml DMF: 2,6-H_2ndc (0.294 g, 1.37 mmol), $Ni(NO_3)_2 \cdot 6H_2O$ (0.434 g, 1.5 mmol), and dabco (0.336 g, 3 mmol) using an ultrasound bath. A cloudy suspension was transferred to a Teflon vessel (50 ml) and heated at 408 K in autoclave for 48 h. After synthesis, the mother liquor was removed by centrifugation, and the resulting particles were washed several times with fresh DMF.

Desolvation

N,N-dimethylformamide used in the synthesis was exchanged first by dichloromethane (DCM) for 3 days. Afterward, the crystals were filtered under argon flow, and the solvent was removed under vacuum at 423 K for 16 h.

Surface treatment

To realize surface treatment, the activated sample sample A, named as Reference in closed pore phase (*cp*) was used. Firstly, the material was exposed to ethanol. In the following procedure, 20 mg of sample was immersed in 2 ml ethanol (1_EtOH) for 6

hours with subsequent drying under dynamic vacuum. In the second treatment procedure, sample was soaked in ethanol/water mixture (95/5 v.v.) (2_EtOH/H_2O) and dried in argon flow at 100°C (4 h). Additionally, the material was exposed during 3 h to 0.1 mol/L solution of benzoic acid dissolved in EtOH, and afterwards dried under vacuum (sample 4_BA/EtOH).

The chemical vapour deposition of polydimethylsiloxane (PDMS) was carried out in inert atmosphere at 235°C during 6 h (3_PDMS), according to procedure reported earlier.[199]

Reactivation

To check the reversibility of surface deformation, after treatment samples were exposed to reactivation conditions, namely thermal treatment at 150°C under vacuum during 16 h.

Polymer coating

1_DUT-8(Ni)@ODPA-DAM, 1_DUT-8(Ni)@FDA-DAM

The polymers were synthesized by the group of Tao Li and coating procedure was adopted from their work[200] and slightly modified. The macro-sized DUT-8(Ni) crystals solvated in DMF, the following polymers 4,4-(hexafluoroisopropylidene) diphthalic anhydride (6FDA)-2,4,6-trimethyl-1,3-phenylenediamine (DAM) and 4,4′-oxidiphthalicanhydride (ODPA)-2,4,6-trimethyl-m-phenylenediamine (DAM) were used for coating of the DUT-8(Ni) crystals. Firstly, polymer solutions were prepared in the following way: 3 mg of polymer was dissolved in 7.5 ml DCM. Secondly, the solvated crystals were transferred in polymer solution. Subsequently 7.5 ml of petroleum ether were added to the solution to ensure the precipitation of the polymer on the crystals surface. Afterwards, the material was evacuated at 150°C during 16 h.

2_DUT-8(Ni)@FDA-DAM

The macro-sized DUT-8(Ni) crystals solvated in DCM and exposed to coating procedure, which is described above for samples solvated in DMF.

3.4.2 DUT-8(Zn) synthesis and desolvation

Macro-sized particles, DUT-8(Zn)_160 µm

The synthesis procedure of DUT-8(Zn) reported in 2020 was carried out to obtain macro-sized crystals.[15] Typically, $Zn(NO_3)_2 \cdot 6H_2O$ (312 mg, 1.05 mmol, 1.7 eq.) is dissolved in 5 mL N,N-dimethylformadmide (DMF), 2,6-H_2ndc (227 mg, 1.05 mmol, 1.7 eq.) is dissolved in 20 mL DMF and dabco (70 mg, 0.625 mmol, 1 eq.) is dissolved in 5 mL DMF using ultrasound bath before mixing for 20 min. Subsequently, resulting solutions were slowly mixed and heated in an oven at 378 K for 15 min. After pre-treatment the solution was transferred into Pyrex tubes for solvothermal synthesis at 393 K for 48 hours. After cooling to room temperature the crystals were washed several times with DMF. Finally, the product was washed with dichloromethane under renewal of supernatant 9 times during 3 days. In order to desolvate the MOF, the material was filtered in argon flow, evacuated and heated up to 393 K for 16 h.

Micron-sized particles, DUT-8(Zn)_0.5 µm

Supersaturation route, reported by Kavoosi et al. in 2017 resulted in crystal size decrease by increasing dabco amount.[17] All chemicals were dissolved separately: $Zn(NO_3)_2 \cdot 6H_2O$ (446 mg, 1.5 mmol, 0.5 eq.) in 5 mL DMF, H_2ndc (296 mg, 1.37 mmol, 0.5 eq.) in 20 mL DMF and dabco (336 mg, 3 mmol, 1 eq.) in 5 mL DMF using ultrasound bath before mixing for 20 min. A cloudy suspension was produced after mixing of all chemicals, which was followed by ultrasound treatment for 60 min. Afterwards, the mother solution was removed by centrifugation and the resulting particles were washed several times with DMF. Solvent removal was carried out through the solvent exchange procedure as described for macrocrystals.

Submicron-sized, DUT-8(Zn)_0.1 µm

Submicron-sized crystals were obtained by increasing dabco concentration, which ensures even more rapid nucleation. All chemicals were dissolved separately and heated to 353 K prior mixing. Typically, to the hot, clear 2,6-H_2ndc solution (296 mg, 1.37 mmol, 0.3 eq.) in 20 mL DMF, $Zn(NO_3)_2 \cdot 6H_2O$ (446 mg, 1.5 mmol, 0.3 eq.) in 5 ml DMF solution is added. Finally, dabco solution (504 mg, 4.5 mmol, 1 eq.) in 5 ml DMF is added whereby the mixture immediately turns cloudy. The resulting mixture was then treated in an ultrasonic bath for 30 min at 353 K. The mother liquor was

removed by centrifugation and the resulting particles were washed several times with DMF.

Desolvation

The first activation procedure applied is the evacuation of the solvent used during the synthesis under reduced pressure at elevated temperature. The samples were filtered in an argon flow and DMF was removed in dynamic vacuum at 423 K for 16 hours.
Alternatively, the DMF used in the synthesis was exchanged first by a lower boiling point solvent (DCM) during 3 days. Afterwards, it was removed in dynamic vacuum at 423 K for 16 hours.
In the third procedure, using supercritical drying (SCD), DMF was exchanged with ethanol and acetone several times during 3 days. Then samples were desolvated by supercritical CO_2 drying technique, in which ethanol is exchanged with liquid CO_2 at high pressure (i.e. > 73 atm) during several hours. Afterwards, the sample is heated above the supercritical temperature of CO_2 (i.e., 304 K). As a result, framework is occupied by $scCO_2$, which is then slowly vented.

Selectivity experiments

Solution of dichloromethane (DCM)/1-propanol (1-PrOH) in ratio 1/1 (0.05/0.05 mol) was prepared by mixing 3.2 ml of DCM and 3.7 ml of 1-PrOH. 60 mg of the desolvated DUT-8(Zn)_*160* and 60 mg of DUT-8(Zn)_*0.5* were exposed to 400 µm solution of DCM/1-PrOH during 1 h. 10 µl of blank solution (1 h) and solution after adsorption (1 h) were mixed with 5 µl dimethyl malonate (standard), 0.5 ml $CDCl_3$ for ^1H NMR analysis.

Modulated synthesis of DUT-8(Zn)

Synthesis procedure was adopted form an earlier work[201] in order to perform face-selective coordination modulation.

Cubes, DUT-8(Zn)_1.8 µm

The linker 2,6-H_2ndc (0.086 g, 0.40 mmol) was dissolved in 12 ml DMF using ultrasound bath. Afterwards dabco (0.22 g, 0.20 mmol) was added to the first solution. The second solution was prepared using $Zn(CH_3CO_2)_2{\cdot}2H_2O$ (0.120 g, 0.55 mmol) and 18 ml DMF. To synthesize cubes, solution of 2,6-H_2ndc and dabco was mixed with addition of 0.5 ml pyridine. Then, zinc acetate solution containing 0.5 ml acetic

acid was added to the reaction mixture. A cloudy suspension was obtained after mixing of all chemicals, which was transferred to Teflon vessel (50 ml) and heated at 373 K in an autoclave for 24 h. After synthesis, the mother liquor was removed by centrifugation and the resulting particles were washed several times with DMF.

Rods, DUT-8(Zn)_1.4 µm

The linker 2,6-H_2ndc (0.086 g, 0.40 mmol) was dissolved in 12 ml DMF using ultrasound bath. Afterwards dabco (0.22 g, 0.20mmol) was added to the first solution. The second solution was prepared using $Zn(CH_3CO_2)_2 \cdot 2H_2O$ (0.120 g, 0.55 mmol) and 18 ml DMF and 0.5 ml of acetic acid. Then, zinc acetate solution containing 0.5 ml acetic acid was added to the reaction mixture. Two reaction solutions were combined and treated by ultrasound 10 min. A cloudy suspension was obtained after mixing of all chemicals, which was transferred to a Teflon vessel (50 ml) and heated at 373 K in an autoclave for 24 h. After synthesis, the mother liquor was removed by centrifugation and the resulting particles were washed several times with DMF.

Plates, DUT-8(Zn)_1 µm

Firstly 2,6-H_2ndc (0.086 g, 0.40 mmol) was dissolved in 12 ml DMF using ultrasound bath. Afterwards dabco (0.22 g, 0.20 mmol) was added to the first solution. The second solution was prepared using $Zn(CH_3CO_2)_2 \cdot 2H_2O$ (0.120 g, 0.55 mmol) and 18 ml DMF. To synthesize plates, solution of 2,6-H_2ndc and dabco was mixed with 0.5 ml pyridine. Then, zinc acetate solution was added to the reaction mixture. A cloudy suspension was obtained after mixing of all chemicals, which was transferred to Teflon vessel (50 ml) and heated at 373 K in autoclave 24 h. After synthesis, the mother liquor was removed by centrifugation and the resulting particles were washed several times with DMF.

Desolvation

Samples produced by modulated synthesis were washed 3 times with dichloromethane under renewal of supernatant 9 times during 3 days. To remove solvent, samples were filtered in argon flow, evacuated and heated up to 393 K during 16 h.

Chapter 4 The impact of crystal size and morphology on switchability of DUT-8(Ni)

The following results are contained in my own publication.[197]

L. Abylgazina, I. Senkovska, R. Engemann, Sebastian Ehrling, T. E. Gorelik, N. Kavoosi, U. Kaiser, S. Kaskel, “Impact of Crystal Size and Morphology on Switchability Characteristics in Pillared-Layer Metal-Organic Framework DUT-8(Ni)”, *Fronties in Chemistry,* 9, (2021).

4.1 Introduction

Variation of the crystallite size in flexible porous coordination polymers can significantly influence or even drastically change the flexibility characteristics. The impact of crystal morphology, however, on the dynamic properties of flexible metal-organic frameworks (MOFs) is poorly investigated so far.

In this chapter, the influence of crystal size and morphology on gate opening transition in switchable DUT-8(Ni) compound $[Ni_2(2,6\text{-ndc})_2(dabco)]_n$ will be considered, intending to identify the crystal faces significantly affecting the gate opening pressure. The crystal size and the shape are manipulated by synthetic parameters, such as the crystallization method and chemical-modulating agents, which facilitated to control not only the size of the crystals but also the crystal habit. Two different types of modulators are applied: (i) small molecules possessing functional groups chemically related to the organic building blocks of the MOF and (ii) macromolecules, bearing the same functionality.[32] To correlate the gate opening characteristics of the isotherms with the size and morphology of the DUT-8(Ni) crystals, the materials are analysed using scanning electron microscopy (SEM), electron diffraction, and nitrogen physisorption at 77 K.[202]

4.2 Results and discussions

4.2.1 Modulation of crystal size

To systematically vary the size of the DUT-8 crystals, the synthetic procedure was altered in crystallization conditions, without the application of additional chemicals or changing the reaction mixture composition (Figure 4-1). Thus, samples **A**, **B**, and **C** were synthesized under static conditions, or by shaking the reaction vessel, or under rapid heating by microwave irradiation, respectively. Scanning electron microscopy images of the crystals obtained were analyzed by ImageJ software, and the corresponding crystal size distributions were calculated (Figure 4-3). Due to the rod-like morphology of DUT-8(Ni) (Figure 4-2), we decided to use the length (L) to width (W) ratio (aspect ratio) as an appropriate parameter to monitor the changes in the habit, in addition to the length (as it was done previously to monitor the crystal size). In this study, we also have paid increased attention to the crystal width. The DUT-8(Ni) compound, containing DMF in the pores, crystallizes in the monoclinic space group with the cell parameters a = 18.576(3) Å, b = 18.408(2) Å, c = 9.3574(13) Å, and β = 97.545(9).[118] Thus, the length of the rod-like crystal corresponds to the size along the crystallographic c direction running along the pillars. The crystal width, on his part, is defined by the size along a–b crystallographic directions (plain of the layers).

The SEM image of **sample A**, which was heated for 48 h (conventional DUT-8(Ni) synthesis), highlights that the length of crystals varies between 20 and 120 µm, with a mean of 48 µm. The mean width of crystals is 17 µm. The SEM images of **sample B** confirm the influence of the reaction mixture, stirring on the crystal size, decreasing the length of the crystals to 45 µm, and width to 12 µm. Microwave-assisted synthesis leads to further crystal downsizing, yielding crystals with 16 µm in length and 6 µm in width in average.

Thus, different synthesis conditions lead to a successive decrease of the length and the width of the crystal simultaneously, leading to the insignificant differences in the aspect ratio (ca. 3 on average) of these crystals (Table 4-1). The addition of monodentate ligands that mimic the functionality of the corresponding linker in the synthesis solution (coordination modulation) is widely used to control the particle size of MOFs.[203] For example, Kitagawa and co-workers have utilized the “coordination modulation” approach to control the crystal size and shape in a nonswitchable pillared-layer MOF $[Cu_2(1,4\text{-ndc})_2(dabco)]n$ (1,4-ndc−1,4-naphthalenedicarboxylate).[204] This

material can be regarded as isoreticular to switchable DUT-8(Ni), presenting crystal faces terminated by either carboxylate units from the carboxylic linkers or nitrogen atoms from the dabco pillar. The different functionalities of the linker and pillar allow for selective capping of specific faces by the addition of modulators, complementary to the chemistry at particular crystal faces.

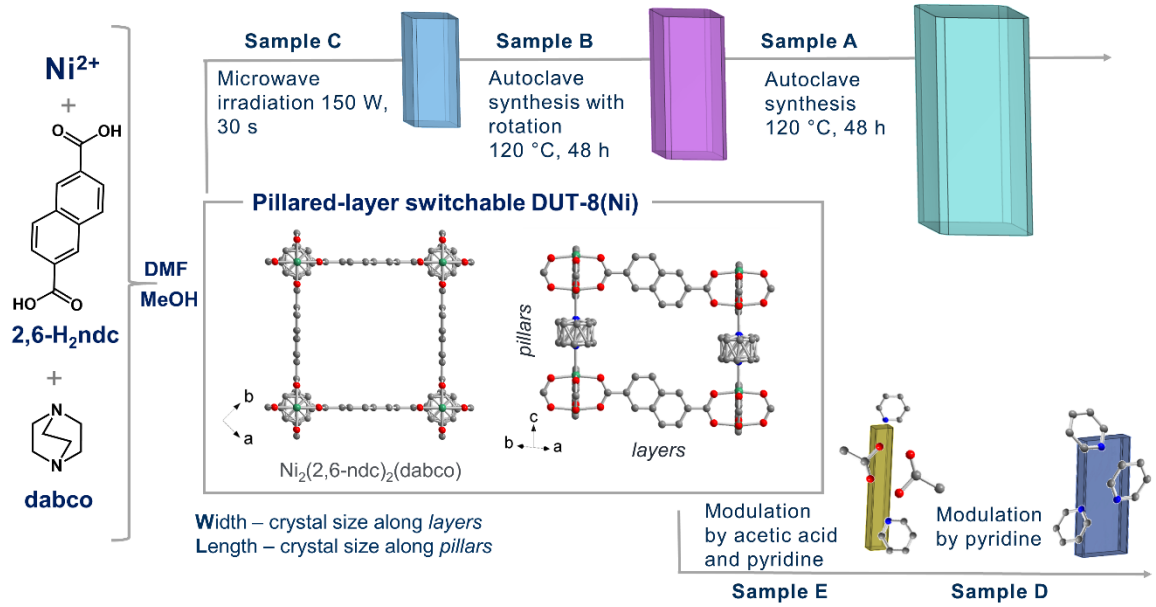

Figure 4-1. Schematic representation modulation of particle size by variation of synthetic conditions.

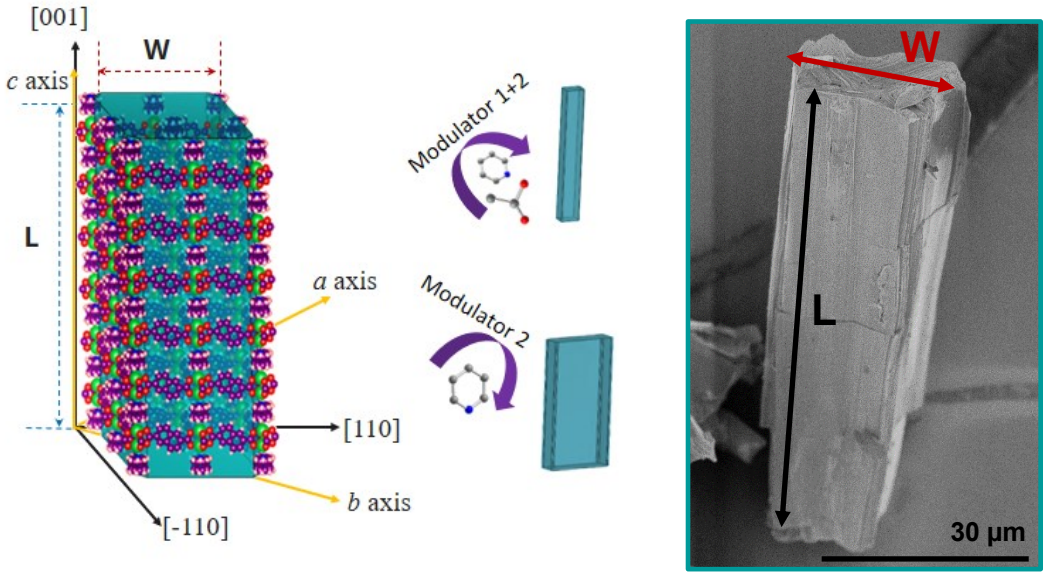

Figure 4-2. Schematic representation of DUT-8(Ni) coordination modulation by acetic acid and pyridine (L-crystal length, W-crystal width).

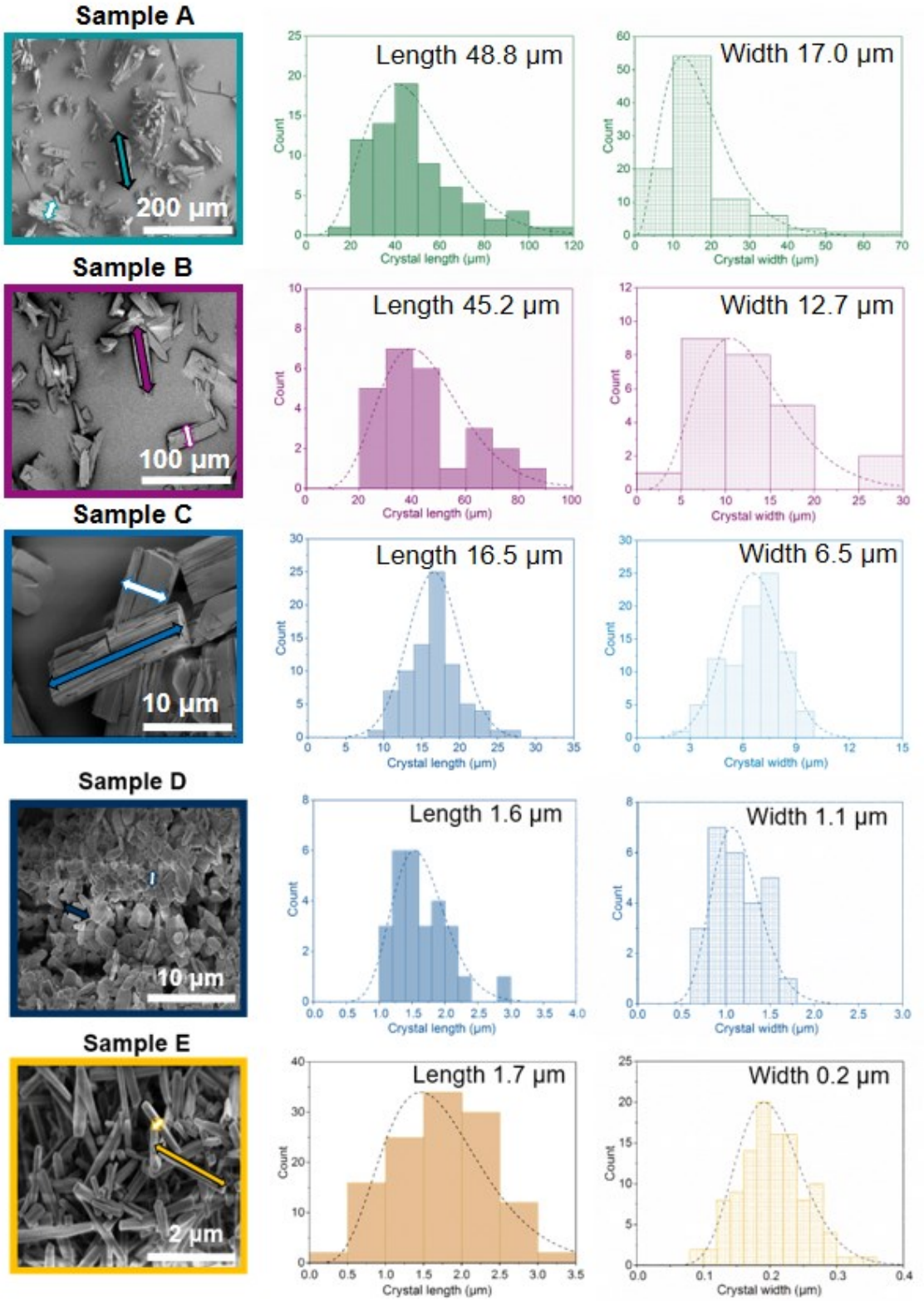

Figure 4-3. SEM images and particle size distributions (length marked as a filled arrow in SEM and width marked as an empty arrow in SEM) of the investigated samples.

The addition of molecules containing carboxylic groups (Modulator 1) to the synthesis mixture may result in the formation of needles if the crystal growth rate on capped faces is decreased. In the case of DUT-8(Ni), the addition of acetic acid only resulted in the crystals of increased size, and no needles were obtained. Modulation with pyridine (modulator 2), where the N-donor is expected to coordinate to the {001} crystal faces, reported to produce nanosheets, could be adapted to the DUT-8(Ni) system (**sample D**). Synthesis with pyridine as modulator produced uniform plate-shaped crystals. However, in contrast to the expectations, the smallest dimension of the crystal corresponds not to the [001], but to the [110] (or [−110]) direction (Figure 4-4). The length (size in crystallographic c direction) of crystals in D is significantly decreased to 1.6 μm (in comparison with **A**, **B**, and **C**); meanwhile, the expansion in the a–b-plane is 0.3 × 1.1 μm, lowering the aspect ratio to 1.4 and resulting in platelets. Modulation with both pyridine and acetic acid, reported to result in a particle size decrease and formation of nanocubes[205] for $[Cu_2(1,4\text{-ndc})_2(dabco)]_n$, yielded needles (**sample E**) in case of DUT-8(Ni). The crystal dimensions of needle-like sample E are 1.7 μm in length and 0.2 μm in width, increasing the aspect ratio to 8.6 μm. The assignment of the crystallographic directions to the length and the width of crystal in samples D and E was performed by electron diffraction, using TEM (Figure 4-4) by Dr. T. Gorelik (University of Ulm).

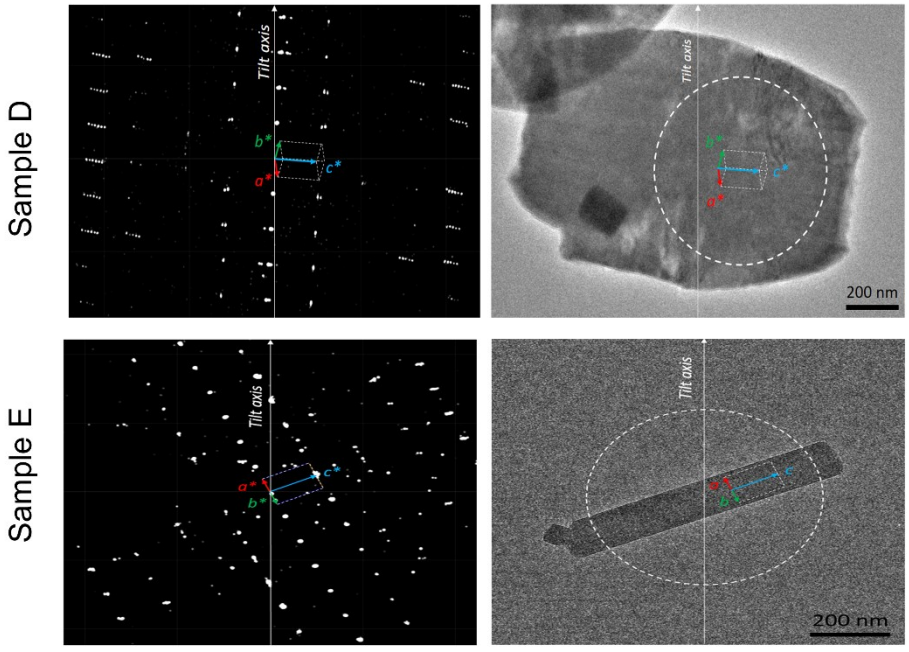

Figure 4-4. TEM images of sample D (plates) and samples E (rods).

In all cases, phase pure DUT-8(Ni) compounds were obtained according to PXRD analysis (Figure 4-5). After the synthesis, all samples were treated uniformly, i.e., washed with dichloromethane and desolvated in a vacuum at 423 K. The solvent removal leads to framework contraction according to PXRD patterns (Figure 4-5), which are in good agreement with the theoretical pattern of DUT-8(Ni) in the *cp* phase. The PXRD patterns of **samples D** and **E**, however, contain small peaks of the remaining op phase, indicating that the part of the sample falls below the critical size to show flexibility.[17, 18] The crystal structures of *op* and *cp* phases are shown in the Figure 4-6.

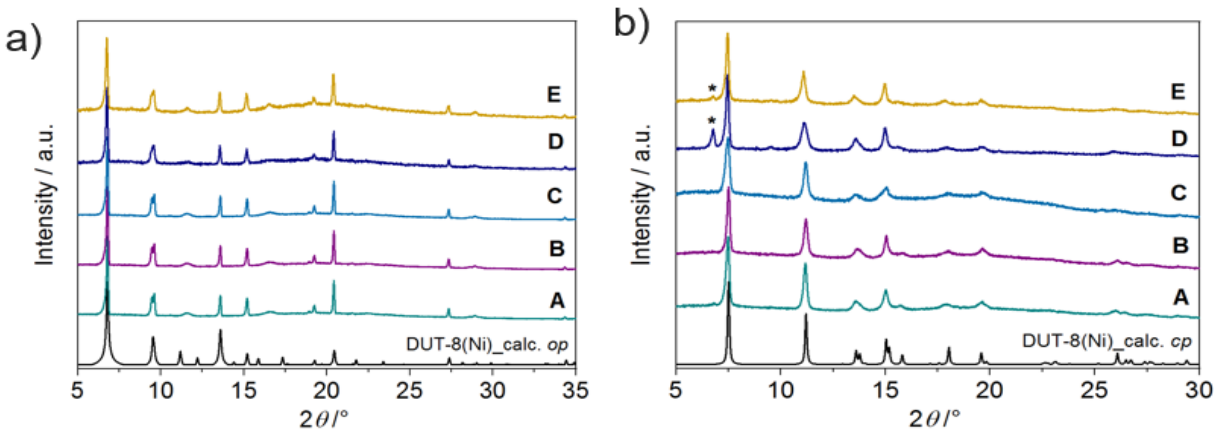

Figure 4-5. PXRD patterns of DUT-8(Ni) samples in the solvated (DMF) and desolvated state.

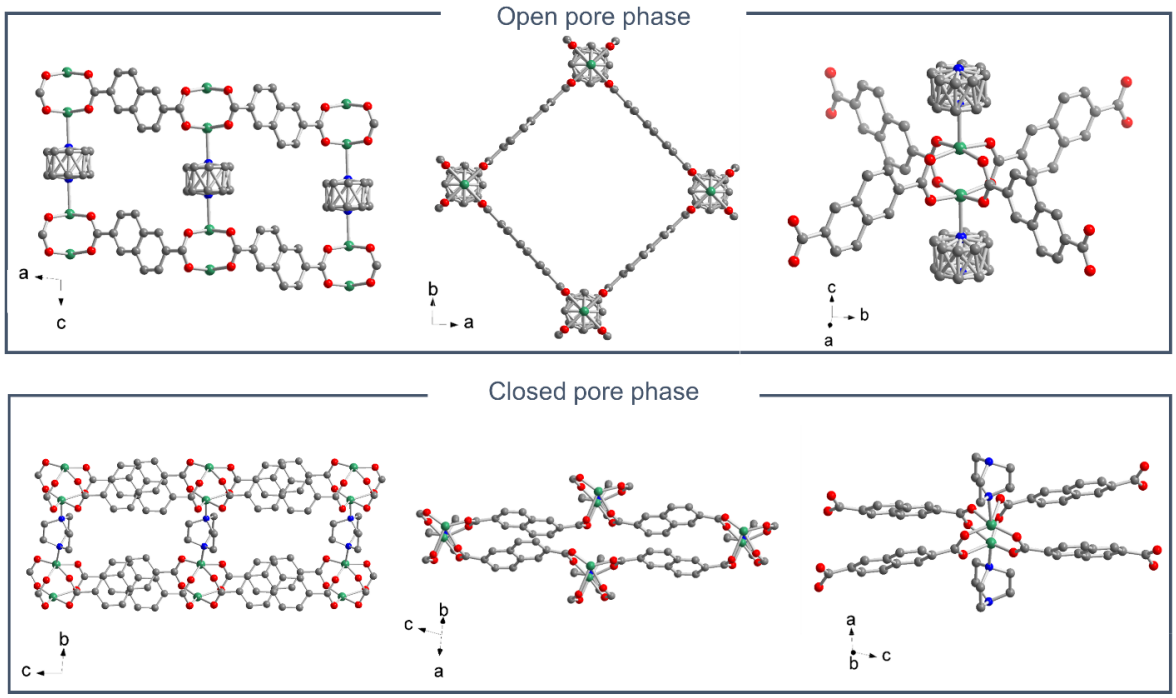

Figure 4-6. Crystal structure of open pore (*op*) and closed pore phase (*cp*) of DUT-8(Ni). C – in grey, O – in red, N – in blue, Ni – in green. Hydrogen atoms are omitted for clarity.

4.2.2 Analysis of adsorption behaviour

The switching behaviour of all samples was investigated by nitrogen adsorption at 77 K, showing that the crystals habit significantly influences the switching and thereby adsorption behaviour of DUT-8(Ni) (Figure 4-7). To understand the effects on the isotherm and the relationship between the size, morphology, and isotherm shape, it is important to identify characteristic quantities, which can be extracted from the isotherm and related to the sample characteristics, thermodynamics, and kinetics of the switching process. Therefore, as the main characteristics for the discussion and comparison of the gate pressure isotherms, typical for DUT-8(Ni), we will use the following quantities:

(i) Uptake at highest relative pressure reached in the adsorption experiment (or in plateau). It represents the specific pore volume of the particular sample. In relation to the theoretical pore volume, it reflects the fraction of crystallites (α_{max}) transformed to the op phase at given conditions. In the powdered samples, the phase transformation often does not go to completion.[124] The reason here is that some of the crystallites cannot be stimulated to open at a particular pressure because of the high activation barrier for opening. Higher pressures[206] or adsorption enthalpies[137] would enable the stimulation of these crystals, exhibiting higher activation energy, forcing additional crystallites to transform, but the maximum pressure in the adsorption experiments is limited to the saturation pressure of the chosen adsorptive (1 atm at 77 K).

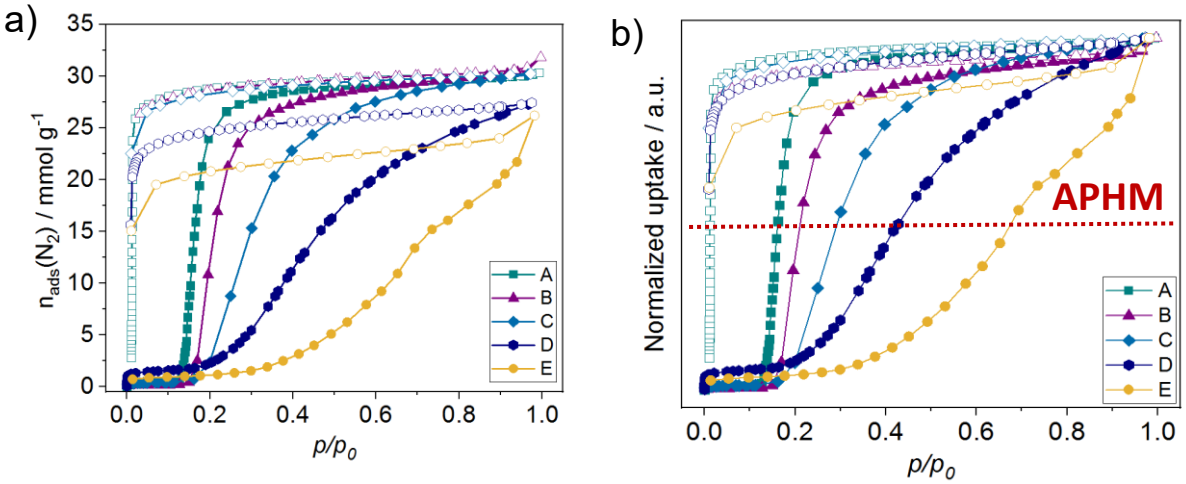

Figure 4-7. Nitrogen physisorption isotherms at 77 K for the investigated samples.

The samples **A**, **B**, and **C** reach almost full nitrogen uptake at 77 K after opening, indicating complete phase transition in almost all crystallites (Table 4-1). The isotherms of samples **D** and **E**, however, do not reach a plateau upon adsorption up to high relative pressures, indicating that a part of the sample remains in the *cp* phase.[18] Consequently, the specific pore volume and α_{max} for these samples are lower than expected for a complete transition.

Table 4-1. Characteristics of the investigated samples.

Sample	APHM	Length (L)/ µm	RSD / %	PDI	Width (W)/ µm	RSD / %	PDI	Aspect ratio (L/W)	Total pore volume / $cm^3\ g^{-1}$	α_{max}
A	0.17	48.8	43.6	0.19	17.0	63.2	0.40	2.9	1.05	0.99
B	0.21	45.2	37.5	0.14	12.7	45.8	0.21	3.5	1.06	1.00
C	0.30	16.5	20.7	0.04	6.5	24.3	0.05	2.5	1.05	0.98
D	0.44	1.6	26.5	0.07	1.1	24.7	0.06	1.4	0.95	0.89
E	0.69	1.7	37.1	0.13	0.2	24.1	0.06	8.6	0.90	0.85
PAA_1	0.19	52.9	56.6	0.32	17.1	50.8	0.25	3.1	1.03	0.97
PAA_2	0.23	55.0	18.3	0.03	15.2	23.0	0.05	3.3	1.06	1.00
PAA_3	0.26	53.3	16.7	0.03	8.0	26.7	0.07	6.7	1.03	0.97

RSD, relative standard deviation; PDI, polydispersity index; APHM estimated for the normalized isotherms

(ii) *Relative adsorption pressure at half maximum uptake (APHM) as a measure of the average gate opening activation energy (ΔG^*).* In general, the first-order phase transitions show a hysteresis, because of the kinetic barriers controlling the nucleation of the new phase.[50] The hysteresis width depends on the barrier and the rate at which the thermodynamic conditions change within a given experiment.[124] The ideal hysteresis loop of single crystallite (single grain) in the adsorption isotherm would have a rectangular shape corresponding to the Preisach model,[207] where the only change in porosity is due to structure transition events. The hysteresis loop will have a more complex shape for a powdered sample as an ensemble (arrangement), consisting of quasi “non-interacting grains”. Thus, the distribution of nucleation barriers of the individual grains controls the transition pressure spread over a wider pressure range. This is typically reflected by the less-steep adsorption branch in the gating region.[9]

The first derivative of the adsorption branch of the nitrogen physisorption isotherm reflects the distribution of transition pressures over the sample and, correspondingly, the distribution of gate opening activation energies (Figure 4-12). So, the APHM represents the average width or breadth of the hysteresis (taking into account non-significant changes in the gate closing pressure) and, thereby, the average activation energy of the grains within the sample. Dependence of the relative adsorption pressure at half maximum uptake from the crystal dimensions (length and width) and shape (aspect ratio) is summarized in Table 4-1 and is shown in Figure 4-8**.** It can be clearly seen that the aspect ratio is not the determining parameter, influencing the gate opening pressure. The APHM changes also do not systematically follow the changes in the crystal length. The APHM for sample **E** is larger than that for sample **D**, although the crystals are almost equal in length (Figure 8-1). Analyzing the trend for all the samples, and especially the APHMs for the samples D and E (Figure 4-8) it is evident that the systematic changes in the width of the crystals lead to the systematic APHM changes. Thus, obviously, the crystal width determines the gate opening pressure in DUT-8(Ni). To confirm the dominant influence of particle width on dynamic properties upon adsorption of nitrogen at 77 K ones more, an additional crystal series was prepared, utilizing PAA as a modulator (Figure 8-2). The same chemicals present in the synthetic mixture ensure the same terminating groups on the crystal outer surface, which is not necessarily the case if modulators, differing in functional groups, are used to influence the morphology (as it is the case for samples A, B, and C vs. D vs. E).

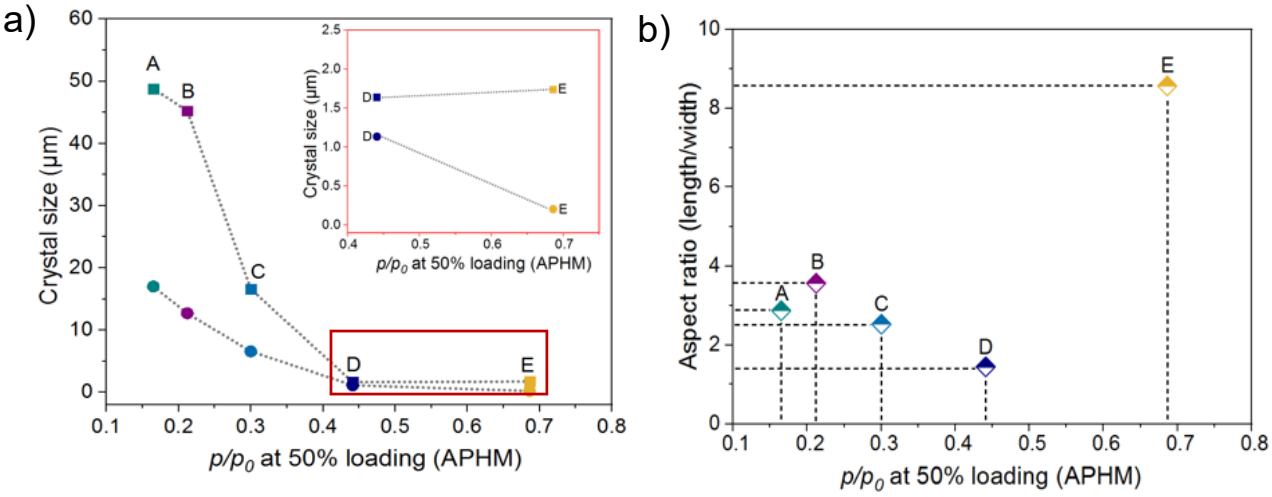

Figure 4-8. Relationship between the relative adsorption pressure at half maximum uptake (APHM) and the crystal dimensions (length-squares and width-circles) (a) and shape (aspect ratio) (b).

The impact of the surface termination on the flexibility of DUT-8(Ni), however, has been recently analyzed by the group of Düren.[208] In PAA-modulated syntheses (PAA_1, PAA_2, and PAA_3), a low amount of a polymer does not modify the morphology, yielding needles (PAA_1) or intergrowth of needles with a wheat sheaf habit (in samples PAA_2 and PAA_3) (Figure 4-9). With regard to crystal dimensions, the length was maintained approximately in the same range (53–55 µm), while the critical parameter (width) varies from 17 to 8 µm. The change in crystal width affects the adsorption profile, which is reflected in the APHM shift to the higher values, with decreasing width of the needles, confirming the trend observed in the first A–E series (Figure 4-10).

Thermogravimetric analysis, IR-, and NMR-spectroscopy measurements were performed (Figure 8-3, 8-4, 8-5), confirming the absence of residual modulators in D, E, PAA_1, PAA_2, and PAA_3, at least within the limit of quantitation of the methods.

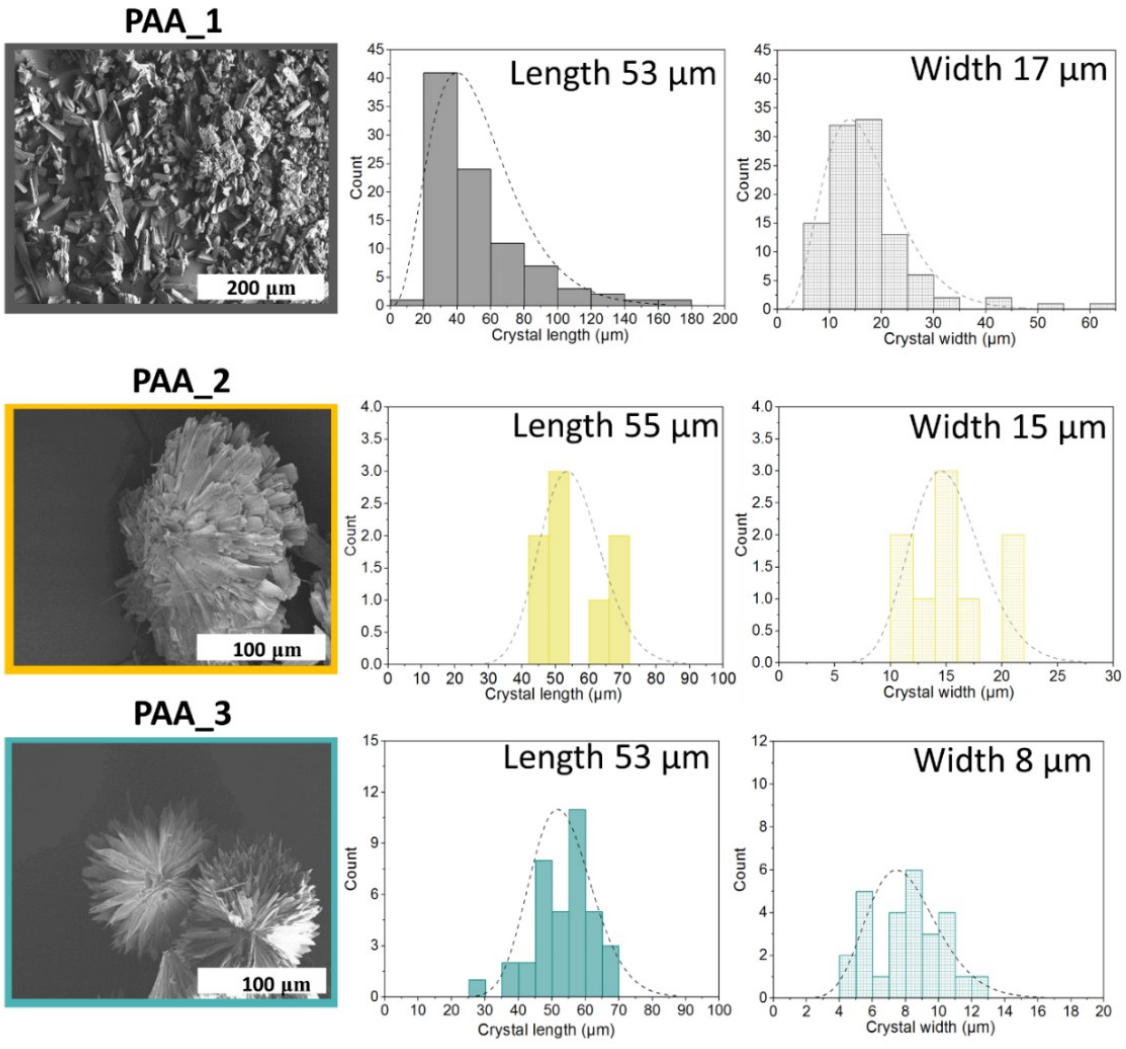

Figure 4-9. SEM images and corresponding particle size distribution of PAA-modulated samples.

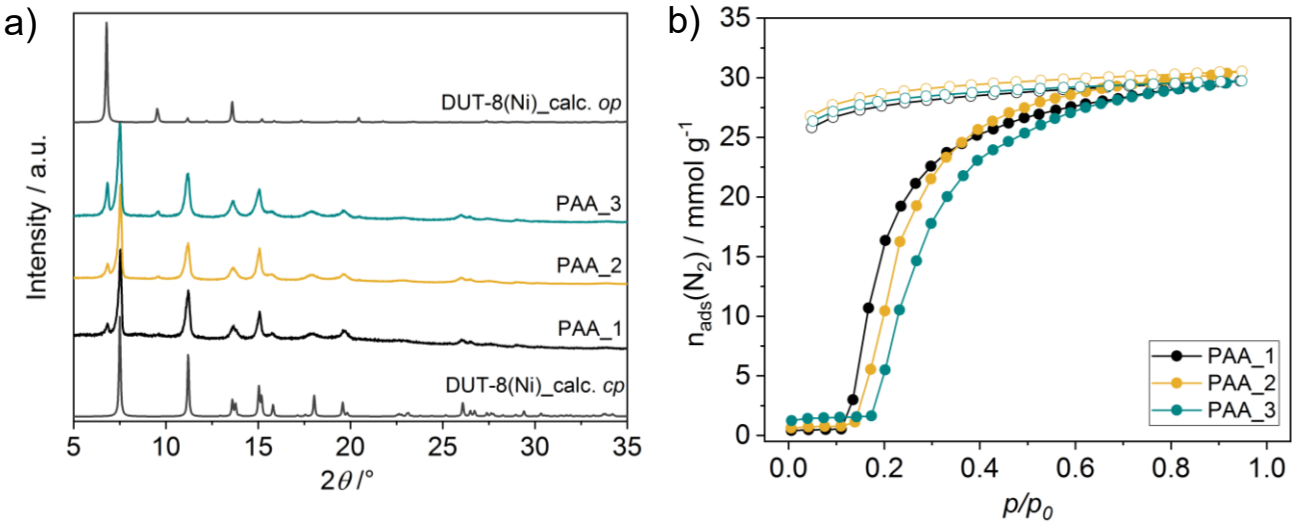

Figure 4-10. a) Nitrogen physisorption isotherms at 77 K and b) PXRD patterns of DUT-8(Ni) modulated by polyacrylic acid (PAA) after desolvation.

The changes in the APHM with width, considering all samples from this study, as well as a reference sample from Miura *et al*. (2017),[18] are not linear and follow logarithmic function in the range of the crystal sizes investigated (Figure 4-11).

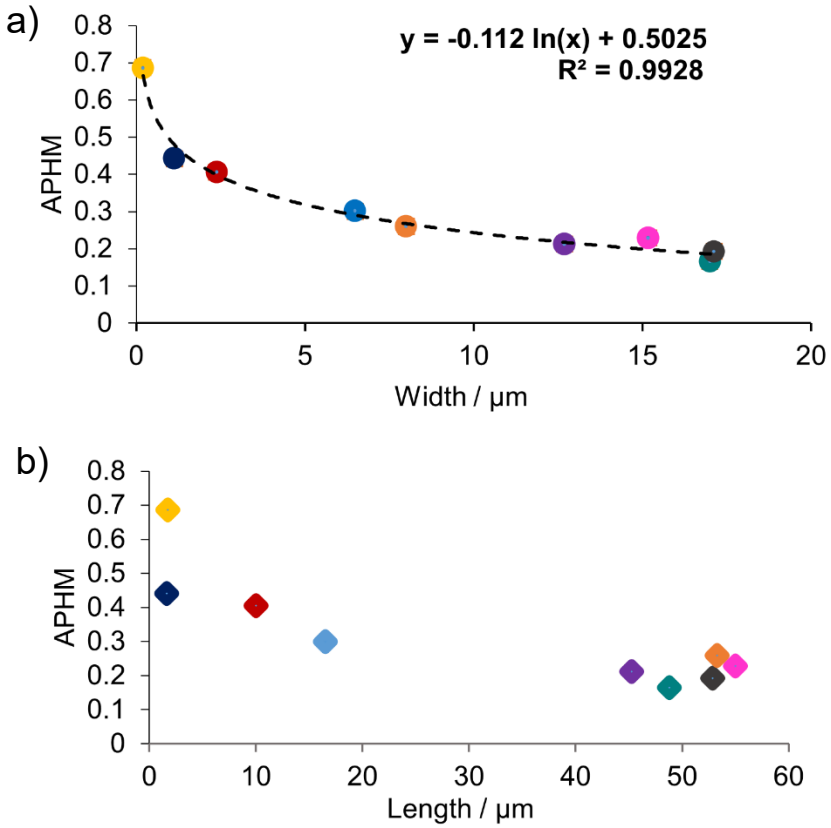

Figure 4-11. Dependence of the relative adsorption pressure at half maximum uptake (APHM) from the crystal width (A) and the crystal length (B). Samples **A** – blue, **PAA-1** – black, **PAA-2** – pink, **PAA-3** – orange, **B** – red, **C** – green, sample from ref (Miura et al., 2017) – cyan, **D** – violet, **E** – yellow. The fit function is shown as a dashed line.

Moreover, the steepness of the adsorption branch in the gating region decreases with decreasing crystal size, pointing at the significant broader activation energies distribution in the small grains in comparison to the large crystallites (Figure 4-12). Taking into account the decreasing α_{max} for the small crystallites, the crystal width approaches a certain critical value where the transition is completely suppressed due to the height of the barrier (ΔG^*), which cannot be overcome at given conditions. Another potential explanation for the observations is based on thermodynamic arguments, most importantly the differences in free energies of the empty *cp* and *op* frameworks ($\Delta F = F_{cp}-F_{op}$), originating from differences in surface energy and, probably, less important gradients of the adsorbed phase.

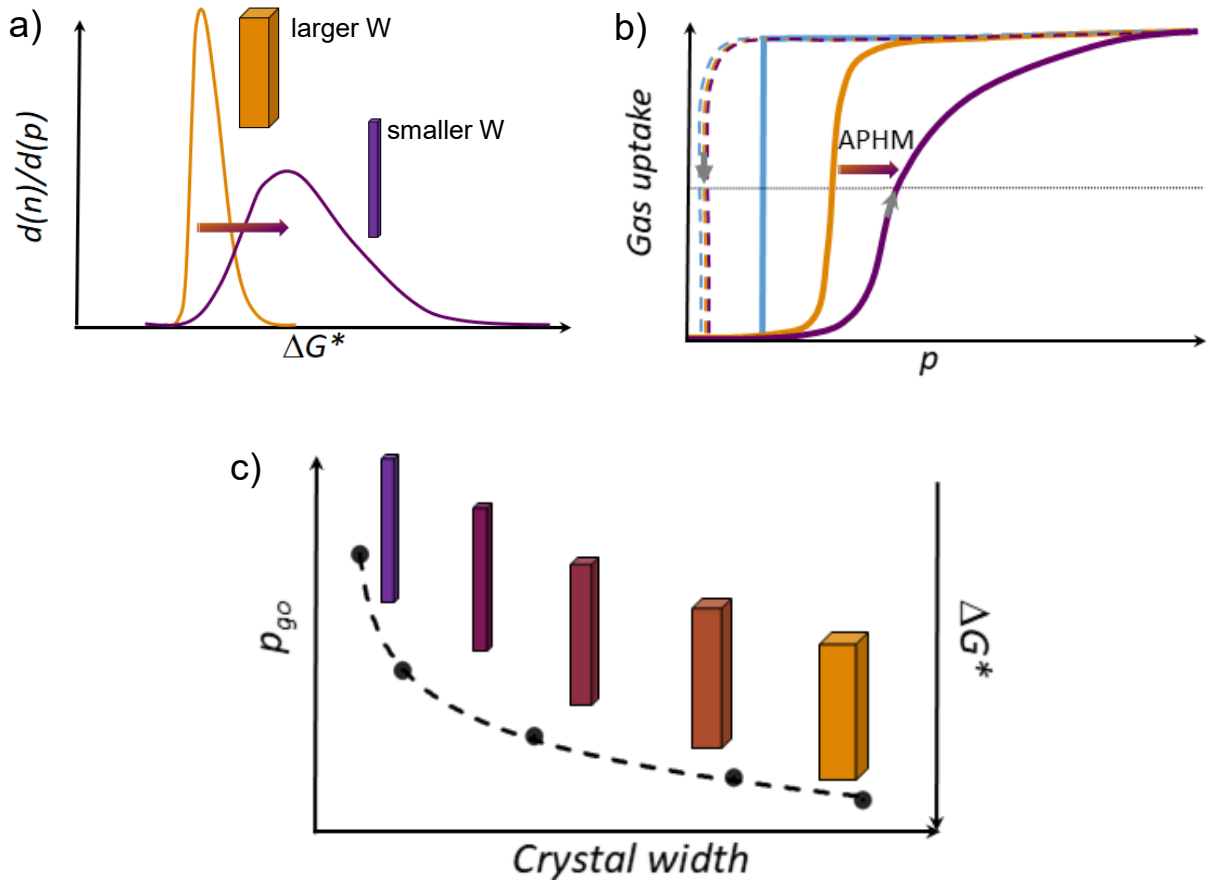

Figure 4-12. Overview of crystal-size-dependent behavior in DUT-8(Ni). a) Distribution of activation energies (1G*) in the sample, depending on the crystal width (W). b) Rectangular gate opening isotherm (blue) corresponding to an ideal single grain-switching event. Orange: schematic representation of the isotherm usually obtained for macro-sized crystals. Violet: typical isotherm characteristic for micron-sized particles (adsorption: solid line, desorption: dashed line). c) Dependence of the gate opening pressure from W.

Important arguments of why the crystal width represents the critical value for gate opening can be discussed by analysing the relationship between the crystal morphology and the structure of the pores. DUT-8 in the *op* phase has square channels running along the crystallographic *c* direction (Figure 4-13). The walls of the channels are built mainly from aromatic naphthalene cores of 2,6-ndc linkers. The corners are formed by rows of alternating paddle wheel–dabco units (Figure 4-14). The channels can be considered as virtually isolated since the analysis of the geometrical pore parameters of at least the static crystal structure suggests only small interconnection windows between the main channels accessible for guest molecules with 3.6 Å in diameter (kinetic diameter of nitrogen molecule[209]). Essentially, with decreasing width of the crystals, i.e., with reduced dimensions in the a–b plane (referring to the op structure), the surface on the top and the bottom of the crystal (area of {001} faces), where the molecules enter the channels, is reduced.

The reduced number of entry channels accessible for the molecules represents a "bottleneck" and reduces the initial energetic gain of the adsorption enthalpy, leading to an increased barrier for the guest-induced transformation. The data obtained in this study show that the barrier for the transition from *cp* to *op* phase in DUT-8(Ni) increases with a decrease in the area of crystal faces essential for initiation of adsorption (faces perpendicular to the direction of channels), illustrating the importance of local nucleation starting at the crystal surface as the factor determining the kinetics of the switching process.

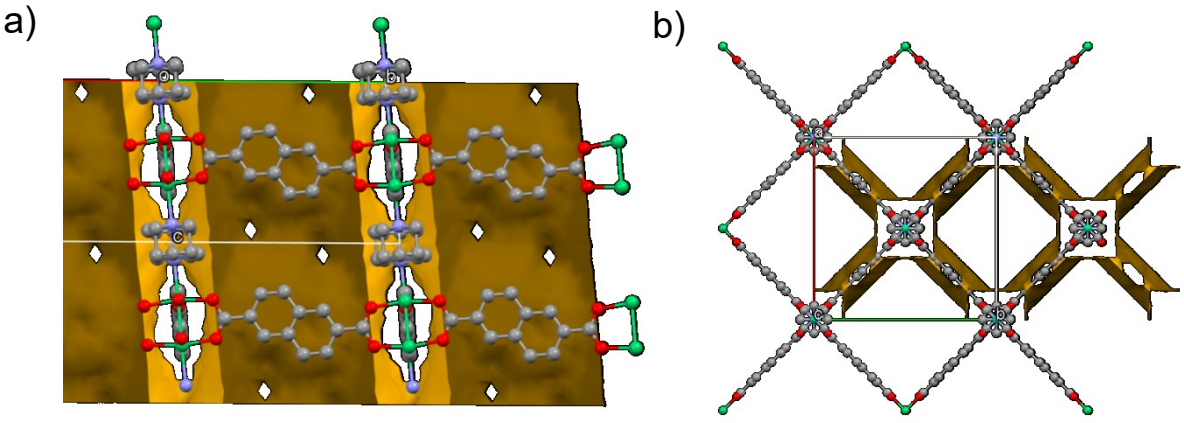

Figure 4-13. View on the crystal structure along a) [110] and b) [001].

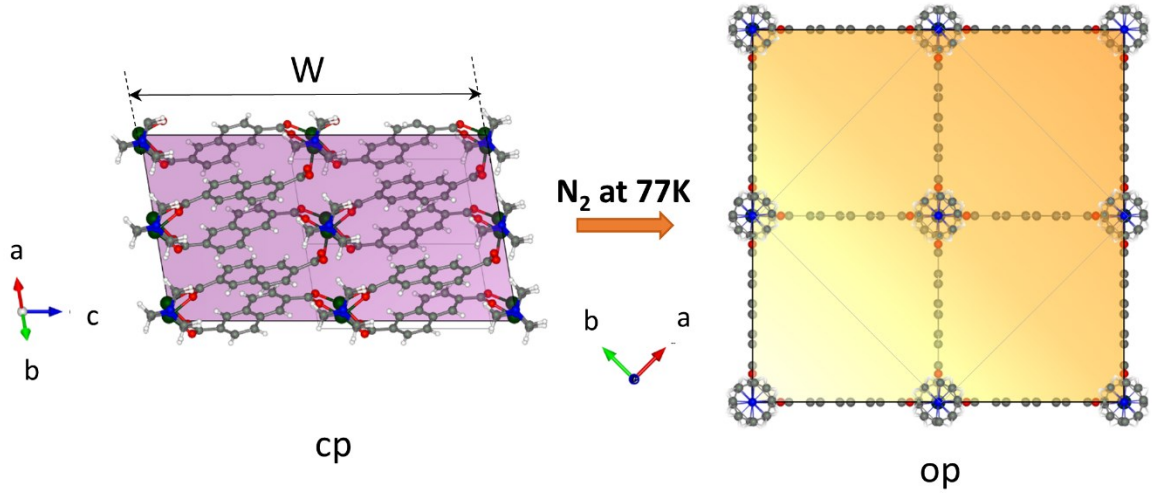

Figure 4-14. View on the crystal in the cp and op phase along the pore channel (generated by the VESTA 3.5.5 software) (Momma and Izumi, 2011). The colored face is the face representing the entry of the channel-like pore structure.

4.2.3 Conclusion

The modulation approach was successfully used to affect the size and shape of the flexible pillared layer DUT-8(Ni) MOF crystals, showing gate opening behaviour upon adsorption of nitrogen at 77 K, to investigate the dependency of structural transition from crystals' size and shape.

It could be explicitly seen that the crystal dimensions perpendicular to the axis of the channel-like pores influence the gate opening pressure. It indicates a higher activation barrier to result from reduced areas of facets, exposing the pore entry to the surface, providing a rationale for the observations, as the pores in DUT-8(Ni) are preferably accessible from the facets perpendicular to the channels. Since the width of the crystal determines the area of these faces, the crystal width (and not the lengths or the aspect ratio) controls the gate-opening process. The decrease in the crystal width also results in the less steep adsorption branch in the gating region, pointing to the broadening of activation energy distribution.

Chapter 5 The impact of crystal size and morphology on switchability of DUT-8(Zn)

The sections of this chapter are contained in my own publication.[13]

L. Abylgazina, I. Senkovska, S. Ehrling, V. Bon, P. Petkov, J. D. Evans, S. Krylova, A.Krylov and S.Kaskel, "Tailoring adsorption induced switchability of a pillared layer MOF by crystal size engineering", *CrystEngComm,* 23**,** (2020) 538.

5.1 Introduction

The pillared layer framework DUT-8(Zn) $[Zn_2(2,6\text{-ndc})_2(dabco)]_n$, is a prototypical switchable MOF, showing characteristic adsorption and desorption induced open phase (*op*) to closed phase (*cp*) transformation associated with huge changes in cell volume. The strong impact of the crystal or grain size on the switching characteristics of the "gate pressure" pillared layer MOF $[Ni_2(2,6\text{-ndc})_2dabco]_n$, DUT-8(Ni)[14] is described in Chapter 4. Small DUT-8(Ni) crystals (below 500 nm in size) do not undergo the *op* to *cp* transition upon desolvation.[18] The same behaviour is also characteristic for submicron-sized crystals of DUT-8(Co).[16] The macro-sized crystals of DUT-8(Co), however, do not show any responsivity to nitrogen (at 77 K) or carbon dioxide (at 195 K) during adsorption, in contrast to DUT-8(Ni), that shows pronounced switchability under the same conditions.[16] This suggests that the influences of particle size and metal node are interconnected and both aspects change the flexibility characteristics at a similar order of magnitude. Moreover, there may be more factors overlooked in the past, contributing to the phase transition energetics.

In the following, the detailed study of the adsorption induced switching of DUT-8(Zn) is presented.[15] In addition to the influence of the metal node and the particle size, we also demonstrate the influence of solvent molecules in the pores and the subsequent desolvation procedure on the framework response.

5.2 Results and discussions

5.2.1 Crystal size dependent guest removal and adsorption

DUT-8(Zn) can be synthesised using a solvothermal pathway resulting in macro-sized particles with average particle size of 160 µm (DUT-8(Zn)_160 µm). By supersaturation route it is possible to control the size of the particles and to produce micron- (DUT-8(Zn)_0.5 µm) and submicron-sized particles (DUT-8(Zn)_0.1 µm). SEM images of the samples and corresponding particle size distributions are shown in Figure 5-1. Powder X-ray diffraction (PXRD) patterns for all as-synthesized crystals are in good agreement with the pattern of DUT-8(Zn) calculated from the crystal structure (Figure 5-2), indicating that all samples are phase pure.

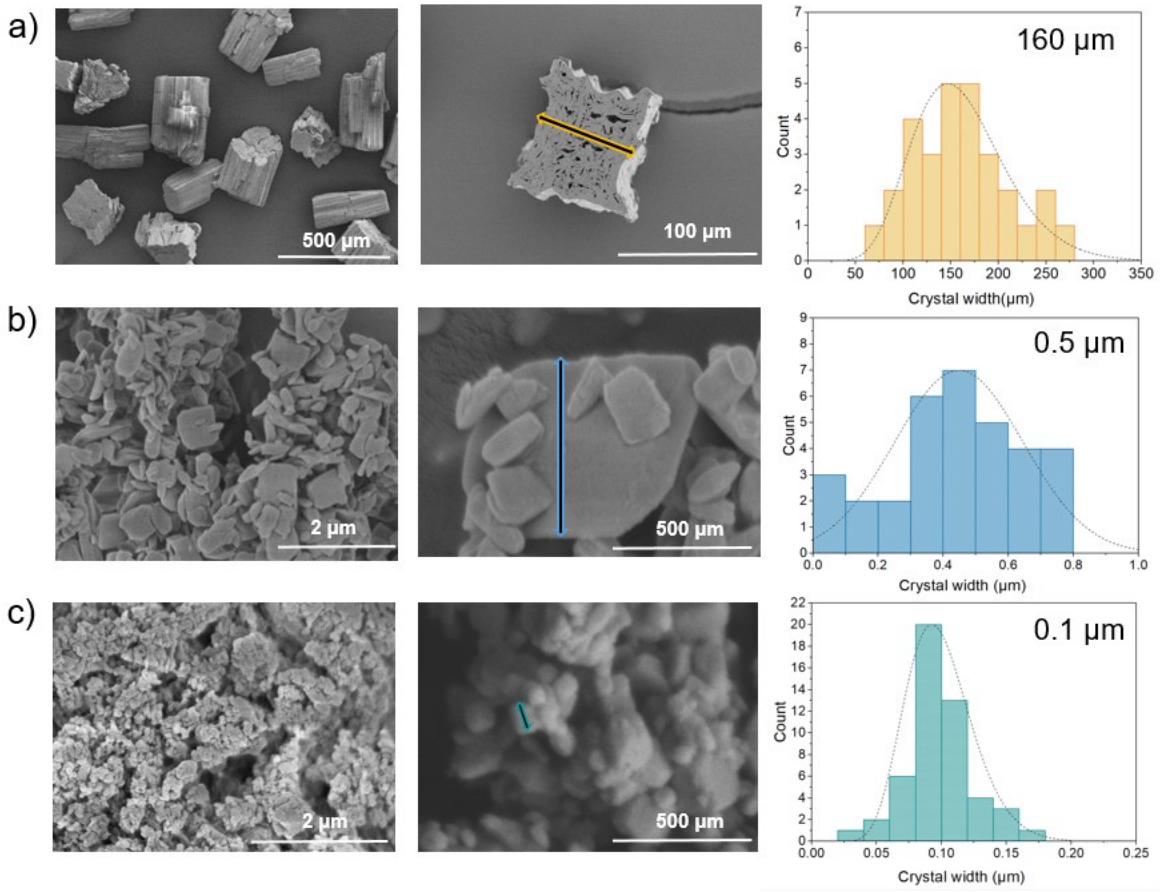

Figure 5-1. SEM images of DUT-8(Zn) samples.

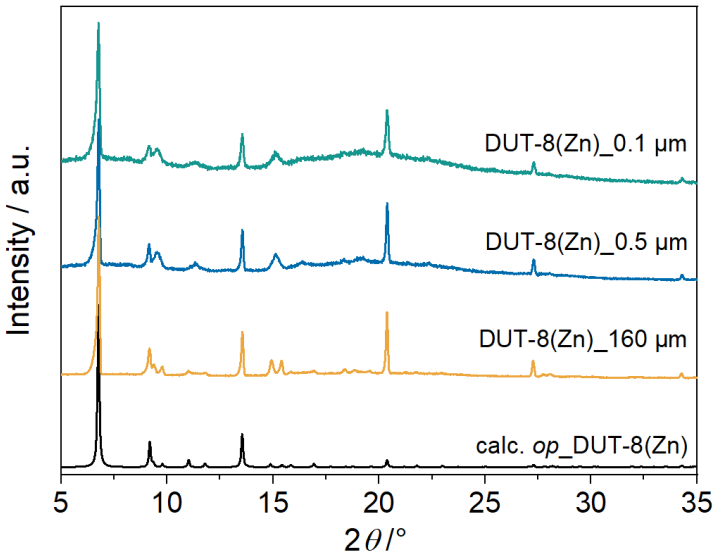

Figure 5-2. PXRD patterns of DUT-8(Zn) samples solvated in DMF.

Crystal structure of open and closed pore phases

To analyse the crystal structure, as made crystals were subjected to single-crystal X-ray analysis. The structure of DUT-8(Zn) was solved and refined by Dr. V. Bon in the monoclinic space group *C*2/m, which is different from the *P*4/n reported earlier from Rietveld refinement,[15] indicating conformational isomerism also in this compound, as discussed in detail for DUT-8(Ni).[118, 156] As expected, the overall crystal structure is based on paddle wheel units, which are interconnected by 2,6-ndc forming 2D layers, which are further linked by neutral dabco ligands to form a 3D framework with primitive cubic underlying topology (Figure 5-3). According to the crystallographic data, Zn···Zn distance in DUT-8(Zn)_160 µm_*op* is 2.966 Å, which is significantly longer than in DUT-8(Ni) and DUT-8(Co) (2.653 and 2.691 Å).[16] The length of the Zn–N bond is 2.084 Å. The comparison of this value with corresponding M–N bond lengths in DUT-8(Ni) and DUT-8(Co), shows that the value in DUT-8(Zn) is in between. The Zn–Zn–N angle is 178.65°, and comparable with that observed in DUT-8(Ni) (177.59°) (Table 8-3).[118]

Since the quality of the single crystals after solvent removal was not sufficient to collect a high quality dataset, a structural model was refined by against powder X-ray diffraction data in a triclinic space group Dr. V. Bon (Figure 5-4). The main cluster deformation is reflected in the change of M···M and M–O distances. The Zn atoms move apart, resulting in a change of the Zn···Zn distance from 2.97 (in the *op*) to 3.80

Å (in the *cp*) (Table 8-3), which leads to a strong elongation of some Zn–O bonds. In the cause of that the coordination polyhedron changes from quadratic pyramidal to distorted tetrahedral, since two Zn–O bonds are disintegrated (Figure 5-3).[210]

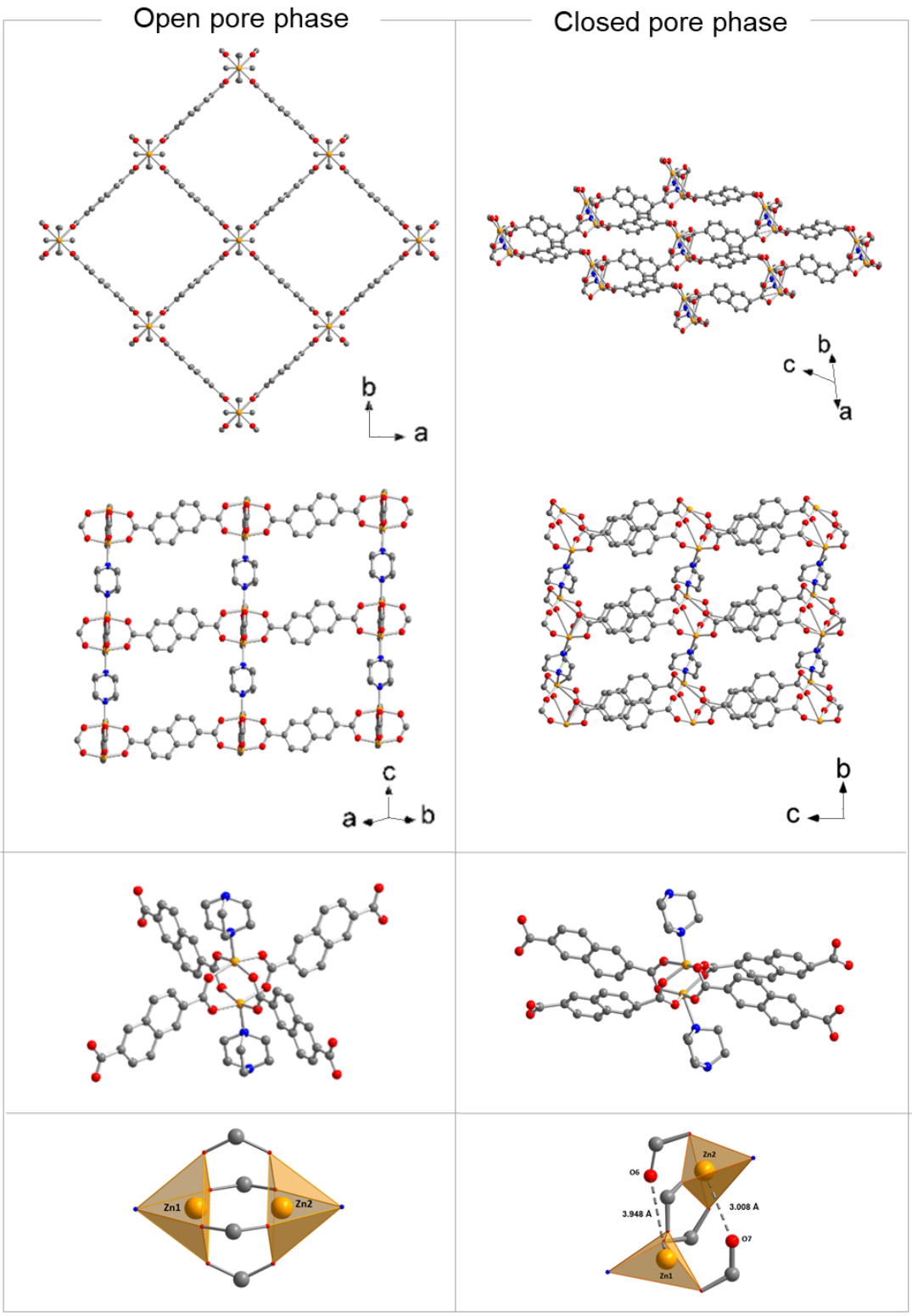

Figure 5-3. Crystal structure of DUT-8(Zn) in open and closed pore phase.

Crystal data for as made *[Zn_2(2,6-ndc)$_2$(dabco)(DMF)$_x$]$_n$* (DUT-8(Zn)_160 µm_*op*): $C_{30}H_{24}O_8N_2Zn_2$ (framework only, solvent molecules are omitted), M = 671.25 g mol^{-1}, monoclinic, *C2/m* (No. 12), a = 19.000(4) Å, b = 18.070(4) Å c = 9.6700(19) Å, β = 95.87(3)°, V = 3302.6(11) Å^3, Z = 2, λ = 0.79990 Å, T = 296 K, θ_{max} = 29.996°, reflections/parameter 2895/106, R_{int} = 0.0988, R_1 = 0.1070, wR_2 = 0.3048, S = 1.131 largest diff. peak 1.536 e. Å^{-3} and hole -1.445 e Å ^{3}.

Crystal data for DUT-8(Zn)_160 µm_*cp* *[Zn_2(2,6-ndc)$_2$(dabco)]$_n$:* $C_{30}H_{24}O_8N_2Zn_2$, M = 671.25 g mol^{-1}, triclinic, *P1* (No. 1), a = 7.1276(12) Å, b = 8.5505(13) Å, c = 13.1270(23) Å, α = 84.148(23)°, β = 116.032(19)°, γ = 108.462(16)°, V = 681.24(56) Å^3, Z = 1, λ = 1.54059 Å, T = 296 K, 2θ_{range} = 5 - 70°, Profile function Thompson-Cox-Hastings, U = 0.4946, V = 0.0066, W = 0.00343, X = 0.4260, Y = 0.1735, refined motion groups/degree of freedom 9/45, R_p = 0.0547, R_{wp} = 0.0791.

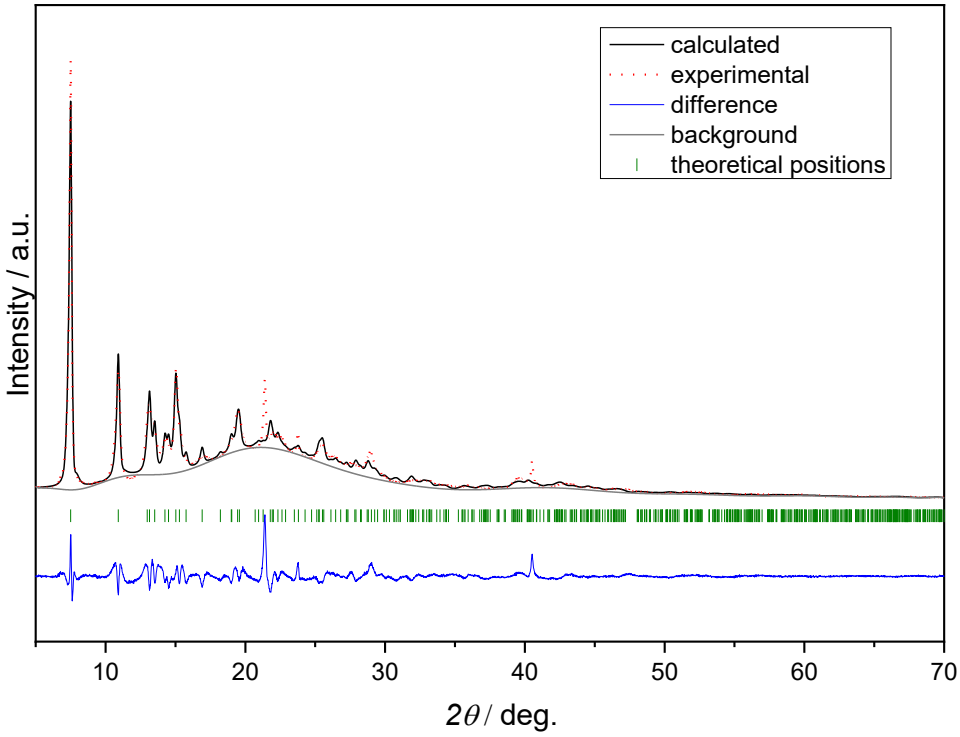

Figure 5-4. Rietveld plot of the closed pore phase of macro-sized DUT-8(Zn)_160_*cp*.

Desolvation

The stress acting on the framework during desolvation depends on surface tension and capillary forces imposed on the structure by the liquid- to gas-phase transformation of included solvent molecules, which is high especially when the solvent has a high boiling point and/or high surface tension.[176] A common approach to reduce the stress is to exchange the solvent with a low-boiling point/low-surface-tension solvent (these parameters tend to be correlated) prior to heating the sample under vacuum.[177] The most gentle desolvation approach is supercritical drying (SCD) using carbon dioxide as a working fluid.[178] SCD avoids the liquid–gas phase transition and thus any capillary forces.

Depending on the guest molecules present in the pore and desolvation technique applied, the forces acting on the framework can be varied[123] and indirect information of the relative robustness of the network can be extracted. The schematic illustration of procedures used for desolvation DUT-8(Zn) samples and resulting phase composition are shown in Figure 5-5. To represent structural transition of a porous material, new symbolic language was implemented.[65] The structural changes, the spatiotemporal evolution of the framework, are of course highly complex. However, for simplification and rationalization it is easier to simplify the phenomena considering only two different states of the framework. The open pore phase containing solvent symbolized by a colored square (specified color for each sample), while empty square represents solvent-free open framework. The closed pore state (*cp*) symbolized by a squeezed rhombus. The change between the states of the framework is shown by arrow representing the direction of the process in time (Figure 5-5). The conditions, causing structural changes are arranged below the arrow. For example, the condition responsible for the pore contraction is an evacuation (pump). As a result, it is possible to line-up all structural changes along consecutive arrows as a history time-line for the material. This structure provides a clear arrangement of “transformations” and “conditions”. Multiple phase formation indicated by line coding.

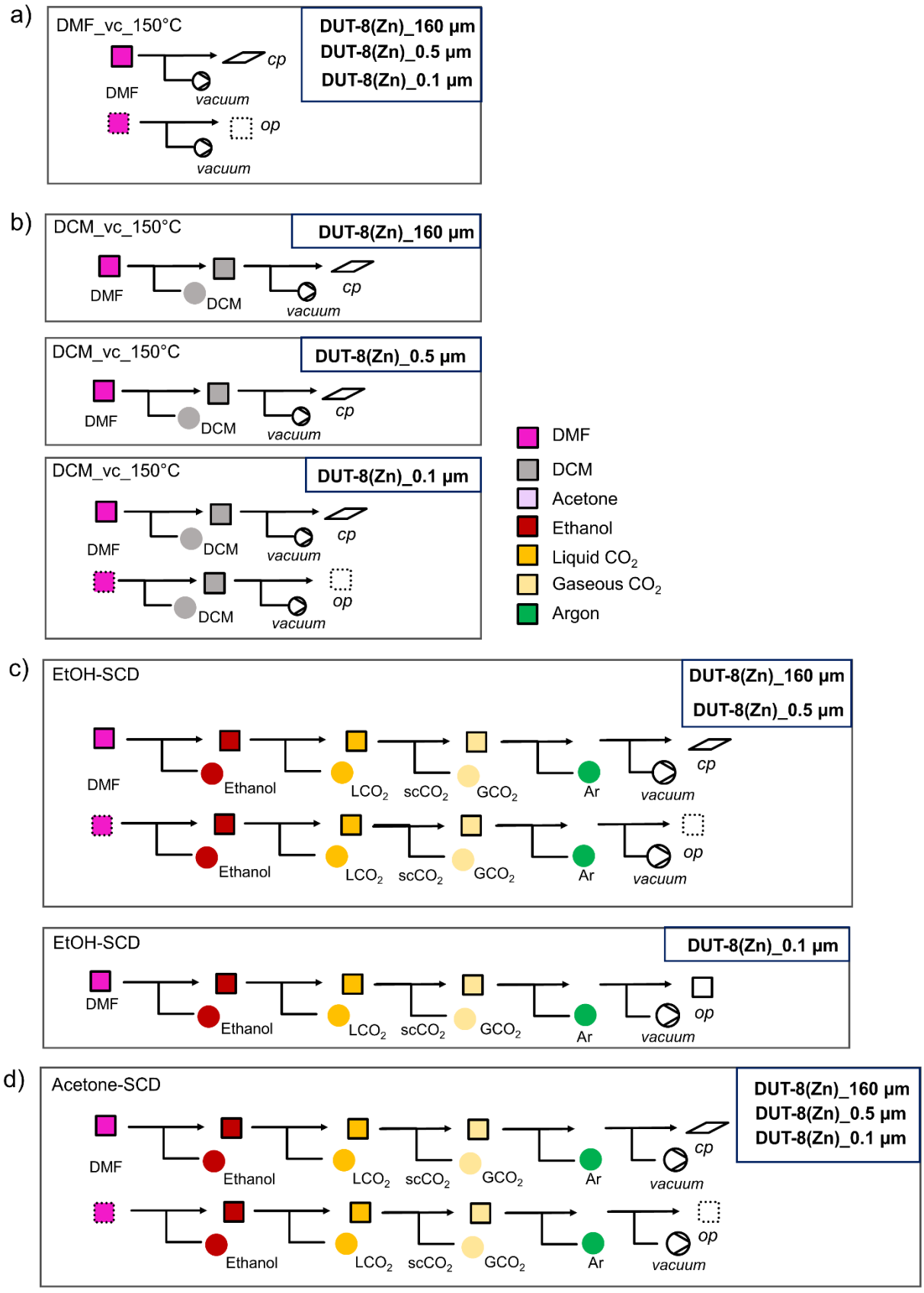

Figure 5-5. Schematic representation of procedures used for desolvation of DUT-8(Zn) samples a) evacuation under heating; b) solvent exchange with subsequent evacuation under heating; c), d) solvent exchange with subsequent SCD.

In a first series, according to the procedure reported earlier,[15] the desolvation of the DUT-8(Zn) crystals was performed by direct removal of DMF (solvent used during the synthesis) in vacuum at 423 K. DMF can be considered as a larger molecule among the solvents investigated here, with a kinetic diameter of 5.5 Å, and a very large dipole moment (3.8 D).[211] Therefore, both strong attractive interaction between MOF and DMF and slower diffusion rate should be expected.

The direct removal of DMF results in a mixture of closed pore (*cp*) and open pore (*op*) phases in the sample DUT-8(Zn)_160 µm_DMF (Figure 5-5, 5-6a), in agreement with results reported in 2012.[15] PXRD patterns of micron-sized DUT-8(Zn)_0.5 µm_DMF and submicron-sized crystals DUT-8(Zn)_0.1 µm _DMF indicate that the major part of the sample remains in the *op* phase with only an insignificant amount of *cp* phase. After activation, the samples were dissolved in DCl/D_2O and DMSO-d^6 mixture, and subjected to NMR analysis to reveal residual DMF molecules (Figure 8-6).

In order to reduce the stress during solvent removal, DMF was exchanged with dichloromethane before desolvation under reduced pressure at 423 K during 16 h. DCM is a molecule with a smaller kinetic diameter (4.70 Å),[212] smaller dipole moment (1.62 D)[35] and low boiling point (312.6 K), therefore, in comparison to DMF, it should be easier to remove.

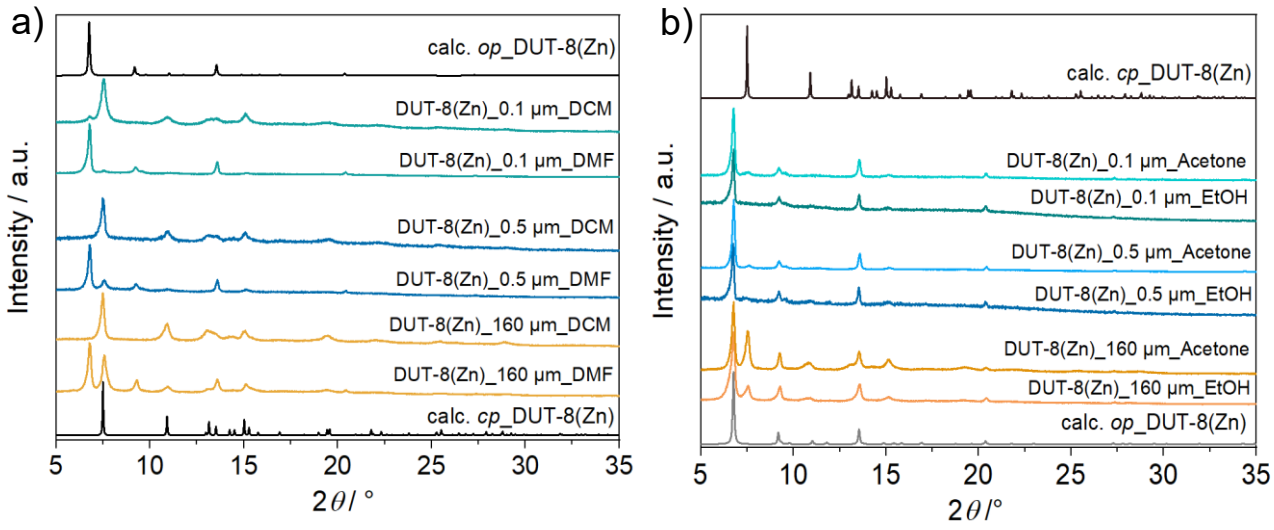

Figure 5-6. PXRD patterns of DUT-8(Zn) samples after different solvent removal procedures applied a) (DMF) indicates desolvation from DMF in vacuum at 423 K, (DCM) indicates desolvation from DCM in vacuum at 423 K; b) DUT-8(Zn) samples desolvated by SCD. The calculated pattern of the *op* and *cp* phases DUT-8(Zn) are given for comparison.

According to PXRD (Figure 5-6a), the desolvation of DUT-8(Zn)_160 µm_DCM and DUT-8(Zn)_0.5 µm_DCM triggers the structural transformation from *op* to *cp* phase, in which the framework undergoes a significant shearing to minimize the amount of void space. The submicron-sized crystals DUT-8(Zn)_0.1 µm_DCM show mainly the *cp* phase with a small amount of *op* phase.

To further reduce the stress on the framework, all samples were subjected to supercritical CO_2 drying (SCD) after washing several times with ethanol and acetone (Figure 5-6b). In this case, the macrosized particles DUT-8(Zn)_160 µm_EtOH yield a mixture of *op* and *cp* phases, the fraction of the *cp* phase in micron-sized particles DUT-8(Zn)_0.5 µm_EtOH is very small, and DUT-8(Zn)_0.1 µm_EtOH (submicron-sized) completely remain the original *op* phase, as observed for as-synthesized form. This indicates the robustness of the system under supercritical CO_2 activation conditions. However, ^{1}H NMR revealed the small amount of EtOH remained in samples after desolvation (Figure 8-8-1). Due to the interaction of EtOH with DUT-8(Zn), micron-sized and submicron-sized samples were washed by acetone and afterwards activated by SCD. PXRD patterns of samples correspond to *op* phase with small fraction of *cp* (Figure 5-6b). According to ^{1}H NMR spectra, there is no residual solvent in the pores (Figure 8-8-2).

SEM images (Figure 5-7) collected after each desolvation procedure show that there is no significant influence on crystal surface upon removal of solvent from pores. The desolvation of macro-sized DUT-8(Zn)_160 µm leads to crystals cracking and deformation due to framework contraction. The drying of micron DUT-8(Zn)_0.5 µm and submicron DUT-8(Zn)_0.1 µm crystals results in particles aggregation, despite the surface remains homogeneous and smooth. Only the surface of samples was shown to be significantly changed after washing by ethanol and subsequent SCD. The residual amount of ethanol revealed by ^{1}H NMR and the surface deformation caused by ethanol and SCD points on chemical interaction with micron- and submicron-sized particles of DUT-8(Zn).

Comparing the structural response of DUT-8(Zn) towards different desolvation techniques, it may be hypothesized that the energy barrier for framework closing increases with decreasing particle size (Figure 5-8). The small particles can rest in the metastable desolvated *op* state while the large particles transform into the thermodynamically preferable *cp* state. For SCD the desorption stress is so small that the transformation of largest particles is incomplete. Contrastingly, the deformation

stress of DCM is larger resulting in the smallest particles to transform almost completely.

The results of activation from DMF, however are rather unexpected. The surface tension and capillary forces are expected to be higher for DMF than for DCM and, therefore, support the closing, which is not the case. There are likely differences in the diffusion rates, which can also play a role.

The calculated yields and the result of the elemental analysis of DUT-8(Zn) samples in pure *op* or *cp* phases are shown in Table 8-4, 8-5 (appendix).

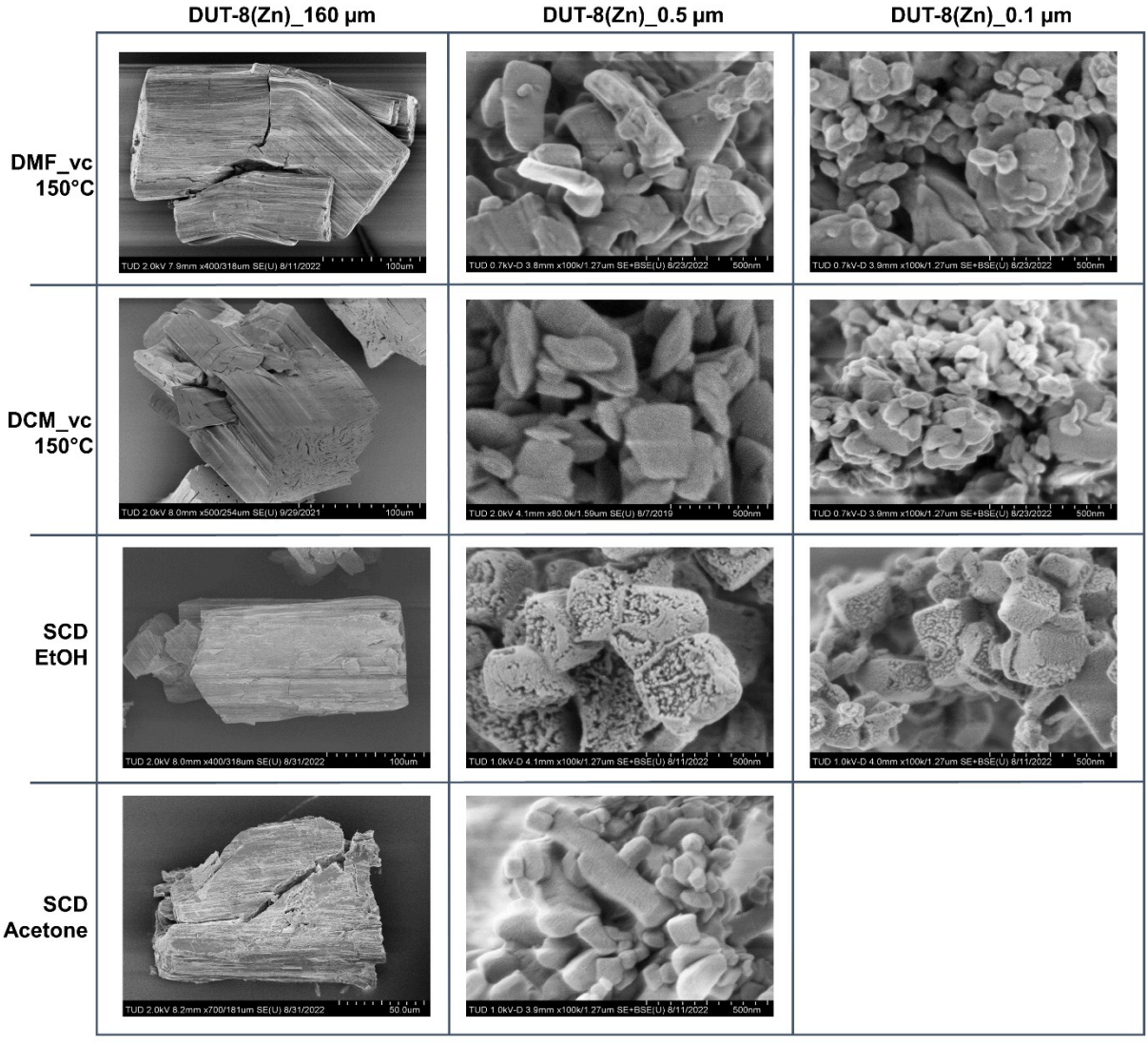

Figure 5-7. SEM images of samples after solvent removal procedures.

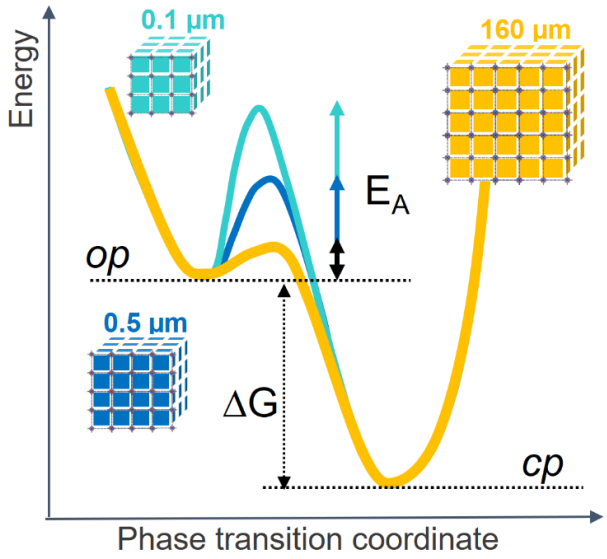

Figure 5-8. Schematic representation of the energy diagrams for phase transitions from the *op* to *cp* phase depending on particle size.

Adsorption behaviour

Switching transformations from closed to open pore phases and vice versa induced by adsorption stimuli and their dependence on the crystal size was previously studied in isomorphous DUT-8(Ni) and DUT-8(Co) systems, revealing striking differences in adsorption behaviour, due to characteristic differences in framework's elastic response.[16] The underlying electronic differences, in case of Ni, Co and Zn should be reflected in closing/opening characteristics of respective MOFs. Indeed, DUT-8(Zn) samples demonstrate pronounced differences in their adsorption isotherms compared to the Co and Ni analogues. Since the solvent removal techniques described above produce samples with varying ratio of *op/cp* phases, and the exact ratio is difficult to extract from PXRD patterns, we evaluated the porosity and structural response of all samples by means of adsorption of nitrogen at 77 K, carbon dioxide at 195 K, and chloromethanes at 249–298 K.

Samples desolvated from DMF. The obtained N_2 (77 K) physisorption isotherms can be classified as type Ia, characteristic for microporous rigid materials (Figure 5-9a). The maximum nitrogen uptake follows the trend expected from PXRD data, where samples with higher amount of the *op* phase show the highest uptake and vice versa. The *cp* fraction remains in the *cp* state and is not responsive to nitrogen over the entire pressure range.

The adsorption of CO_2 at 195 K (Figure 5-9b), a guest with higher adsorption enthalpy, demonstrates some structural dynamics. However, the presence of mixed phases in the samples makes it difficult to interpret the data. The PXRD patterns collected after adsorption reveal a slightly increased amount of the *cp* phase in comparison to the samples before experiments in case of micron-sized DUT-8(Zn)_0.5 µm_DMF and submicron sized DUT-8(Zn)_0.1 µm_DMF samples. This fact is pointing toward a possible breathing mechanism of the *op* phase during the adsorption/desorption cycle (Figure 5-10).

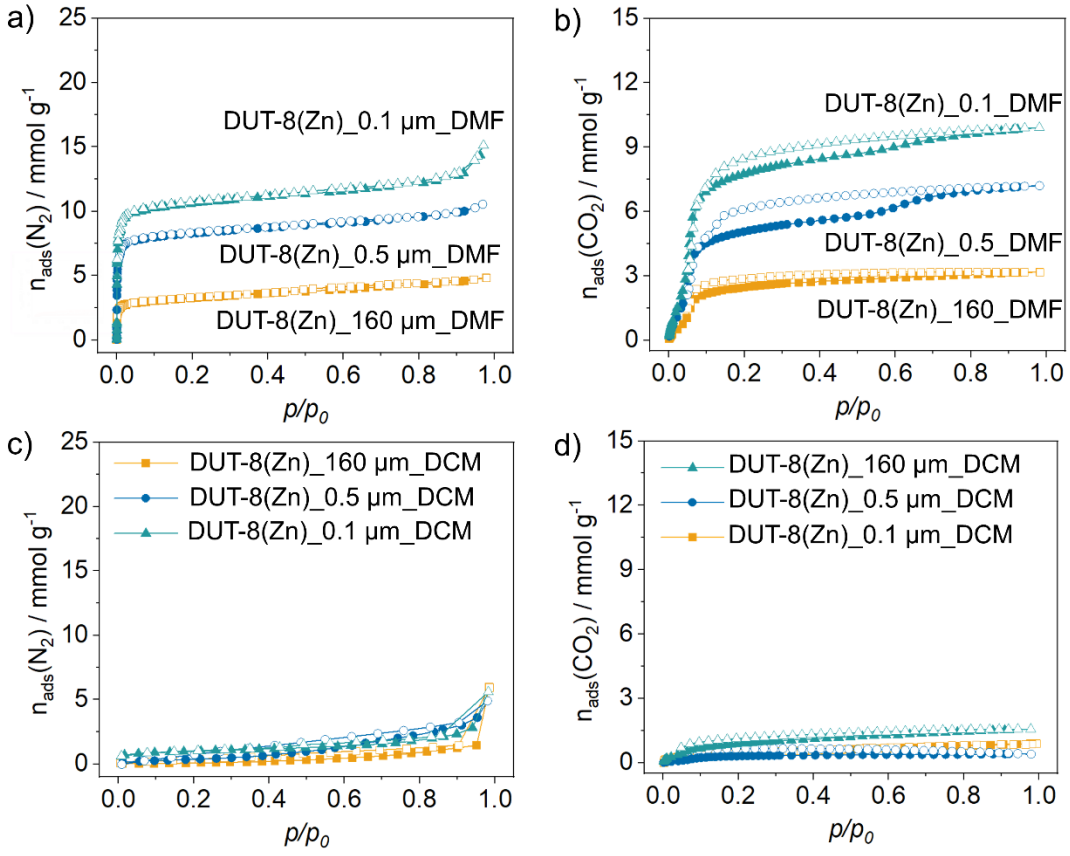

Figure 5-9. Nitrogen at 77 K and carbon dioxide physisorption at 195 K on: a, b) Samples activated from DMF; c,d) Samples activated from DCM.

Samples desolvated from DCM. Analysis of PXRD patterns of the samples desolvated from DCM shows a transition to the *cp* phase upon activation (Figure 5-6a). The N_2 and CO_2 physisorption isotherms show low uptake, indicating the high stability of the *cp* phase under these conditions (Figure 5-9c,d). However, more polar, small molecules, such as chloromethane at 249 K and dichloromethane at 298 K (kinetic diameters 4.05 and 4.70 Å, respectively)[213] are able to provoke structural transition in macro-sized particles DUT-8(Zn)_160 µm_*cp* (Figure 5-11). The isotherms are characterized by typical gate opening shape with a gate opening relative pressure of 0.87 and 0.80, respectively. More interesting, the chloromethanes can discriminate between the particles of different size. The isotherms of DUT-8(Zn)_0.5 µm_*cp* display no structural changes (Figure 5-11). This observation clearly shows, that the decreasing particle size, and associated increase in outer surface area and surface energy adds to the energy barrier of *cp*–*op* phase transformation.[214]

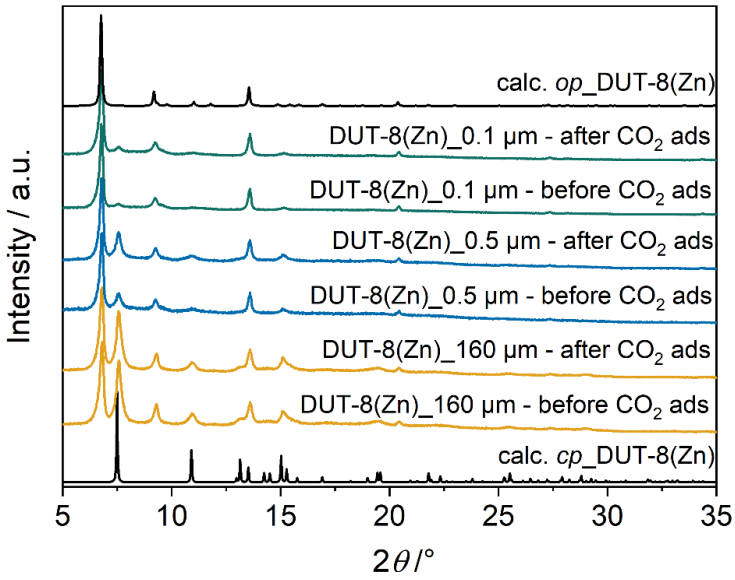

Figure 5-10. PXRD patterns of DUT-8(Zn) samples desolvated from DMF, before and after CO_2 physisorption measurements.

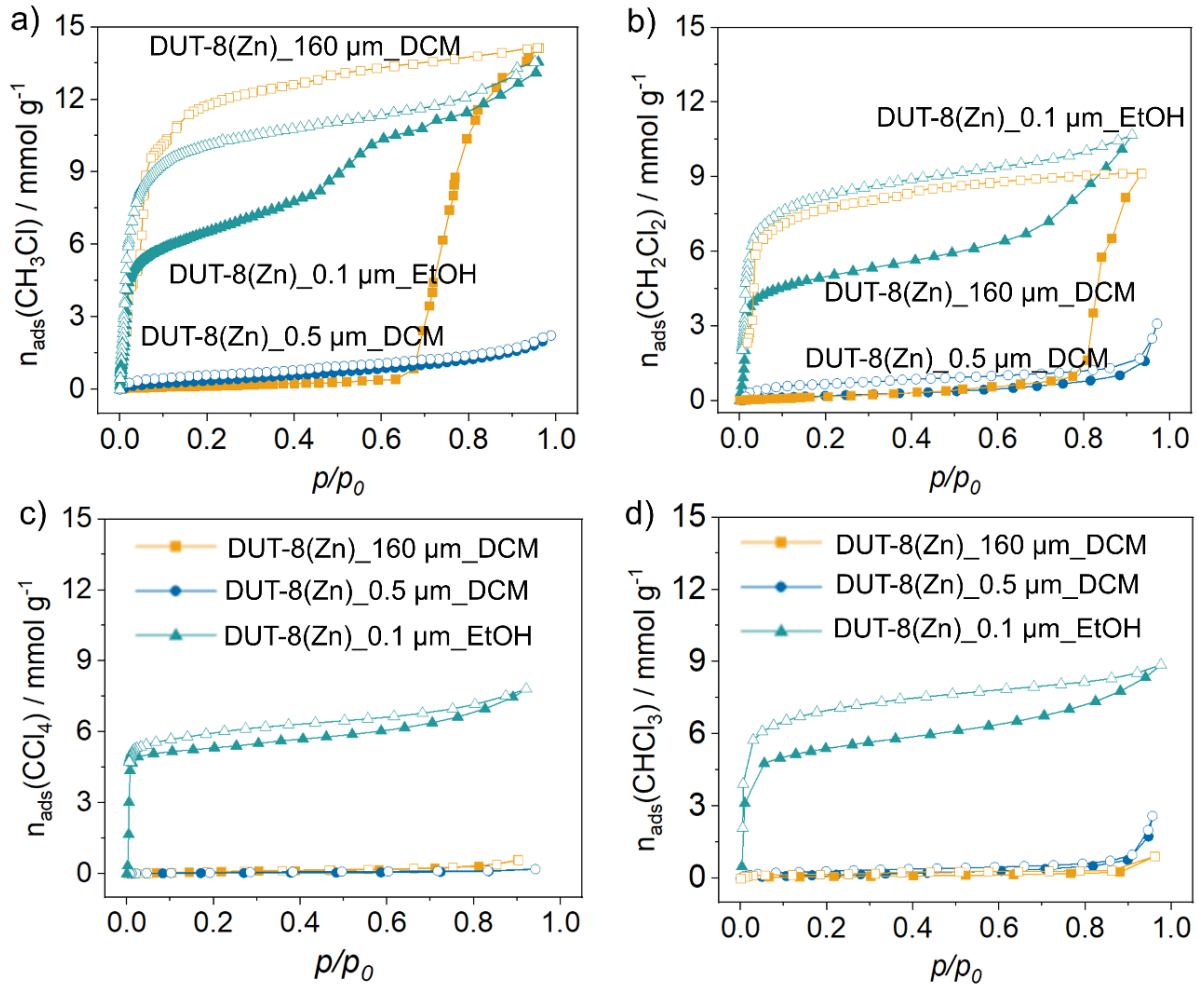

Figure 5-11. Adsorption isotherms of chlorosubstituted methanes for DUT-8(Zn) samples.

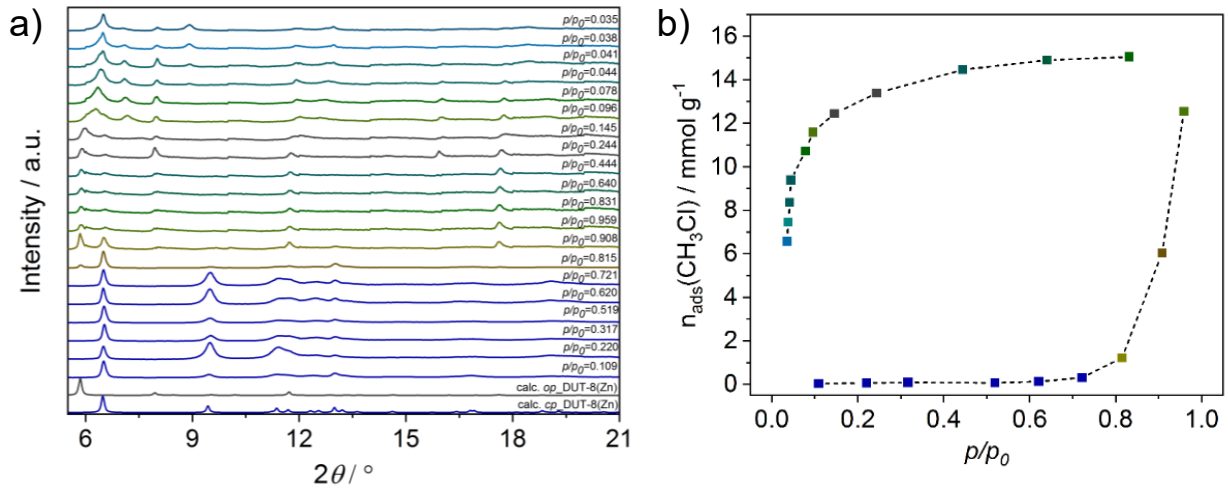

Figure 5-12. a) *In situ* PXRD patterns collected during CH_3Cl adsorption at 249 K on macro-sized sample DUT-8(Zn)_160 µm_*cp* and b) corresponding isotherm.

To analyse the structural phases induced by CH_3Cl adsorption, parallelised adsorption/diffraction experiments were performed on DUT-8(Zn)_160 µm_*cp* at KMC-2 beamline of BESSY II synchrotron (Figure 5-12). In the pre-gate region of the isotherm, the analysis of the PXRDs indicated the existence of pure *cp* phase. At p/p_0 = 0.815 the pattern indicates a first order transition of the structure from nonporous *cp* to porous *op* phase without appearance of any intermediate phases. PXRD patterns measured at saturation at p/p_0 = 0.959 (the highest pressure reached) and upon desorption of chloromethane until "gate closing" show coexistence of *cp* and *op* phases. The intensity of reflections belonging to op phase is strongly influenced by strong absorption and diffuse scattering, attributed to adsorbed chloromethane.

The effect is nicely seen in the PXRDs measured upon "gate closing" at p/p_0 between 0.14 and 0.24, in which reduction of CH_3Cl amount in the pores significantly increases the intensity of the op phase reflections. Further desorption of the CH_3Cl from the pores induces a phase transition to an intermediate phase (ip) in the range of p/p_0 = 0.09–0.03.

The first reflection at 2θ = 6.5° could correspond to the cp phase, however a few additional reflections appear at 2θ = 7.05, 8.05 and 8.95° that are not attributed to op or cp phases. However, severe peak broadening and limited number of reflections hinders quantitative analysis of the PXRD patterns. In contrast to CH_2Cl_2, $CHCl_3$ and CCl_4 are unable to initiate the switching for micron-sized DUT-8(Zn)_0.5 µm_*cp* or for macro-sized DUT-8(Zn)_160 µm_*cp* at 298 K (Figure 5-11). The adsorption enthalpies

for $CHCl_3$ and CCl_4 may be expected to be higher, than for CH_3Cl and CH_2Cl_2. However, as the size differs considerably, significant differences in maximal loadings per formula unit of MOF (n_{max}) can be estimated (Table 5-1).[212]

Table 5-1. Chloromethane characteristics.[212]

Adsorptive	Kinetic diameter* / Å	n_{max}/ mol·fu^{-1}	E_{ads}/ kJ·mol^{-1}	n_{max}·E_{ads} / kJ fu^{-1}
CCl_4	5.83	7	62	434
$CHCl_3$	5.47	9	57	513
CH_2Cl_2	4.70	11	51	561
CH_3Cl	4.05	19	36	684

E_{ads} – adsorption energy at 300 K, *Kinetic diameters are given as Lennard-Jones parameters taken from ref[213]

Hence, the total adsorption energy (n_{max}·E_{ads}) per Zn_2(2,6-ndc)$_2$dabco formula unit (fu) of MOF decreases continuously from chloromethane to tetrachloromethane (Table 5-1). This provides an energetic reason for the absence of structural response $CHCl_3$ and CCl_4. In addition, the smaller kinetic diameter also favours adsorption kinetics and a reduced activation barrier can be expected for CH_3Cl and CH_2Cl_2 (Figure 5-10).

Samples desolvated supercritically (SCD). All SCD samples, prior to adsorption contain predominantly the *op* phase. The physisorption of N_2 at 77 K, CO_2 at 195 K, chloromethane at 249 K, and dichloromethane at 298 K reveal the switchable behaviour of the samples (breathing), since stepwise isotherms with hysteresis were observed. The structural response (the hysteresis width) and uptake vary significantly with the particle size (Figure 5-11, 5-13). The influence of the solvent used for SCD drying was investigated for the micron-sized (0.5 µm) and submicron-sized (0.1 µm) crystals. Both of them follow the similar adsorption pathway, therefore only the micron-sized DUT-8(Zn)_0.5 µm will be discussed. Upon adsorption of N_2 (Figure 5-13c), the switchable behaviour of DUT-8(Zn)_0.5 µm_EtOH results in breathing type of isotherm with hysteresis, while desolvation from acetone leads to rigidification of the sample DUT-8(Zn)_0.5_acetone resulting in type I isotherm. In case of CO_2 adsorption (Figure 5-13d), the opposite trend is observed, the desolvation from acetone leads to the more pronounced breathing behaviour of DUT-8(Zn)_0.5 µm_acetone in comparison with sample DUT-8(Zn)_0.5 µm_EtOH .

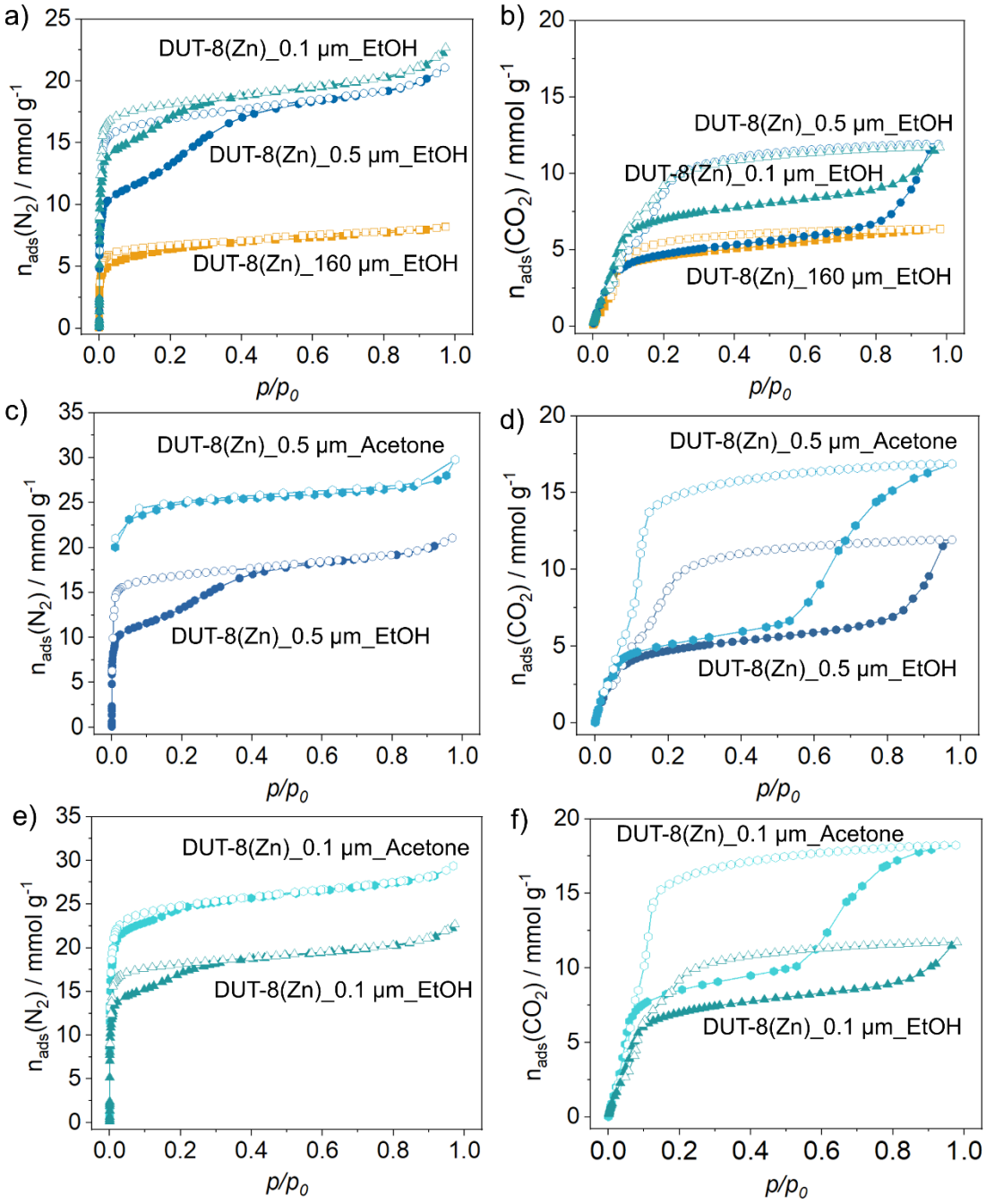

Figure 5-13. Nitrogen adsorption at 77 K and carbon dioxide physisorption at 195 K on: a, b) the comparison differently-sized crystals activated by SCD from EtOH; c, d) Micron-sized and e), f) submicron-sized crystals activated by SCD from EtOH and acetone.

In order to provide insight into breathing mechanism, *in situ* experiments were performed during CO_2 adsorption at 195 K on DUT-8(Zn)_0.1 µm_*op* dried from EtOH (Figure 8-8-3), because other SCD samples have small fraction of *cp* phase (Figure 5-6b). Micropore filling occurs at low relative pressure (Figure 8-8-3). Starting from p/p_0 = 0.128 in the adsorption branch, the small additional peaks appear in the PXRD

patterns, that are attributed to formation of the *cp* phase. The *cp* phase is visible in the in situ data in all patterns collected at relative pressures higher than 0.128 and in desorption branch, up to p/p_0 = 0.061. At the last point measured at p/p_0 = 0.009, some residual amount of the *cp* phase is present. We can conclude, that during the adsorption of carbon dioxide, breathing of the structure occurs, suggesting a more labile paddle wheel is present, in comparison to the Ni and Co analogues that show type I adsorption isotherm without any signs of switchability.[16]

An important observation is that the critical size for DUT-8(Zn), which suppress switchability is considerably smaller (< 50 nm), compared to DUT-8(Ni) (< 200 nm) and DUT-8(Co).[16] In addition, reduced desorption stress is needed, since the pure *op* phase could be achieved only by SCD activation. In contrast, the submicron-sized particles of DUT-8(Ni) and DUT-8(Co) withstand the removal of DCM under vacuum without transformation.

5.2.2 Spectroscopic investigations of DUT-8(Zn) samples

For further investigations, the following samples are chosen: “as made” DUT-8(Zn) samples in DMF (DUT-8(Zn)_160 µm, DUT-8(Zn)_0.5 µm, DUT-8(Zn)_0.1 µm) and samples after desolvation from DCM in *cp* state (DUT-8(Zn)_160 µm_*cp*, DUT-8(Zn)_0.5 µm_*cp*) and after SCD in *op* phase (DUT-8(Zn)_0.1 µm_*op*).

IR-spectroscopy

The asymmetric stretching vibrations of the carboxylate in the recorded range are not influenced by the structural transition. For both compounds in the *cp* phases DUT-8(Zn)_160 µm_*cp* and DUT-8(Zn)_0.5 µm_*cp* the bands are at 1602 cm^{-1} and in the *op* phase (DUT-8(Zn)_0.1 µm_*op*) at 1605 cm^{-1} (Table 5-2, Figure 5-14). The symmetric stretching for both compounds in the *cp* phase is at 1467 cm^{-1} and 1465 cm^{-1} in the *op* phase. Furthermore, it is observed that the scissor deformation $\delta(COO^-)$ is slightly affected by the present phase. In the *cp* phase the vibration can be observed at 806 cm^{-1} and in the op phase at 813 cm^{-1}. No differences were found in asymmetric vibrations of the dabco molecule in micron-sized DUT-8(Zn)_0.5 µm_*cp* and sub-micron sized crystals DUT-8(Zn)_0.1 µm_*op* (1057 cm^{-1} for *cp* and *op* phases).

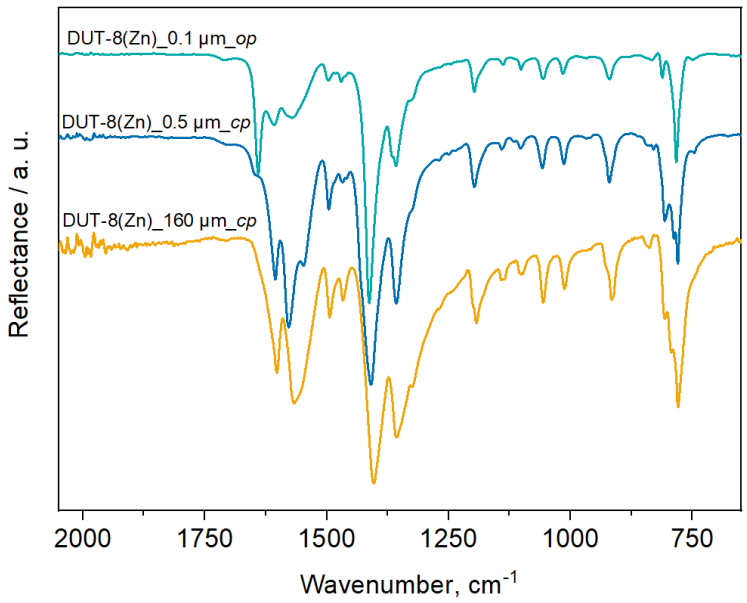

Figure 5-14. IR-spectra of DUT-8(Zn) samples.

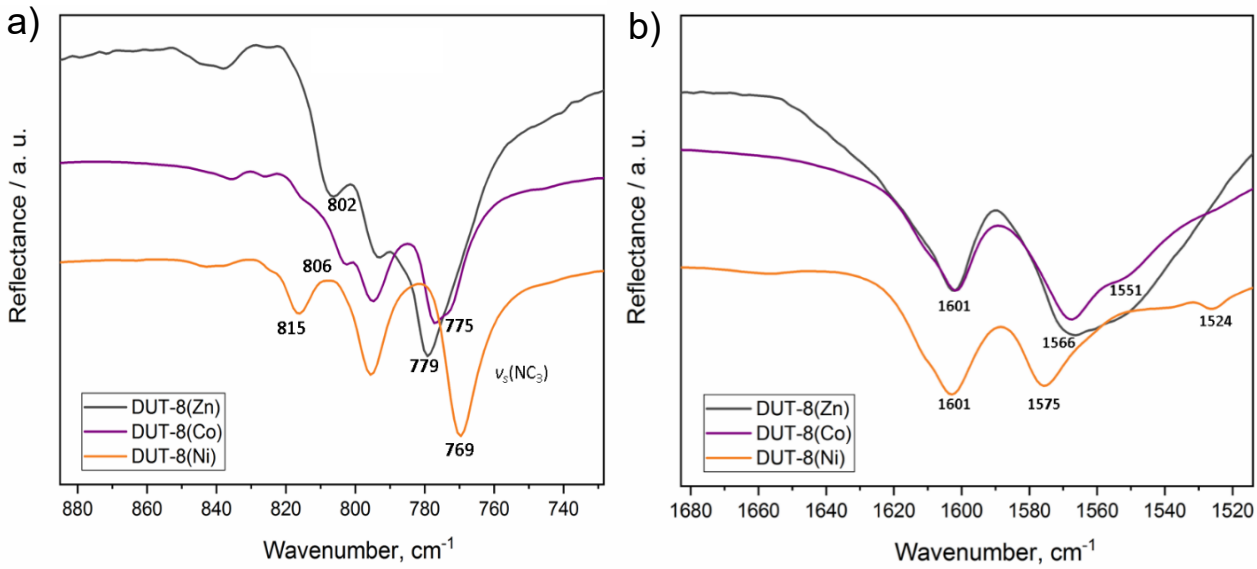

Figure 5-15. a), b) IR-spectra of DUT-8(Ni), DUT-8(Co), and DUT-8(Zn) in the closed pore state.

Table 5-2. Wavenumbers of expected and observed vibrations.

Vibration	*v* observed in DUT-8(Zn)_160 µm_*cp* / cm^{-1}	*v* observed in 8(Zn)_0.5 µm_*cp* / cm^{-1}	*v* observed in 8(Zn)_0.1 µm_*op* / cm^{-1}
$\nu_{as}(COO^-)$	1602	1602	1605
$\nu_{s}(COO^-)$	1467	1467	1465
$\delta(COO^-)$	806	806	813
$\nu_{as}(NC_3)$	1056	1056	1056
$\nu_{s}(NC_3)$	780	780	782

Comparing the spectra of the *cp* phases of macro-sized DUT-8(Ni), DUT-8(Co) and DUT-(Zn) crystals (Figure 5-15), one can see, that despite the stronger cluster deformation observed from crystallographic data for DUT-8(Zn) compound, the vibrations of the carboxylates (COO^-) in the recorded range are not significantly influenced, *i.e.* the asymmetric stretching vibration is at 1602 cm^{-1}, the symmetric stretching at 1467 cm^{-1}. The scissor deformation is more affected, since this appears at 816 cm^{-1} for Ni, at 802 cm^{-1} for Co and at 806 cm^{-1} for Zn.

Asymmetric vibrations are not influenced by metal node (1056 cm^{-1} for all compounds). The symmetric stretching vibrations of NC_3 are sensitive to metal and the positions of the bands differ (Zn: 779 cm^{-1}, Co: 776 cm^{-1}, Ni: 769 cm^{-1}) as shown in Figure 5-15a.

Raman spectroscopy

It was already shown, that Raman spectroscopy is a powerful tool to reveal the differences in switchability of the frameworks due to the differences in the lattice vibration frequencies.[215] In order to characterize the open pore phase, “as made” samples of DUT-8(Zn) in DMF were investigated first. The characteristic band appears at 23 cm^{-1} for all investigated samples of DUT-8(Zn) (Figure 5-16a). The obtained characteristic lattice vibration bands values for DUT-8(Zn) are almost the same as for DUT-8(Ni) and DUT-8(Co) (23 cm^{-1}, 24 cm^{-1}).[16, 215]

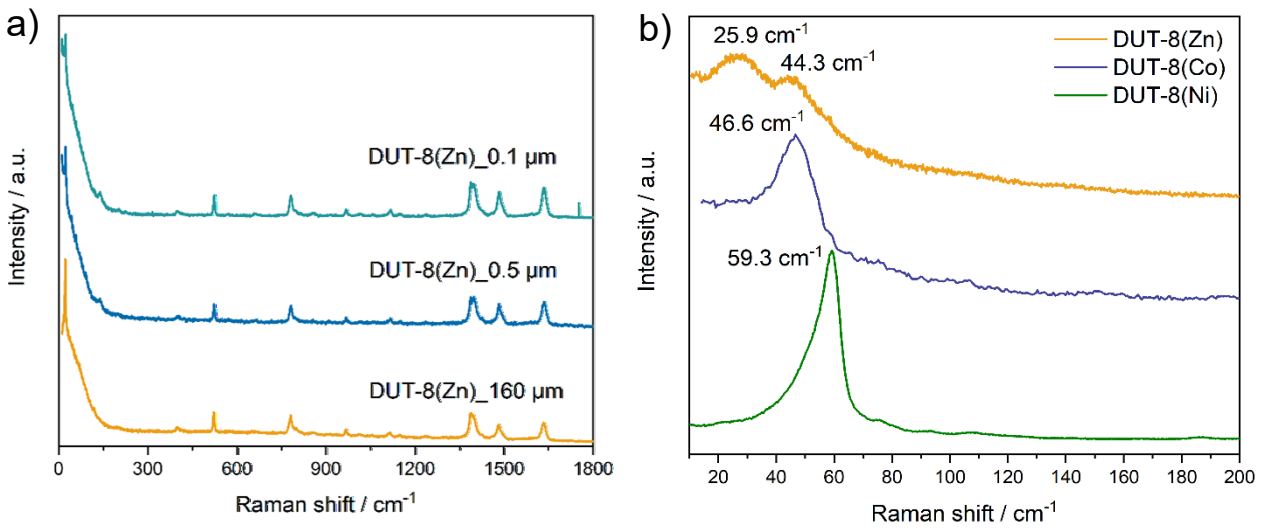

Figure 5-16. Raman spectra of samples in a) wide spectral range of DUT-8(Zn) samples solvated in DMF and b) the low frequency spectra of desolvated macro-sized DUT-8(Zn)_160 µm_DCM in comparison with macro-sized crystals DUT-8(Ni) and DUT-8(Co).

The desolvated macro-sized sample DUT-8(Zn)_160 µm_*cp* as analysed shows two bands at 25.9 and 44.3 cm^{-1} (Figure 5-16b, Figure 8-9). The appearance of the second lattice vibration mode in the spectrum is obviously attributed to the drastic changes in the environment of the Zn atoms in the *cp* state, facilitating additional vibration modes of the framework constituents.

The decrease in frequency for the closed pore phase from 59.3 and 46.6 cm^{-1} for DUT-8(Ni) and DUT-8(Co), respectively, to 44.3 cm^{-1} for DUT-8(Zn) indicates that the force constant for DUT-8(Zn)_*cp* framework is lower compared to Co. However, the difference between Co and Ni (4 cm^{-1}) is more pronounced as for Co and Zn (2 cm^{-1}).

Solid state NMR spectroscopy

The investigation MOFs and their interactions with adsorbed guest molecules is widely performed by NMR spectroscopy.[216, 217] It was previously revealed that it is possible to distinguish between *op* and *cp* phases of DUT-8(Ni) by solid-state NMR.[216]

The investigations of DUT-8(Ni) and DUT-8(Co) were performed by selective labelling of carbon atoms of the carboxyl groups of 2,6-H_2ndc with ^{13}C.[218] However, diamagnetic properties DUT-8(Zn) allow to investigate this system without the isotope enrichment of the linker. The measurements were performed by Marcus Rauche in the group of Prof. Dr. Eike Brunner (Chair of Bioanalytical Chemistry, TU Dresden).

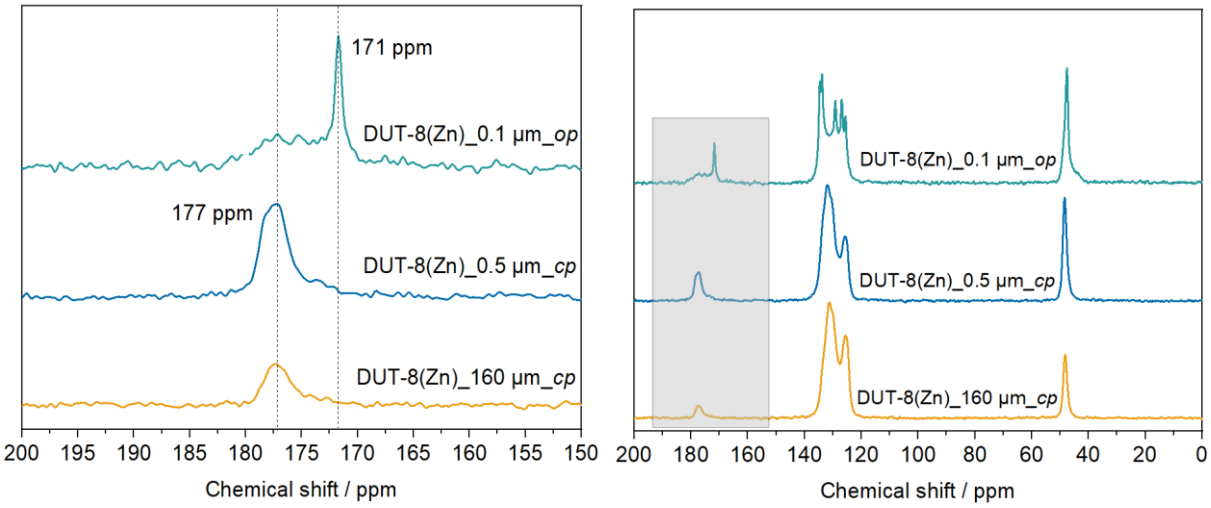

Figure 5-17. ^{13}C CP MAS NMR spectra of desolvated DUT-8(Zn)_160 µm_*cp*, DUT-8(Zn)_0.5 µm_*cp* and DUT-8(Zn)_0.1 µm_*op*.

The ^{13}C NMR chemical shift of DUT-8(Zn) samples is 171 ppm in DMF, which is slightly less than of pure 2,6-ndc linker (173 ppm) (Figure 8-10).[216] However, the values of chemical shifts are considerable higher for DUT-8(Ni) and DUT-8(Co) solvated in the solvents with different polarity (in DMF 270 ppm and 540 ppm, respectively). The solvent-dependent chemical shift was related to the influence of solvent on the isotropic Fermi contact coupling constant. The latter impacts the electron spin density distribution around the di-metal clusters.[218]

The desolvation of DUT-8(Zn)_160 µm and DUT-8(Zn)_0.5 µm results in the framework contraction (*cp* phase). The phase transition is accompanied by decent isotropic chemical shift increase 177 ppm (Figure 5-17). The chemical shift of desolvated DUT-8(Zn)_0.1 µm in *op* is identical to the signals of samples in the solvated state 171 ppm.

In contrast, the carboxylates of DUT-8(Ni) in *cp* and *op* state exhibit significantly higher chemical shifts 229 and 226 ppm, respectively.[216] But, the difference between the values is less pronounced than for desolvated *op* and *cp* phases of DUT-8(Zn).

5.2.3 DFT simulations

Theretical calculations were performed by Dr. Petko St. Petkov, Dr. Jack D. Evans.

First, atomistic simulation was applied to the paddle wheel unit to capture the behaviour of the molecular hinge present in the frameworks. Constrained geometric optimisations of a representative paddle wheel were performed, where the N– Zn–Zn

and Zn–Zn–N angles were fixed and subsequently scanned for angles between 180° and 150° (Table 5-3). In contrast to the previous reports for Ni, Co and combination of both metals in the paddle wheel,[16, 219] the minimum energy configuration for the Zn paddle wheel is observed at 180°. Deformation of this unit to angles associated with the *cp* phase (approx. 155°) did not produce decomposition of the paddle wheel and requires almost 6 kJ mol^{-1}. This apparent rigidity of the Zn paddle wheel unit in the op phase is not reflected experimentally, suggesting that framework interactions and a more complex deformation mode are required to reproduce the transitions present in DUT-8(Zn).

Table 5-3. Relative energy for the constrained geometry scans of the M-M-N for the representative Zn paddle wheel.

Zn-Zn-N angle / °	**relative energy / kJ mol^{-1}**
180	0.00
175	0.04
170	0.54
165	1.61
160	3.36
155	5.92
150	9.53

The geometry of DUT-8(Zn) in the *op* and the *cp* phase was subject to energy minimization in periodic boundary conditions, using a unit cell of one Zn paddle wheel (PW) unit, two 2,6-ndc ligands, and one dabco pillar. During the energy minimization the cell shape, volume, and atomic positions were relaxed. The geometry of the *cp* phase was obtained starting from *op* phase after NPT MD simulation at 300 K and 1 atm pressure. The MD simulation performed in a fully flexible cell resulted in spontaneous *op*–*cp* transformation of the DUT-8(Zn) in 2 ps. Key interatomic distances and angles for *op* and *cp* phase are collected in Table 5-4. We observe good agreement between the experimental and calculated geometry parameters.

Table 5-4. Characteristic geometric parameters in DUT-8(Zn): Zn…Zn distance in the paddle wheel, Zn-O(carboxylic) bond lengths, Zn-N(dabco) bond lengths, and Zn-Zn-N(dabco) angle.

Distances and angles	***op***	***cp***
Zn…Zn / Å	2.82	3.78
Zn – O / Å	2.06	1.99, 2.02, 2.02, 3.78
		2.03, 2.01, 2.11, 3.61
Zn – N / Å	2.10, 2.11	2.11, 2.14
Zn – Zn – N / °	174	119

The calculated interatomic distances show, in line with experimental data, that upon closure the Zn paddle wheel undergoes significant structural deformation in comparison to DUT-8(Ni) and DUT-8(Co).[16] The Zn···Zn distance elongates by 0.97 Å, from 2.82 in *op* to 3.79 in the *cp* phase. Another notable deformation in the Zn PW is the Zn–O distances. From the analysis of the MD trajectories (Figure 8-11) is visible that two of the total eight Zn–O distances in the Zn-PW are significantly elongated upon closure. In the minimized geometry of the *cp* phase, two Zn–O distances are elongated up to 3.78 and 3.61 Å, while the other six Zn–O distances are much smaller affected, 2.01– 2.11 Å. Such deformation in the Zn-PW is responsible for the much less strain in the closed phase in comparison to DUT-8(Ni). The strain energy for DUT-8(Ni), where the Ni-PW stays intact upon closure, was calculated to be +102 kJ mol^{-1}, while for DUT-8(Zn) it is only +78 kJ mol^{-1} (Table 5-5) due to the Zn-PW partial distortion. On the other hand, the contribution from the dispersion interaction between 2,6-ndc linkers is very similar for DUT-8(Ni) and DUT-8(Zn), −188 kJ mol^{-1}, and −181 kJ mol^{-1}, respectively, leading overall to a higher stabilization of the *cp* vs. *op* phase for DUT-8(Zn) (−104 kJ mol^{-1}) in comparison to DUT-8(Ni) (−86 kJ mol^{-1}). These findings suggest that framework dynamics for DUT-8(Zn) and DUT-8(Ni) are dominated by the strain in the framework related to the stiffness of the paddle wheel hinge.

Table 5-5. Relative energy (ΔE) of the transformation of open to closed forms for DUT-8(Zn) and DUT-8(Ni), change of strain energy E_{str} and change of London dispersion energy ΔE_{disp}. All values are in kJ mol^{-1} per formula unit.

	DUT-8(Zn)	DUT-8(Ni)
ΔE	-104	-86
E_{str}[a]	+78	+102
ΔE_{disp}[b]	-182	-188

[a]The strain energy E_{str} was calculated as follows: from total energy of each system the corresponding dispersion energy was removed. The resulting value for closed pore form was subtracted from the one of the open pore form.
[b]The change in the dispersion energy ΔE_{disp} was calculated as follows: the dispersion energy in the closed pore form was subtracted from the dispersion energy of the open pore form.

5.2.4 Thermal analysis and thermo-responsivity of DUT-8(Zn)

In order to estimate thermal stability of DUT-8(Zn) samples**,** thermogravimetric analysis (TGA) was performed in synthetic air flow (5 K min^{-1}). Interestingly, the analysis discloses decreasing thermal stability with decreasing size of the crystals. The decomposition of macro-sized DUT-8(Zn)_160 µm_*cp* starts at 400°C, whereas sample DUT-8(Zn)_0.5 µm_*cp* starts to decompose at 380° K already (Figure 5-18). The decomposition proceeds in both samples in one step.

Despite relatively small difference in average crystal size between sample DUT-8(Zn)_0.5 µm_*cp* and sample DUT-8(Zn)_0.1 µm_*op***,** the thermal stability of sample DUT-8(Zn)_0.1 µm_*op* is considerably lower than for DUT-8(Zn)_0.5 µm_*cp*, showing the first decomposition step starting from 220°C already, presumable associated with the dabco elimination.

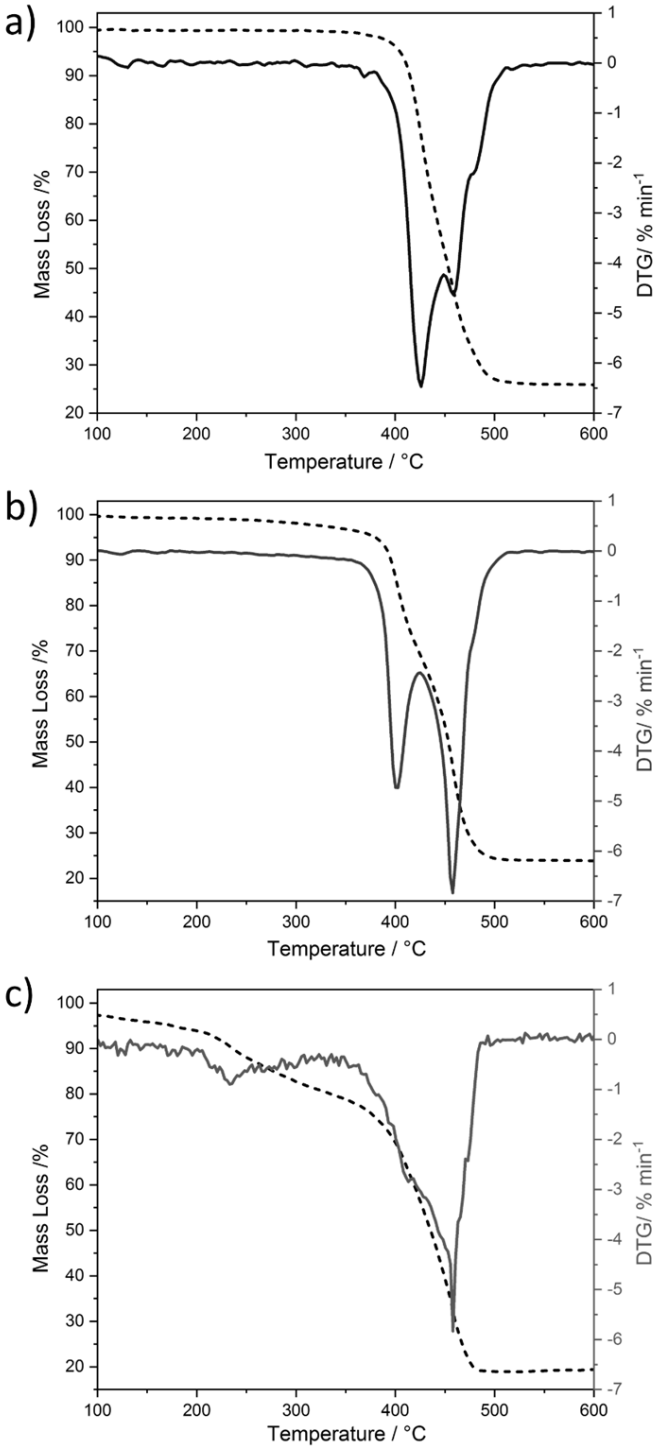

Figure 5-18. TGA (black) and DTG (blue) of: a) DUT-8(Zn)_160 µm_*cp* ; b) DUT-8(Zn)_0.5 µm_*cp*; c) submicron-sized sample DUT-8(Zn)_0.1 µm_*op*.

The temperature-induced framework contraction or expansion can be achieved without changing chemical composition.[53, 220-223] Previously, temperature induced phase transitions were observed in DUT-8(Ni).[224] Starting from the *op* or *cp* phase, depending on the crystal size regime, the structural transition occurs upon heating, which results in a new crystalline confined closed phase pore phase (*ccp*). The new phase was shown to be an interpenetrated framework, as a result of bond breaking/reformation under the increased temperature.

The transition from *cp* to *ccp* in DUT-8(Ni) is observed in the temperature range 400-430°C. For investigation of thermo-responsive behaviour of DUT-8(Zn)_160 µm_*cp*, the variable-temperature PXRD (VT-PXRD) was performed in the range from 25°C up to 402°C in the N_2 flow (Figure 5-19a). As can be seen from VT-PXRD patterns, starting from 227°C, the main reflections at 2θ = 7.3, 10.7, 15 gradually shifted to 2θ = 7.7, 11, 15.7 by reaching 377°C. At this temperature, the reflections at 2θ = 13, 14 are absent. The same structural response was observed by thermal treatment of the sample DUT-8(Zn)_160 µm_*cp* in the pre-heated oven in the N_2 flow for 16 h. PXRD patterns were recorded after reaching the 300°C, 325°C and 350°C (Figure 5-19b). Unlike DUT-8(Ni), there is no phase transition in macro-sized DUT-8(Zn)_160 µm from *cp* to *ccp*. The comparison of PXRD pattern at 350°C with theoretical PXRD pattern of DUT-(Ni)_*ccp* reveals the mismatch of the main peaks. The temperature-driven changes in macro-sized DUT-8(Zn) could be associated with the changes in unit cell parameters, pointing on the possible negative thermal expansion (NTE). Several MOFs shrink with increasing temperature, reaching colossal NTE value.[225-227]

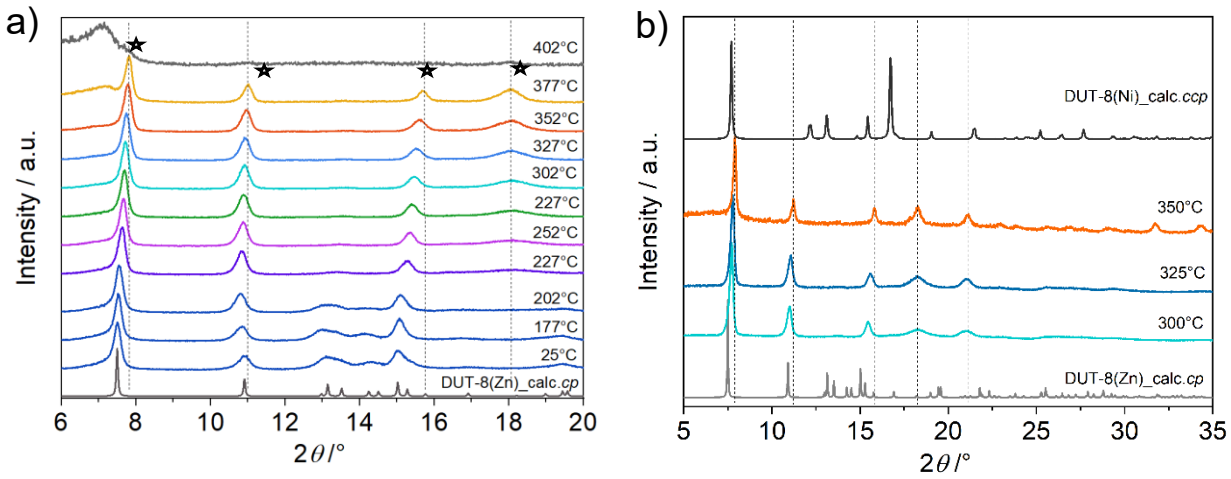

Figure 5-19. a) VT-PXRD measurements under N_2 atmosphere on sample DUT-8(Zn)_160 µm_*cp* in a temperature range from 25 °C to 400 °C, b) PXRD patterns of sample collected after heating in oven.

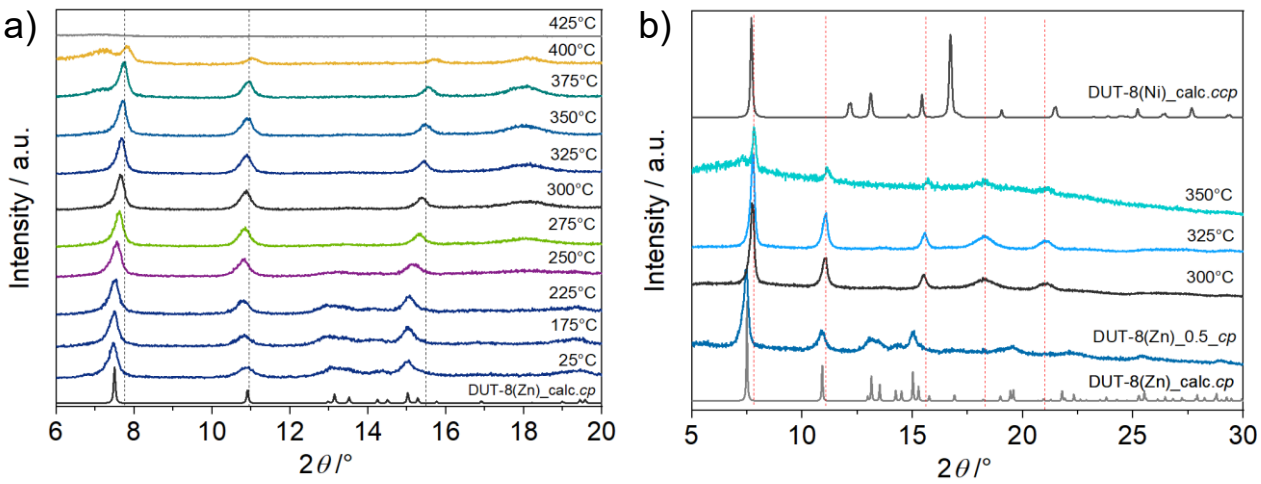

Figure 5-20. a) VT-PXRD measurements under N_2 atmosphere on sample DUT-8(Zn)_0.5 µm_*cp* in a temperature range from 25°C to 400°C, b) PXRD patterns of sample collected after heating in oven.

Considering submicron-sized DUT-8(Ni), the phase transition from *op* phase to *ccp* was observed at 235°C, reaching complete transition at 400°C. In case of metastable *op* phase of submicron-sized DUT-8(Zn) (Figure 5-21a), framework begins to disintegrate at 175°C, which is not in the agreement with TGA results, which revealed thermal stability up to 220°C. Such inconsistency could be related to different heating conditions.

However, the heating conditions are quite critical for metastable *op* phase of submicron-sized DUT-8(Zn)_0.1 µm_*op*. The sample was heated in the furnace until certain temperatures for 16 h in N_2 flow. PXRD patterns were recorded after reaching 150°C, 185°C, 205°C and 250°C. As can be seen from PXRD (Figure 5-21b), submicron-sized crystals DUT-8(Zn)_0.1 µm_*op* transformed to interpenetrated *ccp* phase already at 185°C with significant loss of crystallinity.

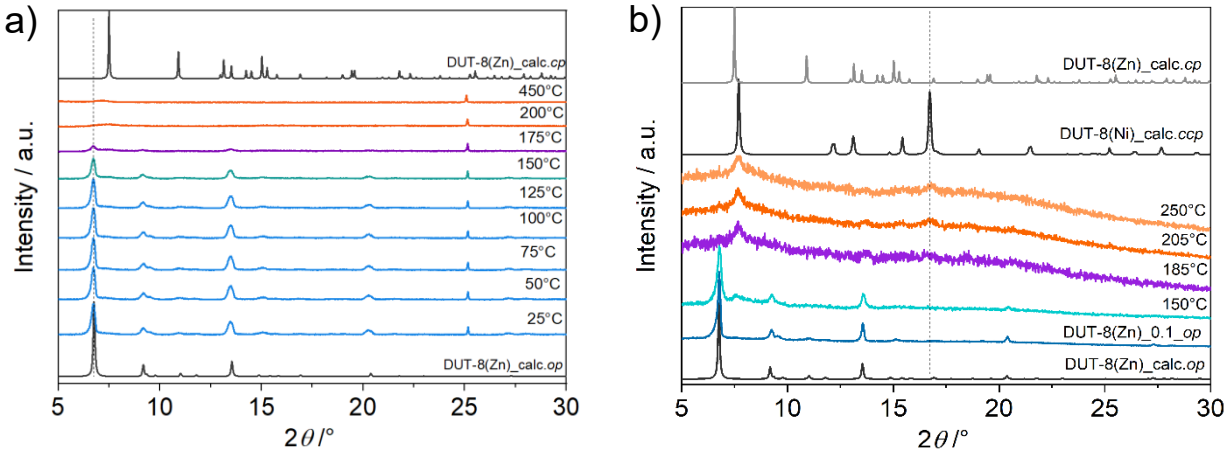

Figure 5-21. a) VT-PXRD measurement under N_2 atmosphere on sample DUT-8(Zn)_0.1 µm_*op* in a temperature range from 25°C to 400°C, b) PXRD patterns of sample collected after heating in oven.

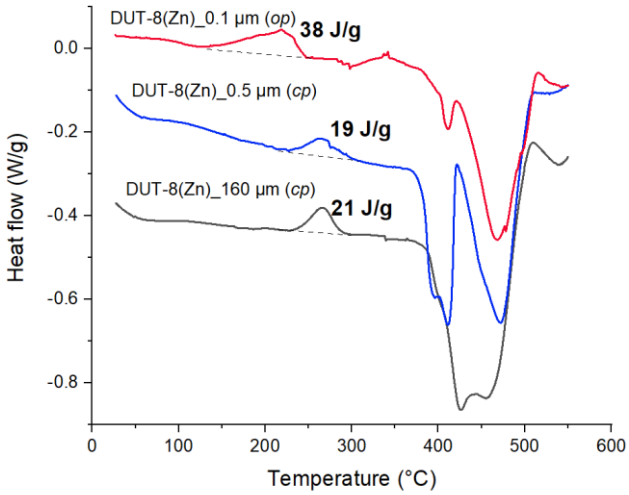

Figure 5-22. DSC curves of DUT-8(Zn)_160 µm_*cp,* DUT-8(Zn)_0.5 µm_*cp,* DUT-8(Zn)_0.1 µm_*op* in Ar flow with a heating rate of 2 K·min^{-1} in the temperature range from von 50 to 500 °C.

Thermal effect of structural response was studied using DSC (Figure 5-22). DUT-8(Zn) samples were exposed to heating in argon flow at 2 min^{-1}. The DSC curves of DUT-8(Zn)_160 µm_*cp* and DUT-8(Zn)_0.5 µm_*cp* exhibit the exothermic effect in almost the same range 225-300°C. The determined enthalpy of effects is slightly bigger for macron-sized crystals (-21 J g^{-1}) than for micron-sized (-19 J g^{-1}). However, the structural transition in DUT-8(Ni) from *cp* to *ccp* is accompanied by huge exothermic effect releasing -193 J g^{-1}. Such energetic difference points out that there is no phase transition in macro-sized DUT-8(Zn)_160_*cp* and micron-sized DUT-8(Zn)_0.5_*cp*. However, the small exothermic effects (-21 J g^{-1}, -19 J g^{-1}) could be related to the framework shrinkage. The followed endothermic peaks are associated with the decomposition of samples starting from 400°C for macro-sized samples and 380°C for micron-sized sample, which correlate with TGA data.

The temperature-driven structural response in DUT-8(Zn)_0.1 µm_*op* occur in the range 150-220°C, which is in agreement with PXRD patterns recorded after reaching the certain temperature (Figure 5-21). The enthalpy of the exothermic effect was determined to be about -38 J g^{-1}. In submicron-sized DUT-8(Ni), the enthalpy of transition from *op* to *ccp* in is about −367 J g^{-1}. Such huge energy release is associated with bond breaking/reformation, forming interpenetrated framework. In case of DUT-8(Zn), the phase transition from *op* to *ccp* is accompanied by quite small exothermic effect (-38 J g^{-1}), due to the loss of crystallinity and disintegration upon heating.

5.2.5 Liquid and vapour phase adsorption

Liquid phase adsorption

To study the physisorption behaviour of the DUT-8(Zn) in the liquid phase, the macro-sized sample and micron-sized samples with average size of 160 µm and 0.5 µm, respectively were prepared. PXRD patterns for as made crystals in DMF are in good agreement with the calculated pattern of DUT-8(Zn) (Figure 5-23). Desolvation of samples from DCM leads to the formation of thermodynamically stable *cp* phases.
To screen the switching ability of DUT-8(Zn) against the variety of adsorptives, the DUT-8(Zn)_160 µm and DUT-8(Zn)_0.5 µm samples in the closed pore phase state were exposed to different polar and non-polar solvents for 24 h (Table 5-6). The state of the samples after adsorption experiment was monitored by PXRD.

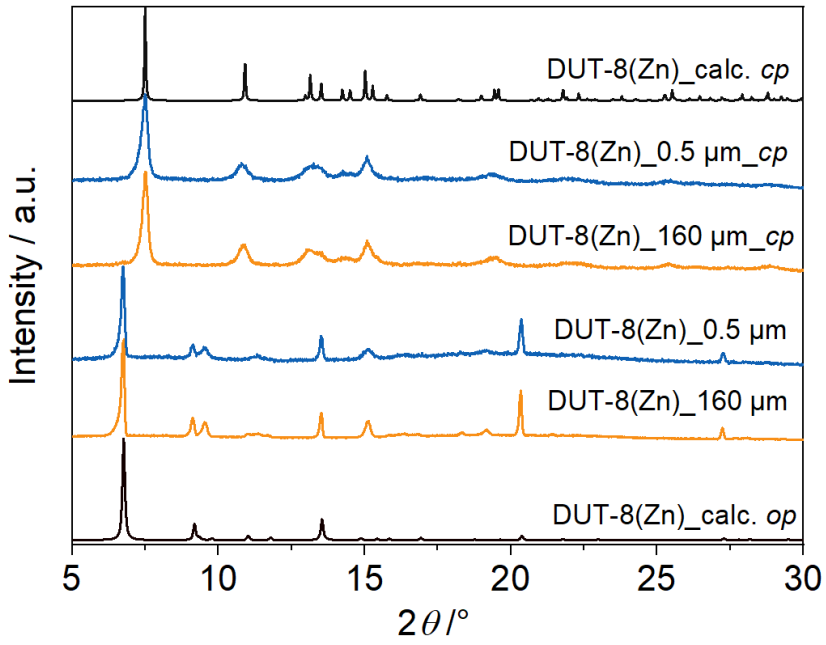

Figure 5-23. PXRD patterns of “as made” macro- and micron-sized particles of DUT-8(Zn) and after solvent removal in comparison with the calculated patterns of the *op* and *cp* phases of DUT-8(Zn).

In particular, reopening of DUT-8(Zn)_160 µm by resolvation is possible using DMF (*op/cp* mixture was obtained after experiment), tetrahydrofurane (THF), acetonitrile (ACN), DCM (Figure 5-24a, 7-12). Alcohols and hexane do not provoke structural transition (Figure 5-24a,b). In contrast, soaking of DUT-8(Zn)_0.5 µm in a series of representative alcohols (ethanol, 1-, 2-propanol, 1-butanol), as well as aprotic polar solvents (DMF, THF, ACN) leads to almost complete reopening of the framework in all cases (Figure 5-24c,d).

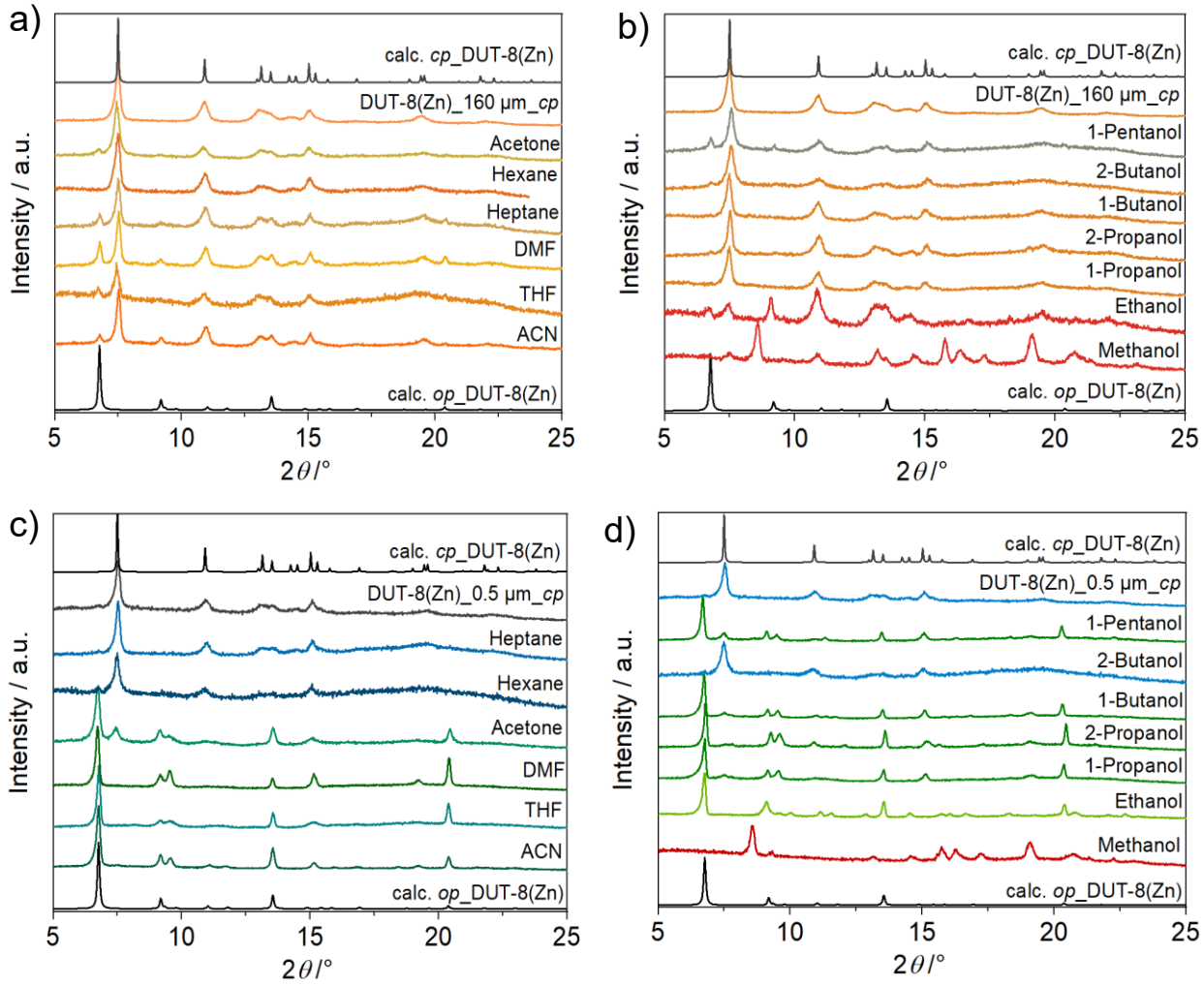

Figure 5-24. PXRD patterns of a-b) DUT-8(Zn)_160 µm_*cp* and c-d), DUT-8(Zn)_0.5 µm_*cp* resolvated in polar (protic, aprotic) and non-polar solvents.

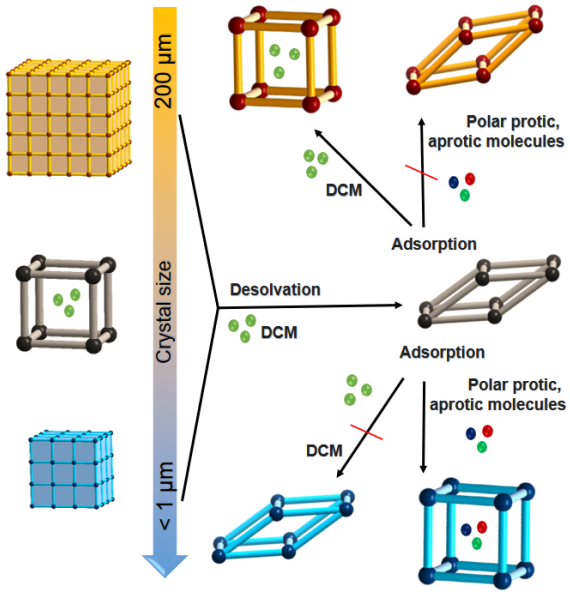

Figure 5-25. Schematic illustration of DUT-8(Zn) responsivity depending on particle size.

Liquid adsorption experiments revealed that the behaviour of macro-sized DUT-8(Zn) crystals is, to some extent, similar to the behaviour of large DUT-8(Ni) crystals,[19] namely *selective response by a crystal structure transformation and subsequent pore opening after exposure specifically to polar aprotic solvents*, *while polar protic solvents, such as alcohols, cannot trigger pore opening.* In contrast, micron-sized crystals (DUT-8(Zn)_0.5 µm) being in closed pore phase response not only to polar aprotic molecules, but also to alcohols by framework reopening (Figure 5-25).

Table 5-6. Overview of the framework state after exposure to solvents in liquid phase.

Solvent	Marco-sized crystals DUT-8(Zn)_160 µm_*cp*	Micron-sized crystals DUT-8(Zn)_0.5 µm_*cp*
Polar molecules: ***aprotic***		
DCM	*op/cp*	*cp/op*
DMF	*op/cp*	*op*
THF	*op/cp*	*op*
ACN	*op/cp*	*op*
Polar molecules: ***protic***		
EtOH	*cp*	*op*
1-PrOH	*cp*	*op*
2-PrOH	*cp*	*op*
1-BuOH	*cp*	*op*
Non-polar molecules: ***aprotic***		
Heptane	*cp*	*cp*

Solid state NMR

As mentioned above, the structural response to DCM was detected in large crystals of DUT-8(Zn), which is not the case for alcohols. On the contrary, phase transitions can be triggered by alcohols and not by DCM in micron-sized DUT-8(Zn)_0.5 µm. To confirm the revealed structural preference of DUT-8(Zn), solid-state NMR was measured due to the distinct differences of carboxylate signals between *op* and *cp* phases (Section 5.2.2) allowing to monitor the liquid-induced phase transitions.

The measurements were performed by Christopher Bachetzky in the group of Prof. Dr. Eike Brunner (Chair of Bioanalytical Chemistry, TU Dresden).

Figure 5-26 shows that already after addition of 1-PrOH, the structural transformations occur in DUT-8(Zn)_0.5 µm, which are complete within 1 hour. Despite adsorption and resolvation studies showed that DCM is not able to provoke the phase transition in micron-sized crystals, NMR spectra show that some of the crystals were transformed to *op* phase after 5 h.

However, after exposure to the mixture of DCM/1-PrOH, the *cp*-to-*op* phase transition was observed already after addition of mixture of solvent (Figure 5-27). Most probably framework reopening is induced by 1-PrOH, rather than DCM.

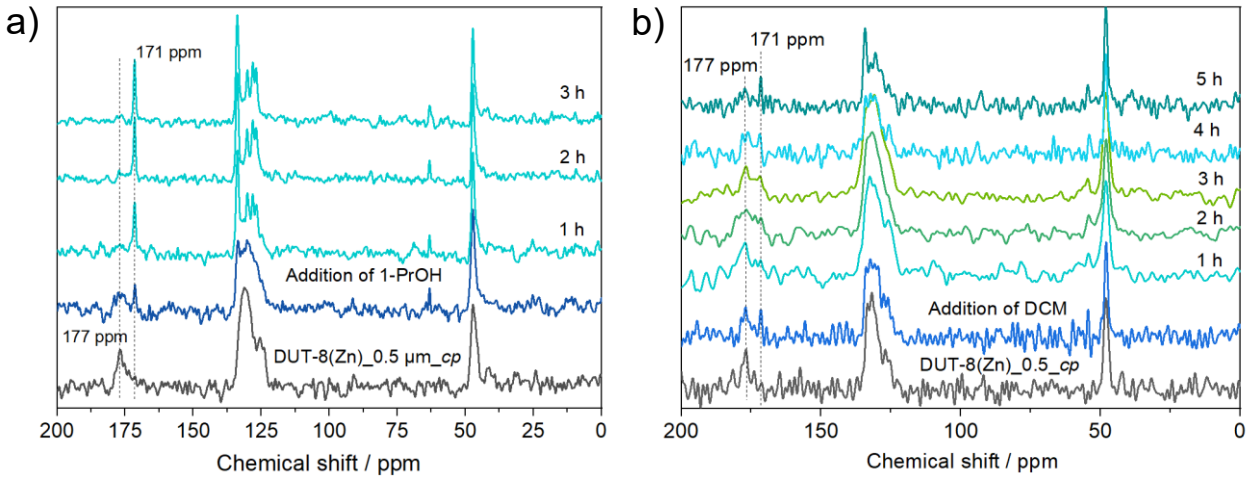

Figure 5-26. ^{13}C CP MAS NMR spectra of micron-sized sample DUT-8(Zn)_ 0.5 µm upon resolvation by a) 1-PrOH and b) DCM.

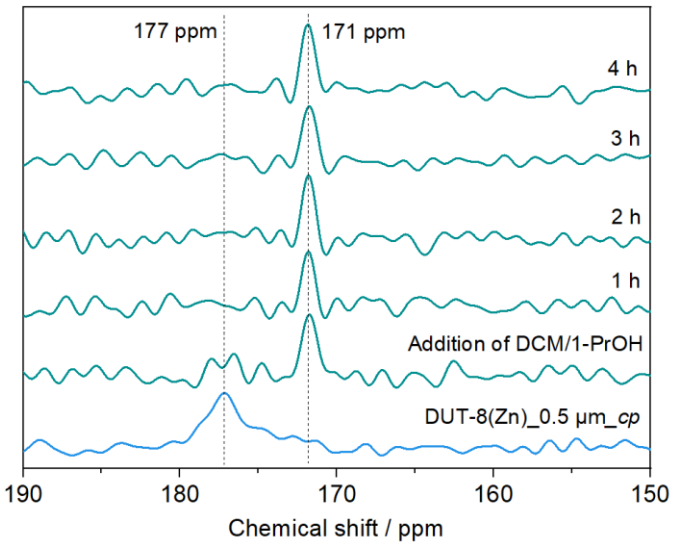

Figure 5-27. ^{13}C CP MAS NMR spectra of DUT-8(Zn)_0.5 µm_*cp* upon resolvation by DCM/1-PrOH.

Moreover, the phase transition driven by DCM interaction with framework was not revealed by NMR in macro-sized DUT-8(Zn)_160 µm. As can be seen from Figure 5-28, only a small signal from *op* phase was detected. It is assumed that not all of the crystals were stimulated to transform from *cp* to *op*. Nevertheless, PXRD pattern after resolvation and adsorption experiments (Figure 8-12, 5-11b) confirm that DCM is able to interact with large crystals, triggering phase transition at least for part of the crystals.

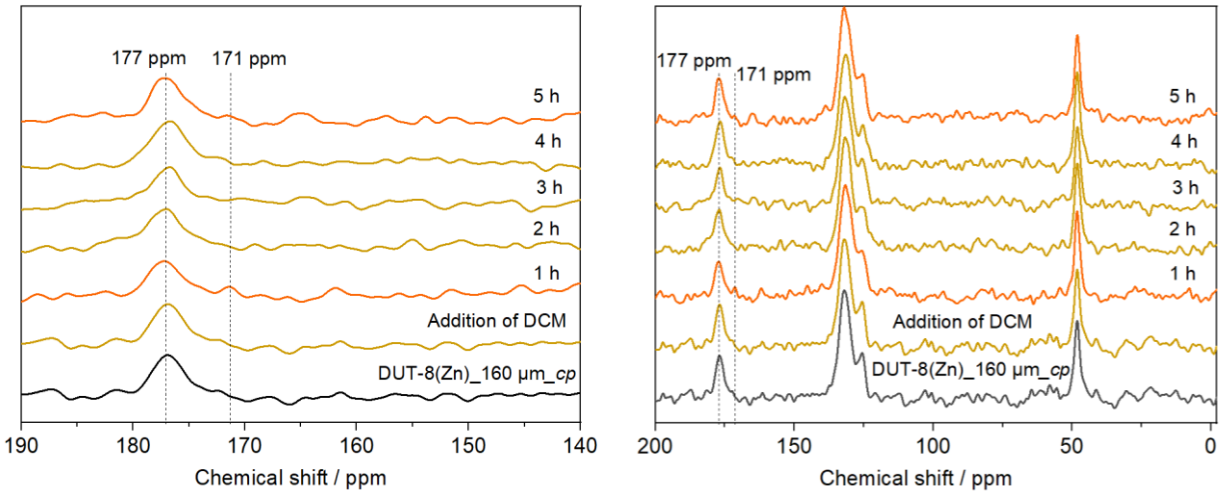

Figure 5-28. ^{13}C CP MAS NMR spectra of DUT-8(Zn)_160 µm_*cp* upon resolvation by DCM.

Vapour phase adsorption

It was shown in Section 5.2.1 that macro-sized crystals were selectively responsive only towards chloromethane and DCM upon adsorption, meanwhile micron-sized crystals were not structurally transformed in the vapour adsorption experiments.[13] Liquid phase adsorption experiments confirm these properties, showing that large crystals are more responsive to DCM than smaller ones (Figure 8-12). Despite, THF and ACN can easily be adsorbed in liquid state by micron-sized sample DUT-8(Zn)_0.5 µm_*cp* and part of macro-sized DUT-8(Zn)_160 µm_*cp* crystals, during vapour adsorption experiments the pressure in the vapour adsorption measuring system is not sufficient to stimulate phase transition at 298 K as shown in Figure 5-29a,b. However, by increasing temperature of adsorption to 303 K, it can be clearly seen that crystal downsizing leads to decrease of activation barrier for the phase transition.

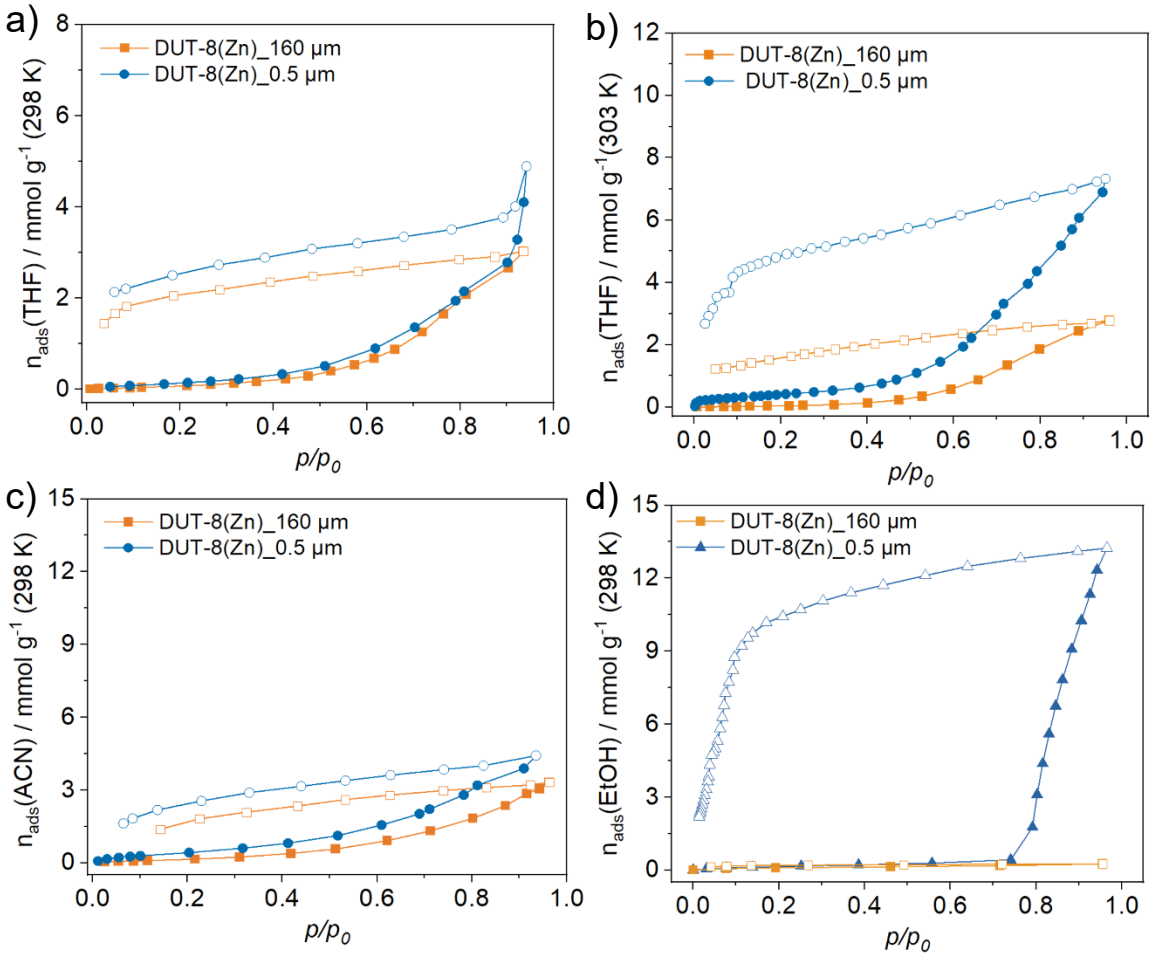

Figure 5-29. Vapor adsorption isotherms of macro- and micron-sized DUT-8(Zn): a) THF at 298 K, b) THF at 303 K, c) ACN at 298 K, d) EtOH at 298 K.

Vapour adsorption of ethanol at 298 K reveals almost no uptake at low pressure with subsequent sharp uptake at p/p_0 = 0.8, corresponding to a structural transition from the non-porous closed pore to the porous open pore phase in DUT-8(Zn)_0.5 µm_*cp*, meanwhile DUT-8(Zn)_160 µm_*cp* remain in *cp* phase in the course of adsorption-desorption cycle (Figure 5-29d), reflecting the results of the liquid phase adsorption: *the macro-sized crystal are non responsive to alcohols, but micron-sized crystals response to alcohol exposure by opening.*

5.2.6 Modulation of crystal size and shape

To broaden the crystal size range and to study the dependence of gate opening pressure from crystal size, the crystals with different sizes are needed. In case of DUT-8(Ni), it was shown, that the influence of crystal width on adsorption has exponential character, therefore the width deviation in micron particle size range has more impact on the gate opening in comparison to the size deviations in macrocrystals. To increase the sensitivity of the study, three micron-sized DUT-8(Zn) crystals with crystal width 1.8, 1.4 and 1 µm were produced by modulated synthesis (Figure 5-31, 5-32).[201] PXRD patterns are in good agreement with theoretical pattern of DUT-8(Zn) in the solvated open pore phase (Figure 5-30). However, the differences in the intensities of reflexes recorded from (001) plane point on preferential orientation of the crystals in X-ray beam and consequently, on possible differences in crystal morphology.

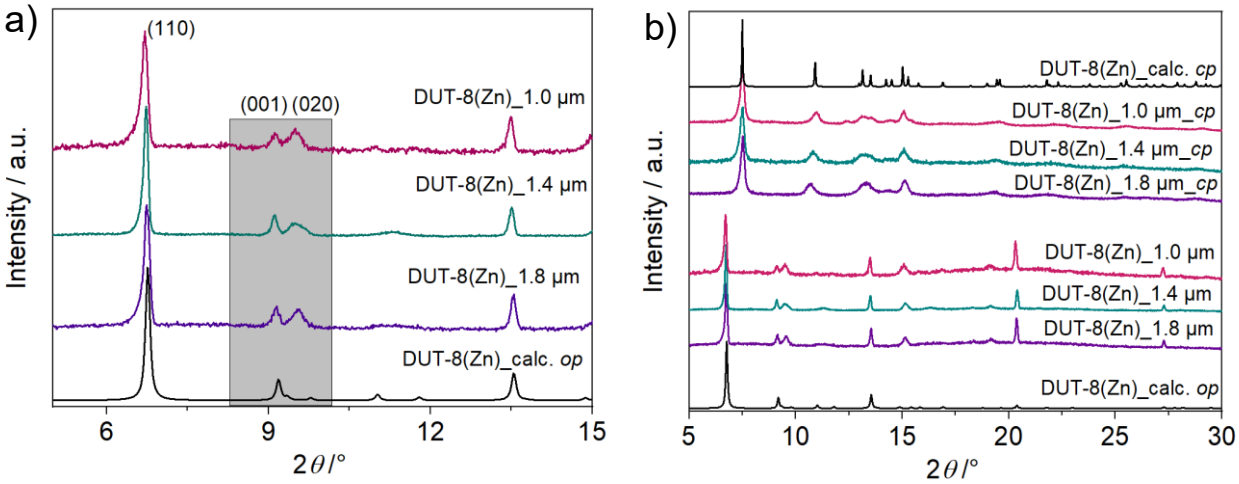

Figure 5-30. a) PXRD patterns of "as made" samples in DMF, b) full range PXRD patterns of solvated in DMF samples (*op*) and desolvated samples (*cp*).

In fact, SEM images show that the DUT-8(Zn)_1.8 µm sample crystallises as cube-like particles, DUT-8(Zn)_1.4 µm has rod-like morphology and DUT-8(Zn)_1.0 µm are plates (Figure 5-31). As critical particle size, the dimensions corresponding to the [110] plane was considered, since it was demonstrated for DUT-8(Ni) system, that it represents the critical size in this pillared-layer MOFs. The orientation of the crystallographic axis was determined by election diffraction (Figure 5-33) performed by Dr. T. Gorelik (University of Ulm). The solvent removal process was performed identically for all samples, stimulating framework contraction and the structural transition from *op* to the *cp* phase (Figure 5-30b).

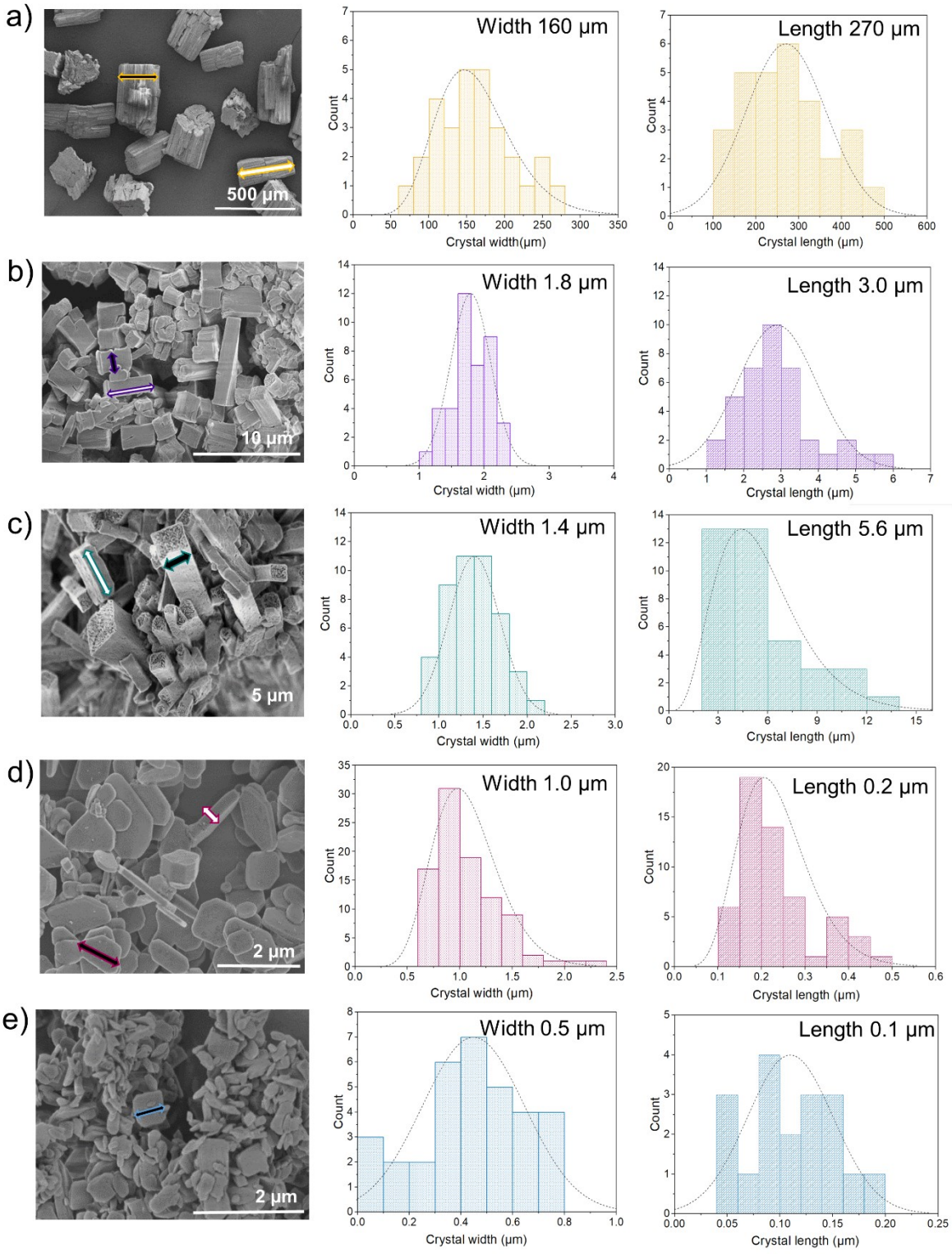

Figure 5-31. SEM images and particle size distribution of investigated DUT-8(Zn) samples.

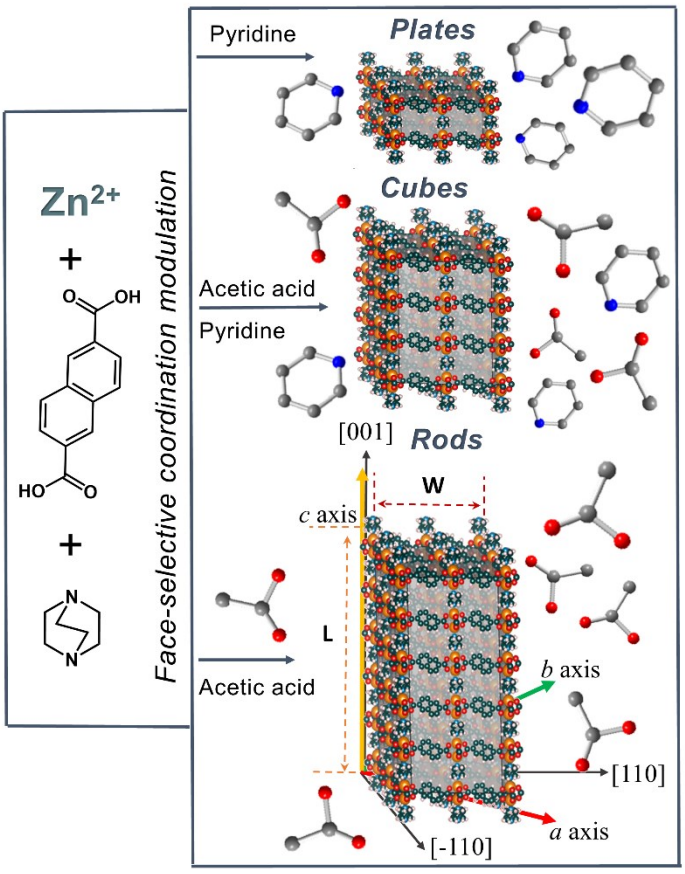

Figure 5-32. Schematic representation of crystal shape modulation (generated by the VESTA 3.5.5 software) (Momma and Izumi, 2011).

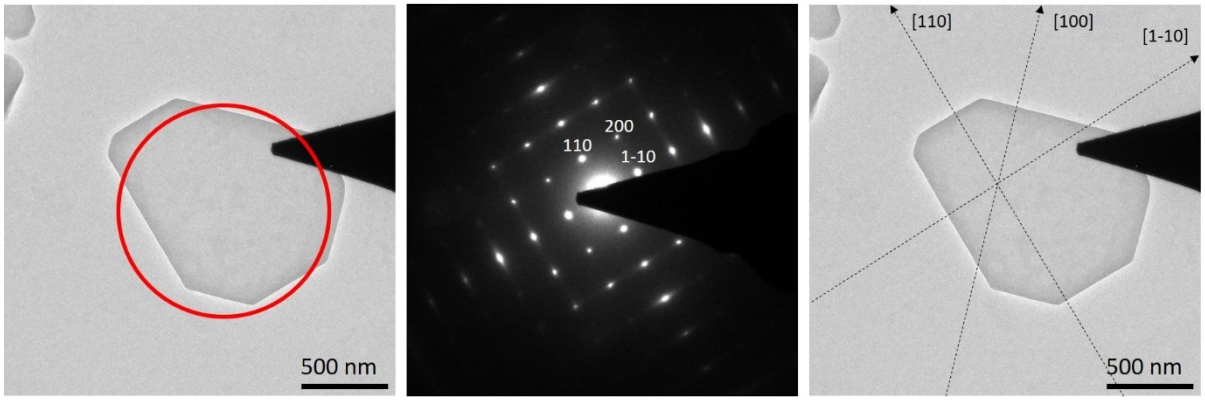

Figure 5-33. TEM image and electron diffraction patterns of plates DUT-8(Zn)_1.0

Chloromethane adsorption

Since nitrogen could not be used as a probe molecule in case of DUT-8(Zn), chloromethane adsorption at 249 K was studied. For characterization of isotherms, the quantities, introduced in section 4.2.2, are used:

(i) relative adsorption pressure at half maximum uptake (APHM) as a measure of the average gate opening activation energy (ΔG^*);

(ii) uptake at highest relative pressure reached in the adsorption experiment (or in plateau), which represents the specific pore volume of the particular sample. In relation to the theoretical pore volume, it reflects the fraction of crystallites (α_{max}) transformed to the *op* phase at given conditions.

Typical gate-opening isotherms upon adsorption of CH_3Cl (249 K) were obtained for DUT-8(Zn)_160 µm, DUT-8(Zn)_1.8 µm and DUT-8(Zn)_1.4 µm with α_{max} reaching 0.78, 0.77 and 0.7 at p/p_0=0.96, respectively (Figure 5-34a, Table 5-7). Smaller crystals DUT-8(Zn)_1.0 µm and DUT-8(Zn)_0.5 µm remains in the *cp* in the whole pressure range upon adsorption of chloromethane at 249 K. Thus, behaviour of DUT-8(Zn) upon adsorption of CH_3Cl follows the trend observed for DUT-8(Ni) upon adsorption of nitrogen at 77 K: *crystals smaller than 1 µm lose the ability to perform cp-to-op transition.*

There is no clear dependence of APHM from the crystal dimensions (length and width) (Table 5-8).

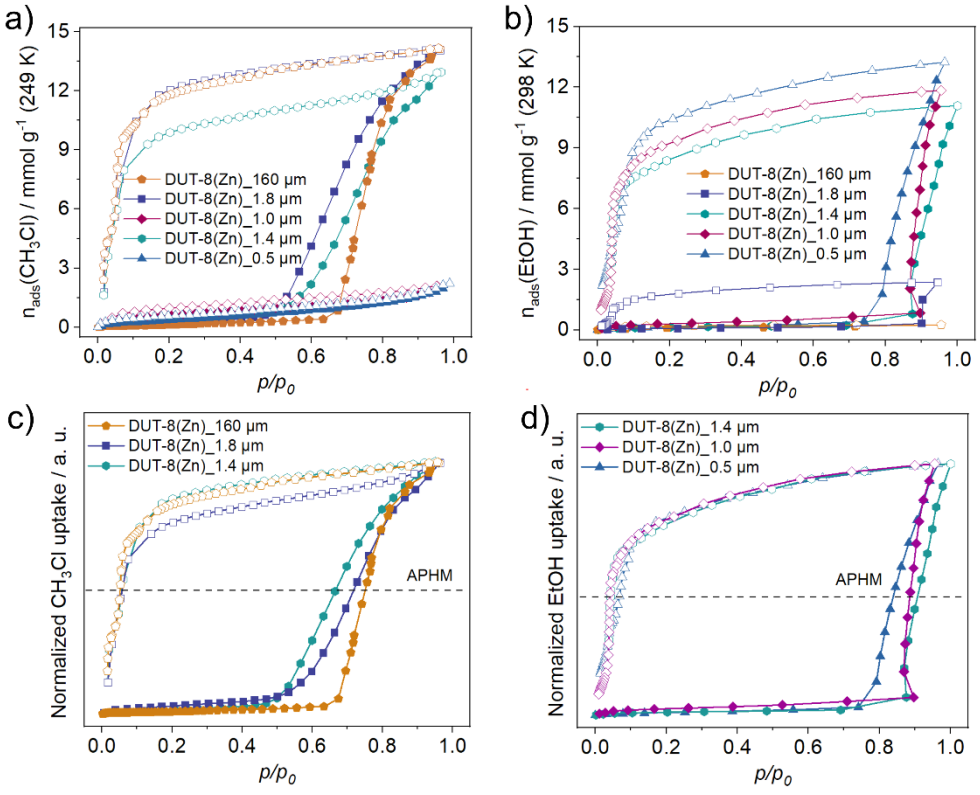

Figure 5-34. a) Chloromethane (249 K), b) Ethanol (298) physisorption isotherms, c), d) corresponding physisorption isotherms with uptake normalized to the maximum value.

Table 5-7. Overview of structural response of DUT-8(Zn) in closed pore phase towards guest molecules depending on size regime and α_{max} values.

		W = 160 µm L = 270 µm	1.8 3	1.4 5.6	1.0 0.2	0.5 0.1
Adsorptive	**Measurement conditions**					
DCM	*298 K (p/p_0=0.94, p_0=56.9 kPa)*	*op* 0.58	-	-	-	op 0.10
	312 K (p/p_0=0.88, p_0=96.5 kPa)	-	*op* 0.24	*op* 0.24	*op* 0.29	-
Chloromethane	*249 K* (p/p_0=0.96, p_0=101.33 kPa)	*op* 0.78	*op* 0.77	*op* 0.70	*cp*	*cp*
Ethanol	*298 K* (p/p_0=0.96, p_0=7.7 kPa)	*cp*	*op* 0.14	*op* 0.64	*op* 0.69	*op* 0.77

Dichloromethane adsorption

Upon dichloromethane adsorption at 298 K only 58% of DUT-8(Zn)_160 µm are structurally transformed from *op* to *cp* phase (α_{max}=0.58), while DUT-8(Zn)_0.5 µm mostly remain in *cp* phase (α_{max}=0.1) (Figure 5-11b, Table 5-7).

In order to perform the measurement at the temperature close to boiling point, the isotherms for new samples were measured at 312 K, rising the maximum pressure to 96.5 kPa. However, such measurement conditions do not lead to significant structural changes, reaching only α_{max}= 0.24 for cubes and rods, and 0.29 for plates (Table 5-7, Figure 8-13).

Ethanol adsorption

The smaller the crystals of DUT-8(Zn) are more responsive towards ethanol. This is clearly indicated by adsorption profiles. DUT-8(Zn)_0.5 µm, DUT-8(Zn)_1.0 µm and DUT-8(Zn)_1.4 µm particles show framework reopening induced by ethanol vapour adsorption at 298 K, reaching α_{max} 0.77, 0.69 and 0.54 at p/p_0 = 0.96, respectively (Table 5-7). Meanwhile, DUT-8(Zn)_1.8 µm is shown to be less responsive showing only α_{max} = 0.14 at p/p_0 = 0.95 and the DUT-8(Zn)_160 µm are not responsive at all (Figure 5-34b). APHM changes also do not systematically follow the changes in the crystal length (Table 5-8). However, the systematic increase in the width of the crystals leads to the increase of APHM value. As a result, after reaching the critical size of width, the crystals lose the responsivity towards ethanol.

Thus, the crystal width determines the gate opening pressure in DUT-8(Zn) as well as was shown for DUT-8(Ni) in Chapter 4.

In conclusion, there may be some adsorptives which follows the trend observed for DUT-8 in adsorption of nitrogen: crystal downsizing leads to the increase in gate opening pressure. It is the case for chloromethane in DUT-8(Zn), which is able to open the macro-crystals as well as submicron crystals and the gate opening pressure shifts to the higher value by crystal downsizing. At some critical particle size, the compound becomes non responsive and stays in the *cp* phase upon adsorption.

Some adsorptives, however, follow the opposite trend. To such adsorptives belong THF and EtOH. The macro-crystals are not responsive to these substances and the downsizing induces the responsivity. Obviously, the critical width value in the submicron range exists, transforming the non-responsive *cp* phase to the flexible compound. For EtOH the critical width seems to be around 2 μm. For such adsorptive, the further particle size decrease leads to the shift of the gate opening pressure towards the lower values (Figure 5-29d, 5-34b). It should, however, be emphasised, that the vapour adsorption experiments in high relative pressures region are very sensitive to the temperature stability and should be considered critically.

Table 5-8. Characteristics of the investigated samples.

Samples	Width (W)/ μm	APHM C_2H_5OH	APHM CH_3Cl	RSD/%	PDI	Length (L)/ μm	RSD/%	PDI
DUT-8(Zn)_0.5 μm	0.5	0.85	-	39.6	0.15	0.1	40.8	0.16
DUT-8(Zn)_1 μm	1.0	0.89	-	33.4	0.11	0.2	43.7	0.19
DUT-8(Zn)_1.4 μm	1.4	0.91	0.72	20.7	0.04	5.6	50.1	0.25
DUT-8(Zn)_1.8 μm	1.8	-	0.67	19.2	0.03	3.0	43.1	0.18
DUT-8(Zn)_160 μm	160	-	0.75	31.2	0.09	270	34.8	0.12

RSD, relative standard deviation; PDI, polydispersity index; APHM estimated for the normalized isotherms.

5.2.7 Shape-memory effect

Since alcohols are capable to provoke the opening of micron-sized crystals, vapor physisorption experiments on DUT-8(Zn)_0.5 µm_*cp* at 298 K were performed using 1-PrOH, 1-BuOH in order to compare the behavior during adsorption from liquid and from vapor phase. As mentioned above, vapour adsorption of ethanol at 298 K reveals almost no uptake at low pressure with subsequent sharp uptake at p/p_0 = 0.8, corresponding to a structural transition from the non-porous closed pore to the porous open pore phase. However, PXRD pattern of the sample after adsorption indicates the presence of the open phase after desorption(Figure 5-37c), thus inducing so called shape-memory effect (Figure 5-42).[101]

The adsorption of 1-PrOH was measured up to 0.92 of relative pressure. Under such conditions not all crystals are able to transform, and the gradual increase in the *op* phase content in the course of several adsorion/desorption cycles (Figure 5-35a). To monitor structural composition of the powder, PXRD patterns were recorded after each cycle. Cyclic adsorption/desorption measurements of 1-PrOH confirm accessible shape-memory effect in this system, resulting in the gradual transformation of the initial shape of pores into a metastable shape, which is maintained even after desorption. The first adsoriton cycle results in typical gating isotherm and low amount of 1-PrOH adsorbed (3.4 mmol/g). PXRD revealed switching from *cp* to *op* only for part of the crystals. As a result, in the second cycle the filling of metastable *op* phase occurs in the low region of p/p_0, reaching the plateau which us followed by an increase in uptake corresponding to the phase switching of another portion of crystals. The second cycle is characterized by shifting of gate-opening to the lower relative pressure with slight increase in uptake (4 mmol/g). In the following adsorption cycles, the amount of alcohol adsorbed increases. Thus, the micron-sized crystals DUT-8(Zn)_0.5 µm reconfigure their framework structures in response to the incorporation of 1-PrOH, which triggers the formation of *op* phase during six cycles of adsorption, therefore ensuring porous open phase after desorption (Figure 5-35b).

Vapour adsorption of 1-BuOH confirms sorbate-induced shape memory effect, observed in micron-sized sample. The tendency of gate-opening pressure shift to the lower values of p/p_o is observed, however, the reopening occurs during 4 cycles of alcohol adsorption with uptake of 10 mmol/g. As can be seen from the isotherms, the incorporation of 1-BuOH into the framework occurs more difficult, especially during the

first cycle (Figure 5-36a). The second cycle exhibits more pronounced hysteresis loop. In case of 3 cycles, partial pore accessibility provides pore filling with subsequent plateau region between p/p_0 0.02 to 0.85 bar, followed by phase transition from non-porous to porous state, which is maintained even after the removal of adsorbate. The last adsorption cycle is characterized by increasing 1-butanol uptake and less pronounced hysteresis loop. PXRD data (Figure 5-36b) after adsorption-desorption cycles verify crystal structure transition from closed to open state.

The interaction of framework with alcohols causes considerable deformation of the crystals surface (Figure 8-14, 8-15). The severe surface deformation is caused by chemical interaction of alcohols with framework.

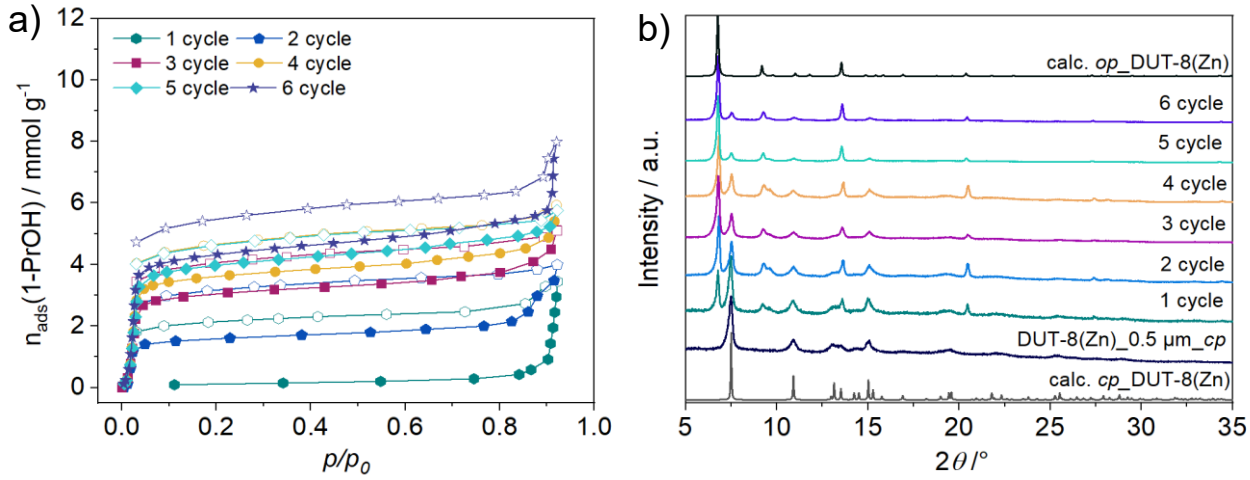

Figure 5-35. a) Cycled physisorption isotherms of 1-PrOH (298 K) and b) corresponding PXRD patterns after each cycle.

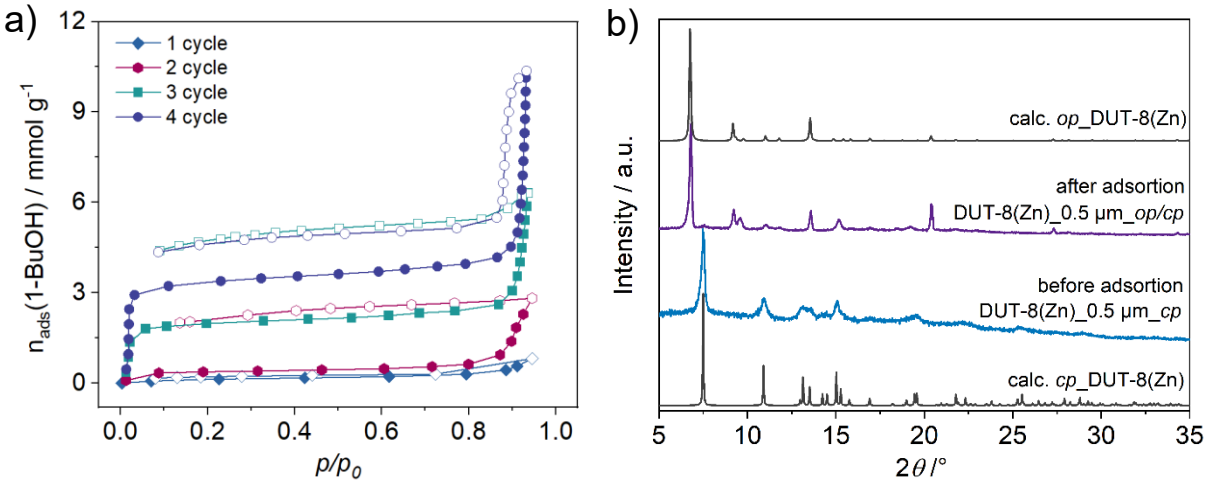

Figure 5-36. a) Cycled physisorption isotherms of 1-BuOH at 298 K and b) corresponding PXRD patterns before adsorption and after four cycles of adsorption.

The cycled adsorption isotherms for 1-PrOH, 1-BuOH were measured up to 0.92 and 0.93 relative pressure, respectively. The increase of relative pressure up to 0.95 in both cases allowed to occur only in one adsorption/desorption cycle almost complete structural transformations.

The comparison of alcohol adsorption isotherms is shown in Figure 5-37a. During adsorption of EtOH, the amount of adsorbed ethanol constitutes 12.8 mmol g^{-1} at the p/p_0=0.96, reaching α_{max} = 0.77 (Table 5-9).

During 1-PrOH adsorption at 298 K, the phase transition from *cp* to *op* is triggered with the total uptake of 7 mmol g^{-1} at p/p_0 = 0.96. In this case α_{max} is only 0.52, meaning that only half of the crystallites transformed to the *op* phase at given conditions.

The adsorption of 1-BuOH at 298 K enables α_{max} = 0.76 at p/p_0 = 0.95, which is comparable to the pore filling reached by EtOH (α_{max} = 0.77). PXRD patterns of the samples after adsorption (5-37b) indicate that the framework stays in the metastable open pore phase after desorption of alcohols after the first cycle.

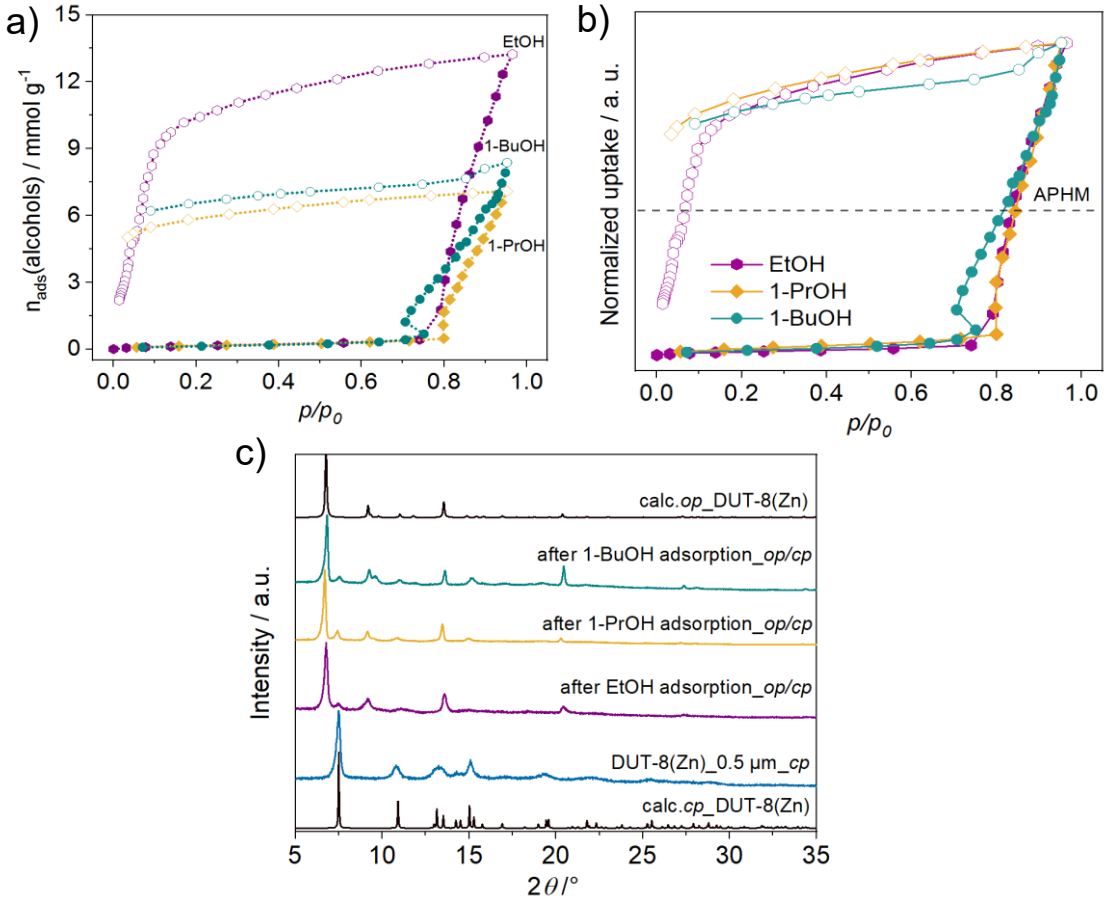

Figure 5-37. a) ROH physisorption isotherms (298.15 K), b) ROH physisorption isotherms with uptake normalized to the maximum value, c) PXRD patterns of DUT-8(Zn)_0.5 µm after ROH adsorption.

Table 5-9. Quantities for characterization of adsorption isotherms.

Adsorptive	Measurement conditions	PXRD after ROH adsorption	APHM ROH adsorption	α_{max} ROH adsorption	α_{max} N_2 adsorption
Ethanol	*298.15 K* (p/p_0=0.96, p_0=7.7 kPa)	*op/cp*	0.85	0.77	0.70
1-PrOH	*298.15 K* (p/p_0=0.95, p_0=3.1 kPa)	*op/cp*	0.84	0.52	0.52
1-BuOH	*298.15 K* (p/p_0=0.95, p_0=1.5 kPa)	*op/cp*	0.82	0.76	0.58

According to vapour adsorption experiments, alcohols are not only able to initiate switching in micron-sized crystals, but also induce shape-memory effect. Such behaviour was also observed in the 2-fold interpenetrated $[Cu_2(bdc)_2(bpy)]_n$,[101] in 3-fold interpenetrated network, $[Zn_2(bpdc)_2(bpb)]_n$,[103] where the *op* phase was retained after adsorption/desorption of the gases (CO_2, N_2 and CO) and in CPM-107 (built from $[Mg_2Ac]^{3+}$ chains connected by bdc linker), which selectively responds to CO_2 over CH_4, N_2, and H_2, demonstrating key-lock effect.[228] Recently, similar effect was shown in $Cu(4\text{-}PyC)_2$, consisting of Cu^{2+} and 4-pyridine carboxylic acid. [108] The structural expansion of $Cu(4\text{-}PyC)_2$ is triggered by adsorption of SO_2.The retained open pore phase is attributed to chemical interaction of SO_2 with open metal sites, as well as Jahn−Teller stabilization effect of the Cu−N bond preventing the rotation of pyridine.

Since the crystallinity of the *op* and *cp* phases of DUT-8(Zn) is not the same, an assumption about the *op/cp* ratio without using an internal standard is problematic. However, adsorption experiments, using N_2 at 77 K can provide this ratio (α_{max}). It was shown in Section 5.2.1, that DUT-8(Zn)_0.5 µm is not responsive towards N_2 at 77 K and therefore the observed uptake should only refer to the retained *op* phase after the alcohol vapour adsorption.

Prior to the measurements, the samples were evacuated at 150 K for 3 h. As expected the recorded N_2 isotherms of DUT-8(Zn)_0.5 µm all refer to a type I isotherm, typical for rigid materials, since only the present o*p* phase may adsorb N_2 (Figure 5-38).

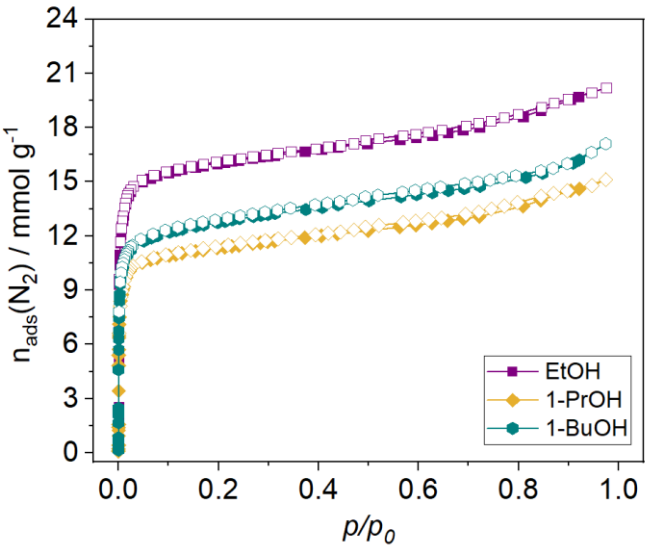

Figure 5-38. Nitrogen physisorption isotherms (77 K) recorded after ROH adsorption.

Although in the PXRD only a small part of the *cp* phase seems to be present, only about 70% (α_{max} = 0.7) of the theoretical pore volume is accessible for N_2 at 77 K after EtOH adsorption. The amount of accessible porosity achieved by 1-PrOH and 1-BuOH adsorption is lower reaching only α_{max} = 0.52 and 0.58, respectively (Table 5-9).

As mentioned above, similar to DUT-8(Zn)_0.5 µm, the modulated crystals also undergo phase switching induced by EtOH at 298 K reaching the different uptake amount depending on crystal size (Figure 5-39a).

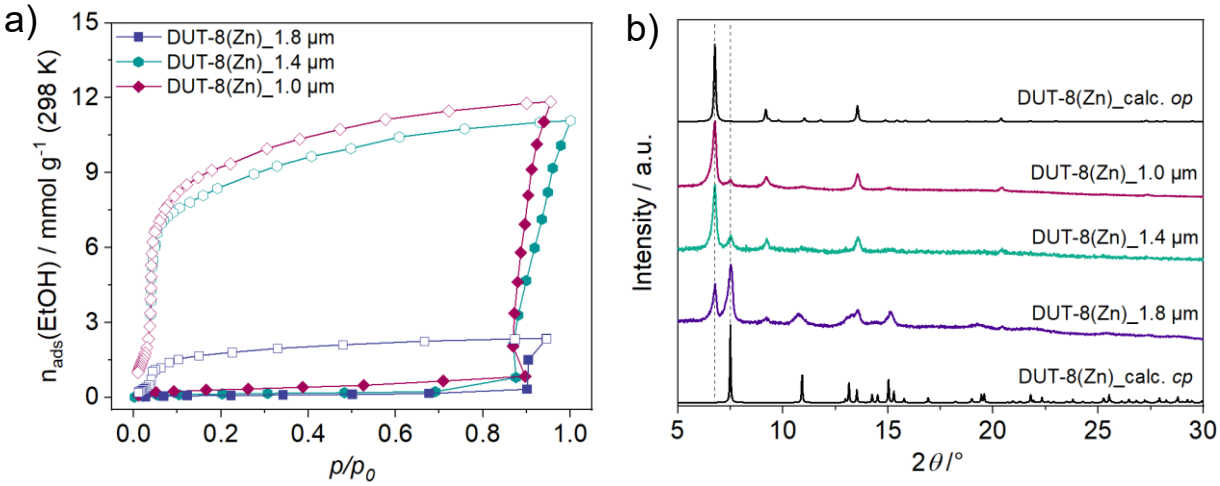

Figure 5-39. a) EtOH physisorption isotherms (298 K) and b) PXRD patterns of DUT-8(Zn) samples after adsorption.

PXRD patterns measured after adsorption indicate that plates of DUT-8(Zn)_1.0 µm and rods of DUT-8(Zn)_1.4 µm remain in the open pore configuration after ethanol desorption and only small amount of crystals remain in *cp* phase (Figure 5-39b). However, only part of DUT-8(Zn)_1.8 cube-like particles can be reopened by EtOH. This could be attributed to the defined particle size regime, which is responsive to alcohols. In DUT-8(Zn)_1.8 µm sample, the size of crystals varies between 1 and 2 µm, meaning that some crystals are exceeding the critical size needed for interaction with EtOH.

The crystal surface and morphology are shown to be drastically changed after EtOH adsorption, which is not a case after DCM adsorption (Figure 5-40, Figures 8-16, 8-17, 8-18). The surface became rough and non-homogeneous, and crystal shape is less defined according to SEM images. Upon exposure of “as made” crystals to ethanol for several days, the surface deformation is observed (Figure 5-40).

The chemical interaction of alcohols with DUT-8(Zn) crystals leads to deformation of crystal surface and most probably to nanostucturing of crystal interior (Figure 5-40).

As a result, framework rigidification can be attributed to nanodomains formation, which contributes to stabilisation of *op* phase. Another reason for suppression of structural mobility could be the presence of defects, which in turn influence switchable behaviour of MOFs.[148] For instance, isomorphous DUT-8(Ni) system being in nano-sized regime is rigid, containing more defects in the form of missing 2,6-ndc^{2-} and dabco linkers and defective paddle wheel units with only one Ni^{2+} ion.[155]

In previously known shape-memory systems,[108, 228] the original *cp* phase could be regenerated upon heating, vacuum or solvent soaking. In our experiments, heating could reproduce closed pore phase according to PXRD patterns (Figure 5-41a,b, Figure 5-42), while subsequent resolvation in corresponding alcohol does not provoke *cp*-to-*op* phase transition in the whole sample and resolvation by DMF leads to framework reopening with appearance of additional peaks.

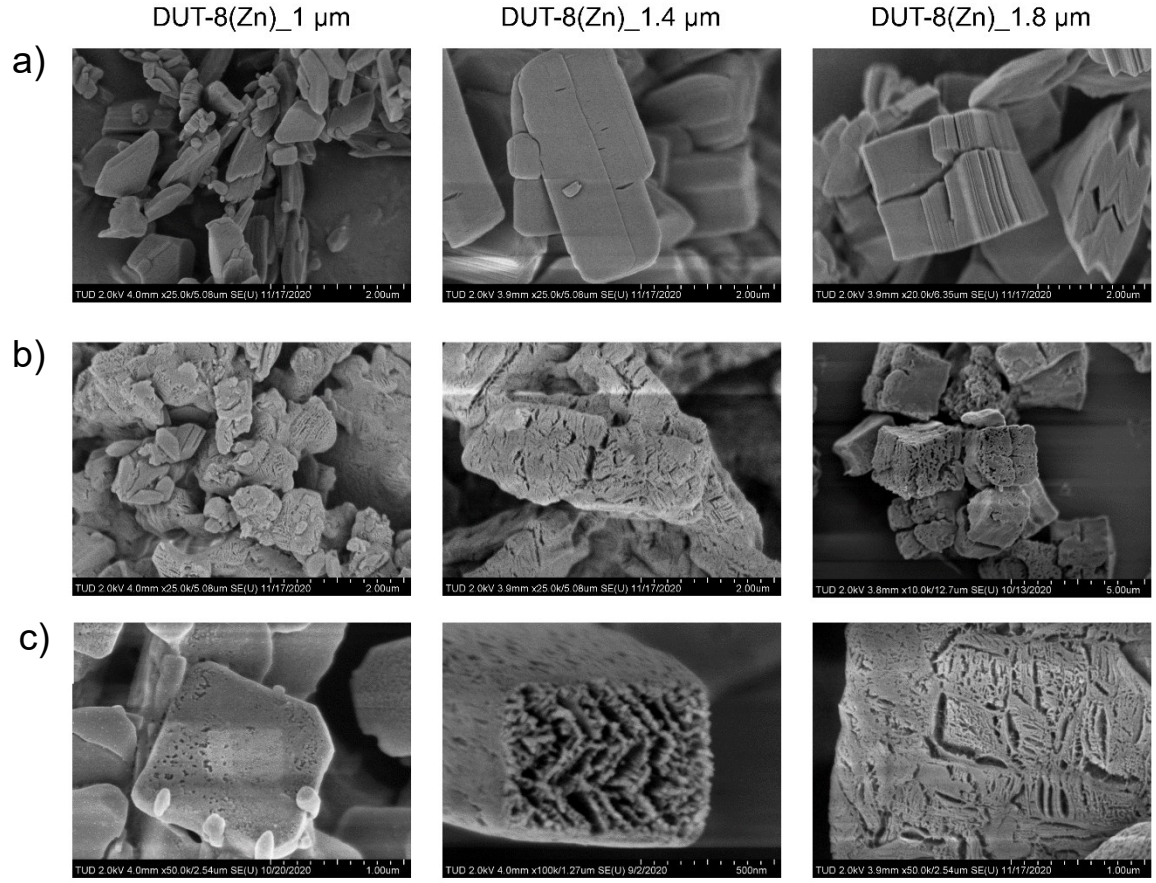

Figure 5-40. SEM images of differently-shaped micron-sized DUT-8(Zn) a) after DCM adsorption, b) EtOH adsorption, c) solvation in EtOH.

The thermal treatment of *op* phase after ethanol adsorption results in phase transition to *cp* (Figure 5-41c). Afterwards, the second adsorption cycle was measured, showing significant decrease in uptake, which could be attributed to the loss of crystallinity due to surface deformation (Figure 5-41d). The surface of the crystals was drastically changed by ROH adsorption (Figure 8-14, 8-15), which could be possible reason of framework rigidification.

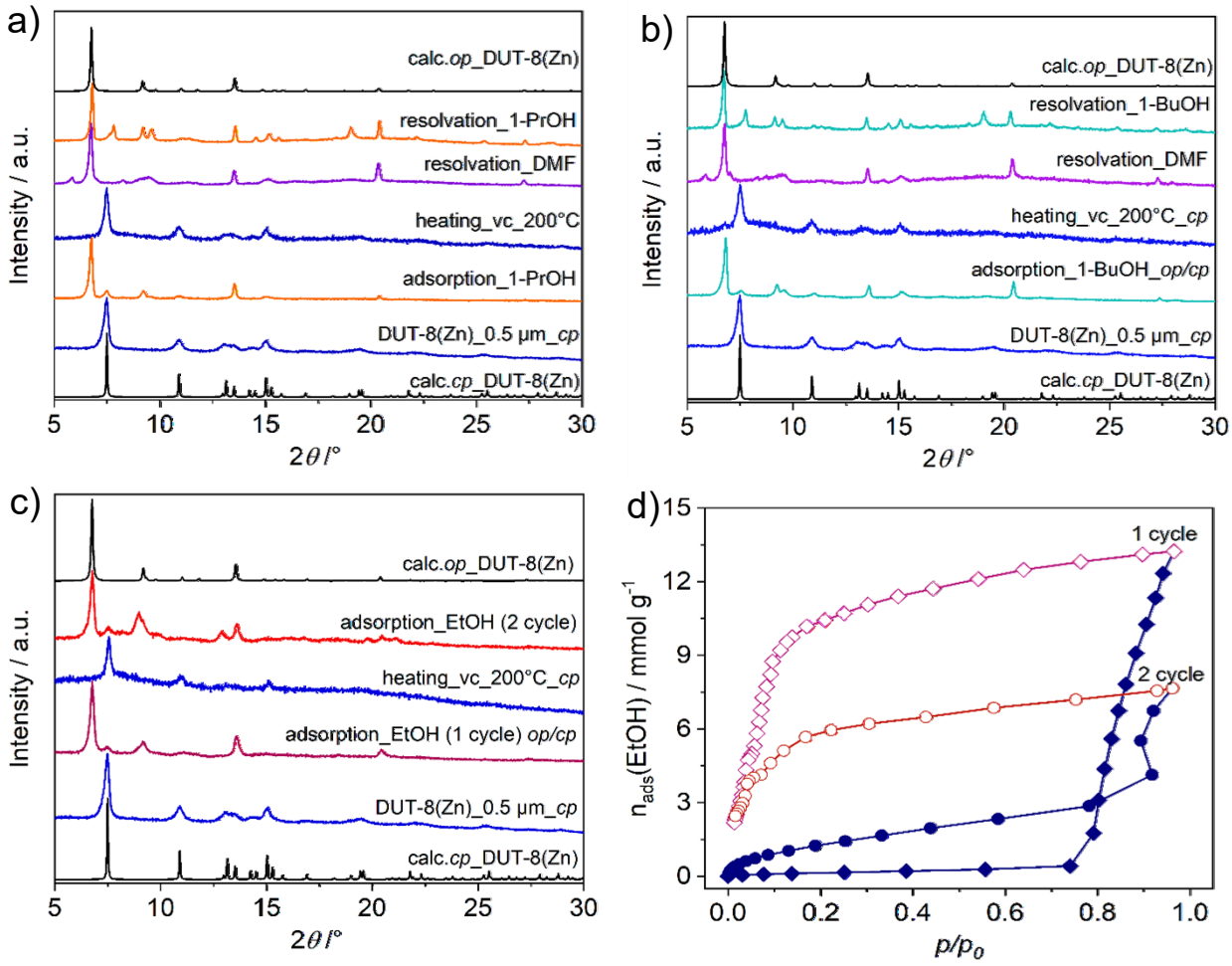

Figure 5-41. PXRD patterns of thermally treated samples a) after 1-PrOH adsorption and resolvation, b) after 1-BuOH adsorption and resolvation, c) after EtOH adsorption, d) 2 cycles of EtOH adsorption isotherms at 298 K.

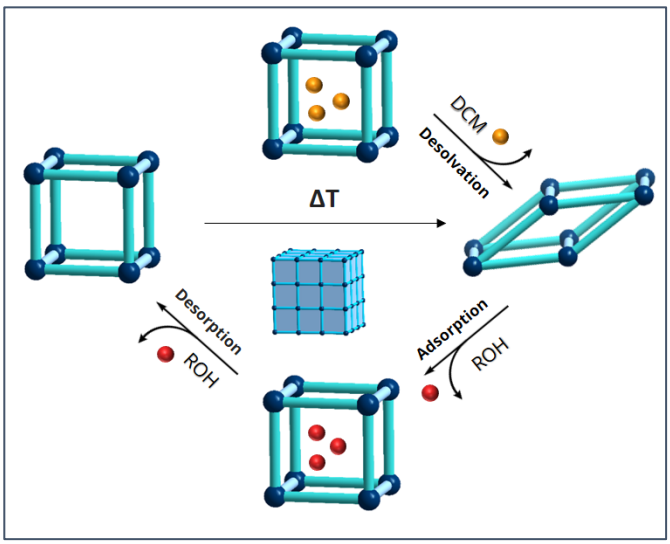

Figure 5-42. Schematic representation of alcohols-induced shape memory effect in DUT-8(Zn)_0.5 µm.

5.2.8 Impact of switchability on the separation ability in the liquid phase

To investigate the selectivity of DUT-8(Zn) in adsorption, depending on switching response towards different solvents, two component adsorption experiments were performed. DCM and 1-PrOH were chosen as adsorptives, since the micon-sized crystals DUT-8(Zn)_0.5 µm_*cp* can be reopened by 1-PrOH, while the macro-sized DUT-8(Zn)_160 µm_*cp* response only to DCM by opening and remains in the *cp* phase upon contact with 1-PrOH in single component adsorption experiments. The selective pore opening of DUT-8(Zn) towards specific guest molecule can be considered as a key-lock system (Figure 5-44).

The rigid submicron-sized DUT-8(Ni) sample (*op*) was chosen as a reference to investigate natural selectivity of DUT-8. The rigid DUT-8(Ni) sample was exposed to the DCM/1-PrOH (1:1 molar ratio) mixture and equilibrated at 293 K for 1 h. The adsorbed amount was monitored by NMR (Figure 8-19). The NMR analysis shows that after 1 h (Table 5-10), the DCM is preferably adsorbed on the sample over 1-PrOH, since DCM/1-PrOH ratio is decreased from 0.71 (before adsorption) to 0.56 (after adsorption).

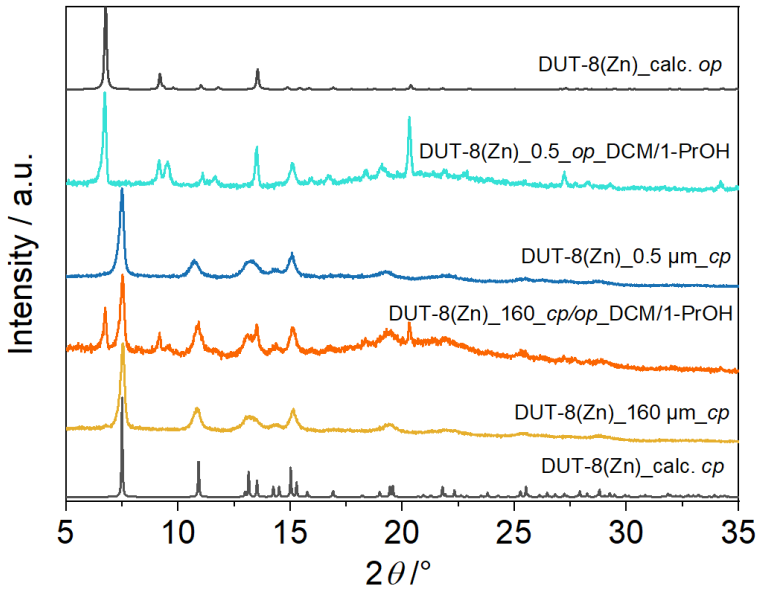

Figure 5-43. a) PXRD patterns of DUT-8(Zn)_160 µm_*cp* and DUT-8(Zn)_0.5 µm_*cp* resolvated in solution of DCM/1-PrOH.

Table 5-10. DCM/1-PrOH ratio of solutions based on integrals of NMR signals.

	DUT-8(Ni)_rigid_*op*	**DUT-8(Zn)_160 µm_*cp***	**DUT-8(Zn)_0.5 µm_*cp***
	DCM/ 1-PrOH ratio	*DCM/ 1-PrOH ratio*	*DCM/ 1-PrOH ratio*
Blank Solution	0.84/1.18 = 0.71	0.85/1.04 = 0.82	1.14/1.4 = 0.81
Solution after adsorption	0.51/0.91 = 0.56	0.7/0.91 = 0.77	0.87/1.38 = 0.63

Concerning the switchable DUT-8(Zn) samples, the state of the samples was monitored by PXRD (Figure 5-43), showing that DUT-8(Zn)_0.5 µm_*cp* was completely transformed to the *op* phase in DCM/1-PrOH solution. In case of macrocrystals DUT-8(Zn)_160 µm_*cp*, not all of the crystals can be reopened in DCM/1-PrOH, which is proven by PXRD. The pattern indicates the mixture of *cp/op* phases.

For DUT-8(Zn)_0.5 µm, the NMR analysis shows that despite the framework is reopened by 1-PrOH, DCM is preferably adsorbed on the sample over 1-PrOH (Table 5-10, Figure 8-20), since DCM/1-PrOH ratio is decreased from 0.81 (before adsorption) to 0.63 (after adsorption) similarly to DUT-8(Ni)_rigid.

DCM/1-PrOH ratios of solution before (0.82) and after adsorption (0.77) by DUT-8(Zn)_160 µm crystals do not differ greatly (Table 8-10, Figure 8-21). Despite DCM triggers the phase switching from *cp* to *op*, both solvents are adsorbed.

Thus, DUT-8(Zn) responsivity is significantly tailored by particle size, which in turn influences the selective adsorption behaviour (Figure 5-44).

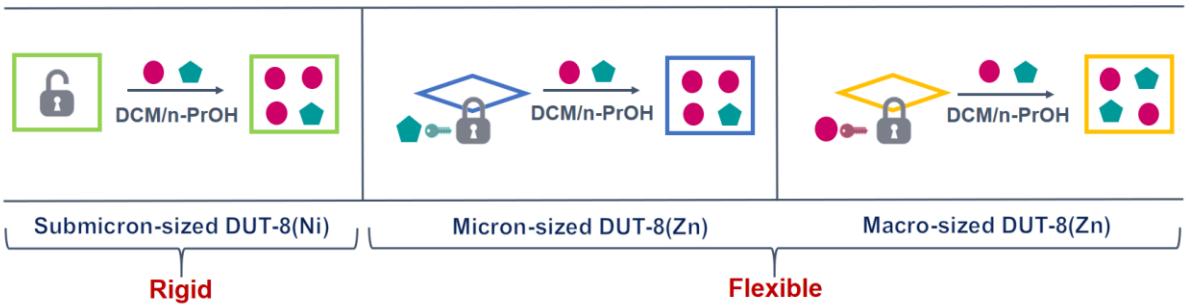

Figure 5-44. Schematic representation of selective adsorption properties of rigid DUT-8(Ni) and flexible DUT-8(Zn).

5.2.9 Conclusion

The critical particle size suppressing switchability in soft porous crystals is not identical for all MOFs but depends on the stiffness of the deforming building blocks, in case of DUT-8(M), the chemical composition of the paddle wheel hinges. For DUT-8(Zn), the smaller strain energy (+78 kJ mol−1) of the node results in a significantly higher energy difference of the empty op and cp hosts ($\Delta E = E_{op} - E_{cp}$), as compared to DUT-8(Ni), resulting in a smaller critical particle size (higher surface energy) required to suppress switchability. This was demonstrated by studying particles of three size regimes: 160 µm (macro-sized), 0.5 µm (micron-sized) and smaller than 0.1 µm (submicron-sized). Crystallites of different size regimes behave also differently upon removal of the guest molecules. Removal of dichloromethane in vacuum at elevated temperature causes high desorption stress favouring the formation of thermodynamically stable phases as the phase transition to the closed pore phase is observed for macro- and micron-sized particles, whereas only for submicron-sized particles a mixture of *cp*/*op* phases was obtained. The application of mild supercritical drying favours the formation of the metastable op phases: the macro-sized particles show a phase mixture of *op* and *cp* phases, whereas the micron and submicron sized particles remain in the metastable open pore phase.The dense *cp* phase of DUT-8(Zn) shows no adsorption-induced pore opening for N_2 at 77 K and CO_2 at 195 K. The higher interaction energies of chloromethane at 249 K and dichloromethane at 298 K allow reopening of the macro-sized crystals upon adsorption, but not the smaller particles. This could indicate an intermediate particle size regime, in which the crystals close as monodomain crystals, without twinning, hence the lack of defects may be responsible for the barrier to reopen the structure.[18, 145]

Crystal downsizing enhances the responsivity of DUT-8(Zn) towards larger palette of adsorptives. Among investigated guest molecules, the alcohols are able to induce so called shape-memory effect in micron-sized crystals. The adsorption of alcohols stimulates phase transition from *cp* to *op* which is maintained even after desorption. The framework rigidification is caused by chemical host-guest interactions leading to surface deformation and possible nanodomain formation. Moreover, crystal downsizing contributes to selective adsorption properties of DUT-8(Zn). Selective adsorption of DCM over 1-PrOH is revealed in micron-sized crystals, which is not the case for macro-sized crystal.

Chapter 6 The impact of surface modification on switchability of DUT-8(Ni)

6.1 Introduction

Modern industrialization requires the development the specific function of hybrid materials for target applications. The functionality of the advanced materials is determined not only by composition, but also by interfaces and surface, which serve as a favoured medium for technological processes.[229] In case of new class of hybrid materials – crystalline porous metal-organic frameworks, high internal surface determines the application pathway in gas storage and separation.[3] However, the outer surface can be considered as surface barrier, causing mass transfer limitations, influencing MOF performance.[230] Moreover, surface barriers may effect on structural transformations in switchable MOFs, which are able to adopt to the changes in the environment.

So far, mostly internal pore surfaces were functionalized rather than outer surfaces of MOF crystals.[231] To modify properties of MOFs, the varying synthetic and self-assembly approaches for surface decoration were developed.[232] Kitagawa *et al*. synthesized HKUST-1 through coordination modulation, changing crystal morphology from octahedron to cubeoctahedron, which potentially allows for control over surface reactivity.[233] Another widely used surface modification technique is solvent-assisted linker exchange, which was performed on DMOF-1. In this work,[234] a monolayer of boron dipyrromethane (BODIPY) molecules were imparted onto the four carboxylate terminated surfaces [100], leaving the two dabco terminated surfaces [001] unmodified.

The modification of surface chemistry leads to either the enhancement or deterioration of MOFs properties.[232] Surface degradation is associated with the formation of defects, for example, after exposure of HKUST-1 to water vapour, therefore hindering the uptake and release of guest molecules.[192]

The crystal surface modification of MOFs can be realized by different polymer coating procedures.[235] By means of post-synthetic modification route, MOF-5 was coated by chemical vapour deposition with PDMS layer, improving stability of material under ambient conditions.[199] To enhance adsorption properties, MOF crystals can be coated by *in situ* polymerization,[236] post-synthetic grafting approach[200] or through surface selective ligand exchange.[237] Addition of polymer to the synthetic procedure may result in simultaneous morphology modification and surface functionalization as was shown for DMOF-1.[238] Originally DMOF-1 has cubic-like morphology, but introduction of

poly(methacrylic acid)$_8$-b-PEG$_{68}$ (PMAA$_8$-b-PEG$_{68}$) in the MOF synthesis yields hexagonal rod-like crystals, which were covered mainly at the side faces {100} and {1-10} with polymer, while dabco-based top faces {001} remained unoccupied.

Polymers are also used as the binders in moulding of switchable MOFs, as was shown for elastic layer-structured ELM-11 [Cu(BF$_4$)$_2$(4,4´-bipyridine)$_2$]. The shaping of ELM-11 into pellets with poly(vinylpyrrolidone) (PVP) leads to slacking of gate adsorption behaviour. Free energy analysis by molecular simulations revealed that less steep CO_2 adsorption isotherm is associated with the external force caused by PVP, resulting in sequential expansion of layers.[239]

Concerning switchable MOFs, there is an interplay of factors affecting structural transformations, including not only the crystal size, morphology and defects, but also crystal surface, matrix interfaces and grain boundries.[41, 144]

The influence of surface functionalization on switchable behaviour of DUT-8(Ni) was studied by T. Düren *et al*. using osmotic framework adsorbed solution theory (OFAST). It was revealed that surface capping of DUT-8(Ni) nanoparticles with different surface groups (DMF, dabco, ndc, fumaric acid) leads to changes in gate-opening/closing pressures.

The investigation of crystal-size dependent switchability in DUT-8(Zn) revealed that crystal downsizing leads to ability of framework to interact with alcohols (Section 4.2.7). Alcohol-induced phase switching from *cp* to *op* is accompanied by surface deformation and therefore rigidification of the system. Interestingly the macro-sized crystals DUT-8(Ni) are not responsive towards protic solvents,[19] such as alcohols, pointing on possible surface chemistry modification. In this regard, DUT-8(Ni) is considered as model DUT-8 system for investigation of the influence of surface treatment procedure on adsorption behaviour of DUT-8(Ni). For this purpose, not only alcohols are used for surface treatment, but also polymer coating procedures are performed.

6.2 Results and discussions

6.2.1 The influence of surface treatment on adsorption behaviour

The particle structure of a MOF sample characterized not only the size, morphology, defects, but also surface exterior is an important parameter influencing the sample property.[9] In this regard, the influence of surface treatment on DUT-8(Ni) switchablity is investigated. For this purpose, ethanol, ethanol/water mixture and PDMS were used for treatment. Ethanol is not able to initiate switching from *cp* to *op,* pointing on the surface modification, while the use of ethanol/water mixture may cause more severe surface changes, since the material is not stable in water. To improve the instability of MOFs at the ambient conditions, PDMS is used to cover the crystal surface.[199] In this case, the polymer may not only improve the stability of DUT-8(Ni), but also modify the adsorption properties. The surface treatment procedures with corresponding sample name are listed in Table 6-1. Firstly, the surface of the desolvated macro-sized DUT-8(Ni) was exposed to ethanol for 6 hours with subsequent drying under dynamic vacuum (sample 1_EtOH). In the second treatment procedure, sample was soaked in ethanol/water mixture (95/5 v.v.) and dried in argon flow at 100°C for 4 h (sample 2_EtOH/H_2O). The chemical vapour deposition of polydimethylsiloxane (PDMS) was carried out in inert atmosphere at 235°C during 6 h (sample 3_PDMS), according to a procedure reported earlier.[199] The phase purity of as made, desolvated and treated samples was identified by PXRD. After exchanging of DMF by DCM, solvent was removed from the pores in dynamic vacuum. PXRD measurement revealed that non-treated pristine DUT-8(Ni) (Reference) underwent structural transformation from open to closed pore phase (254% of volume change) (Figure 6-1a,b).[109]

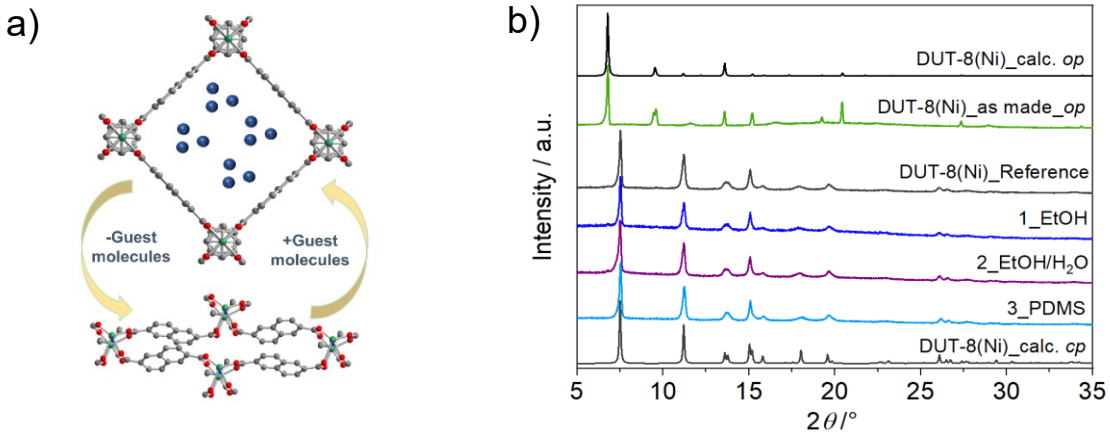

Figure 6-1. a) Representation of DUT-8(Ni) phase transition upon guest removal/adsorption, b) PXRD patterns of DUT-8(Ni) in desolvated state before and after treatment.

Table 6-1. The list of samples with corresponding treatment procedures.

Sample name	Treatment procedure
1_EtOH	Treatment by EtOH for 6 hours with subsequent drying under dynamic vacuum
2_EtOH	Treatment by EtOH/H_2O mixture (95/5 v.v.) with subsequent drying in argon flow at 100°C for 4 hours
3_PDMS	Chemical vapour deposition of PDMS in argon atmosphere at 235°C for 6 hours
4_BA/EtOH	Treatment by 0.1 mol/L solution of benzoic acid EtOH for 3 hours with subsequent drying under vacuum
Reference	non-treated DUT-8(Ni)_*cp*

The described above treatment procedures do not cause any structural changes, indicating that structure of the samples (*cp* phase) is well maintained after the treatment (Figure 6-1b).

The influence of the treatment procedures on surface of samples was investigated by SEM. Solvothermal synthesis produces relatively large rod-shaped crystallites of DUT-8(Ni) with average length 48 and width 17 μm. According to SEM images (Figure 6-2, 6-3), there is not distinct difference between samples before and after treatment by EtOH. The surface is shown to be smooth, besides sample treated by mixture of ethanol/water. In sample treated by ethanol/water mixture, the surface is rough, pointing out on surface deformation, which may drastically influence the structural response and therefore adsorption profile (Figure 6-3d).

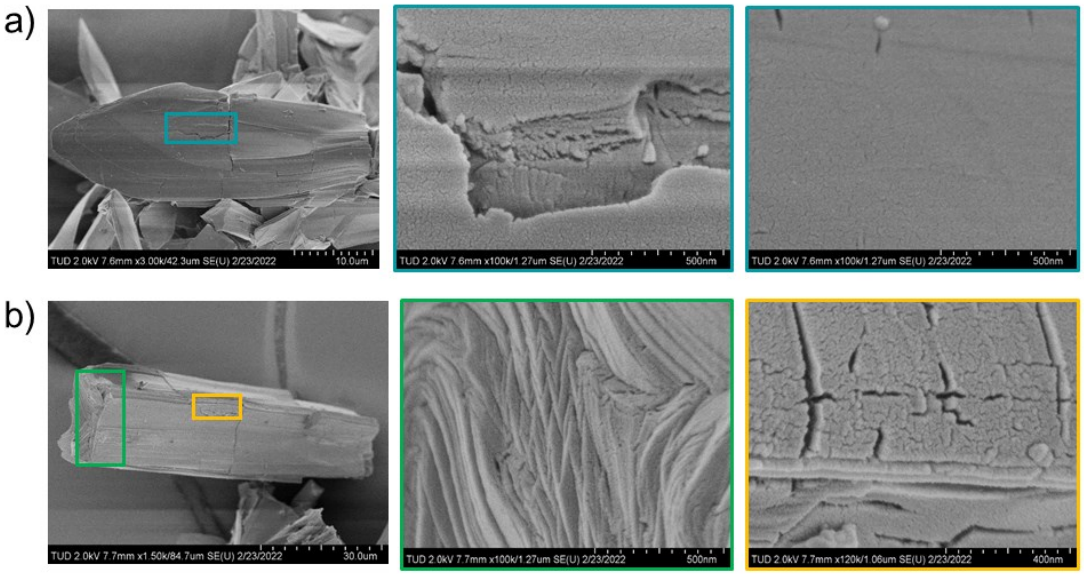

Figure 6-2. SEM images of a) non-treated sample and b) sample exposed to ethanol (1_EtOH).

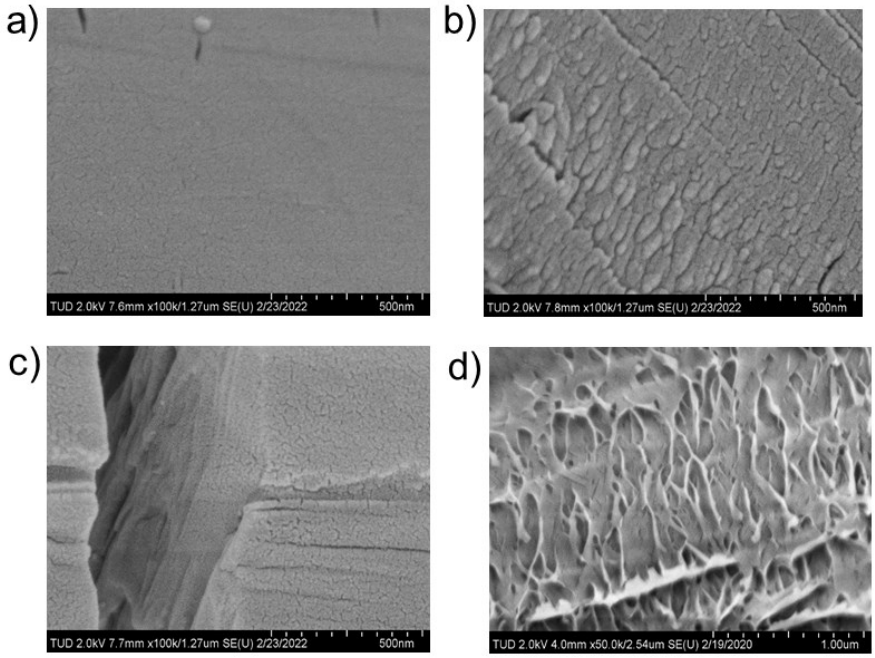

Figure 6-3. SEM images of a) Reference and treated samples b) 1_EtOH, c) 3_PDMS, d) 2_EtOH/H_2O.

Adsorption behaviour

The influence of treatment procedures on structural responsivity was investigated by nitrogen physisorption at 77 K.

The marco-sized crystals of DUT-8(Ni) are switchable in adsorption of N_2 (77 K) experiencing structural transformations from closed pore (*cp*) to open pore (*op*) phases, resulting in typical gate-opening behaviour. There is no structural response of DUT-8(Ni) (Reference) in region of low relative pressure to nitrogen molecules at 77 K. A sudden increase of uptake at pressure of p/p_0=0.15 is referred to the stimuli-induced framework reopening (Figure 6-4).

The treatment of the material by ethanol, ethanol/water mixture, PDMS leads to modification of adsorption profile, increasing activation barrier (Figure 6-4), which can be associated with surface deformation. To monitor the changes in adsorption behaviour, the relative adsorption pressure at half-maximum uptake (APHM) as a measure of the average gate opening activation energy ($1G^*$) is used (Section 4.2.2).[202] The treatment of the material results in decrease of nitrogen uptake, as well as increase of APHM values, pointing on increase of energy barrier for phase transition. The APHM of DUT-8(Ni) non-treated sample Reference is 0.15, which is lower in comparison with APHM of samples 1_EtOH - 0.19, 2_ EtOH/H_2O - 0.55. In the sample treated by PDMS 3_PDMS, APHM value is shifted to 0.25 (Figure 6-5).

Upon adsorption of DCM, a guest with higher adsorption enthalpy, the average energetic barrier for phase transition from *cp* to *op* is increased to 0.33 for sample treated by EtOH in comparison with non-treated sample 0.22. (Figure 6-6).

The treatment of the samples modifies the adsorption profile of material, revealing higher average energetic barrier for framework reopening. According to gate-opening pressure shift, the degree of surface deformation increases in the following tendency EtOH<PDMS<EtOH/H_2O. Thus, ethanol/water treatment causes the most severe surface changes.

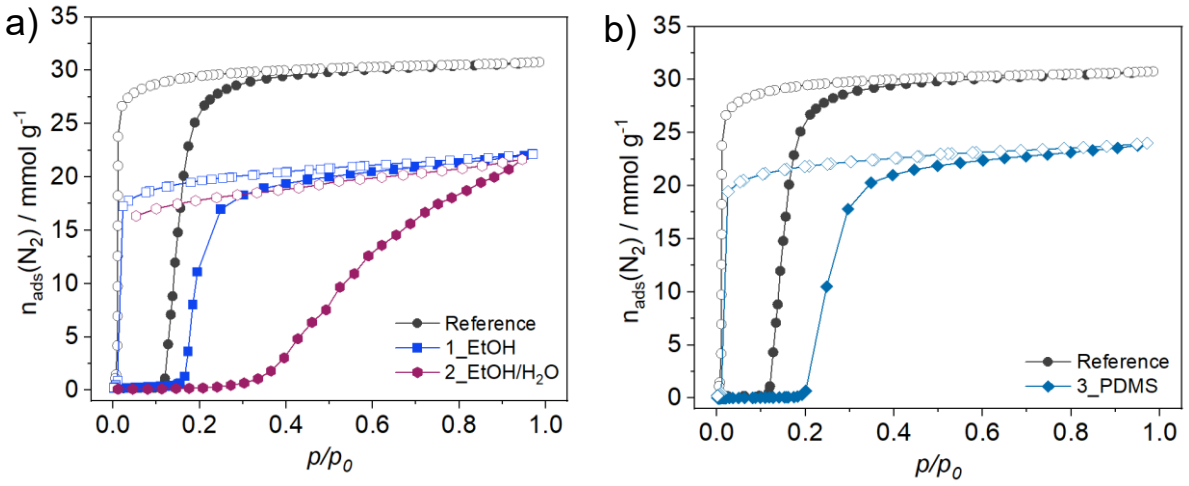

Figure 6-4. Nitrogen physisorption isotherms at 77 K of samples a) treated with ethanol, ethanol/water mixture; b) treated with PDMS.

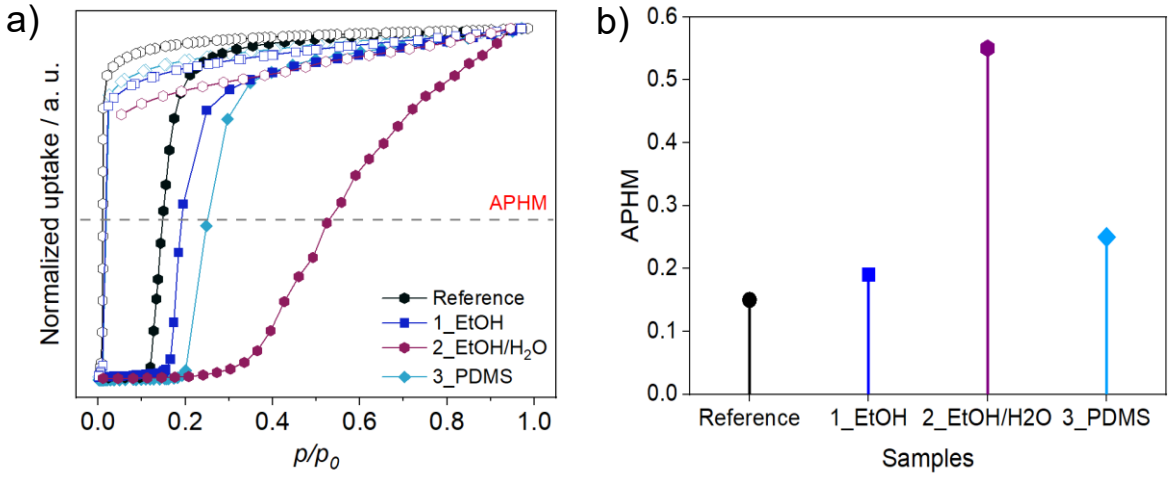

Figure 6-5. a) Nitrogen physisorption isotherms with uptake normalized to the maximum value, b) APHM values.

Additionally, DUT-8(Ni) sample in desolvated state (*cp*) was treated with linear alcohols, which affect adsorption properties similar to ethanol, namely increasing energy barrier for phase transition and limiting nitrogen uptake (Figure 6-7).

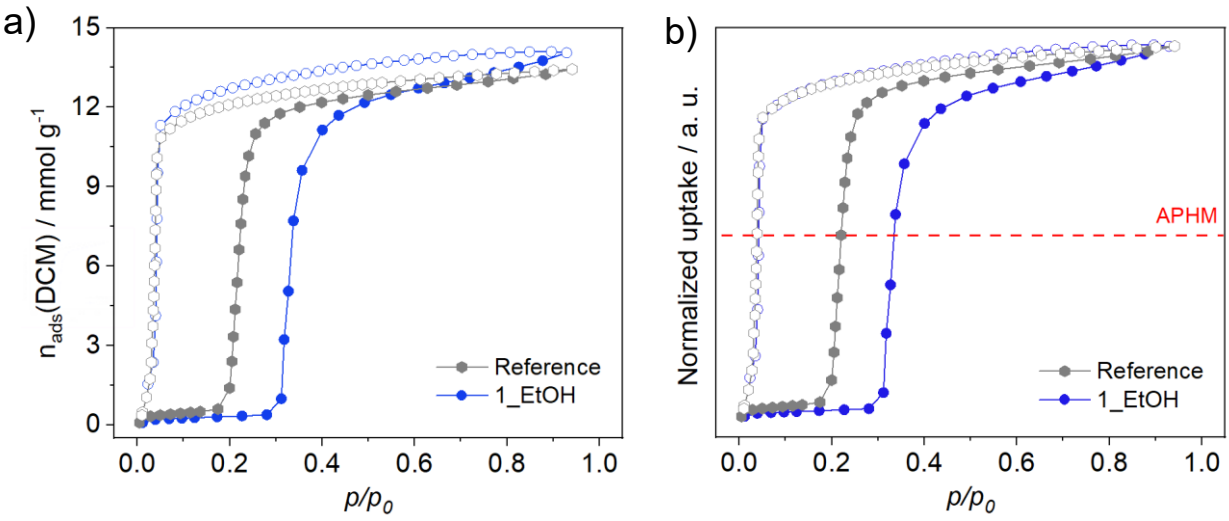

Figure 6-6. a) DCM physisorption isotherms of samples before and after ethanol treatment, b) DCM physisorption isotherms with uptake normalized to the maximum value.

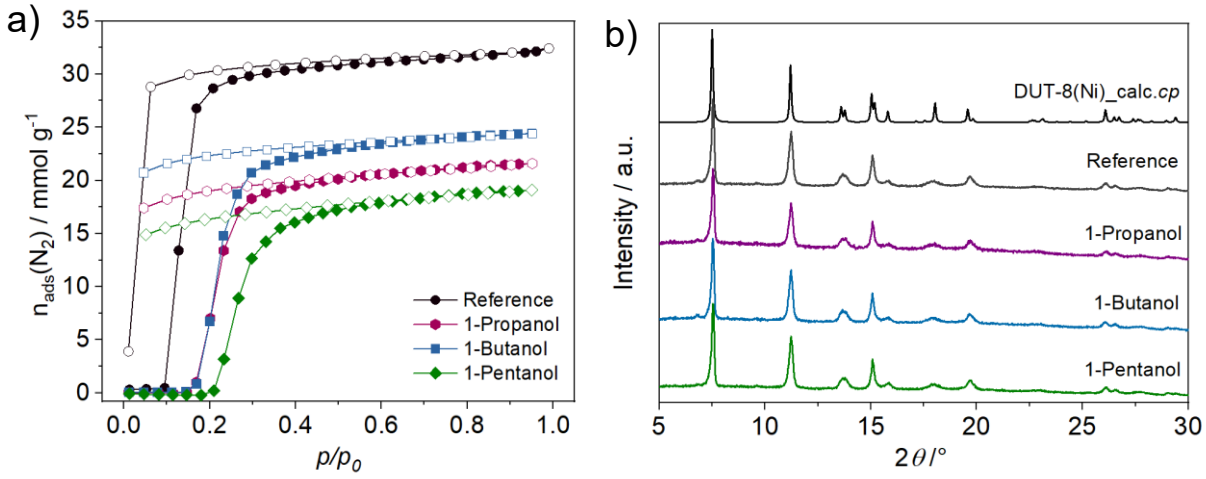

Figure 6-7. a) Nitrogen physisorption isotherms (77 K) and b) PXRD patterns of samples treated by linear alcohols.

Reactivation

The surface deformation is known to be related to surface defects and associated surface barriers, which in turn influence MOF performance. However, the destroyed surface of material can be repaired by dissolving surface barriers in the synthesis solvent.[87] In our case, such method of healing cannot be realised, since immersing of material in DMF leads to phase transition from *op* to *cp* phase.[19] Therefore, thermal treatment under vacuum is applied for material reactivation. The samples treated with ethanol (instead of 6 h, only 30 sec) and ethanol/water mixture were only partially regenerated (Figure 6-8), pointing on stronger interaction of these molecules with framework and possible incorporation onto surface. Furthermore, the discussed surface treatment procedures can also lead to the hydrolysis and subsequent amorphization.

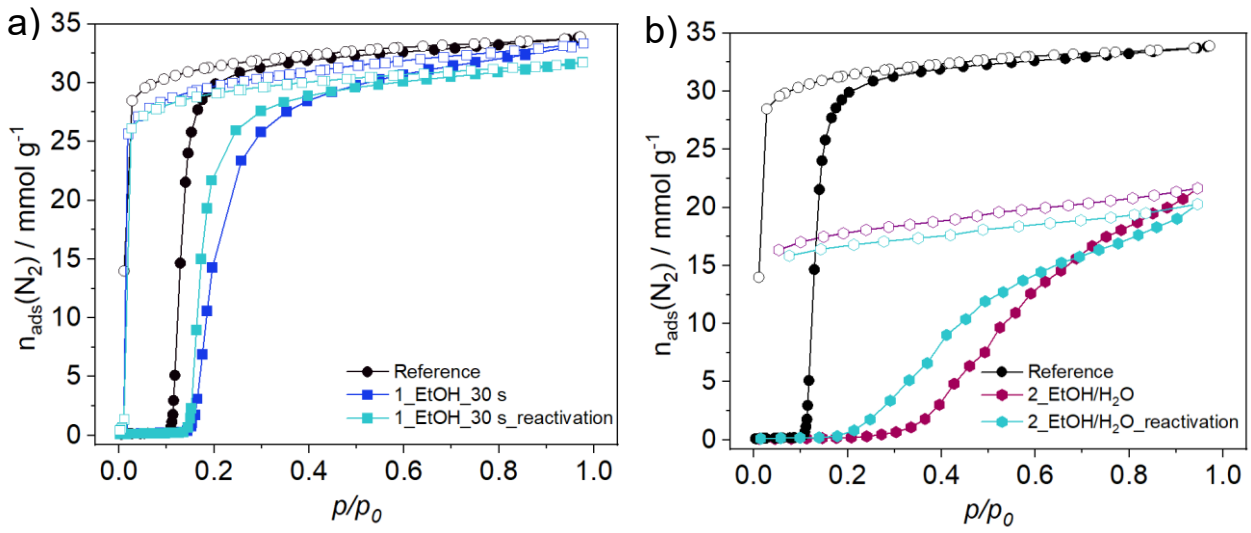

Figure 6-8. Nitrogen physisorption isotherms at 77 K for a) non-treated sample (Reference), sample treated with ethanol (1_EtOH_30 s) and sample after reactivation (1_EtOH_30 s_reactivation); b) non-treated sample (Reference), sample treated with ethanol/water mixture (2_EtOH/H_2O) and sample after reactivation (2_EtOH/H_2O_reactivation).

XPS spectroscopy

In order to investigate the composition of the samples surface, X-ray photoelectron spectroscopy (XPS) was performed by Dr. Johannes Schmidt (TU Berlin).

As shown in Figure 6-9, the full range XPS spectra of DUT-8(Ni) samples demonstrates of C1*s*, O1*s*, N1*s* and Ni2*p* peaks. Specifically, the peak at 856.08 eV corresponds to the 5- coordinated Ni, binding to one N from dabco as well as four carboxylate O from 2,6-ndc. The Ni 2*p*3/2 of reference and all treated DUT-8(Ni) samples indicates bivalent Ni^{2+} state, which are slightly different in binding energies. The comparison of O1*s* peaks, corresponding to C-O bonding of ndc linker, reveals a slight increase of the binding energies for the treated samples (1_EtOH, 2_EtOH/H_2O, 3_PDMS). On the other hand, in N1*s* (N-C in dabco) spectra, the highest binding energy is shown to be for 2_EtOH/H_2O, which coincides with the most significant changes in adsorption behaviour. Compared with those of Reference sample, O1*s* in 3_PDMS have higher binding energy and broadened peaks. The spectra Si2*p* are shown in Figure 8-23 confirming the presence of Si on the surface.

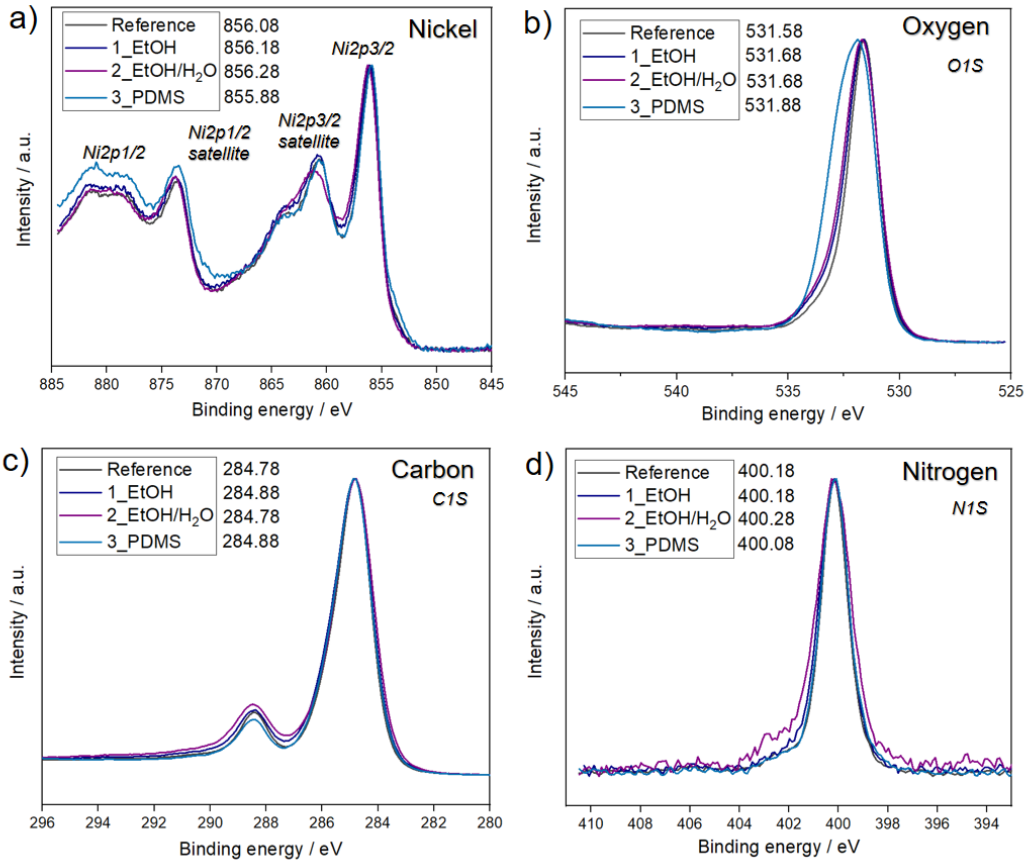

Figure 6-9. XPS spectra a) nickel, b) oxygen, c) carbon, d) nitrogen of treated samples in comparison with non-treated.

Contact angle measurements

By means of XPS and SEM, it was shown that the treatment of samples by EtOH, EtOH/H_2O mixture and PDMS leads to surface modification. In order to further prove the surface modification, the contact angle measurement was performed by Dr. A. Synytska (Leibniz Institute for Polymer Research).

To measure contact angle, 50 mg of the dried powdered material (*cp*) was pressed under 10 tons for 5 min using hydraulic press. SEM images of the pellet surface are shown in Figure 6-10a. Pressing process does not influence on crystal structure itself according to PXRD pattern (Figure 6-11b). However, similarly to ELM-11 pellets,[239] nitrogen adsorption isotherm significantly differs from the reference one, demonstrating gate-opening pressure shift and decrease of uptake (Figure 6-11a). Notably, after nitrogen adsorption measurement, DUT-8(Ni) pellet was crushed as can be seen from SEM images (Figure 6-10b). Interestingly, the adsorption properties of the pressed material, after ethanol treatment, modified in the similar to powdered sample way.

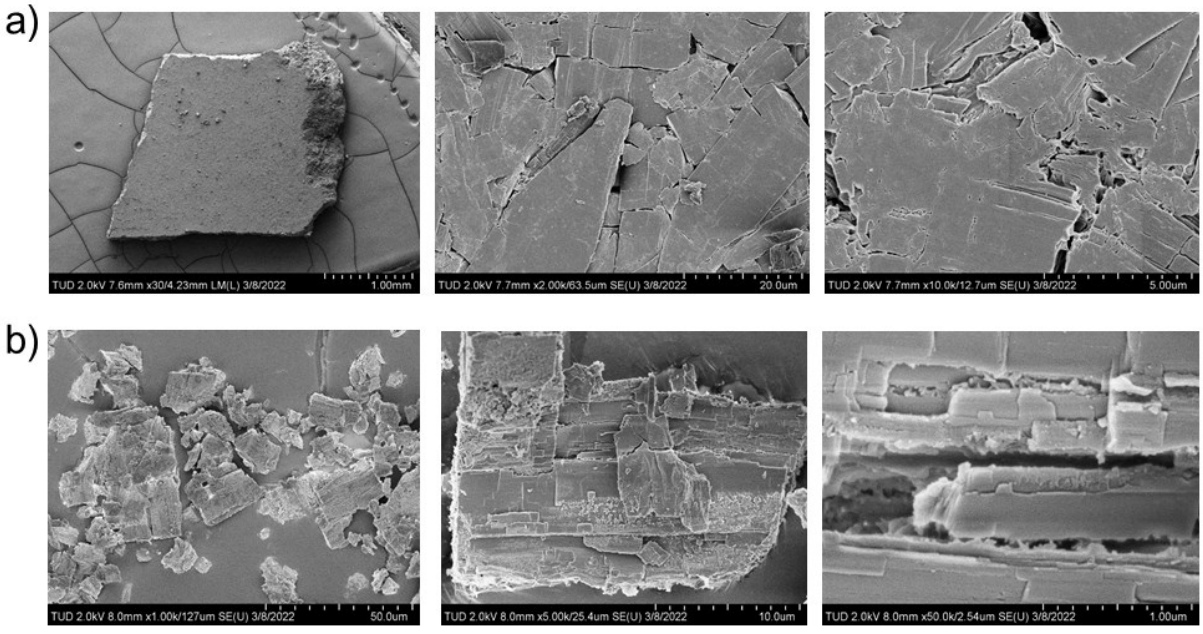

Figure 6-10. SEM images of pellet DUT-8(Ni) a) before and b) after N_2 adsorption at 77 K.

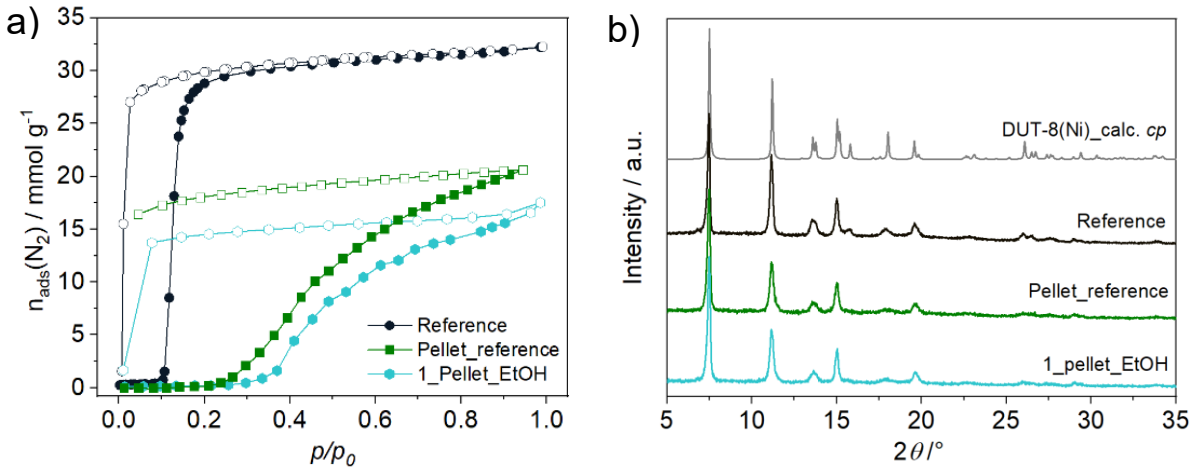

Figure 6-11. a) Nitrogen physisorption isotherms (77 K); b) PXRD patterns for reference DUT-8(Ni), pellet DUT-8(Ni) and pellet DUT-8(Ni) treated with ethanol.

The choice of the probe fluids is limited, because aprotic polar solvents induce phase switching from *cp* to *op*, protic solvents (alcohols) modify the surface. Since the surface of DUT-8(Ni) pellet is hydrophobic, the probe fluids with surface tension less than 50 mN/m are not suitable. In this regards, diiodomethane can be used for measurements, because of inability to reopen the framework and suitable surface tension value (50.8 mN/m).

The static contact angle (CA) measured by diiodmethane droplets constitutes 23° for pristine DUT-8(Ni) pellet (Pellet_reference) (Figure 6-12a, Table 6-2). After ethanol treatment, the surface of sample 1_EtOH_pellet becomes more hydrophilic. It leads to spreading of probe fluid across, maximizing the contact and therefore decreases CA value to 9° (Figure 6-12b).

By means of SEM it was not possible to prove the existence of PDMS layer on the surface of samples 3_PDMS (Figure 6-3c). However, after exposure of DUT-8(Ni) pellet to chemical vapour deposition, CA increases up to 57° (Figure 6-12c), confirming the successful hydrophobic coating by PDMS (sample 3_pellet_PDMS).

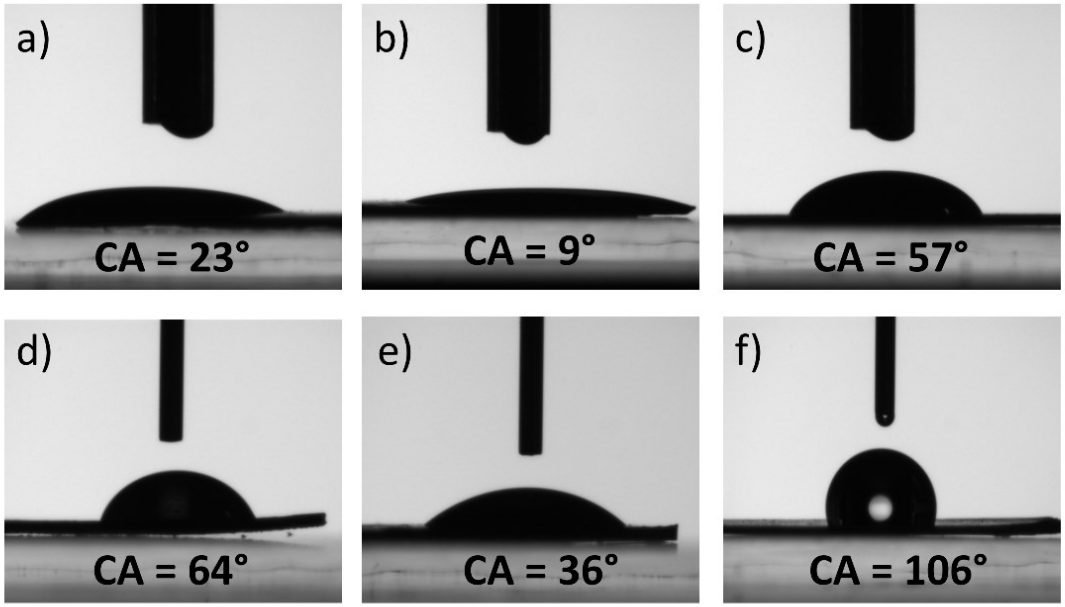

Figure 6-12. The contact angle measured by diiodmethane droplets: a) pristine pellet, b) after ethanol treatment, c) after PDMS coating; water droplets: d) pristine pellet, e) after ethanol treatment, f) after PDMS coating.

The surface tension of water is higher than the value of diiodomethane, which makes water more suitable probe fluid. CA measurements performed by water droplets exhibit the same trend of changes as caused by diiodmethane. But water-based results cannot be reliable due to reactivity of DUT-8(Ni) pellets with water (Table 6-2, Figure 6-12d,e,f).

Table 6-2. The data of contact angle measurements.

Sample	**Static contact angle**	**Receding contact angle**	**Advancing contact angle**
	Diiodomethane, γL= 50,8 [mN/m]		
Pellet_reference	23	12	34
1_pellet_EtOH	9	5	18
3_pellet_PDMS	57	27	63
	Water, γL= 72,0 [mN/m]		
Pellet_reference	64	16	72
1_pellet_EtOH	36	7	54
3_pellet_PDMS	106	7	118

Solid state NMR

It was shown that treatment by ethanol, ethanol/water mixture and PDMS leads to surface modification, which in turn change adsorption properties of DUT-8(Ni). It is assumed that in case of treatment by EtOH or EtOH/H_2O, EtOH is incorporated onto the surface of crystals, blocking the pore entry. As a result, average activation energy for phase transition is increased.

In order to detect the incorporated EtOH, ^{13}C solid state NMR was measured. Due to the low intensity of NMR spectra of non-protonated linker, carbon atoms of the carboxylic groups of 2,6-H_2ndc were selectively labelled (^{13}C) according to a procedure reported earlier.[216] ^{13}C-enriched carboxylic acid was used for synthesis of flexible DUT-8(Ni) crystals, which were desolvated from DCM resulting in *cp* phase (^{13}C_DUT-8(Ni)) (Figure 6-13a). It is assumed that amount of ethanol incorporated onto the surface is quite low, therefore the sample ^{13}C_DUT-8(Ni) was treated by ^{13}C-labelled EtOH in order to enhance the NMR signals (sample ^{13}C_DUT-8(Ni)_EtOH). The treatment procedure was analogous to the one used for sample 1_EtOH (Table 6-1).

The comparison of NMR spectra is shown in Figure 6-13b. The isotropic ^{13}C NMR chemical shifts at 229 ppm and 160 ppm are assigned to ^{13}C-enriched carboxylate functionalities and aromatic carbons, respectively in samples ^{13}C_DUT-8(Ni) and ^{13}C_DUT-8(Ni)_EtOH. The chemical shift at 32 ppm is referred to dabco in both samples.

The treatment of sample by ^{13}C EtOH results in the appearance of three additional signals at 134, 128 and 48 ppm. The signals at 128 and 47 ppm in sample ^{13}C_DUT-8(Ni)_EtOH could be attributed to ethanol. Usually, the paramagnetic influence of Ni leads to high chemical shift of the carboxylates signal 226 ppm instead of 173 ppm. In a similar way Ni may influence the original signals of ethanol at 58 and 17 ppm, shifting the signals to 128 and 48 ppm, respectively.

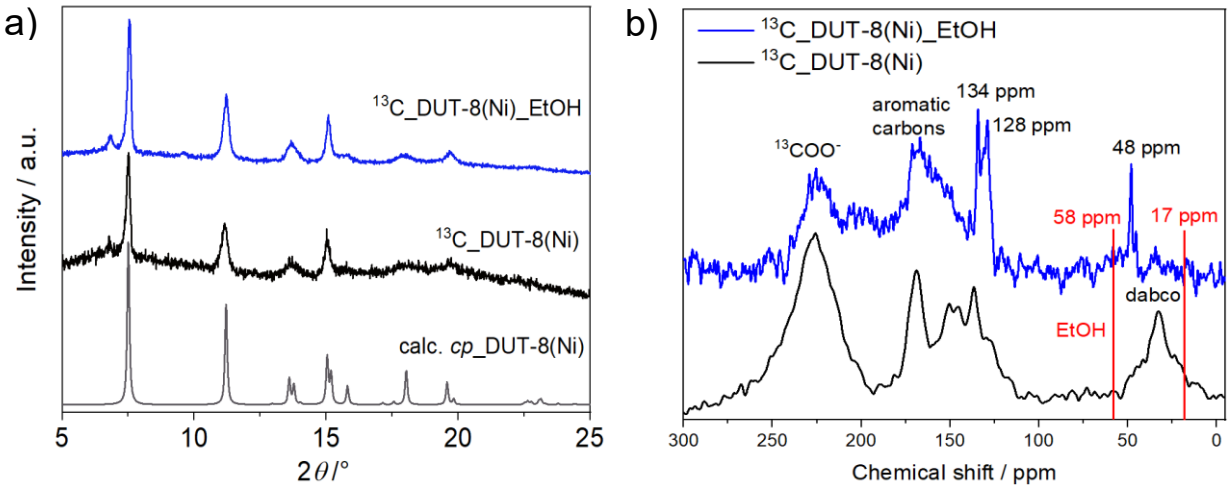

Figure 6-13. a) PXRD patterns of samples with ^{13}C labelled 2,6-ndc linker before and after treatment with ^{13}C EtOH, b) Solid-state NMR spectra.

Treatment with ^{13}C benzoic acid

Additionally, the surface was treated by ^{13}C-labelled benzoic acid (BA) using non-labelled pristine material resulting in sample 4_BA/EtOH. Despite ethanol treatment was shown to significantly change adsorption profile of DUT-8(Ni), ^{13}C-labelled benzoic acid was dissolved in ethanol, because other polar solvents induce phase switching.[19] The comparison of SEM images shows significant surface changes caused by treatment with solution of BA in EtOH (Figure 6-14). To prove the influence of benzoic acid itself on adsorption behaviour, the nitrogen adsorption isotherms of 1_EtOH and 4_BA/EtOH samples were compared (Figure 6-15a), indicating only slight difference in the slope of isotherm. In this case, the increase of the gate-opening pressure, i. e. the modified adsorption profile is caused by EtOH rather than BA. The treatment by BA/EtOH does not affect the crystal structure (Figure 6-15b), preserving the initial *cp* phase of sample.

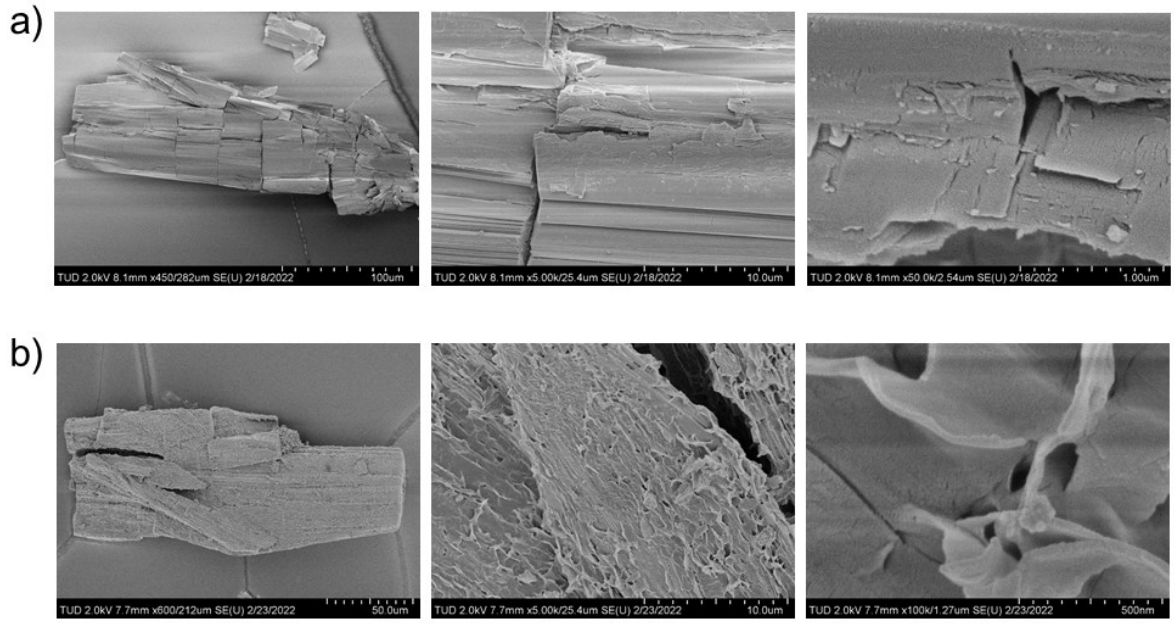

Figure 6-14. SEM images a) before treatment and b) after treatment by benzoic acid dissolved in EtOH.

Despite insignificant influence on adsorption behaviour of BA, ^{13}C solid state NMR reveals the presence of BA incorporated on the crystal surface (Figure 6-16). As can be seen from spectra the signal of labelled ^{13}C BA is 167 ppm, which is slightly shifted in comparison with the signal of BA solved in EtOH (169 ppm). The enrichment of BA by ^{13}C allows to detect BA, while the signal of MOF is quite weak without labelling of carbon atoms of the carboxylic groups with ^{13}C isotope.

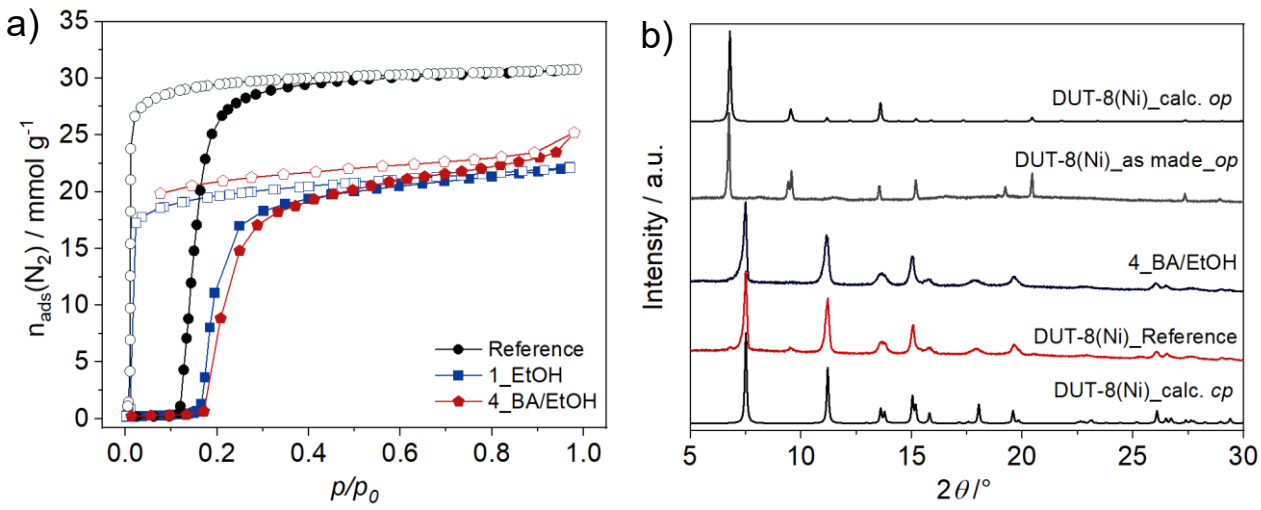

Figure 6-15. a) Nitrogen physisorption isotherms of samples before and after treatment by ethanol 1_EtOH and ^{13}C-labelled benzoic acid solved in ethanol 4_BA/EtOH, b) PXRD pattern of 4_BA/EtOH in comparison with non-treated DUT-8(Ni).

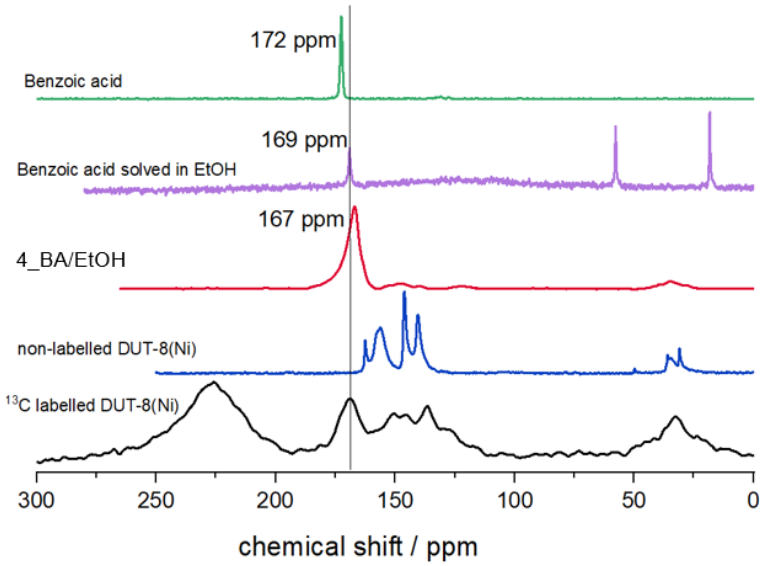

Figure 6-16. Solid state NMR spectra of 4_BA/EtOH in compassion with non-labelled and ^{13}C labelled DUT-8(Ni)_*cp*.

6.2.2 The influence of polymer coating on framework switchability

In this section, the influence of polymer coating on the framework responsivity is investigated. The deposition of PDMS on the crystals in *cp* phase resulted in the increased energy barrier for phase transition upon adsorption of nitrogen (Section 6.2.1). In the following, the polymer coating of the solvated crystals in *op* phase and resulting properties will be discussed.

The large DUT-8(Ni) crystals 1_DUT-8(Ni)@FDA-DAM, which were solvated in DMF before coating, were successfully coated by 6FDA*DAM (Figure 6-17) according to SEM images (Figure 6-18). Meanwhile, the solvent exchange from DMF to DCM prior the surface coating, leads to insufficient surface coverage by polymer of sample in 2_DUT-8(Ni)@FDA-DAM (Figure 6-19), meaning that DMF contributes to the precipitation of polymer on crystal surface.

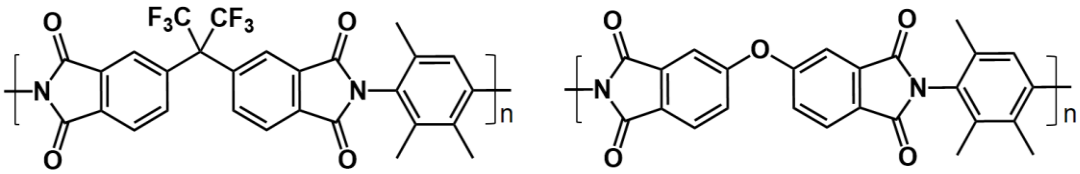

Figure 6-17. Chemical structure of 6FDA-DAM and ODPA-DAM.

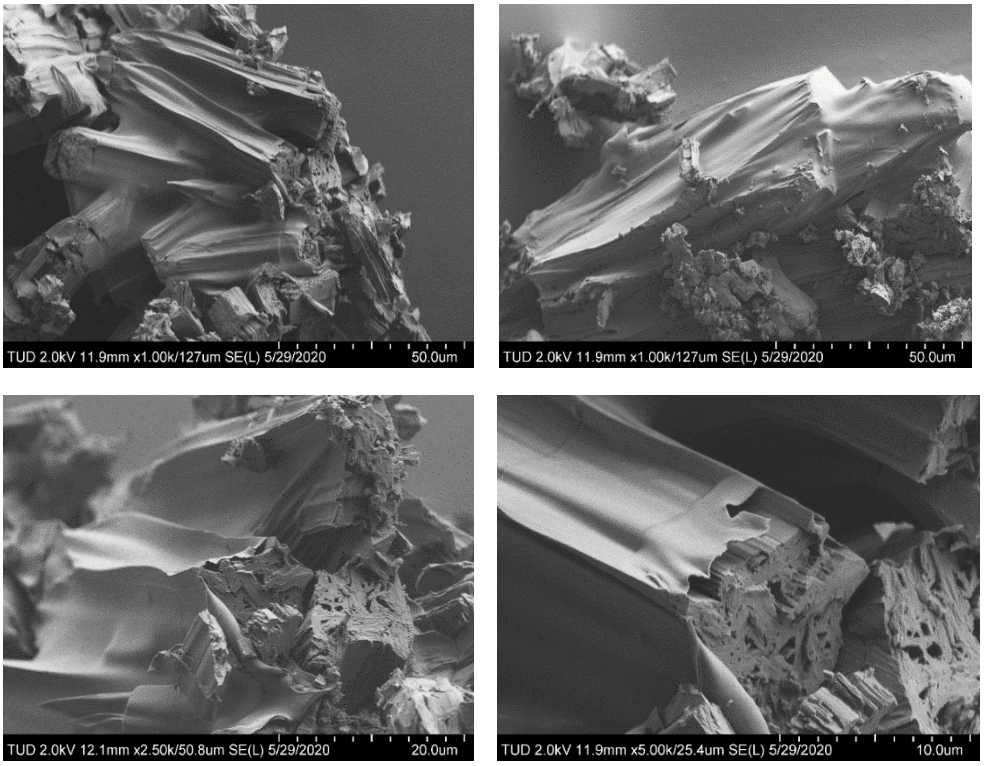

Figure 6-18. SEM images of polymer coated crystals 1_DUT-8(Ni)@FDA-DAM.

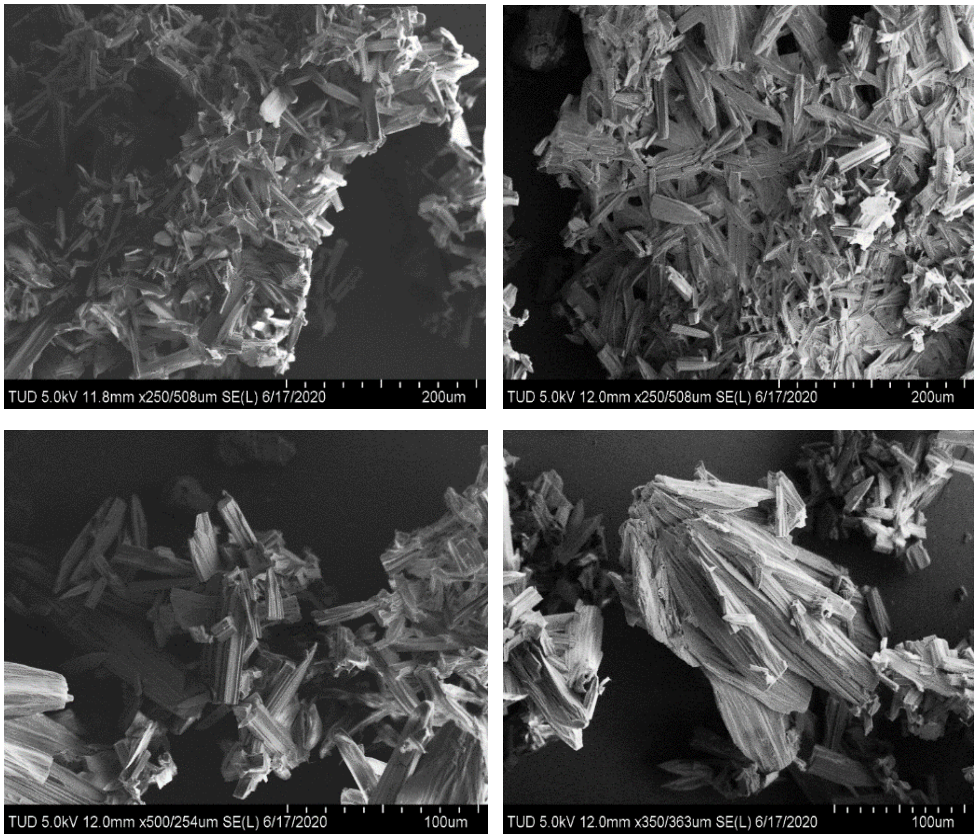

Figure 6-19. SEM images of polymer coated crystals 2_DUT-8(Ni)@FDA-DAM.

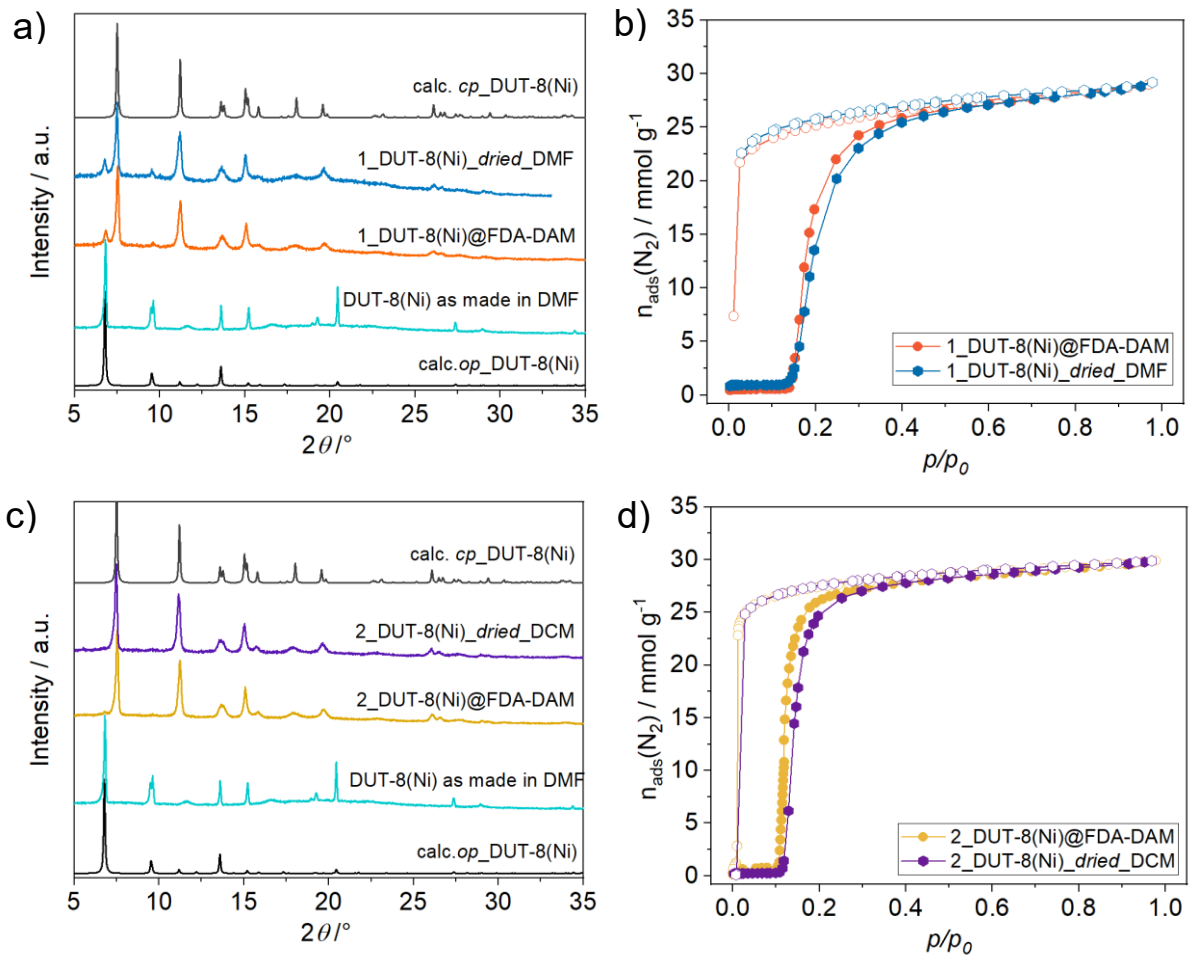

Figure 6-20. a) PXRD patterns and b) N_2 physisorption isotherms at 77 K of non-coated 1_DUT-8(Ni)_*dried*_DMF and polymer coated crystals 1_DUT-8(Ni)@FDA-DAM dried from DMF, c) PXRD patterns and d) N_2 physisorption isotherms at 77 K of non-coated 2_DUT-8(Ni)_*dried*_DCM and polymer coated crystals 2_DUT-8(Ni)@FDA-DAM dried from DCM.

The influence of polymer coating on phase switching of DUT-8(Ni) was monitored by PXRD and N_2 adsorption. As can be seen from PXRD patterns (Figure 6-20a,c), polymer does not interfere the phase transition from *op* to *cp* phase. The reflex of *op* phase in 1_DUT-8(Ni)@FDA-DAM is associated with incomplete closing of framework due to slower diffusion rate of DMF from the pores. PXRD patterns of 2_DUT-8(Ni)@FDA-DAM confirm the complete structural transformation upon desolvation process.

The reverse process, framework reopening, was investigated upon adsorption N_2 at 77 K. The comparison of adsorption isotherms reveals that the phase transition pathway of 1_DUT-8(Ni)@FDA-DAM from *cp* to *op* is almost identical to reference sample 1_DUT-8(Ni)_DMF (Figure 6-20b). The possible explanation of such behaviour can be related to the pore entry accessibility. Previously it was shown that

the surface on the top and the bottom of the crystal (area of 001 faces) is the entry for molecules into the channels (Section 4.2.2). As can be seen from SEM images (Figure 6-18), after coating and subsequent solvent removal, the pore entry is not covered by polymer and therefore accessible to guest molecules.

Since the coating procedure did not lead to sufficient surface coating of sample 2_DUT-8(Ni)@FDA-DAM, there are no distinct changes in adsorption profile (Figure 6-20d).

Analogous experiments were performed using ODPA-DAM polymer (Figure 6-17). The small difference in polymer structure results in significant difference of polymer coating on MOF surface 1_DUT-8(Ni)@ODPA-DAM (Figure 6-21). There is no homogenous layer of polymer on the surface as in case of 1_DUT-8(Ni)@FDA-DAM, rather irregular rough coating. According to SEM images, polymer ODPA-DAM is able to hold aggregates of crystals and withstand stress caused by desolvation procedure. However, the solvent removal again leads to small amount of *op* phase remained. (Figure 6-22a).

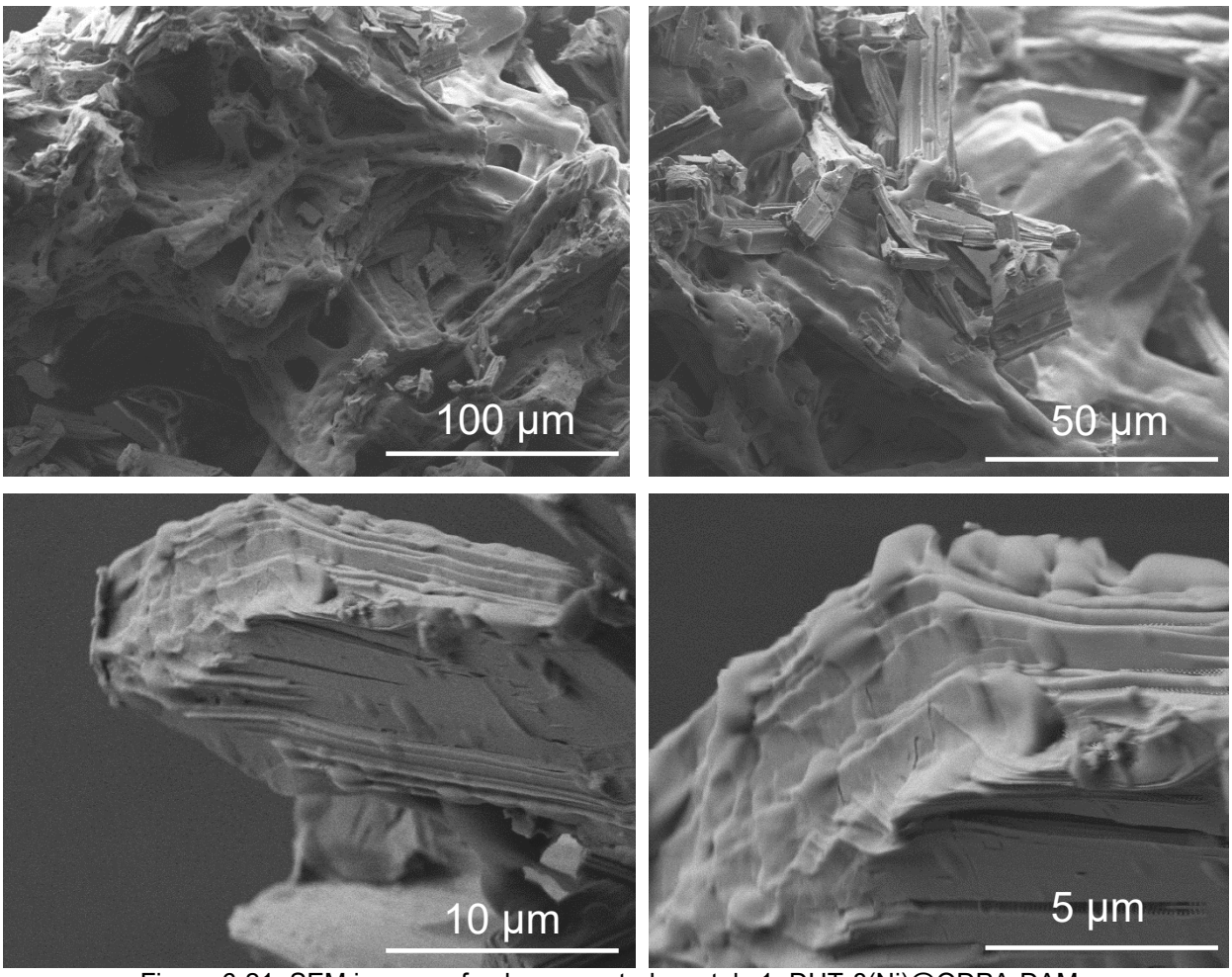

Figure 6-21. SEM images of polymer coated crystals 1_DUT-8(Ni)@ODPA-DAM.

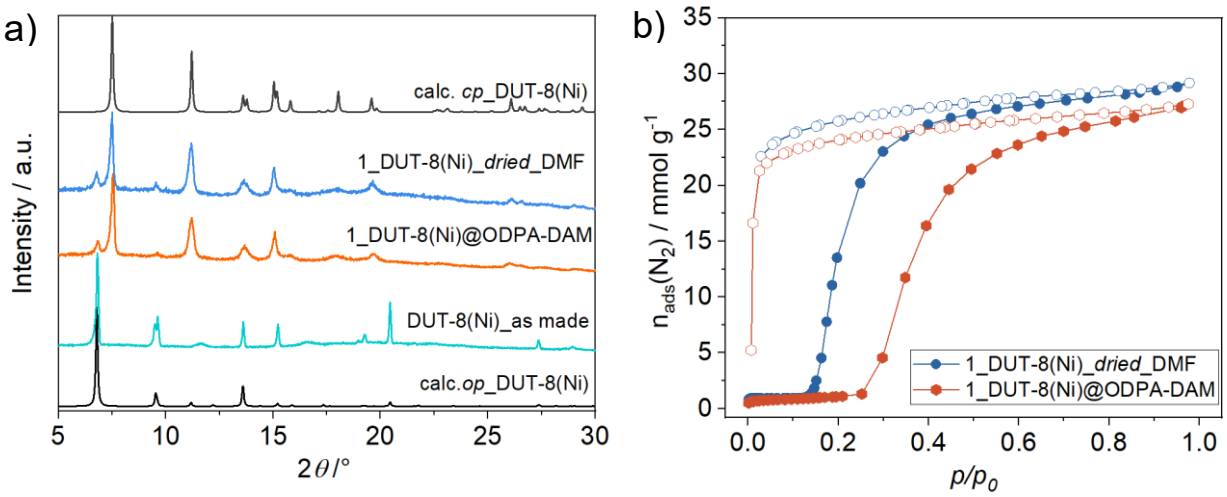

Figure 6-22. a) PXRD patterns and b) N_2 physisorption isotherms at 77 K of non-coated 1_DUT-8(Ni)_*dried*_DMF and polymer coated crystals 1_DUT-8(Ni)@ODPA-DAM dried from DMF.

Interestingly, the coating by ODPA-DAM influnces the adsortion-induced switchability of DUT-8(Ni). The significant increase of gate-opening pressure is observed in adsorption isotherm (Figure 6-22b). The increase of activation barrier for phase transition can be related to inaccessibility of pore entry (area of 001 faces) covered by polymer.

The amount of polymer loading was determined by means of TGA (Figure 8-24). The theoretical residual mass of material after TG analysis constitutes 23% (Table 6-3). The residual mass of polymer coated samples is less, therefore it is possible to estimate the polymer content.

Since the coating procedure is facilitated by presence of DMF in solution, both samples 1_DUT-8(Ni)@FDA-DAM and 1_DUT-8(Ni)@ODPA-DAM were successfully covered by polymers, reaching polymer content of 5.6% and 10.5% by mass, respectively. As expected, in sample 2_DUT-8(Ni)@FDA-DAM, the amount of polymer is not detectable.

Table 6-3. TG analysis data.

Sample	Residual Mass, %	Polymer Content, %
DUT-8(Ni) (calculated)	23	
1_DUT-8(Ni)@ODPA-DAM	20.59	10.5
1_DUT-8(Ni)@FDA-DAM	21.69	5.6
2_DUT-8(Ni)@ODPA-DAM	26.10	-

Thus, the polymer coating does not influence the phase transition from *op* to *cp* upon desolvation. However, depending on the polymer nature, the surface coating is enhanced, leading to the increase of activation barrier for adsorption induced framework opening.

6.2.3 Conclusion

The surface treatment procedures were shown to irreversibly affect the switchable behaviour. Alcohols, water and PDMS modify the surface chemistry, which leads to increase of average activation barrier for phase switching form *cp* to *op* upon adsorption of nitrogen at 77 K. The surface modification was proved by SEM images, showing the most severe surface changes caused by ethanol/water mixture. By means of XPS, it was shown that chemical composition of the surface was changed after treatment procedures. Solid-state NMR confirms the surface chemistry modification caused by ethanol, since the ^{13}C NMR spectra show the signals, which could be attributed to ethanol. Furthermore, contact angle measurements show that ethanol treatment increases the hydrophilicity of the DUT-8(Ni) surface, while PDMS deposition leads to hydrophobic surface. For CA measurements, DUT-8(Ni) powdered sample was pressed, which in turn changes the slope of gating isotherm.

The coating of surface with polyimide polymers affects adsorption properties only if the crystals are completely covered, blocking pore entry. As a result, more energy for phase transition from *cp* to *op* is needed, therefore the gate-opening pressure was observed to increase.

Thus, it was shown that surface exterior of the crystals is an important parameter influencing phase transitions in switchable DUT-8(Ni).

Chapter 7 Conclusion and Outlook

7.1 Conclusion

There are several parameters influencing switchable behaviour of DUT-8(M) system, including metal node, crystal size, the nature of the guest molecules, surface termination and desorption stress. In the context of this thesis, several key questions were addressed:

(i) What is the critical size of the anisotropic crystals influencing switchability?
(ii) Why the systematic variation of critical parameter influences switchable behaviour?
(iii) What is the possible mechanism directing the phase transition?
(iv) How does the crystal surface affect the phase transition?
(v) How does the modulation of crystal size and shape influence the structural features of DUT-8(Zn)?
(vi) How does the desolvation procedure influence switchability of DUT-8(Zn)?
(vii) How does the crystal size influence thermoresponsivity of DUT-8(Zn)?

To answer general questions (i-iv), DUT-8(Ni) was considered as a model system. The modulation approach was successfully used to modify the size and shape of DUT-8(Ni) crystals. The brick-like morphology of DUT-8(Ni) leads to two size parameters: length (size along the crystallographic *c* direction running along the pillars) and width (size along *a*–*b* crystallographic directions (plain of the layers)) to monitor size-dependent phase transition. To correlate the gate opening characteristics of the isotherms with the size and morphology of the DUT-8(Ni) crystals, the materials were analysed using scanning electron microscopy, electron diffraction, and nitrogen physisorption at 77 K. It could be explicitly seen that the crystal dimensions perpendicular to the channel-like pores influence the gate opening pressure. It indicates a higher activation barrier resulting from reduced areas of facets, exposing the pore entry to the surface. A rationale for the observations is that the pores in DUT-8(Ni) are preferably accessible from the facets perpendicular to the channels. Since the width of the crystal determines the area of those faces, the crystal width (and not the length) controls the gate-opening process. The decrease in the crystal width also results in the less steep adsorption branch in the gating region, pointing to the broadening of activation energy distribution.

Additionally to particle size and shape, the influence of crystal surface on adsorption behaviour of DUT-8(Ni) was investigated. In this regards, the surface of DUT-8(Ni) was exposed to different surface treatment procedures by ethanol, ethanol/water mixture and polymers. The surface modification was proven by SEM, NMR, XPS, and contact angle measurements. In most of the cases, surface modification leads to increase of the gate-opening pressure, reflecting the increase of activation barrier for phase switching form *cp* to *op* upon adsorption of nitrogen at 77 K. The surface treatment procedures were shown to irreversibly affect the switchable behaviour, since the reactivation procedures do not lead to the recovery of the initial adsorption behaviour.

Concerning DUT-8(Zn) (v-vii), it was shown that the properties of compound significantly depend on crystal size. The critical particle size suppressing switchability depends on the stiffness of the deforming building blocks, in case of DUT-8(M), electronic structure of the metal in the paddle wheel hinges. For DUT-8(Zn), the smaller strain energy (+78 kJ mol^{-1}) of the node results in a significantly higher energy difference between the empty *op* and *cp* frameworks ($\Delta E = E_{op} - E_{cp}$), as compared to DUT-8(Ni) (-86 kJ mol^{-1}), resulting in a smaller critical particle size (higher surface energy) required to suppress switchability. This was demonstrated by studying particles of three size regimes: 160 µm (macro-sized), 0.5 µm (micron-sized) and smaller than 0.1 µm (submicron-sized).

Crystallites of different size regimes behave also differently upon removal of the guest molecules. Removal of dichloromethane in vacuum at elevated temperature causes high desorption stress favouring the formation of thermodynamically stable phases as the phase transition to the closed pore phase is observed for macro- and micron-sized particles, whereas only for submicron-sized particles a mixture of *cp*/*op* phases was obtained. The application of mild supercritical drying enables the formation of the metastable op phases: the macro-sized particles show a phase mixture of *op* and *cp* phases, whereas the micron and submicron sized particles remain in the metastable open pore phase. The dense *cp* phase of DUT-8(Zn) shows no adsorption-induced pore opening for N_2 at 77 K and CO_2 at 195 K. The higher interaction energies of chloromethane at 249 K and dichloromethane at 298 K allow reopening of the macro-sized crystals upon adsorption, but not the smaller particles. This could indicate an intermediate particle size regime, in which the crystals close as monodomain crystals,

without twinning, hence the lack of defects may be responsible for the barrier to reopen the structure.[18, 145]

Crystal downsizing enhances the responsivity of DUT-8(Zn) towards polar and non-polar molecules, which was revealed by liquid phase adsorption. Among investigated guest molecules, the alcohols induced so called shape-memory effect in micron-sized crystals. The adsorption of alcohols stimulates phase transition from *cp* to *op* which is maintained even after desorption. The framework rigidification is caused by chemical host-guest interactions leading to surface deformation and possible nanodomain formation.

It was shown that DUT-8(Zn) responsivity is significantly tailored by particle size, which in turn influenced the selective adsorption behaviour. By means of NMR, selective adsorption of DCM over 1-PrOH was revealed in micron-sized crystals, which was not the case for macro-sized crystals. Thus, crystal size engineering provides an opportunity not only to control the structural dynamics of MOFs, but also to enhance the responsivity towards guest molecules with specific features and to influence selectivity.

Moreover, thermoresponsive behaviour of DUT-8(Zn) was investigated by VT-PXRD. It was revealed that irrespective of particle size DUT-8(Zn)_*cp* undergoes contraction upon heating, pointing on possible negative thermal expansion. However, submicron-sized DUT-8(Zn)_*op* loses the crystallinity in the course of heating.

7.2 Outlook

The important parameters influencing switchablity of DUT-8(Ni) and DUT-8(Zn) were investigated in this work. However, several new questions were raised relating particularly to DUT-8(Zn) selectivity and thermoresponsivity, which can be addressed in the future.

The specific host-guest interactions in DUT-8(Zn), which are tailored by particle size, contribute to the selective molecular recognition properties. However, for the development of application pathway, it is necessary to get the deep insight into mechanism of recognition phenomena which could be associated with external surface composition of differently-sized crystals.

In case of DUT-8(Ni), further investigation of surface composition is needed for deep understanding of the external surface contribution into the interplay of relevant parameters for tuning the material functions.

Chapter 8 Appendix

Table 8-1. Synthesis conditions for DUT-8(Ni) samples. Chapter 3.

Sample name	Compound	Amount, g	Solvent	Modulator	Conditions
A	$Ni(NO_3)_2*6H_2O$ H_2ndc DABCO	0.407 0.303 0.100	6 ml DMF 15 ml DMF 9 ml MeOH		Static synthesis in autoclave, 393 K, 48 h
B	$Ni(NO_3)_2*6H_2O$ H_2ndc DABCO	0.407 0.303 0.100	6 ml DMF 15 ml DMF 9 ml MeOH		Rotation of autoclave, 393 K, 48 h
C	$Ni(NO_3)_2*6H_2O$ H_2ndc DABCO	0.407 0.303 0.100	6 ml DMF 15 ml DMF 9 ml MeOH		Microwave irradiation 150 W, 30 s
D	$Ni(NO_3)_2*6H_2O$ H_2ndc DABCO	0.145 0.096 0.112	1.5 ml DMF 7 ml DMF 1.5 ml DMF	0.05 ml Pyridine	Static synthesis in autoclave, 393 K, 24 h
E	$Ni(NO_3)_2*6H_2O$ H_2ndc DABCO	0.145 0.096 0.112	1.5 ml DMF 7 ml DMF 1.5 ml DMF	0.05 ml Pyridine 0.05 ml Acetic acid	Static synthesis in autoclave, 393 K, 24 h
PAA_1	$Ni(NO_3)_2*6H_2O$ H_2ndc DABCO	0.204 0.152 0.050	3 ml DMF 7.5 ml DMF 4.5 ml MeOH	0.001 g PAA	Static synthesis in autoclave, 393 K, 48 h
PAA_2	$Ni(NO_3)_2*6H_2O$ H_2ndc DABCO	0.204 0.152 0.050	3 ml DMF 7.5 ml DMF 4.5 ml MeOH	0.005 g PAA	Static synthesis in autoclave, 393 K, 48 h
PAA_3	$Ni(NO_3)_2*6H_2O$ H_2ndc DABCO	0.204 0.152 0.050	3 ml DMF 7.5 ml DMF 4.5 ml MeOH	0.010 g PAA	Static synthesis in autoclave, 393 K, 48 h

Table 8-2. Synthesis conditions for DUT-8(Zn) samples. Chapter 3.

Sample name	Compound	Amount, g	Solvent	Modulator	Conditions
DUT-8(Zn)_160 μm	$Zn(NO_3)_2*6H_2O$ H_2ndc DABCO	0.312 0.227 0.070	5 ml DMF 20 ml DMF 5 ml DMF		Static synthesis in autoclave, 393 K, 48 h
DUT-8(Zn)_0.5 μm	$Zn(NO_3)_2*6H_2O$ H_2ndc DABCO	0.446 0.296 0.336	5 ml DMF 20 ml DMF 5 ml DMF		Ultrasound-assisted synthesis, 60 min
DUT-8(Zn)_0.1 μm	$Zn(NO_3)_2*6H_2O$ H_2ndc DABCO	0.446 0.296 0.504	5 ml DMF 20 ml DMF 5 ml DMF		Ultrasound-assisted synthesis, 353 K, 30 min
Cubes of DUT-8(Zn)_1.8 μm	$Zn(CH_3CO_2)_2*2H_2O$ H_2ndc DABCO	0.120 0.086 0.22	18 ml DMF 12 ml DMF	0.5 ml Pyridine 0.5 ml Acetic acid	Static synthesis in autoclave, 373 K, 24 h
Rods of DUT-8(Zn)_1.4 μm	$Zn(CH_3CO_2)_2*2H_2O$ H_2ndc DABCO	0.120 0.086 0.22	18 ml DMF 12 ml DMF	0.5 ml Acetic acid	Static synthesis in autoclave, 373 K, 24 h
Plates of DUT-8(Zn)_1 μm	$Zn(CH_3CO_2)_2*2H_2O$ H_2ndc DABCO	0.120 0.086 0.22	18 ml DMF 12 ml DMF	0.5 ml Pyridine	Static synthesis in autoclave, 373 K, 24 h

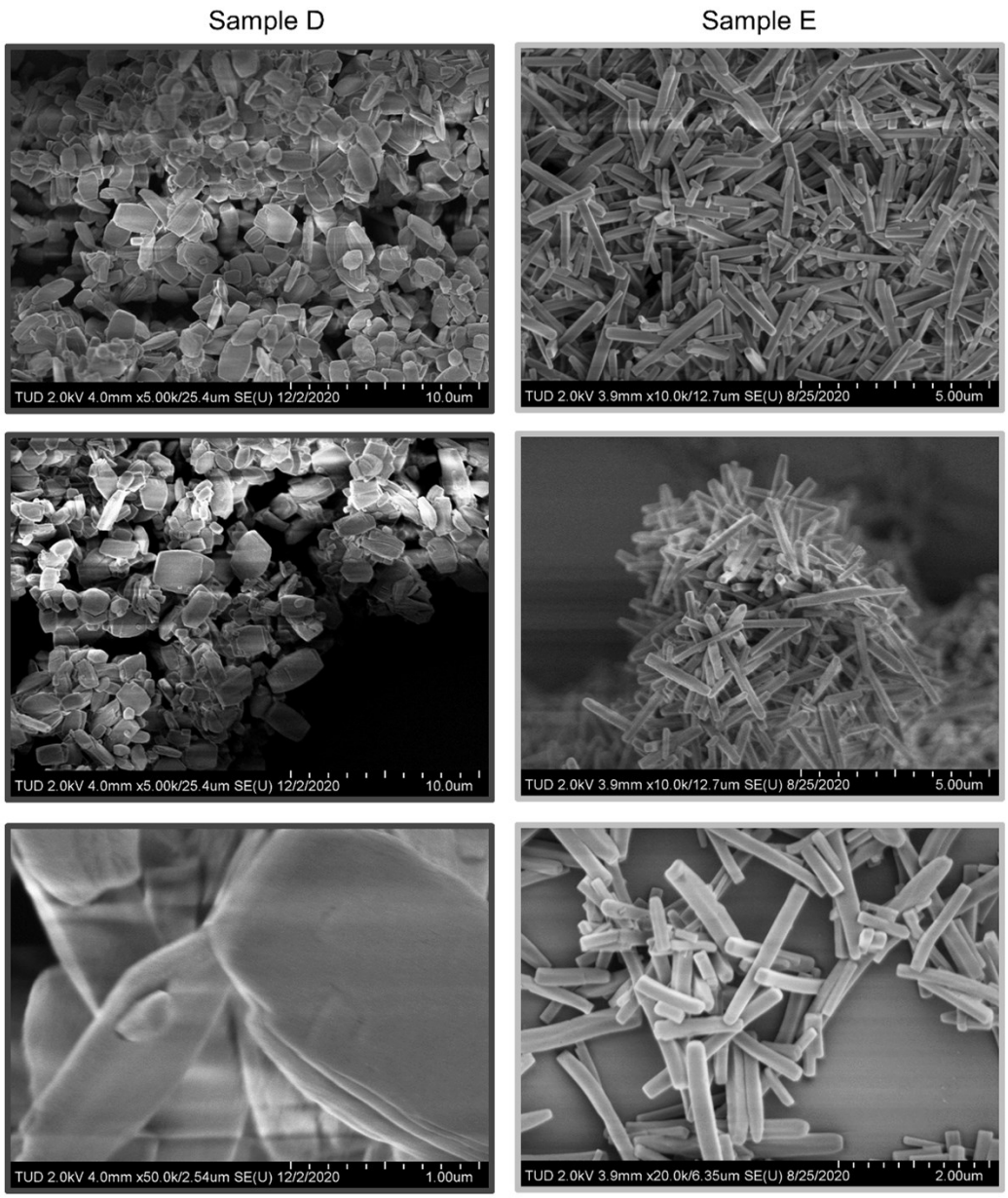

Figure 8-1. SEM images of sample **D** and sample **E**. Chapter 4.

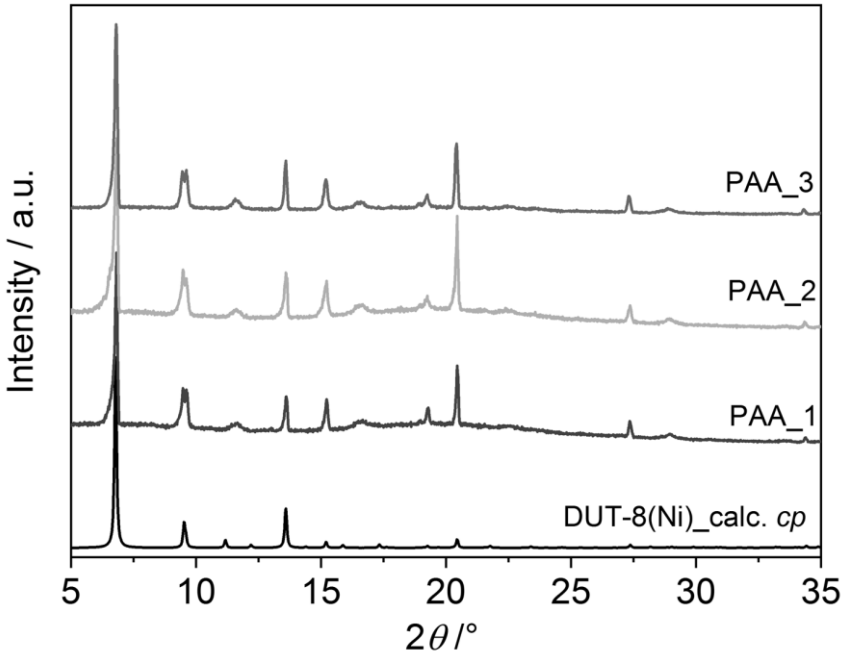

Figure 8-2. PXRD patterns of the investigated as made DUT-8(Ni) samples. Chapter 4.

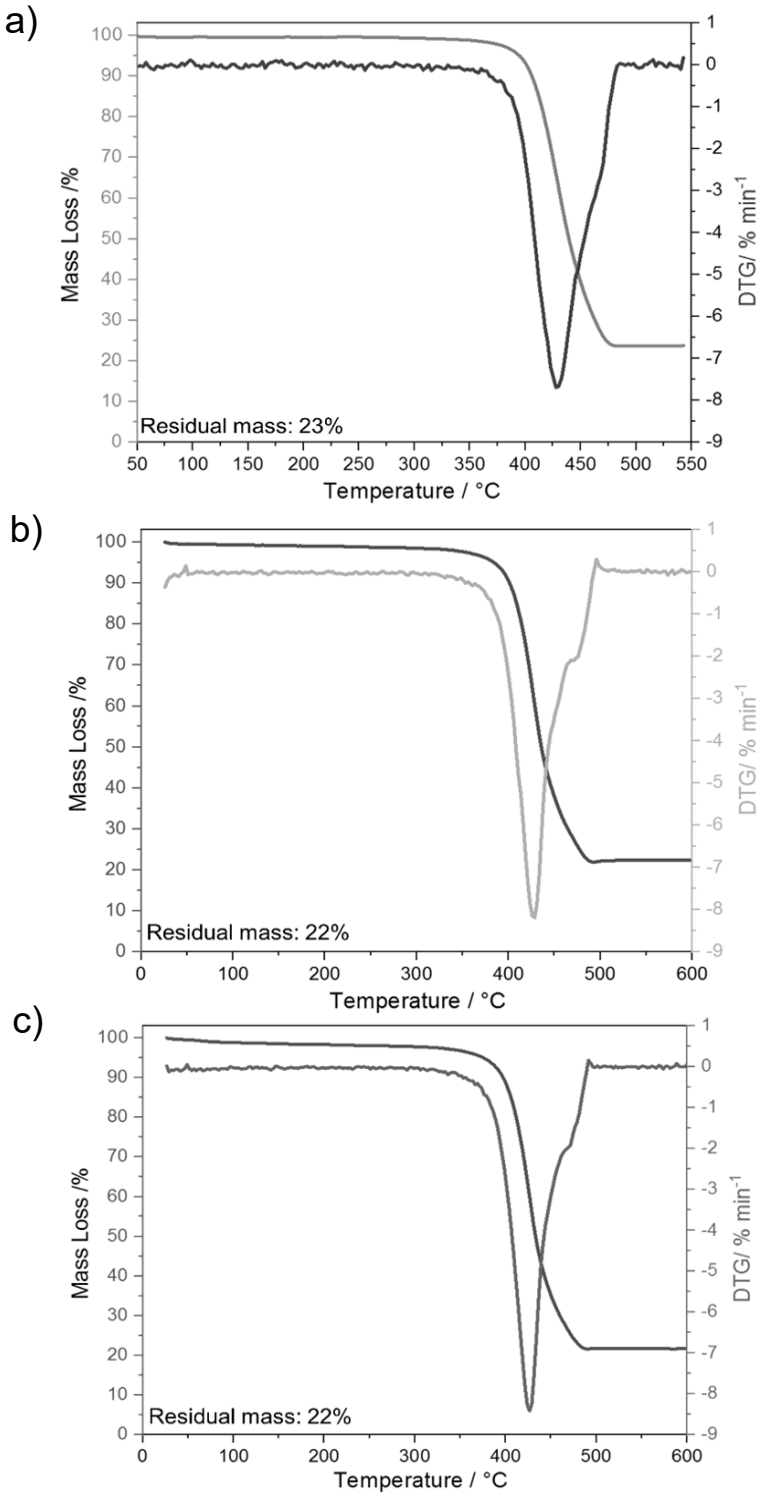

Figure 8-3. TGA of sample: a) PAA_1; b) PAA_2; c) PAA_3. The expected residual mass is 23%. Chapter 4.

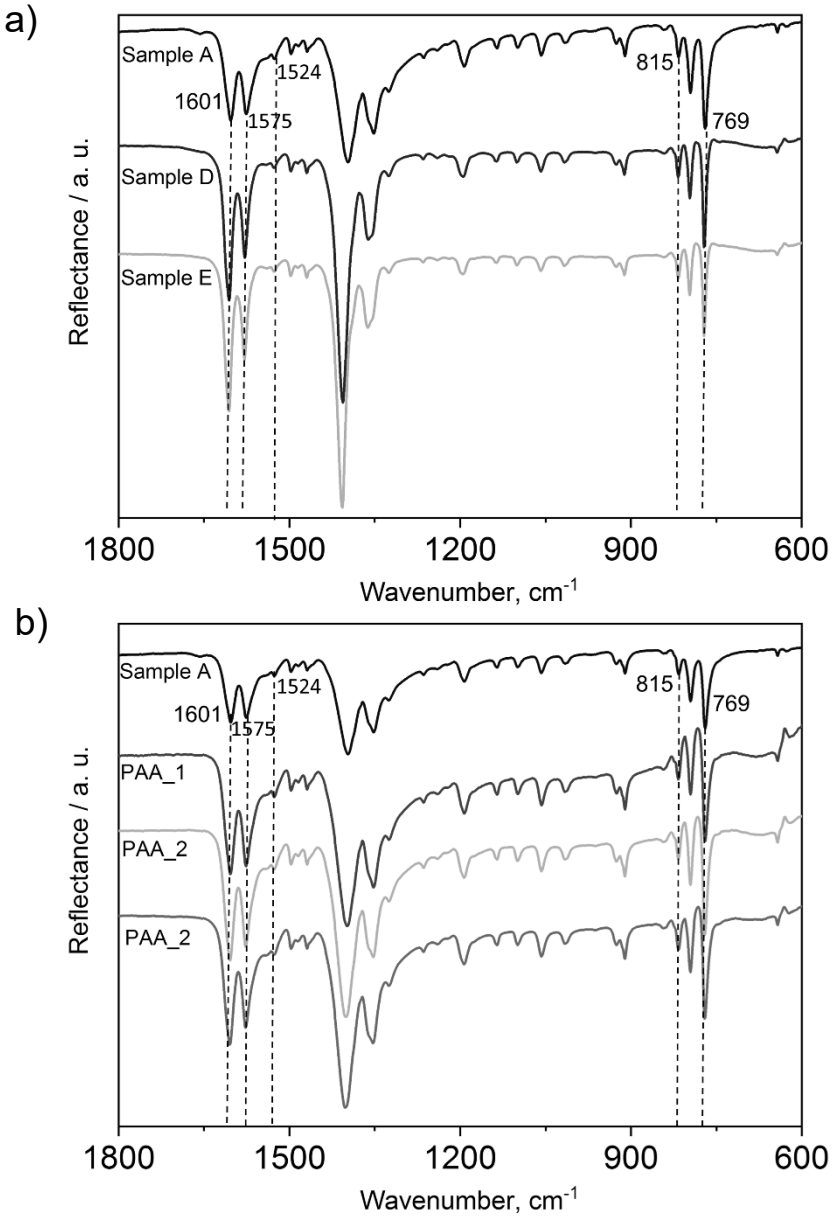

Figure 8-4. IR spectra of: a) samples D and E modulated by pyridine and acetic acid/pyridine; b) samples PAA_1, PAA_2, PAA_3 modulated by polyacrylic acid, in comparison to non-modulated sample A. Chapter 4.

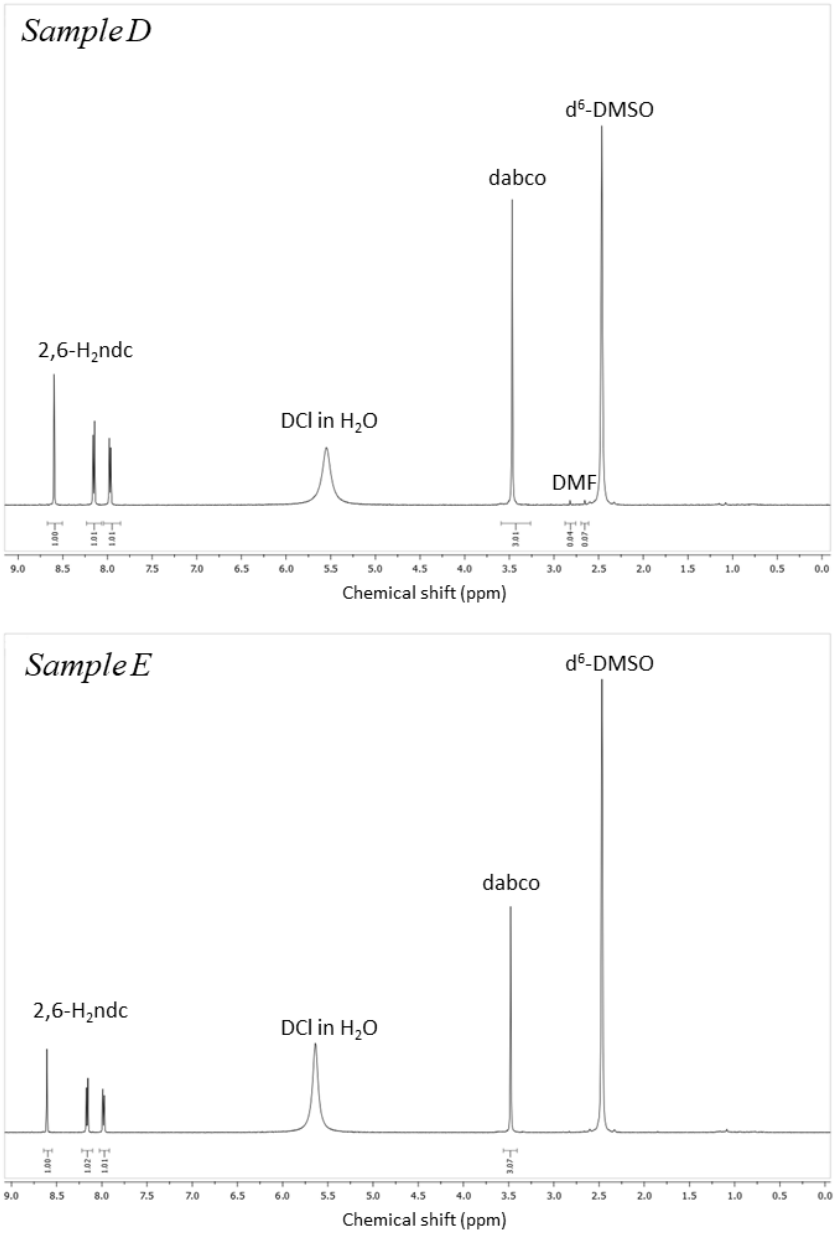

Figure 8-5. ^{1}H NMR spectra of samples D and E modulated by pyridine and acetic acid/pyridine, respectively. Chapter 4.

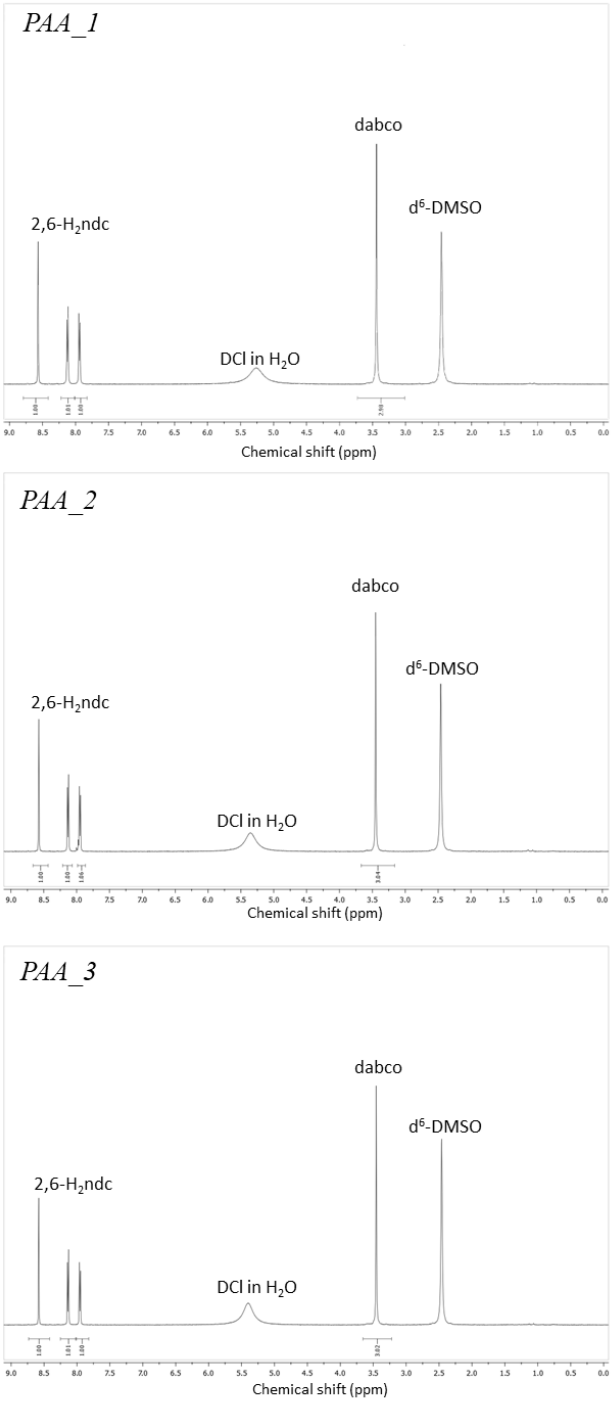

Figure 8-5. ^{1}H NMR spectra of samples PAA_1, PAA_2, PAA_3 modulated by polyacrylic acid. Chapter 4.

Table 8-3. Bond lengths and angles in DUT-8(M) (M = Ni, Co, Zn) (crystallographic data). Chapter 5.

	M—O / Å	**M—N / Å**	**M…M / Å**	**M-M-N angle / °**
M = Ni				
$Ni_2(bdc)_2dabco$[117]	1.966(1)	2.053(1)	2.683(8)	180.0
DUT-8(Ni)_*op*[16]	1.983(7) - 2.008(7)	2.042(1)	2.653(5)	177.59(9)
DUT-8(Ni)_*cp*[16]	1.787(5) - 2.425(2)	1.905(8) 2.085(6)	2.735(9)	153.92(5)
M = Co				
$Co_2(bdc)_2dabco$[240]	2.028(2)	2.092(5)	2.683(5)	180.0
DUT-8(Co)_*op*[16]	2.027(3) - 2.031(3)	2.110(7)	2.691(2)	171.81(8)
DUT-8(Co)_*cp*[16]	1.70(9) -2.20(7)	2.15(9) 2.13(9)	2.636(3)	141.50(0)
M = Zn				
$Zn_2(bdc)_2dabco$[90]	2.0314(2)	2.0440(4)	2.9521(9)	180.0
DUT-8(Zn)_*op*	2.029(4) 2.034(4)	2.076(7)	2.962(8)	178.26(15)
DUT-8(Zn)_*cp*	1.638(2) - 2.548(6)	2.293 2.098	3.804	112.02(3) 117.31(4)

Table 8-4. The yield of DUT-8(Zn) samples. Chapter 5.

Sample	Sample weight, mg	Yield (based on Zn^{2+}), %
DUT-8(Zn)_160 µm_*cp*	220 mg	62
DUT-8(Zn)_0.5 µm_*cp*	295 mg	58
DUT-8(Zn)_0.1 µm_*op*	350 mg	69

Table 8-5. Elemental analysis of DUT-8(Zn) samples. Chapter 5.

Sample	Elements	C, %	N, %	H, %
	calc.	52.325	3.779	4.069
DUT-8(Zn)_160 µm_*cp*	found	52.84	3.89	4.15
DUT-8(Zn)_0.5 µm_*cp*	found	52.92	3.45	4.06
DUT-8(Zn)_0.1 µm_*op*	found	49.63	4.21	3.95

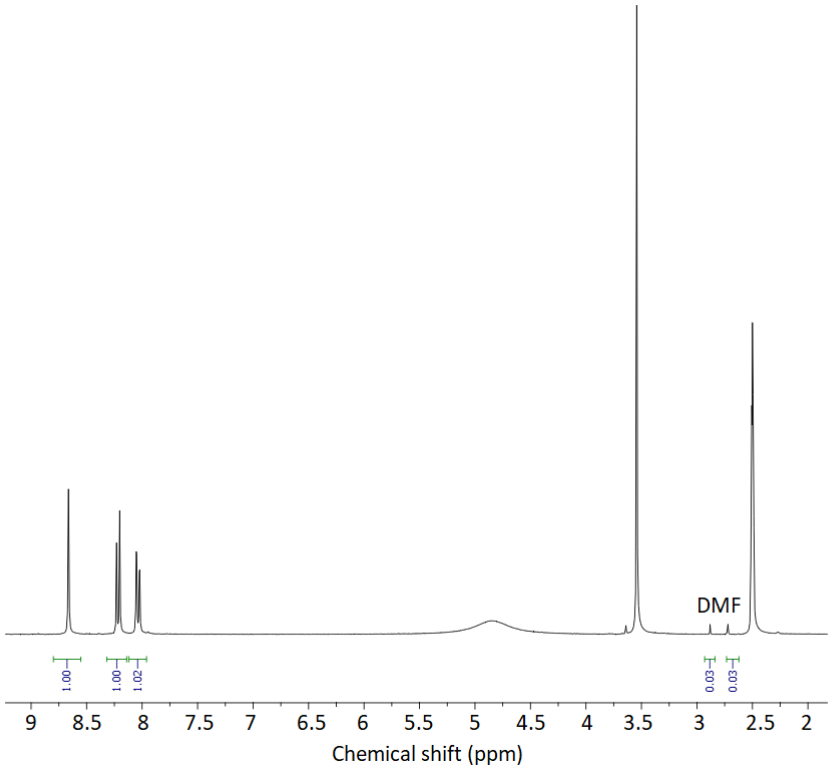

Figure 8-6. ^{1}H NMR spectra of sample DUT-8(Zn)_160 µm_DMF digested in DCl/D_2O d^6-DMSO. Chapter 5.

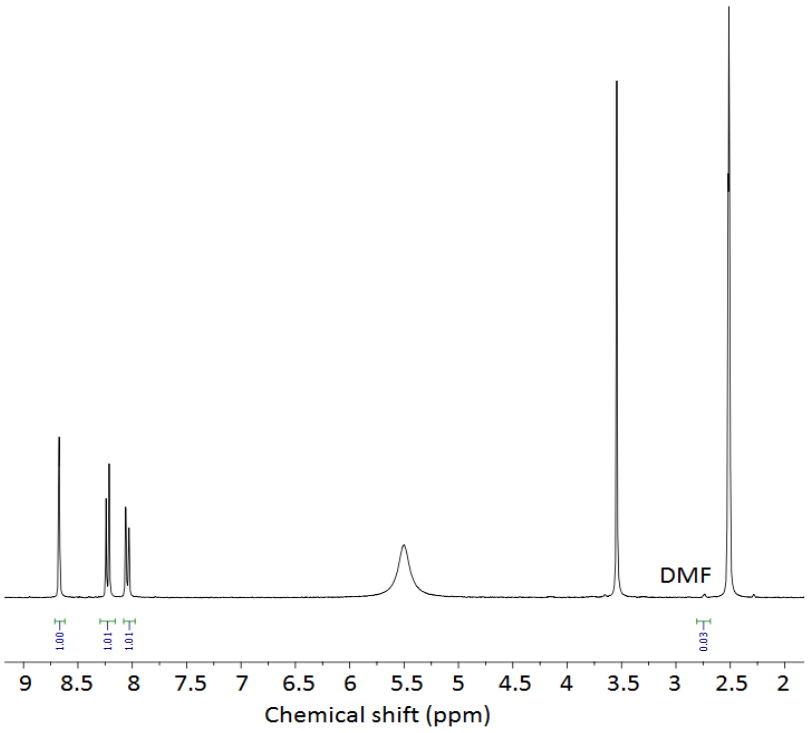

Figure 8-6. ^{1}H NMR spectra of sample DUT-8(Zn)_0.5 µm_DMF digested in DCl/D_2O d^6-DMSO. Chapter 5.

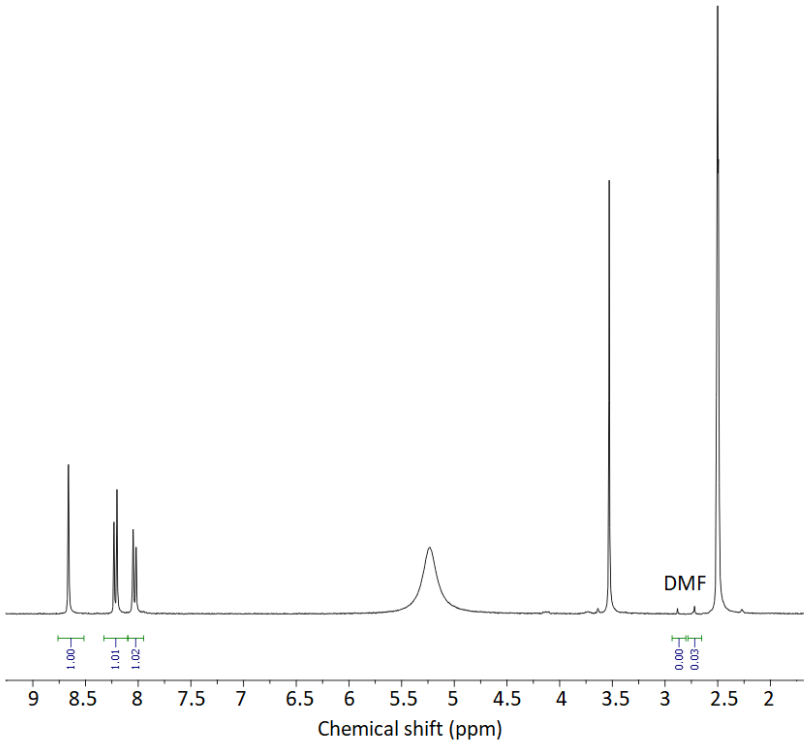

Figure 8-6. ^{1}H NMR spectra of sample DUT-8(Zn)_0.1 µm_DMF digested in DCl/D_2O d^6-DMSO. Chapter 5

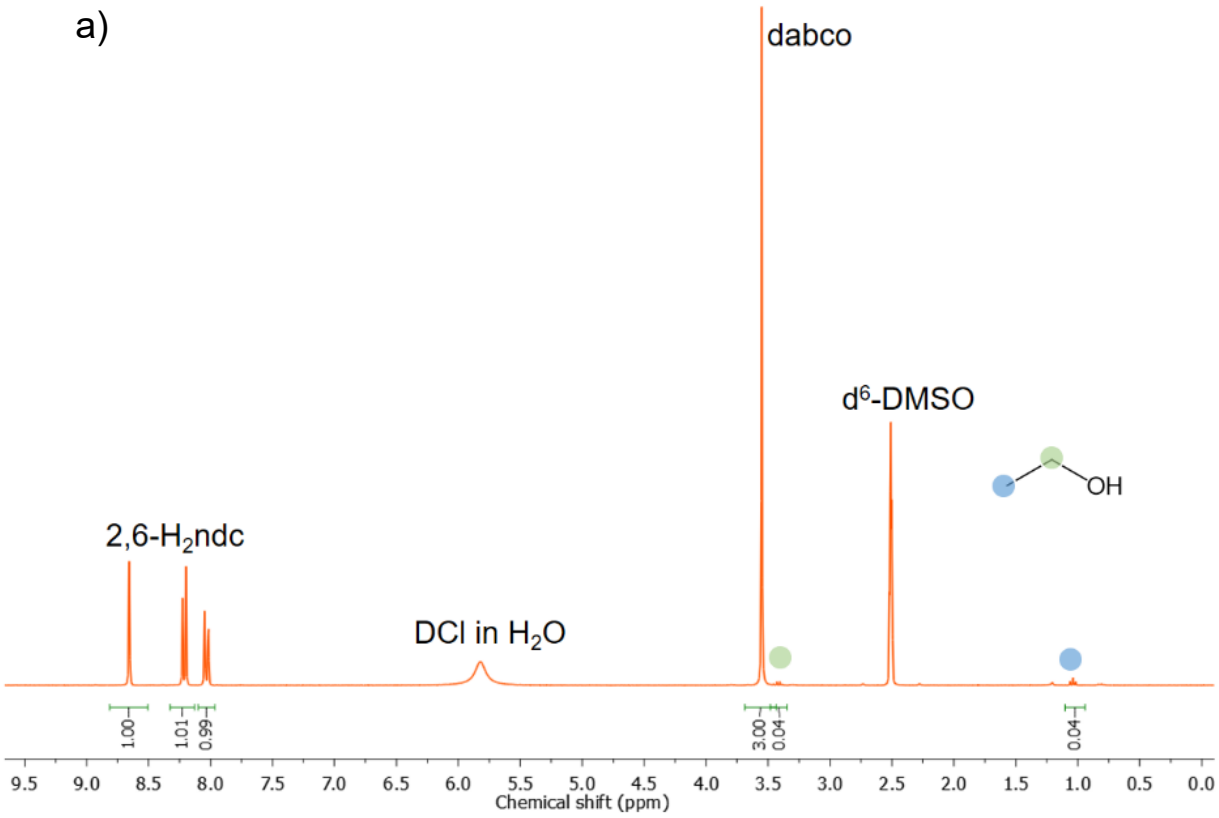
a)
dabco
d6-DMSO
OH
2,6-H2ndc
DCl in H2O
1.00
1.01
0.99
3.00
0.04
0.04
9.5 9.0 8.5 8.0 7.5 7.0 6.5 6.0 5.5 5.0 4.5 4.0 3.5 3.0 2.5 2.0 1.5 1.0 0.5 0.0
Chemical shift (ppm)

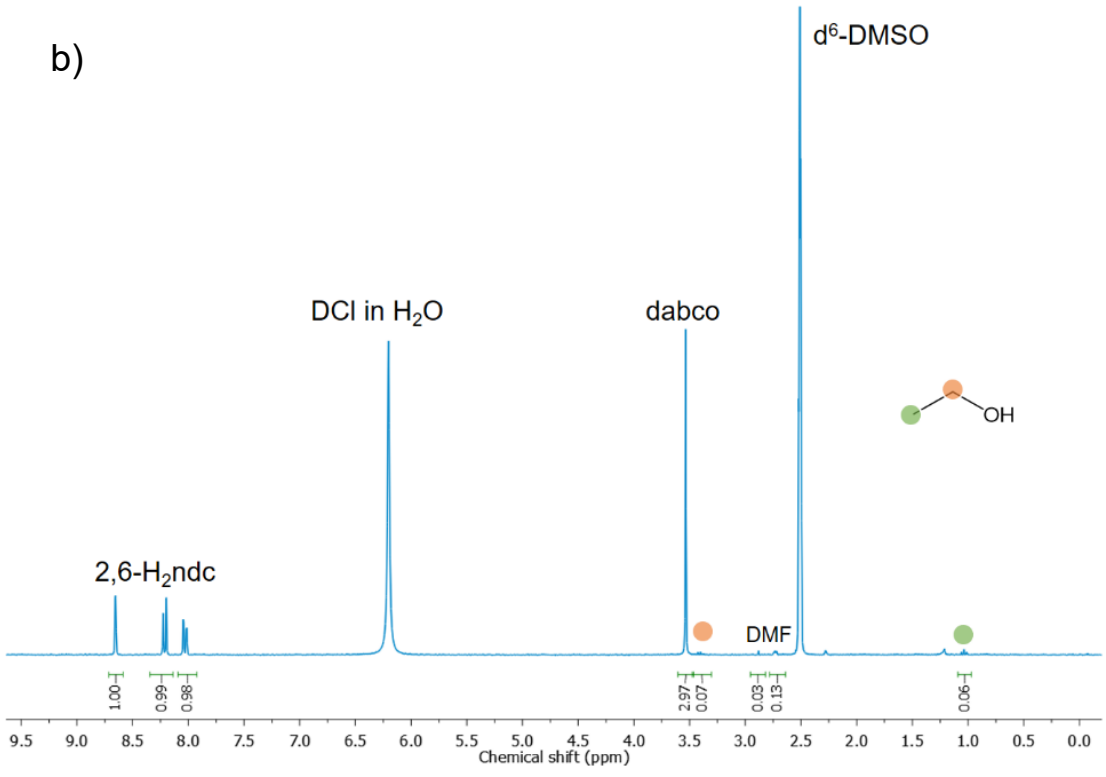
b)
d6-DMSO
DCl in H2O
dabco
OH
2,6-H2ndc
DMF
1.00
0.99
0.98
2.97
0.07
0.03
0.13
0.06
9.5 9.0 8.5 8.0 7.5 7.0 6.5 6.0 5.5 5.0 4.5 4.0 3.5 3.0 2.5 2.0 1.5 1.0 0.5 0.0
Chemical shift (ppm)

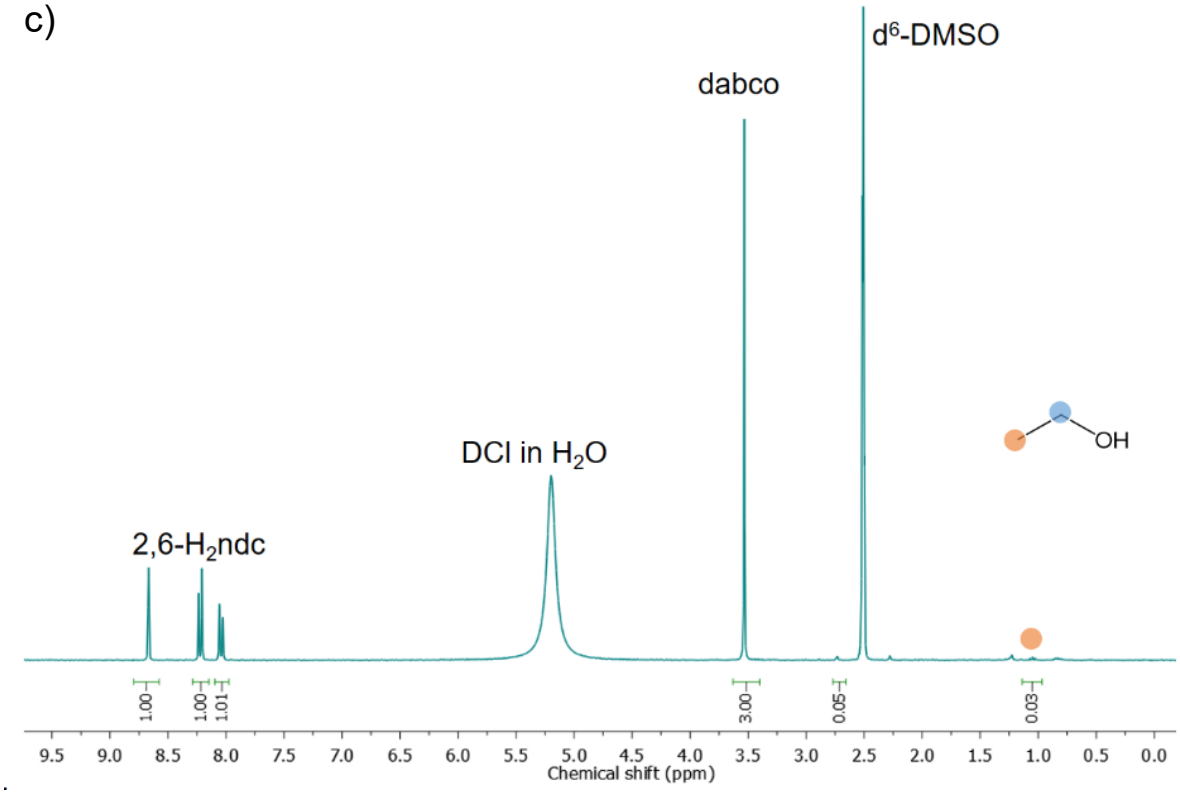

Figure 8-8-1. ^{1}H NMR spectra of a) macro-sized crystals DUT-8(Zn)_160_EtOH_SCD, b) micron-sized DUT-8(Zn)_0.5_EtOH_SCD, c) DUT-8(Zn)_0.1_EtOH_SCD digested in DCl/D_2O d^6-DMSO. Chapter 5.

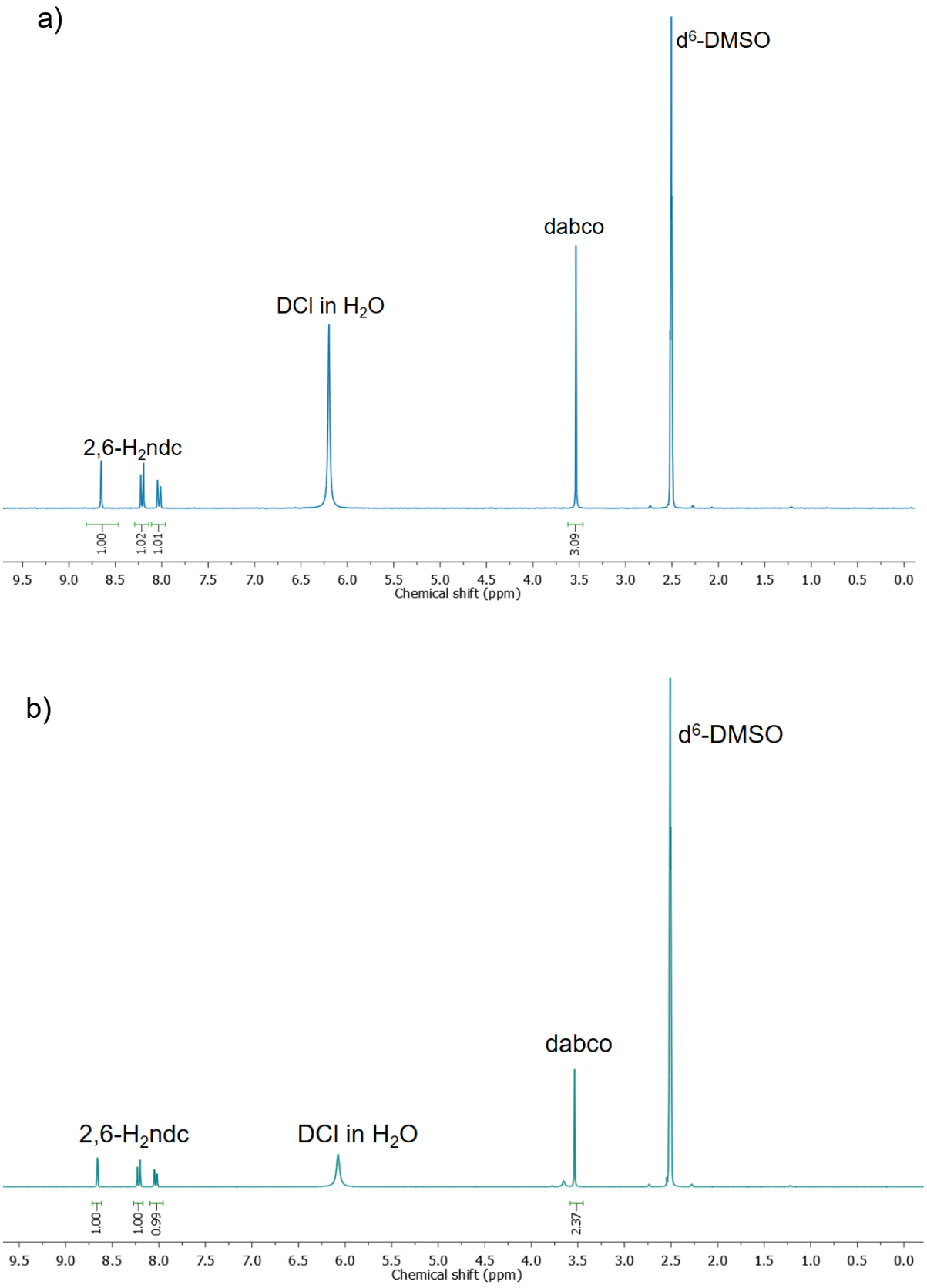

Figure 8-8-2. ^{1}H NMR spectra of a) micron-sized crystals DUT-8(Zn)_0.5_acetone_SCD, c) submicron-sized crystals DUT-8(Zn)_0.1_acetone_SCD digested in DCl/D_2O d^6-DMSO. Chapter 5.

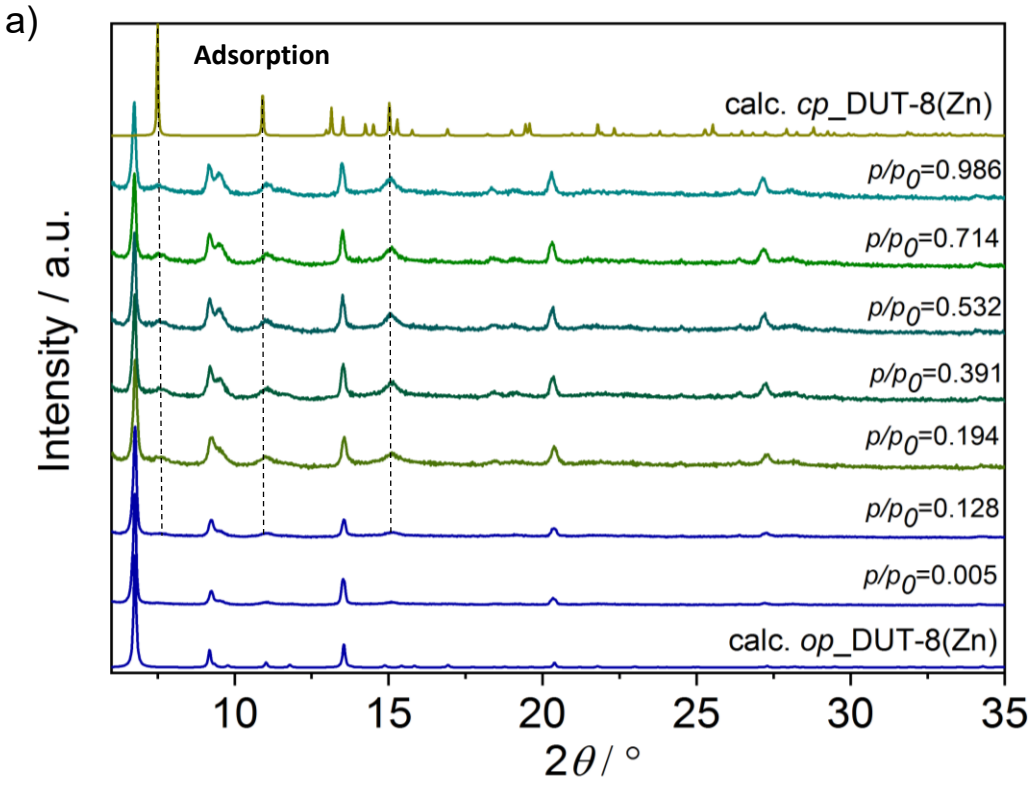
a)
Adsorption
calc. cp_DUT-8(Zn)
p/p0=0.986
p/p0=0.714
p/p0=0.532
p/p0=0.391
p/p0=0.194
p/p0=0.128
p/p0=0.005
calc. op_DUT-8(Zn)
Intensity / a.u.
10
15
20
25
30
35
2θ / °

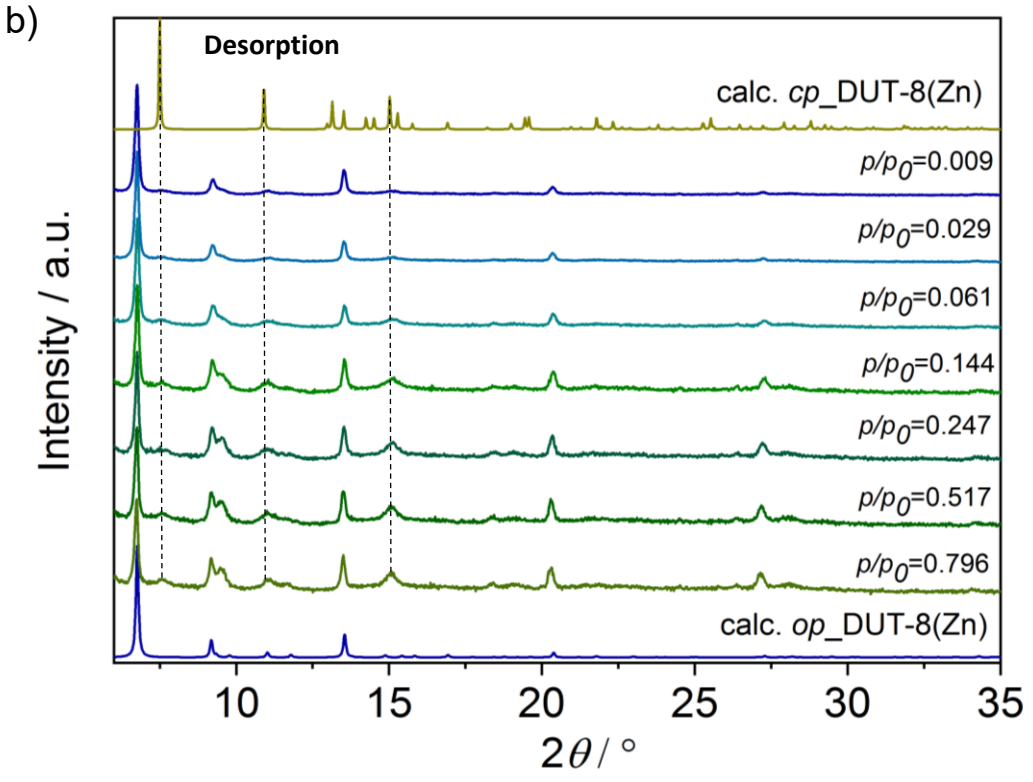
b)
Desorption
calc. cp_DUT-8(Zn)
p/p0=0.009
p/p0=0.029
p/p0=0.061
p/p0=0.144
p/p0=0.247
p/p0=0.517
p/p0=0.796
calc. op_DUT-8(Zn)
Intensity / a.u.
10
15
20
25
30
35
2θ / °

c)

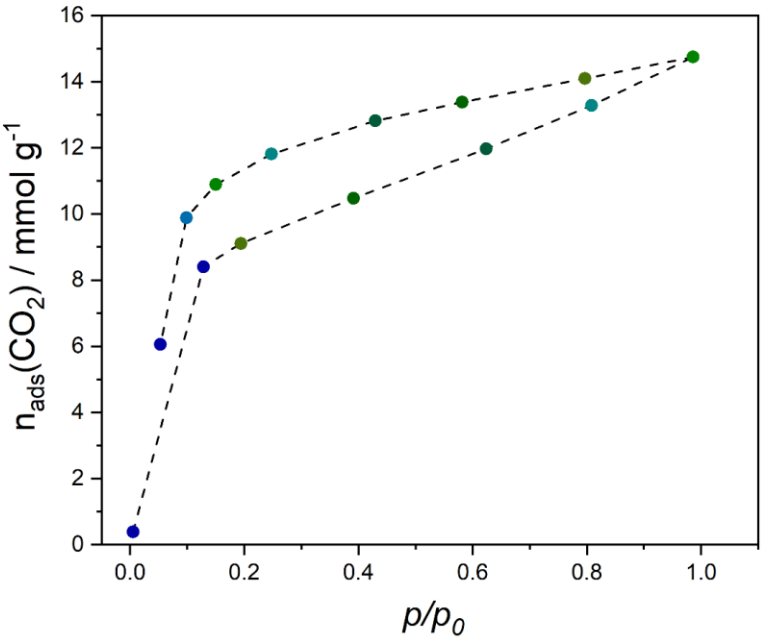

Figure 8-8-3. PXRD patterns collected during *in situ* CO_2 adsorption (a) and desorption (b) at 195 K on submicron-sized sample DUT-8(Zn)_0.1 µm_*op*; c) corresponding in situ physisorption isotherm. Chapter 5.

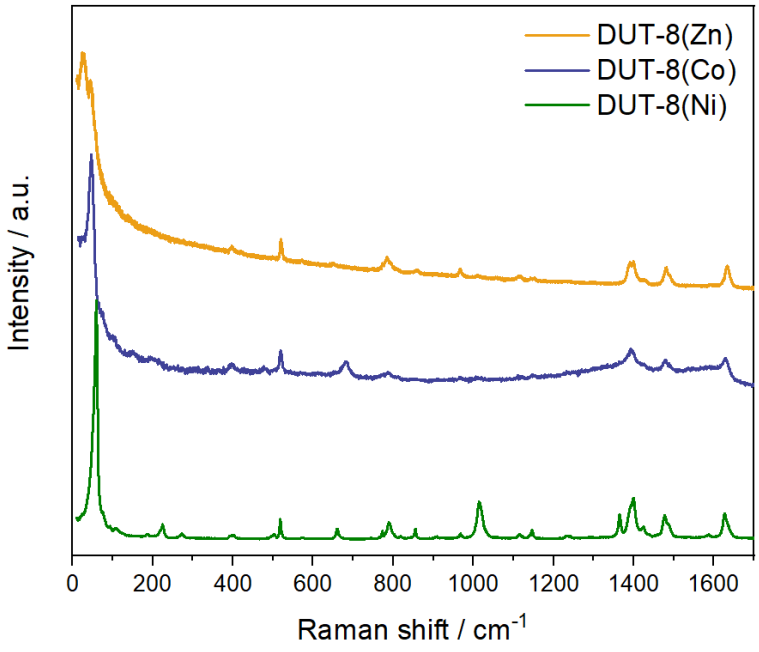

Figure 8-9. Full Raman spectra of macro-sized crystals DUT-8(Zn)_160 µm_*cp* in comparison with DUT-8(Ni) and DUT-8(Co). Chapter 5.

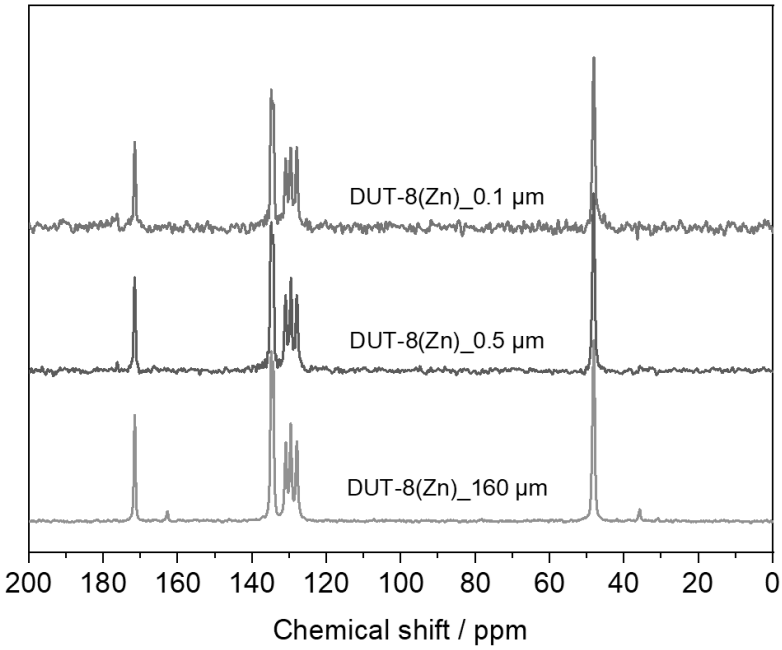

Figure 8-10. ^{13}C CP MAS NMR spectra of DUT-8(Zn)_*op* samples solvated in DMF. Chapter 5.

a)

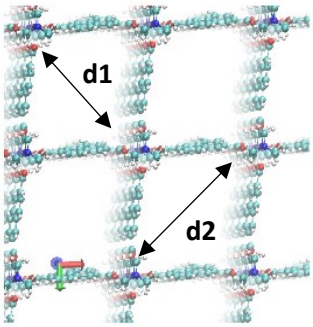

initial *op* phase

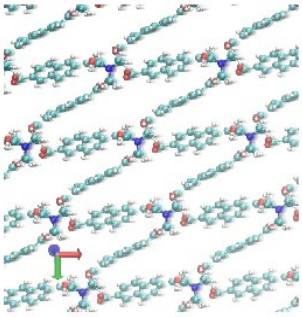

intermediate phase after 1 ps

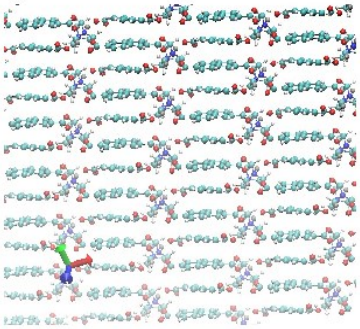

cp phase after 5.5 ps MD simulation

b)

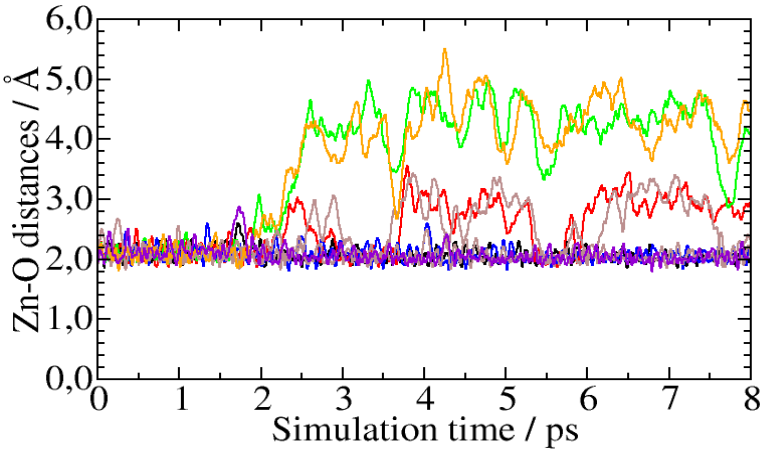

c)

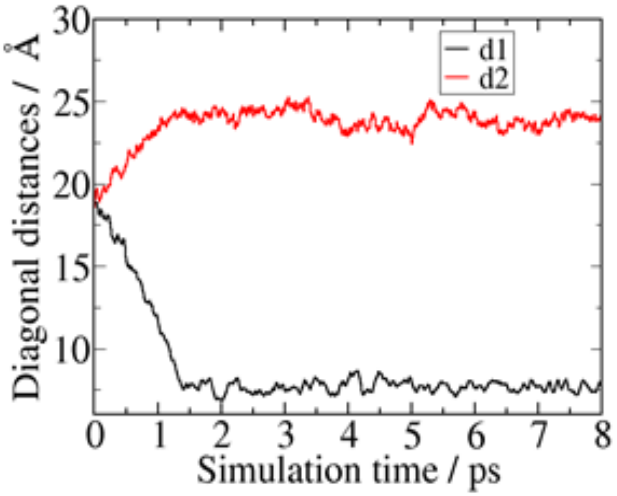

Figure 8-11. a) Snapshots from the *ab initio* MD (NPT) simulation at 300 K and 1 atm of DUT-8(Zn) starting from minimized *op* phase; b) changes in the Zn - O distances in the paddle wheel during the MD simulation, different colors represent each separate Zn - O distance in the paddle wheel; c) change in the diagonal distances of the square pore in the DUT-8(Zn) during the *op* - *cp* transformation in the MD simulation, when d1 = d2 the pore of the MOF is open , when d1 << d2 the pore is closed.
Chapter 5.

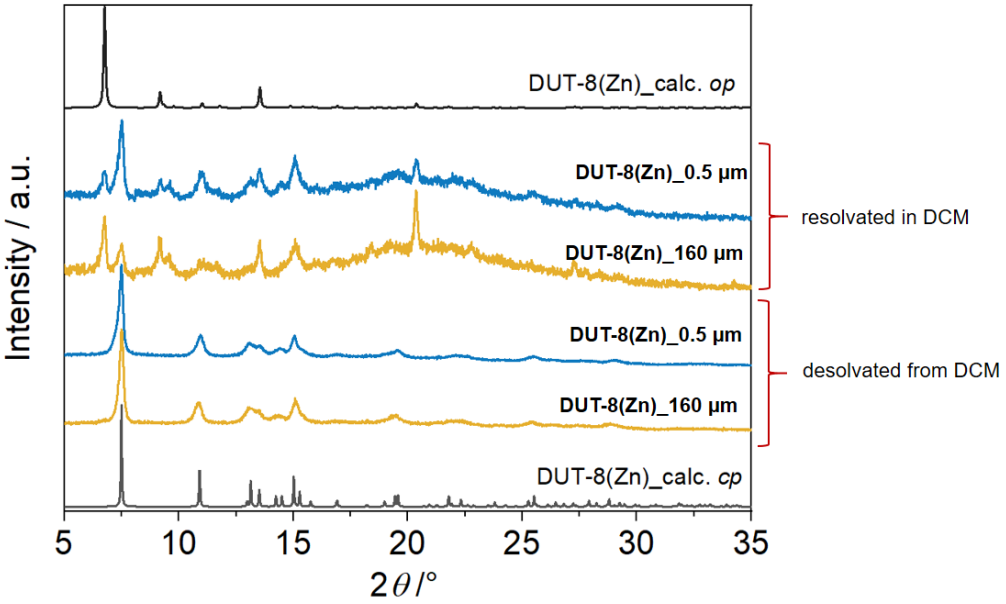

Figure 8-12. PXRD patterns of DUT-8(Zn)_160 µm and DUT-8(Zn)_0.5 µm resolvated in DCM. Chapter 5.

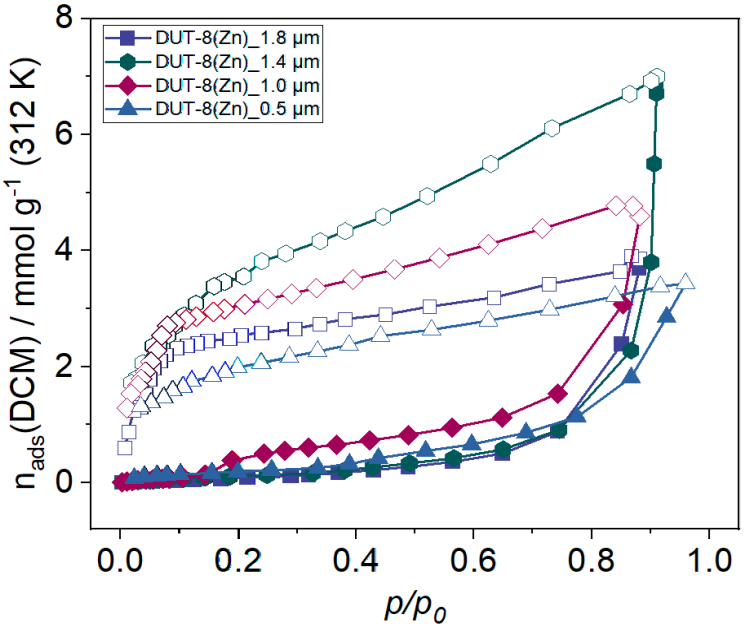

Figure 8-13. Vapor adsorption of dichloromethane at 312 K. Chapter 5.

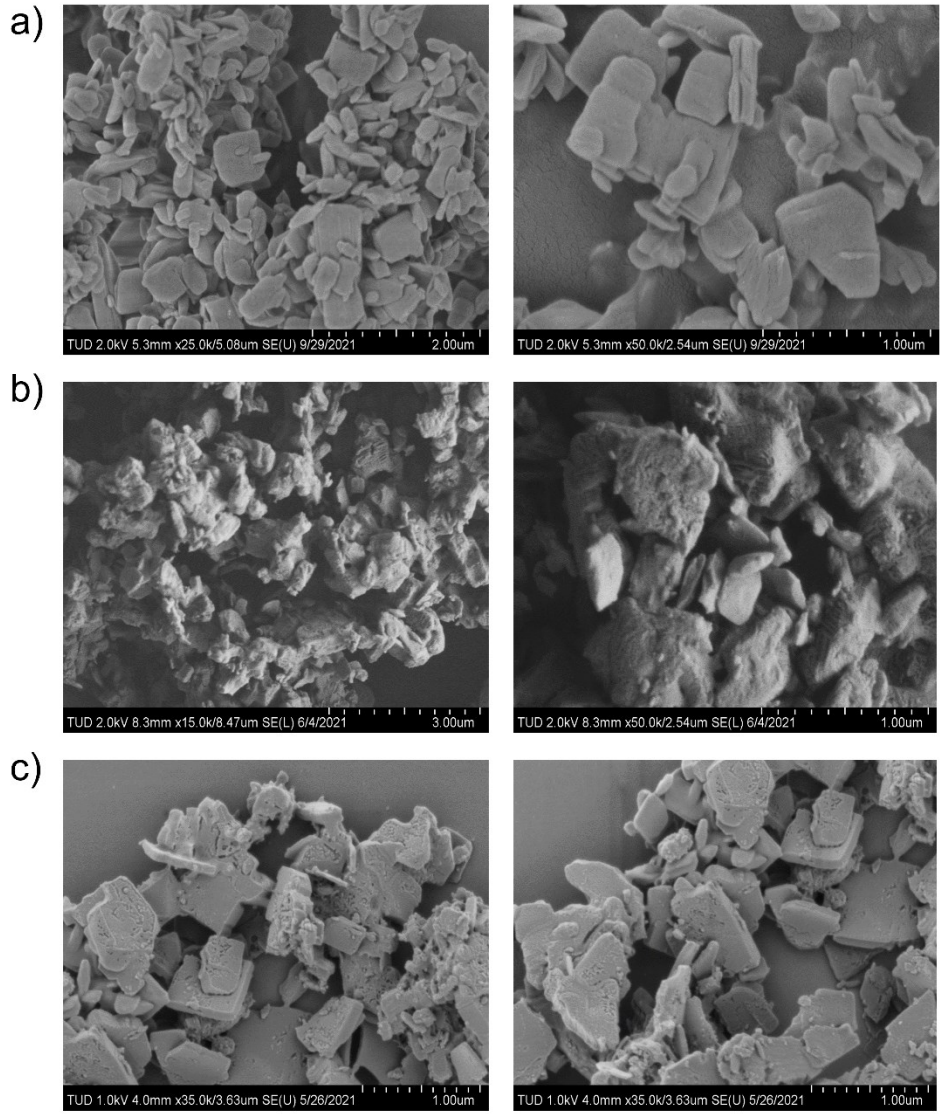

Figure 8-14. SEM images of micron-sized crystals DUT-8(Zn)_0.5 μm a) before adsorption, b) after EtOH adsorption (1 cycle), c) resolvated in EtOH. Chapter 5.

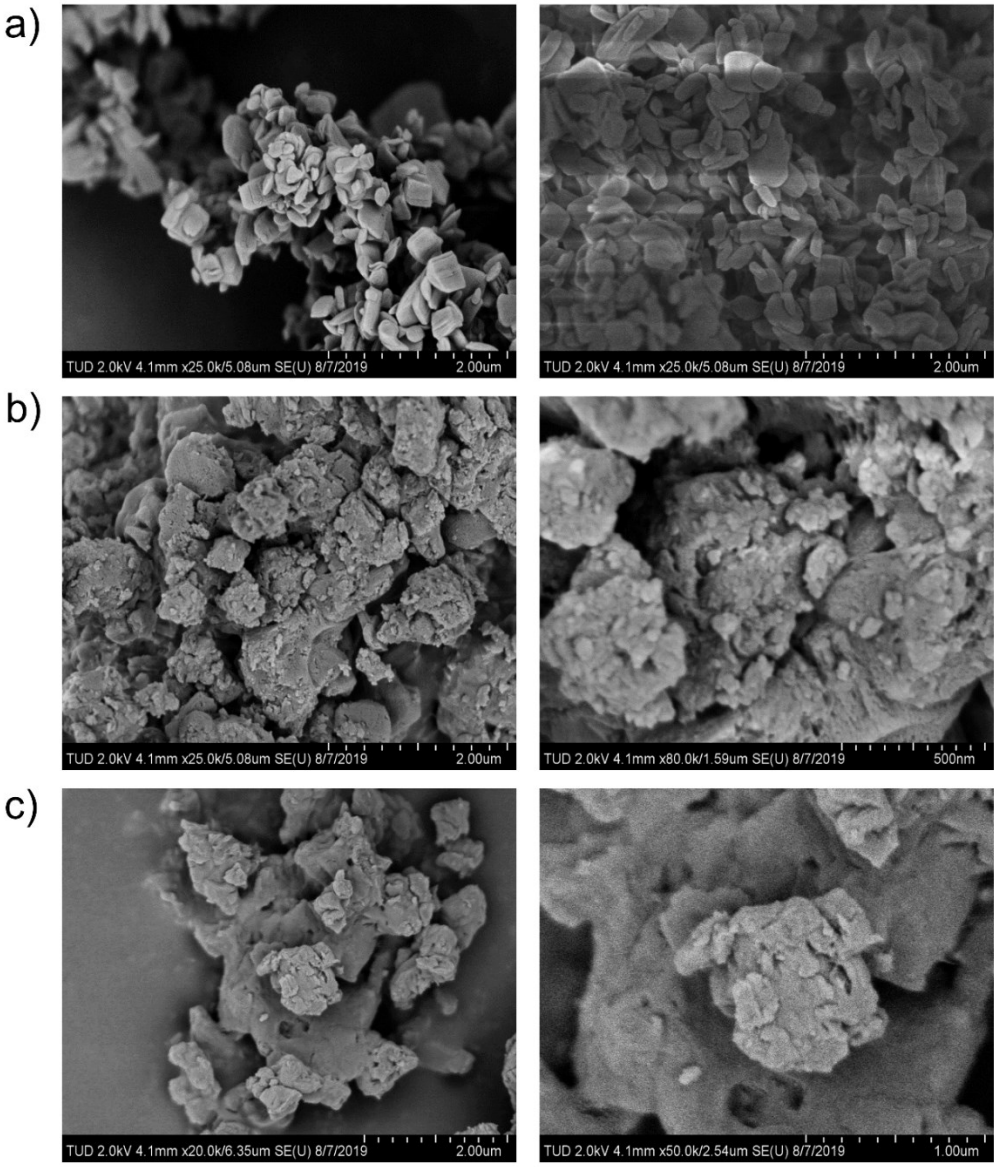

Figure 8-15. SEM images of micron-sized crystals DUT-8(Zn)_0.5 µm a) before adsorption, b) after adsorption of 1-PrOH (6 cycles), b) after adsorption of 1-BuOH (4 cycles). Chapter 5.

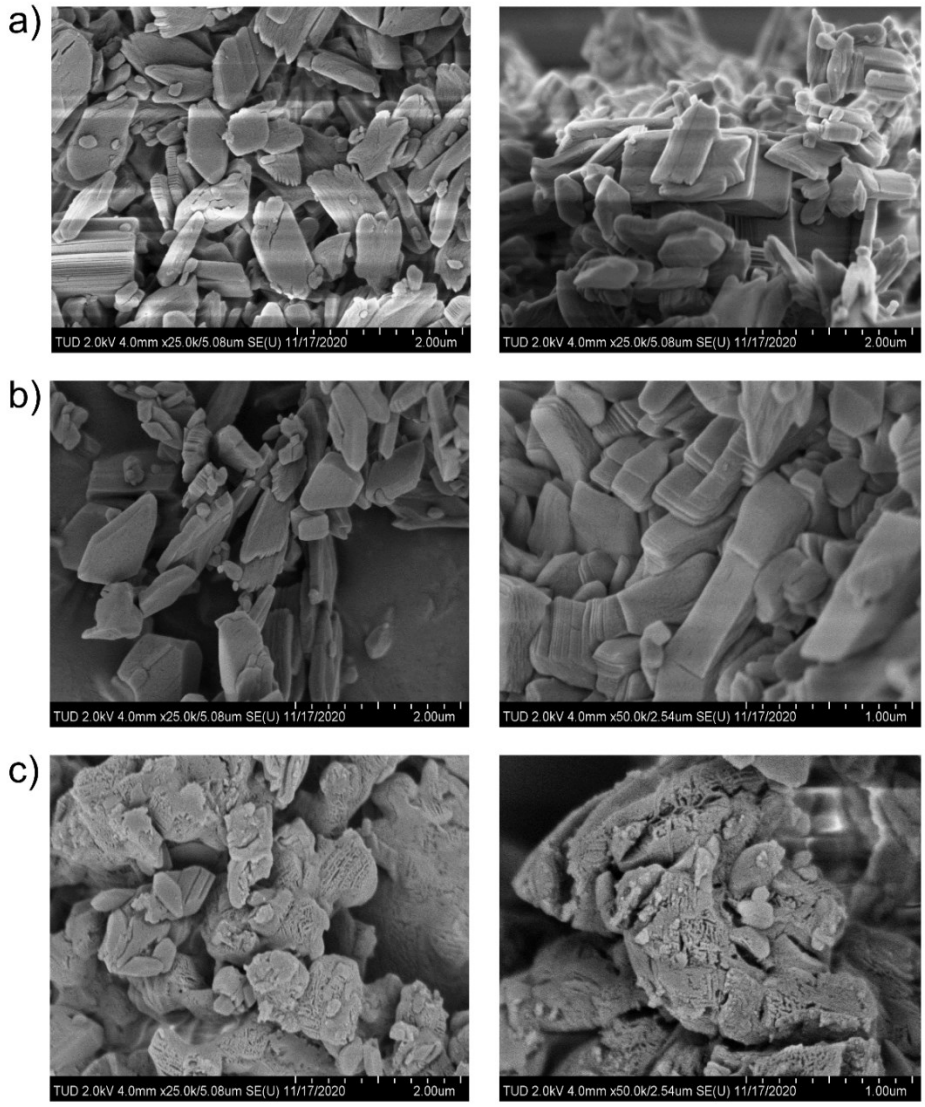

Figure 8-16. SEM images of plates DUT-8(Zn)_1 µm after a) desolvation from DCM, b) adsorption of DCM c) adsorption of EtOH. Chapter 5.

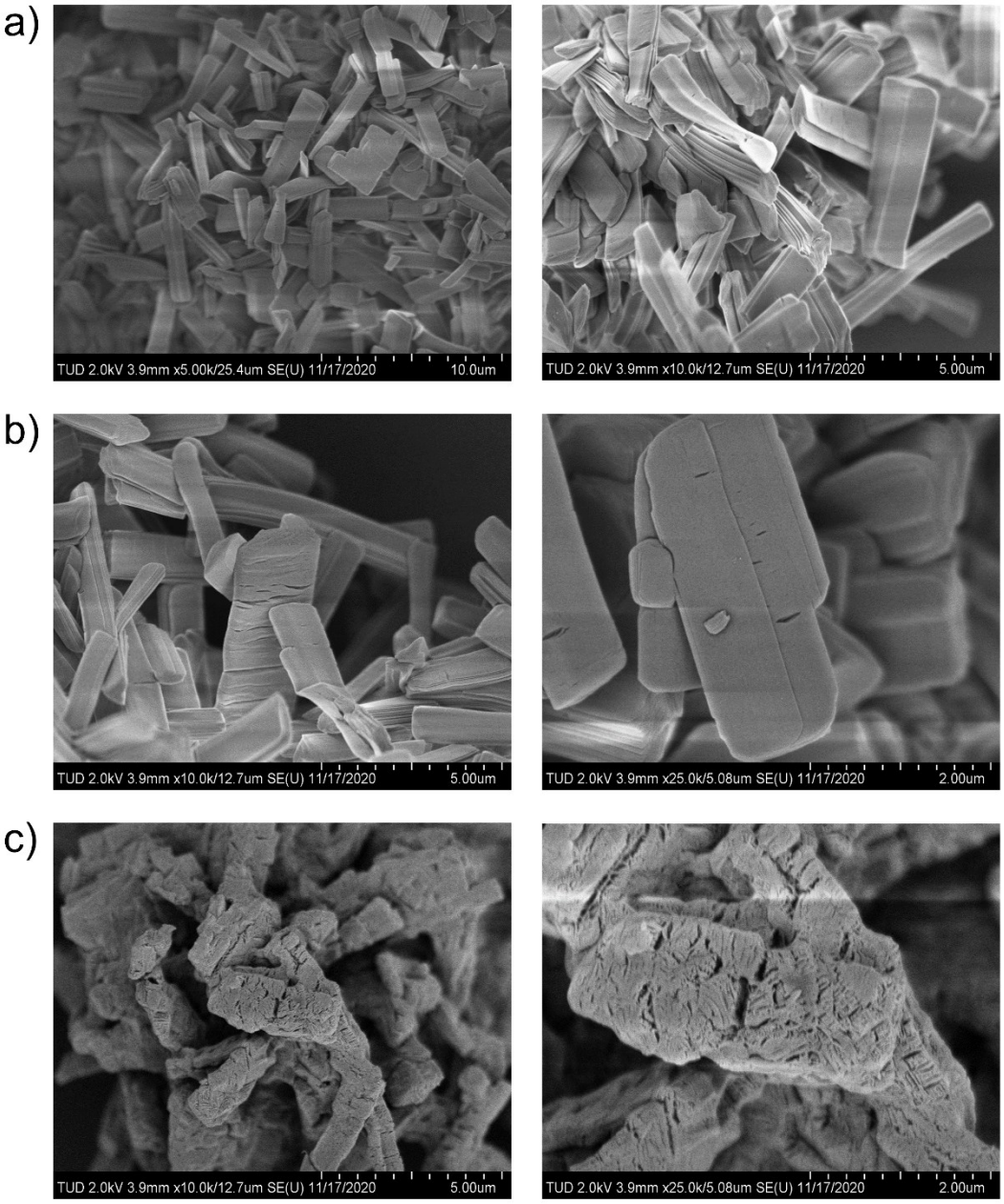

Figure 8-17. SEM images of rods DUT-8(Zn)_1.4 µm after a) desolvation from DCM, b) adsorption of DCM c) adsorption of EtOH. Chapter 5.

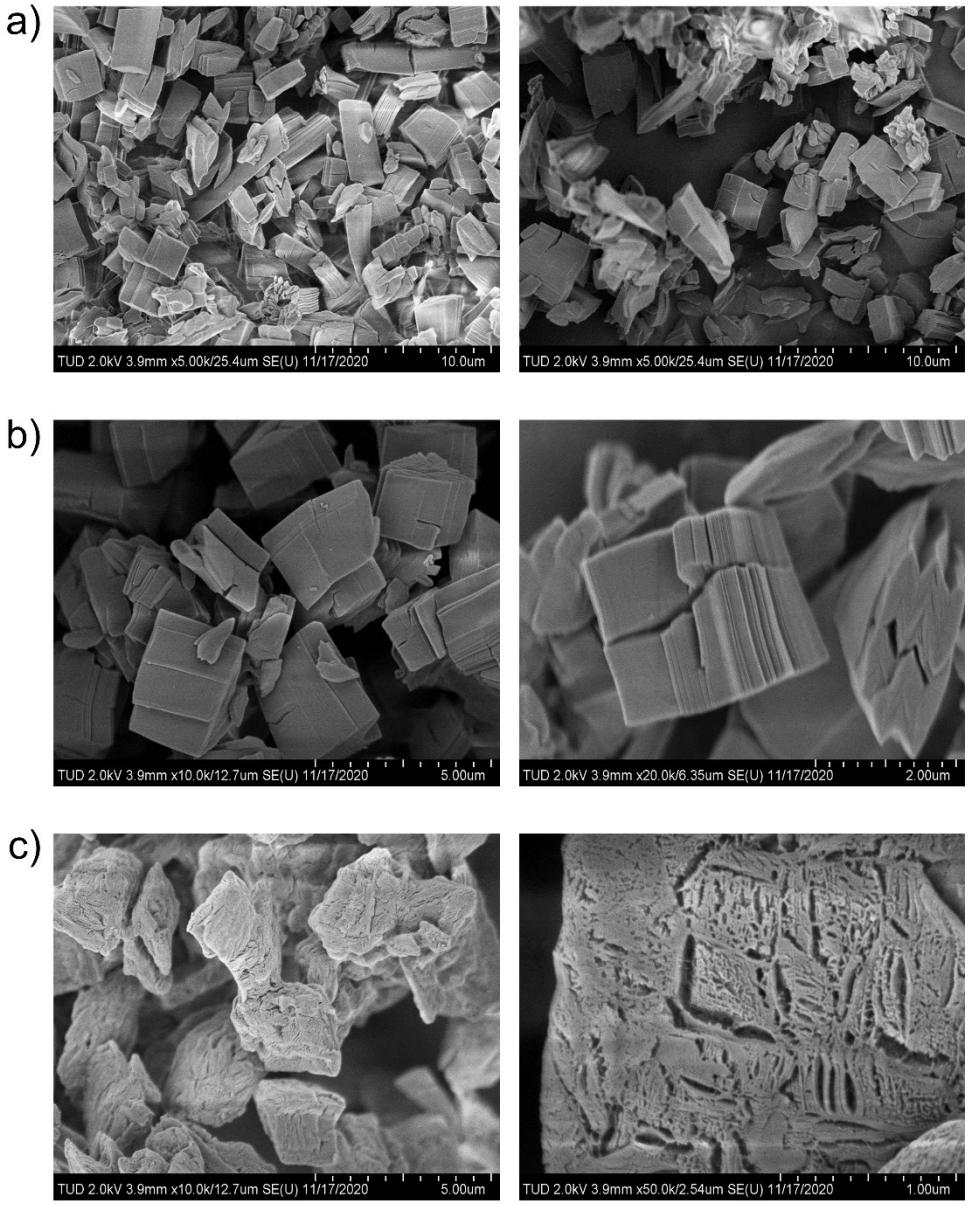

Figure 8-18. SEM images of cubes DUT-8(Zn)_1.8 µm a) desolvation from DCM, b) adsorption of DCM c) adsorption of EtOH. Chapter 5.

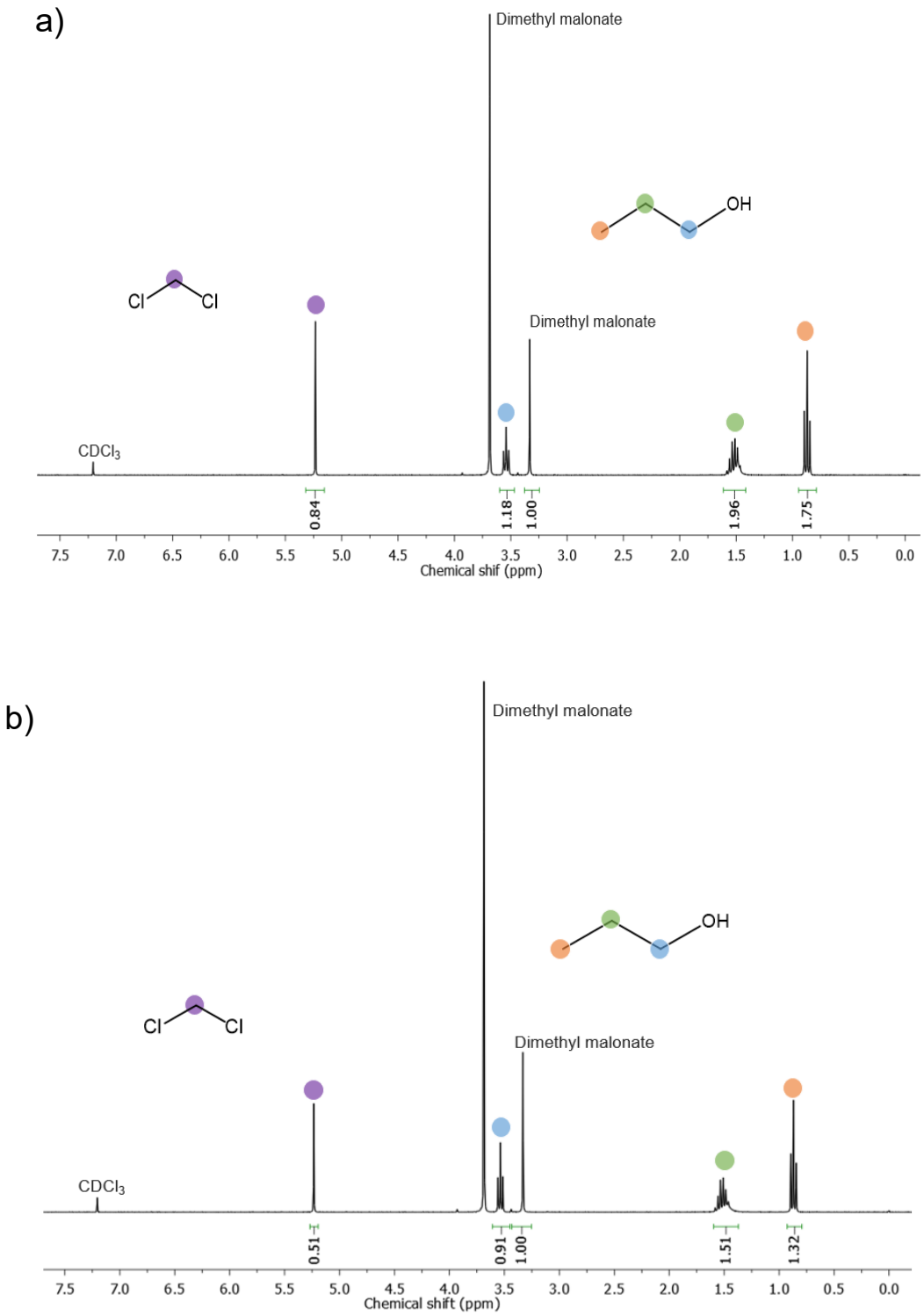

Figure 8-19. ^{1}H NMR spectra of DCM/1PrOH solutions a) blank, b) after adsorption by DUT-8(Ni)_rigid containing signals of 1-PrOH (δ 3.34 (t, *J* = 3.54, 2H), 1.35 (m, *J* = 1.52, 2H), 0.83 (t, *J* = 0.87, 3H)), DCM (δ 5.23 (s, *J* = 5.23, 2H)) (300 MHz, d^{6}-DMSO). Chapter 5.

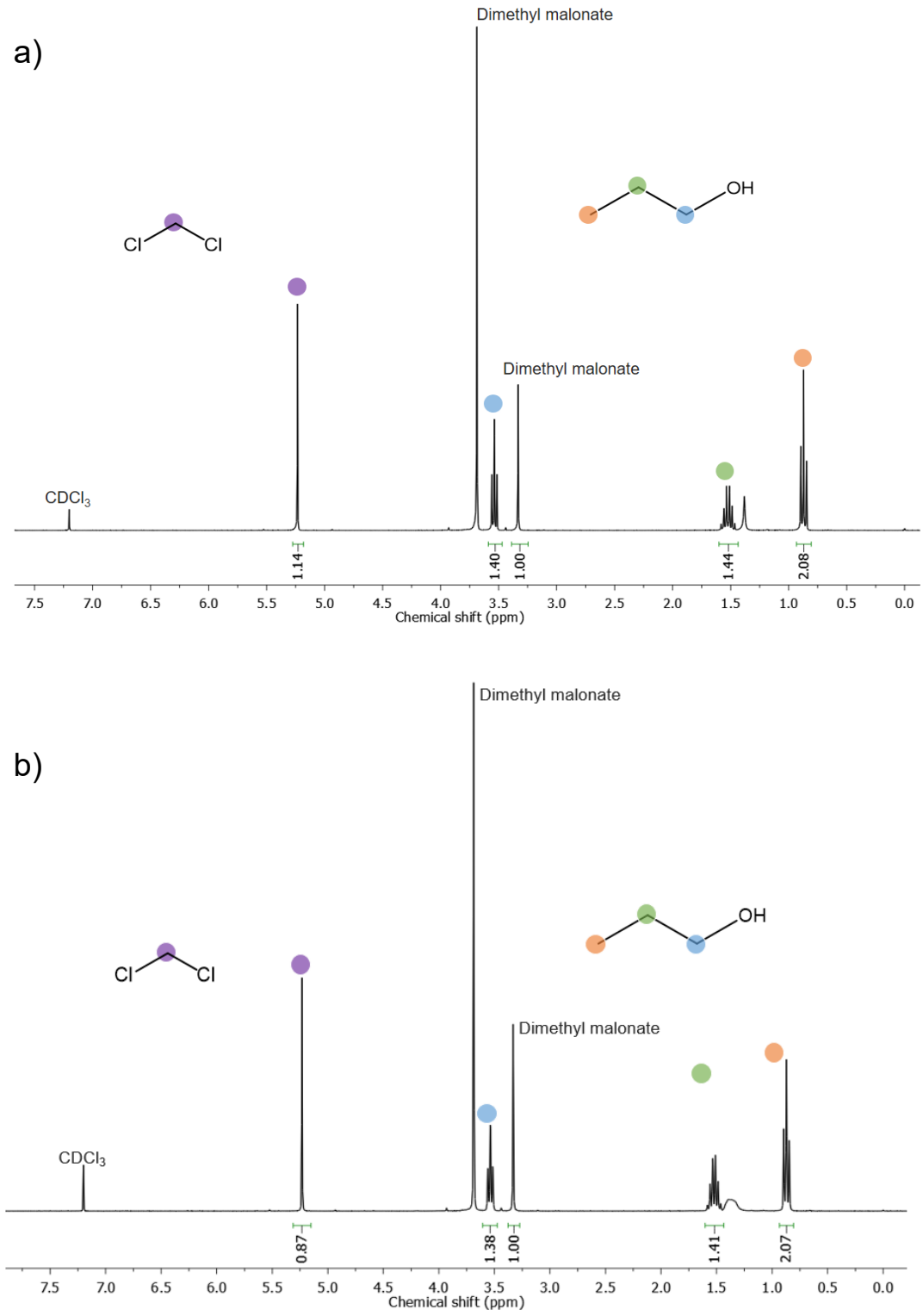

Figure 8-20. ^{1}H NMR spectra of DCM/1PrOH solutions a) blank, b) after adsorption by micron-sized DUT-8(Zn)_0.5 µm containing signals of 1-PrOH (δ 3.34 (t, *J* = 3.54, 2H), 1.35 (m, *J* = 1.51, 2H), 0.83 (t, *J* = 0.87, 3H)), DCM (δ 5.23 (s, *J* = 5.23, 2H)) (300 MHz, d^{6}-DMSO). Chapter 5.

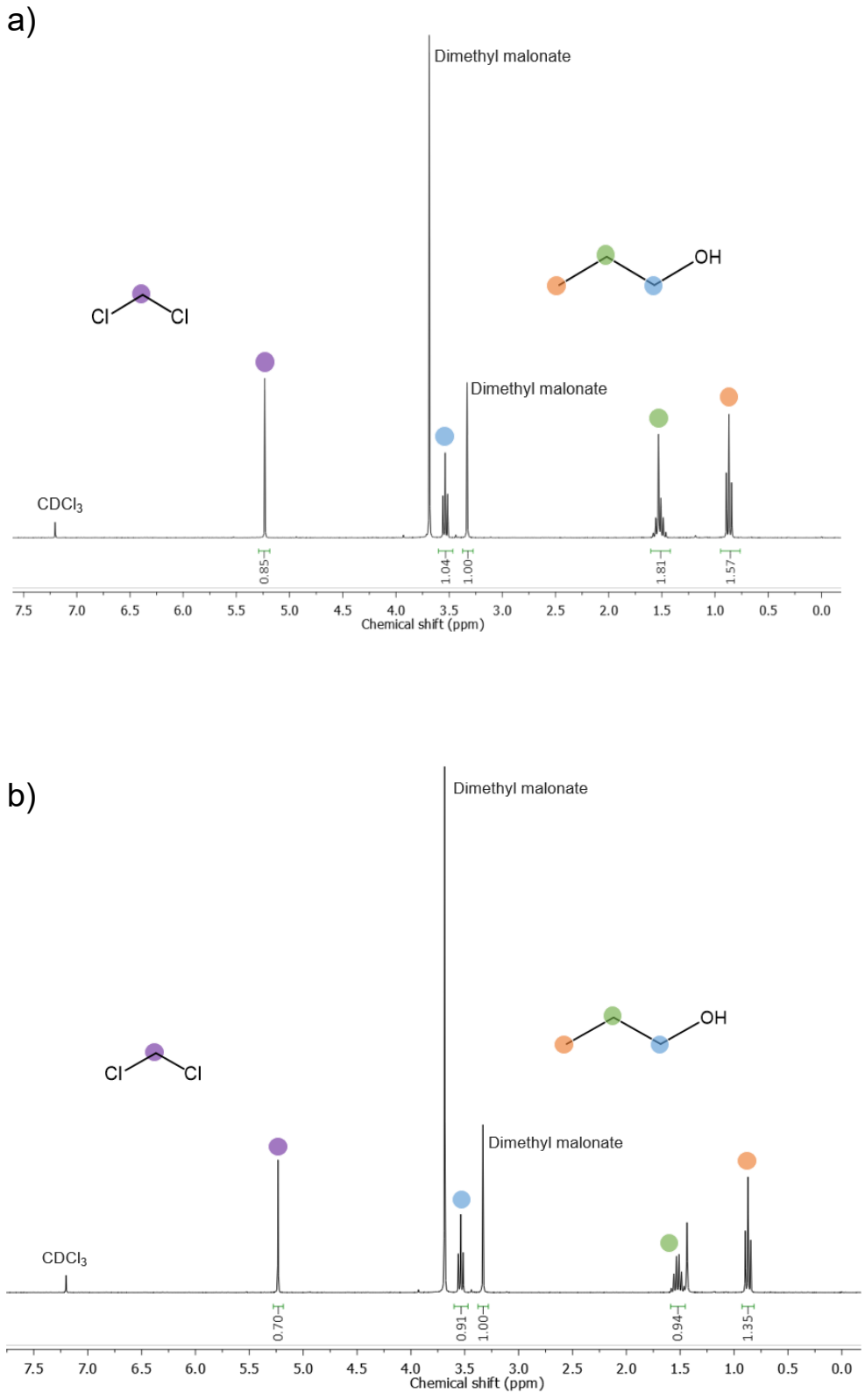

Figure 8-21. ^{1}H NMR spectra of DCM/1PrOH solutions a) blank, b) after adsorption by macro-sized DUT-8(Zn)_160 µm containing signals of 1-PrOH (δ 3.34 (t, *J* = 3.54, 2H), 1.35 (m, *J* = 1.52, 2H), 0.83 (t, *J* = 0.87, 3H)), DCM (δ 5.23 (s, *J* = 5.23, 2H)) (300 MHz, d^{6}-DMSO). Chapter 5.

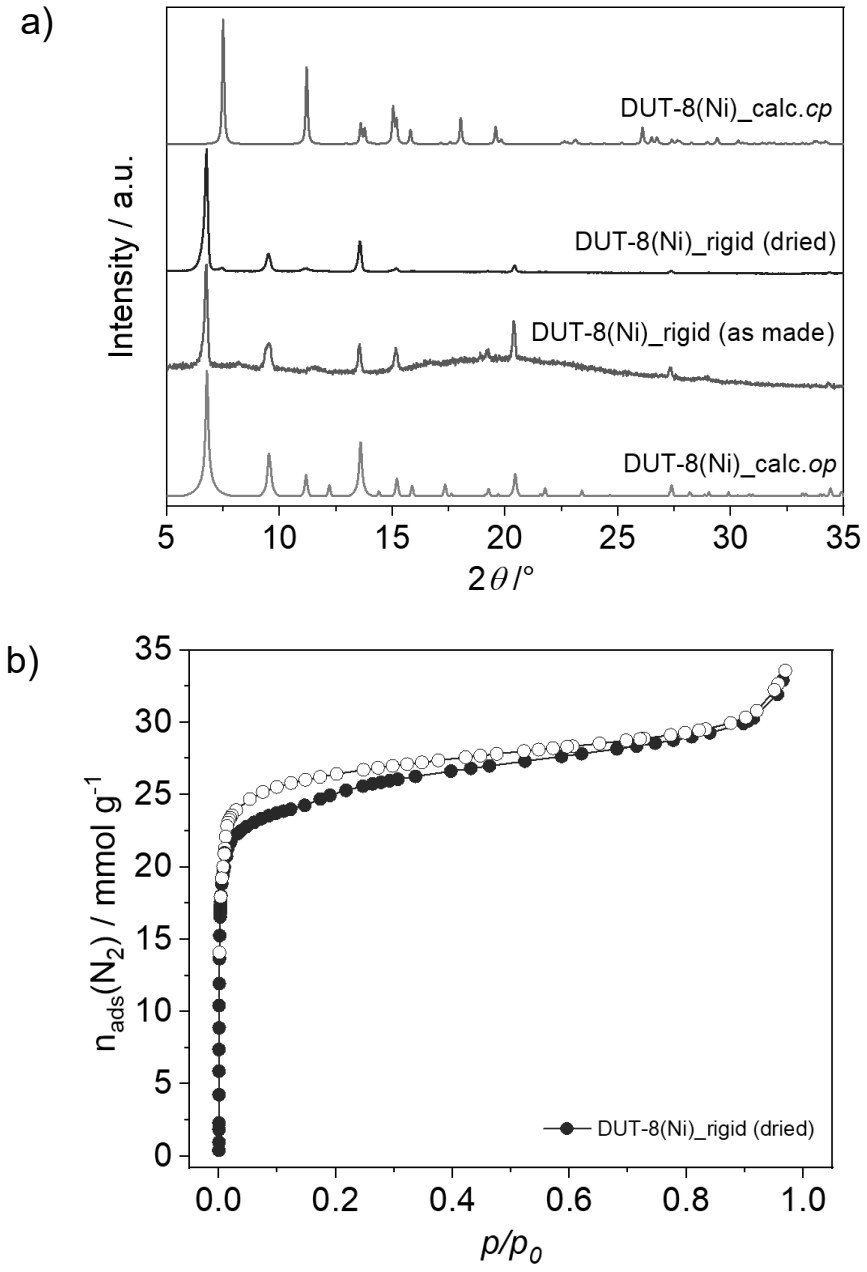

Figure 8-22. Characterization of DUT-8(Ni)_rigid a) PXRD patterns of as made and dried sample; b) Nitrogen physisorption isotherm (77 K). Chapter 5.

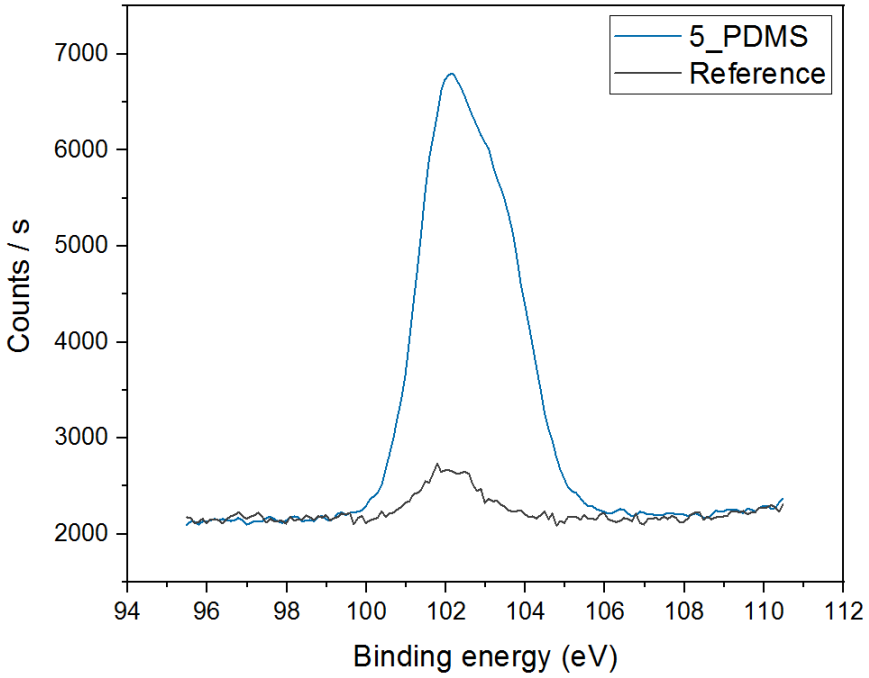

Figure 8-23. Silicon XPS spectrum of PDMS coated sample. Chapter 6.

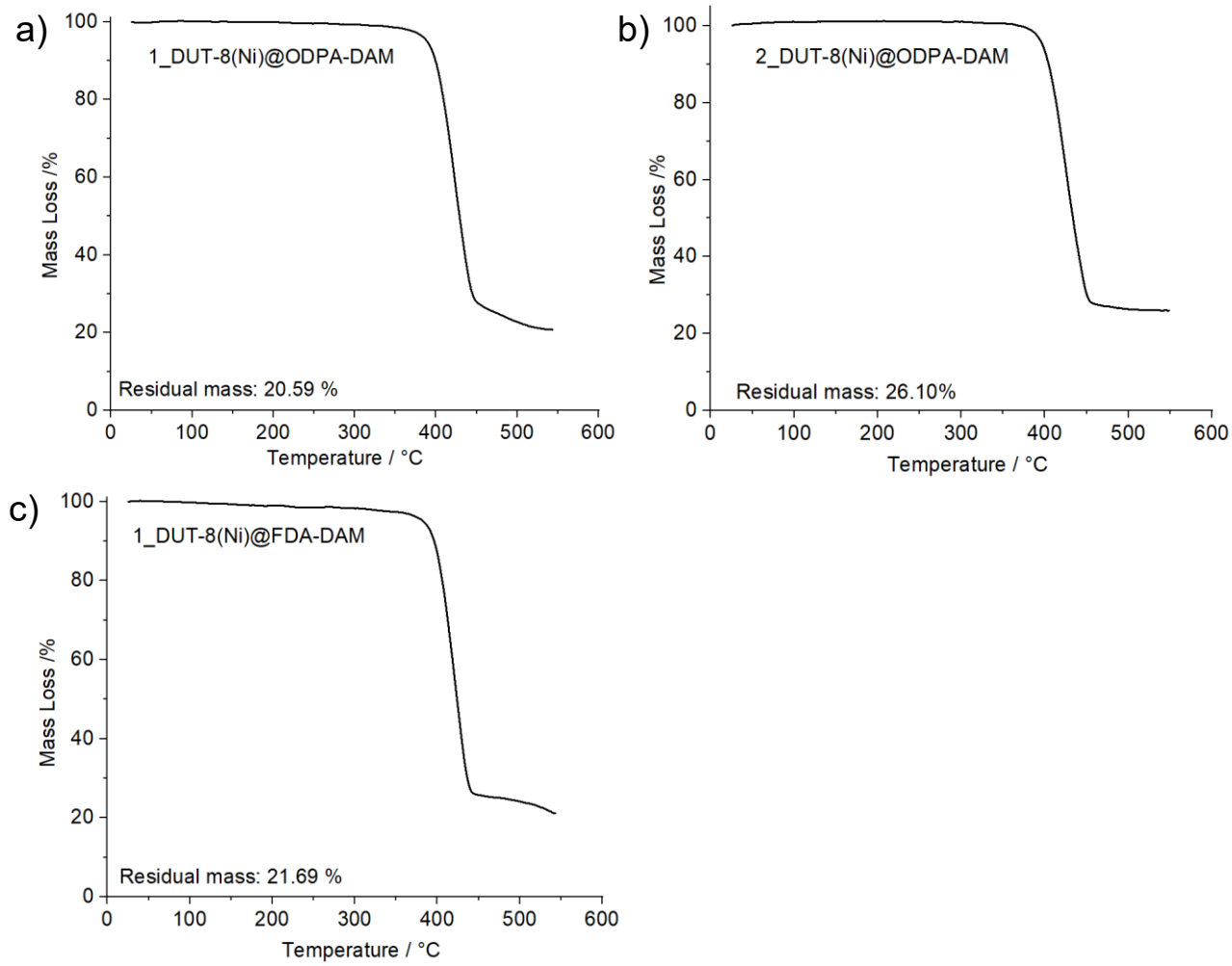

Figure 8-24. TGA of: a) sample 1_DUT-8(Ni)@ODPA-DAM; b) sample 2_DUT-8(Ni)@ODPA-DAM, c) 1_DUT-8(Ni)@FDA-DAM. The expected residual mass is 23%. Chapter 6.

References

1. R. Freund, S. Canossa, S. M. Cohen, W. Yan, H. Deng, V. Guillerm, M. Eddaoudi, D. G. Madden, D. Fairen-Jimenez, H. Lyu, L. K. Macreadie, Z. Ji, Y. Zhang, B. Wang, F. Haase, C. Wöll, O. Zaremba, J. Andreo, S. Wuttke and C. S. Diercks, *Angewandte Chemie International Edition*, 2021, **60**, 23946-23974.
2. H. Deng, S. Grunder, K. E. Cordova, C. Valente, H. Furukawa, M. Hmadeh, F. Gándara, A. C. Whalley, Z. Liu, S. Asahina, H. Kazumori, M. O'Keeffe, O. Terasaki, J. F. Stoddart and O. M. Yaghi, *Science*, 2012, **336**, 1018-1023.
3. R. Freund, O. Zaremba, G. Arnauts, R. Ameloot, G. Skorupskii, M. Dincă, A. Bavykina, J. Gascon, A. Ejsmont, J. Goscianska, M. Kalmutzki, U. Lächelt, E. Ploetz, C. S. Diercks and S. Wuttke, *Angewandte Chemie International Edition*, 2021, **60**, 23975-24001.
4. O. K. Farha, I. Eryazici, N. C. Jeong, B. G. Hauser, C. E. Wilmer, A. A. Sarjeant, R. Q. Snurr, S. T. Nguyen, A. Ö. Yazaydın and J. T. Hupp, *Journal of the American Chemical Society*, 2012, **134**, 15016-15021.
5. S. Horike, S. Shimomura and S. Kitagawa, *Nature Chemistry*, 2009, **1**, 695-704.
6. A. Schneemann, V. Bon, I. Schwedler, I. Senkovska, S. Kaskel and R. A. Fischer, *Chemical Society Reviews*, 2014, **43**, 6062-6096.
7. T. Rodenas, I. Luz, G. Prieto, B. Seoane, H. Miro, A. Corma, F. Kapteijn, F. X. Llabrés i Xamena and J. Gascon, *Nature Materials*, 2015, **14**, 48-55.
8. Q. Hou, S. Zhou, Y. Wei, J. Caro and H. Wang, *Journal of the American Chemical Society*, 2020, **142**, 9582-9586.
9. S. Ehrling, H. Miura, I. Senkovska and S. Kaskel, *Trends in Chemistry*, 2021, **3**, 291-304.
10. D. Tanaka, A. Henke, K. Albrecht, M. Moeller, K. Nakagawa, S. Kitagawa and J. Groll, *Nature Chemistry*, 2010, **2**, 410-416.
11. X. Yang, H.-L. Zhou, C.-T. He, Z.-W. Mo, J.-W. Ye, X.-M. Chen and J.-P. Zhang, *Research*, 2019, **2019**, 9463719.
12. T. Kundu, M. Wahiduzzaman, B. B. Shah, G. Maurin and D. Zhao, *Angewandte Chemie International Edition*, 2019, **58**, 8073-8077.
13. L. Abylgazina, I. Senkovska, S. Ehrling, V. Bon, P. St. Petkov, J. D. Evans, S. Krylova, A. Krylov and S. Kaskel, *CrystEngComm*, 2021, **23**, 538-549.
14. N. Klein, C. Herzog, M. Sabo, I. Senkovska, J. Getzschmann, S. Paasch, M. R. Lohe, E. Brunner and S. Kaskel, *Phys Chem Chem Phys*, 2010, **12**, 11778-11784.
15. N. Klein, H. C. Hoffmann, A. Cadiau, J. Getzschmann, M. R. Lohe, S. Paasch, T. Heydenreich, K. Adil, I. Senkovska, E. Brunner and S. Kaskel, *Journal of Materials Chemistry*, 2012, **22**.
16. S. Ehrling, I. Senkovska, V. Bon, J. D. Evans, P. Petkov, Y. Krupskaya, V. Kataev, T. Wulf, A. Krylov, A. Vtyurin, S. Krylova, S. Adichtchev, E. Slyusareva, M. S. Weiss, B. Büchner, T. Heine and S. Kaskel, *Journal of Materials Chemistry A*, 2019, **7**, 21459-21475.
17. N. Kavoosi, V. Bon, I. Senkovska, S. Krause, C. Atzori, F. Bonino, J. Pallmann, S. Paasch, E. Brunner and S. Kaskel, *Dalton Transactions*, 2017, **46**, 4685-4695.
18. H. Miura, V. Bon, I. Senkovska, S. Ehrling, S. Watanabe, M. Ohba and S. Kaskel, *Dalton Trans*, 2017, **46**, 14002-14011.
19. N. Kavoosi, T. Savchenko, I. Senkovska, M. Maliuta, V. Bon, A. Eychmüller and S. Kaskel, *Microporous and Mesoporous Materials*, 2018, **271**, 169-174.
20. B. F. Hoskins and R. Robson, *Journal of the American Chemical Society*, 1989, **111**, 5962-5964.
21. O. M. Yaghi, G. Li and H. Li, *Nature*, 1995, **378**, 703-706.
22. K. Susumu and K. Mitsuru, *Bulletin of the Chemical Society of Japan*, 1998, **71**, 1739-1753.
23. D. Riou and G. Férey, *Journal of Materials Chemistry*, 1998, **8**, 2733-2735.
24. J. H. Lee, S. Jeoung, Y. G. Chung and H. R. Moon, *Coordination Chemistry Reviews*, 2019, **389**, 161-188.
25. S. R. Batten, N. R. Champness, X.-M. Chen, J. Garcia-Martinez, S. Kitagawa, L. Öhrström, M. O'Keeffe, M. P. Suh and J. Reedijk, *Pure and Applied Chemistry*, 2013, **85**, 1715-1724.
26. H. Li, M. Eddaoudi, M. O'Keeffe and O. M. Yaghi, *Nature*, 1999, **402**, 276-279.
27. S. S.-Y. Chui, S. M.-F. Lo, J. P. H. Charmant, A. G. Orpen and I. D. Williams, *Science*, 1999, **283**, 1148-1150.
28. O. M. Yaghi, M. O'Keeffe, N. W. Ockwig, H. K. Chae, M. Eddaoudi and J. Kim, *Nature*, 2003, **423**, 705-714.

29. H. K. Chae, D. Y. Siberio-Pérez, J. Kim, Y. Go, M. Eddaoudi, A. J. Matzger, M. O'Keeffe, O. M. Yaghi, D. Materials and G. Discovery, *Nature*, 2004, **427**, 523-527.
30. O. M. Yaghi and H. Li, *Journal of the American Chemical Society*, 1995, **117**, 10401-10402.
31. M. Eddaoudi, J. Kim, N. Rosi, D. Vodak, J. Wachter, M. O'Keeffe and O. M. Yaghi, *Science*, 2002, **295**, 469-472.
32. Y. Han, H. Yang and X. Guo, *Synthesis Methods and Crystallization of MOFs*, Intech open, 2019.
33. M. Safaei, M. M. Foroughi, N. Ebrahimpoor, S. Jahani, A. Omidi and M. Khatami, *TrAC Trends in Analytical Chemistry*, 2019, **118**, 401-425.
34. I. Stassen, N. Burtch, A. Talin, P. Falcaro, M. Allendorf and R. Ameloot, *Chemical Society Reviews*, 2017, **46**, 3185-3241.
35. J.-R. Li, R. J. Kuppler and H.-C. Zhou, *Chemical Society Reviews*, 2009, **38**, 1477-1504.
36. Y. Wang, H. Lv, E. S. Grape, C. A. Gaggioli, A. Tayal, A. Dharanipragada, T. Willhammar, A. K. Inge, X. Zou, B. Liu and Z. Huang, *Journal of the American Chemical Society*, 2021, **143**, 6333-6338.
37. H. D. Lawson, S. P. Walton and C. Chan, *ACS Applied Materials & Interfaces*, 2021, **13**, 7004-7020.
38. M. S. Alhumaimess, *Journal of Saudi Chemical Society*, 2020, **24**, 461-473.
39. H. Li, L. Li, R.-B. Lin, W. Zhou, Z. Zhang, S. Xiang and B. Chen, *EnergyChem*, 2019, **1**, 100006.
40. S. Horike, S. S. Nagarkar, T. Ogawa and S. Kitagawa, *Angewandte Chemie International Edition*, 2020, **59**, 6652-6664.
41. S. Ehrling, I. Senkovska, V. Bon, K. Nguyen, H. Miura and S. Kaskel, 2021, DOI: 10.1016/B978-0-08-102688-5.00115-X.
42. D. Li and K. Kaneko, *Chemical Physics Letters*, 2001, **335**, 50-56.
43. R. Kitaura, K. Fujimoto, S.-i. Noro, M. Kondo and S. Kitagawa, *Angewandte Chemie International Edition*, 2002, **41**, 133-135.
44. C. Serre, F. Millange, C. Thouvenot, M. Noguès, G. Marsolier, D. Louër and G. Férey, *Journal of the American Chemical Society*, 2002, **124**, 13519-13526.
45. S. Kitagawa, R. Kitaura and S. Noro, *Angewandte Chemie International Edition*, 2004, **43**, 2334-2375.
46. K. Uemura, R. Matsuda and S. Kitagawa, *Journal of Solid State Chemistry*, 2005, **178**, 2420-2429.
47. G. Férey and C. Serre, *Chemical Society Reviews*, 2009, **38**, 1380-1399.
48. S. K. Elsaidi, M. H. Mohamed, D. Banerjee and P. K. Thallapally, *Coordination Chemistry Reviews*, 2018, **358**, 125-152.
49. K. Biradha and M. Fujita, *Angewandte Chemie International Edition*, 2002, **41**, 3392-3395.
50. J. D. Evans, V. Bon, I. Senkovska, H.-C. Lee and S. Kaskel, *Nature Communications*, 2020, **11**, 2690.
51. S. Ehrling, I. Senkovska, V. Bon, K. D. Nguyen, H. Miura and S. Kaskel, in *Comprehensive Coordination Chemistry III*, eds. E. C. Constable, G. Parkin and L. Que Jr, Elsevier, Oxford, 2021, 328-375.
52. S. Krause, N. Hosono and S. Kitagawa, *Angewandte Chemie International Edition*, 2020, **59**, 15325-15341.
53. F. Bigdeli, C. T. Lollar, A. Morsali and H.-C. Zhou, *Angewandte Chemie International Edition*, 2020, **59**, 4652-4669.
54. R. Haldar, L. Heinke and C. Wöll, *Advanced Materials*, 2020, **32**, 1905227.
55. C. Jabbour, S. Chaemchuen, T. Yuzakova, F. Verpoort and N. Aljammal, *Catalysts*, 2019, **9**, 512.
56. S. Bureekaew, S. Shimomura and S. Kitagawa, *Science and Technology of Advanced Materials*, 2008, **9**, 014108.
57. A. Kirchon, L. Feng, H. F. Drake, E. A. Joseph and H.-C. Zhou, *Chemical Society Reviews*, 2018, **47**, 8611-8638.
58. Q. Chen, Z. Chang, W.-C. Song, H. Song, H.-B. Song, T.-L. Hu and X.-H. Bu, *Angewandte Chemie International Edition*, 2013, **52**, 11550-11553.
59. J. Tian, L. V. Saraf, B. Schwenzer, S. M. Taylor, E. K. Brechin, J. Liu, S. J. Dalgarno and P. K. Thallapally, *Journal of the American Chemical Society*, 2012, **134**, 9581-9584.
60. J. Seo, C. Bonneau, R. Matsuda, M. Takata and S. Kitagawa, *Journal of the American Chemical Society*, 2011, **133**, 9005-9013.
61. C. R. Murdock, B. C. Hughes, Z. Lu and D. M. Jenkins, *Coordination Chemistry Reviews*, 2014, **258-259**, 119-136.

62. P. Horcajada, F. Salles, S. Wuttke, T. Devic, D. Heurtaux, G. Maurin, A. Vimont, M. Daturi, O. David, E. Magnier, N. Stock, Y. Filinchuk, D. Popov, C. Riekel, G. Férey and C. Serre, *Journal of the American Chemical Society*, 2011, **133**, 17839-17847.
63. H. Kajiro, A. Kondo, K. Kaneko and H. Kanoh, *International Journal of Molecular Sciences*, 2010, **11**, 3803-3845.
64. F. J. Sotomayor and C. M. Lastoskie, *Langmuir*, 2017, **33**, 11670-11678.
65. L. Abylgazina, I. Senkovska and S. Kaskel, *ChemRxiv. Cambridge: Cambridge Open Engage*, 2021.
66. F.-X. Coudert, M. Jeffroy, A. H. Fuchs, A. Boutin and C. Mellot-Draznieks, *Journal of the American Chemical Society*, 2008, **130**, 14294-14302.
67. F. Millange, C. Serre and G. Férey, *Chemical Communications*, 2002, DOI: 10.1039/B201381A, 822-823.
68. T. Loiseau, C. Serre, C. Huguenard, G. Fink, F. Taulelle, M. Henry, T. Bataille and G. Férey, *Chemistry – A European Journal*, 2004, **10**, 1373-1382.
69. A. V. Neimark, F.-X. Coudert, C. Triguero, A. Boutin, A. H. Fuchs, I. Beurroies and R. Denoyel, *Langmuir*, 2011, **27**, 4734-4741.
70. C. Triguero, F.-X. Coudert, A. Boutin, A. H. Fuchs and A. V. Neimark, *The Journal of Physical Chemistry Letters*, 2011, **2**, 2033-2037.
71. S. Bourrelly, P. L. Llewellyn, C. Serre, F. Millange, T. Loiseau and G. Férey, *Journal of the American Chemical Society*, 2005, **127**, 13519-13521.
72. N. Aljammal, C. Jabbour, S. Chaemchuen, T. Juzsakova and F. Verpoort, *Catalysts*, 2019, **9**, 512.
73. C. Mellot-Draznieks, C. Serre, S. Surblé, N. Audebrand and G. Férey, *Journal of the American Chemical Society*, 2005, **127**, 16273-16278.
74. C. Serre, F. Millange, S. Surblé and G. Férey, *Angewandte Chemie International Edition*, 2004, **43**, 6285-6289.
75. C. Serre, C. Mellot-Draznieks, S. Surblé, N. Audebrand, Y. Filinchuk and G. Férey, *Science*, 2007, **315**, 1828-1831.
76. S. Surblé, C. Serre, C. Mellot-Draznieks, F. Millange and G. Férey, *Chemical Communications*, 2006, 284-286.
77. K. S. Park, Z. Ni, A. P. Côté, J. Y. Choi, R. Huang, F. J. Uribe-Romo, H. K. Chae, M. O'Keeffe and O. M. Yaghi, *Proceedings of the National Academy of Sciences*, 2006, **103**, 10186-10191.
78. S. A. Moggach, T. D. Bennett and A. K. Cheetham, *Angewandte Chemie International Edition*, 2009, **48**, 7087-7089.
79. C. L. Hobday, C. H. Woodall, M. J. Lennox, M. Frost, K. Kamenev, T. Düren, C. A. Morrison and S. A. Moggach, *Nature Communications*, 2018, **9**, 1429.
80. H. Jobic, D. I. Kolokolov, A. G. Stepanov, M. M. Koza and J. Ollivier, *The Journal of Physical Chemistry C*, 2015, **119**, 16115-16120.
81. C. L. Hobday, S. Krause, S. M. J. Rogge, J. D. Evans and H. Bunzen, *Frontiers in chemistry*, 2021, **9**, 1-10.
82. J. A. Mason, J. Oktawiec, M. K. Taylor, M. R. Hudson, J. Rodriguez, J. E. Bachman, M. I. Gonzalez, A. Cervellino, A. Guagliardi, C. M. Brown, P. L. Llewellyn, N. Masciocchi and J. R. Long, *Nature*, 2015, **527**, 357-361.
83. F. Salles, G. Maurin, C. Serre, P. L. Llewellyn, C. Knöfel, H. J. Choi, Y. Filinchuk, L. Oliviero, A. Vimont, J. R. Long and G. Férey, *Journal of the American Chemical Society*, 2010, **132**, 13782-13788.
84. S. Krause, V. Bon, I. Senkovska, U. Stoeck, D. Wallacher, D. M. Többens, S. Zander, R. S. Pillai, G. Maurin, F.-X. Coudert and S. Kaskel, *Nature*, 2016, **532**, 348-352.
85. F. ZareKarizi, M. Joharian and A. Morsali, *Journal of Materials Chemistry A*, 2018, **6**, 19288-19329.
86. M. Kondo, T. Okubo, A. Asami, S.-i. Noro, T. Yoshitomi, S. Kitagawa, T. Ishii, H. Matsuzaka and K. Seki, *Angewandte Chemie International Edition*, 1999, **38**, 140-143.
87. K. Müller, N. Vankova, L. Schöttner, T. Heine and L. Heinke, *Chemical Science*, 2019, **10**, 153-160.
88. S. Kawata, S. Kitagawa, H. Kumagai, C. Kudo, H. Kamesaki, T. Ishiyama, R. Suzuki, M. Kondo and M. Katada, *Inorganic Chemistry*, 1996, **35**, 4449-4461.
89. X.-L. Luo, Z. Yin, M.-H. Zeng and M. Kurmoo, *Inorganic Chemistry Frontiers*, 2016, **3**, 1208-1226.
90. D. N. Dybtsev, H. Chun and K. Kim, *Angewandte Chemie International Edition*, 2004, **43**, 5033-5036.

91. A. Schneemann, Y. Takahashi, R. Rudolf, S.-i. Noro and R. A. Fischer, *Journal of Materials Chemistry A*, 2016, **4**, 12963-12972.
92. A. Schneemann, E. D. Bloch, S. Henke, P. L. Llewellyn, J. R. Long and R. A. Fischer, *Chemistry – A European Journal*, 2015, **21**, 18764-18769.
93. Z. Wang and S. M. Cohen, *Journal of the American Chemical Society*, 2009, **131**, 16675-16677.
94. S. Henke, A. Schneemann, A. Wütscher and R. A. Fischer, *Journal of the American Chemical Society*, 2012, **134**, 9464-9474.
95. P. Wang, K.-i. Otake, N. Hosono and S. Kitagawa, *Angewandte Chemie International Edition*, 2021, **60**, 7030-7035.
96. S. Wannapaiboon, A. Schneemann, I. Hante, M. Tu, K. Epp, A. L. Semrau, C. Sternemann, M. Paulus, S. J. Baxter, G. Kieslich and R. A. Fischer, *Nature Communications*, 2019, **10**, 346.
97. R. Haldar, N. Sikdar and T. K. Maji, *Materials Today*, 2015, **18**, 97-116.
98. H. Chun, D. N. Dybtsev, H. Kim and K. Kim, *Chemistry – A European Journal*, 2005, **11**, 3521-3529.
99. B. Chen, C. Liang, J. Yang, D. S. Contreras, Y. L. Clancy, E. B. Lobkovsky, O. M. Yaghi and S. Dai, *Angewandte Chemie International Edition*, 2006, **45**, 1390-1393.
100. K. Seki and W. Mori, *The Journal of Physical Chemistry B*, 2002, **106**, 1380-1385.
101. Y. Sakata, S. Furukawa, M. Kondo, K. Hirai, N. Horike, Y. Takashima, H. Uehara, N. Louvain, M. Meilikhov, T. Tsuruoka, S. Isoda, W. Kosaka, O. Sakata and S. Kitagawa, *Science*, 2013, **339**, 193-196.
102. P. V. Dau, M. Kim, S. J. Garibay, F. H. L. Münch, C. E. Moore and S. M. Cohen, *Inorganic Chemistry*, 2012, **51**, 5671-5676.
103. M. Shivanna, Q.-Y. Yang, A. Bajpai, S. Sen, N. Hosono, S. Kusaka, T. Pham, K. A. Forrest, B. Space, S. Kitagawa and M. J. Zaworotko, *Science Advances*, 2018, **4**, eaaq1636.
104. Y. Qi, H. Xu, X. Li, B. Tu, Q. Pang, X. Lin, E. Ning and Q. Li, *Chemistry of Materials*, 2018, **30**, 5478-5484.
105. S. Bureekaew, H. Sato, R. Matsuda, Y. Kubota, R. Hirose, J. Kim, K. Kato, M. Takata and S. Kitagawa, *Angewandte Chemie International Edition*, 2010, **49**, 7660-7664.
106. A. Modrow, D. Zargarani, R. Herges and N. Stock, *Dalton Transactions*, 2011, **40**, 4217-4222.
107. Z. Wang, K. Müller, M. Valášek, S. Grosjean, S. Bräse, C. Wöll, M. Mayor and L. Heinke, *The Journal of Physical Chemistry C*, 2018, **122**, 19044-19050.
108. Y. Chen, K. B. Idrees, F. A. Son, X. Wang, Z. Chen, Q. Xia, Z. Li, X. Zhang and O. K. Farha, *ACS Applied Materials & Interfaces*, 2021, **13**, 16820-16827.
109. V. Bon, N. Klein, I. Senkovska, A. Heerwig, J. Getzschmann, D. Wallacher, I. Zizak, M. Brzhezinskaya, U. Mueller and S. Kaskel, *Physical Chemistry Chemical Physics*, 2015, **17**, 17471-17479.
110. P. V. Dau and S. M. Cohen, *CrystEngComm*, 2013, **15**, 9304-9307.
111. E. R. Engel, A. Jouaiti, C. X. Bezuidenhout, M. W. Hosseini and L. J. Barbour, *Angewandte Chemie International Edition*, 2017, **56**, 8874-8878.
112. F. Millange, N. Guillou, R. I. Walton, J.-M. Grenèche, I. Margiolaki and G. Férey, *Chemical Communications*, 2008, DOI: 10.1039/B809419E, 4732-4734.
113. J. P. S. Mowat, V. R. Seymour, J. M. Griffin, S. P. Thompson, A. M. Z. Slawin, D. Fairen-Jimenez, T. Düren, S. E. Ashbrook and P. A. Wright, *Dalton Transactions*, 2012, **41**, 3937-3941.
114. E. V. Anokhina, M. Vougo-Zanda, X. Wang and A. J. Jacobson, *Journal of the American Chemical Society*, 2005, **127**, 15000-15001.
115. C. Volkringer, T. Loiseau, N. Guillou, G. Férey, E. Elkaïm and A. Vimont, *Dalton Transactions*, 2009, 2241-2249.
116. H. Wang, J. Getzschmann, I. Senkovska and S. Kaskel, *Microporous and Mesoporous Materials*, 2008, **116**, 653-657.
117. P. Maniam and N. Stock, *Inorganic Chemistry*, 2011, **50**, 5085-5097.
118. P. S. Petkov, V. Bon, C. L. Hobday, A. B. Kuc, P. Melix, S. Kaskel, T. Duren and T. Heine, *Phys Chem Chem Phys*, 2019, **21**, 674-680.
119. M. K. Taylor, T. Runčevski, J. Oktawiec, M. I. Gonzalez, R. L. Siegelman, J. A. Mason, J. Ye, C. M. Brown and J. R. Long, *Journal of the American Chemical Society*, 2016, **138**, 15019-15026.
120. N. Bönisch, M. Maliuta, I. Senkovska, V. Bon, P. Petkov, C. Plätzer, P. Müller and S. Kaskel, *Inorganic Chemistry*, 2021, **60**, 1726-1737.
121. Y. Gu, J. Zheng, K. Otake, K. Sugimoto, N. Hosono, S. Sakaki, F. Li and S. Kitagawa, *Angewandte Chemie International Edition*, 2020, **59**, 15517-15521.

122. X. Zhang, Z. Chen, X. Liu, S. L. Hanna, X. Wang, R. Taheri-Ledari, A. Maleki, P. Li and O. K. Farha, *Chemical Society Reviews*, 2020, **49**, 7406-7427.
123. E. J. Carrington, C. A. McAnally, A. J. Fletcher, S. P. Thompson, M. Warren and L. Brammer, *Nature Chemistry*, 2017, **9**, 882-889.
124. J. Anwar and D. Zahn, *Advanced Drug Delivery Reviews*, 2017, **117**, 47-70.
125. D. Li, G. Wang, H.-C. Cheng, C.-Y. Chen, H. Wu, Y. Liu, Y. Huang and X. Duan, *Nature Communications*, 2016, **7**, 11330.
126. J.-C. Nièpce and L. Pizzagalli, in *Nanomaterials and Nanochemistry*, eds. C. Bréchignac, P. Houdy and M. Lahmani, Springer Berlin Heidelberg, Berlin, Heidelberg, 2007, 35-54.
127. S. Yang, *Physics and Chemistry of Nano-structured Materials*, CRC Press., 1999.
128. T. Tian, M. T. Wharmby, J. B. Parra, C. O. Ania and D. Fairen-Jimenez, *Dalton Transactions*, 2016, **45**, 6893-6900.
129. E. Saitoh, A. Kobayashi, M. Yoshida and M. Kato, *Crystal Growth & Design*, 2016, **16**, 7051-7057.
130. P. Li, S.-Y. Moon, M. A. Guelta, L. Lin, D. A. Gómez-Gualdrón, R. Q. Snurr, S. P. Harvey, J. T. Hupp and O. K. Farha, *ACS Nano*, 2016, **10**, 9174-9182.
131. C. Zhang, J. A. Gee, D. S. Sholl and R. P. Lively, *The Journal of Physical Chemistry C*, 2014, **118**, 20727-20733.
132. W. Hatakeyama, T. J. Sanchez, M. D. Rowe, N. J. Serkova, M. W. Liberatore and S. G. Boyes, *ACS Applied Materials & Interfaces*, 2011, **3**, 1502-1510.
133. T. Kiyonaga, M. Higuchi, T. Kajiwara, Y. Takashima, J. Duan, K. Nagashima and S. Kitagawa, *Chemical Communications*, 2015, **51**, 2728-2730.
134. Y. Hijikata, S. Horike, D. Tanaka, J. Groll, M. Mizuno, J. Kim, M. Takata and S. Kitagawa, *Chemical Communications*, 2011, **47**, 7632-7634.
135. S. Tanaka, K. Fujita, Y. Miyake, M. Miyamoto, Y. Hasegawa, T. Makino, S. Van der Perre, J. Cousin Saint Remi, T. Van Assche, G. V. Baron and J. F. M. Denayer, *The Journal of Physical Chemistry C*, 2015, **119**, 28430-28439.
136. R. Numaguchi, H. Tanaka, S. Watanabe and M. T. Miyahara, *The Journal of Chemical Physics*, 2013, **138**, 054708.
137. V. Bon, N. Kavoosi, I. Senkovska and S. Kaskel, *ACS Applied Materials & Interfaces*, 2015, **7**, 22292-22300.
138. S. Krause, V. Bon, H. Du, R. Dunin-Borkowski, U. Stoeck, I. Senkovska and S. Kaskel, *Beilstein Journal of Nanotechnology*, 2019, **10**, 1737-1744.
139. D. Tanaka, K. Nakagawa, M. Higuchi, S. Horike, Y. Kubota, T. C. Kobayashi, M. Takata and S. Kitagawa, *Angewandte Chemie International Edition*, 2008, **47**, 3914-3918.
140. T. Omiya, K. Sasaki, Y. Uchida and N. Nishiyama, *ACS Applied Nano Materials*, 2018, **1**, 3779-3784.
141. Y. Sun, Y. Li and J.-C. Tan, *ACS Applied Materials & Interfaces*, 2018, **10**, 41831-41838.
142. T. Haraguchi, K. Otsubo, O. Sakata, A. Fujiwara and H. Kitagawa, *Journal of the American Chemical Society*, 2016, **138**, 16787-16793.
143. S. Sakaida, K. Otsubo, O. Sakata, C. Song, A. Fujiwara, M. Takata and H. Kitagawa, *Nature Chemistry*, 2016, **8**, 377-383.
144. J. Keupp and R. Schmid, *Advanced Theory and Simulations*, 2019, **2**, 1900117.
145. S. M. J. Rogge, M. Waroquier and V. Van Speybroeck, *Nature Communications*, 2019, **10**, 4842.
146. S. Watanabe, S. Ohsaki, T. Hanafusa, K. Takada, H. Tanaka, K. Mae and M. T. Miyahara, *Chemical Engineering Journal*, 2017, **313**, 724-733.
147. J.-P. Zhang, H.-L. Zhou, D.-D. Zhou, P.-Q. Liao and X.-M. Chen, *National Science Review*, 2017, **5**, 907-919.
148. T. D. Bennett, A. K. Cheetham, A. H. Fuchs and F.-X. Coudert, *Nature Chemistry*, 2017, **9**, 11-16.
149. A. Dhakshinamoorthy, A. M. Asiri and H. Garcia, *Catalysis Science & Technology*, 2016, **6**, 5238-5261.
150. H. Deng, C. J. Doonan, H. Furukawa, R. B. Ferreira, J. Towne, C. B. Knobler, B. Wang and O. M. Yaghi, *Science*, 2010, **327**, 846-850.
151. T. Islamoglu, S. Goswami, Z. Li, A. J. Howarth, O. K. Farha and J. T. Hupp, *Accounts of Chemical Research*, 2017, **50**, 805-813.
152. E. G. Meekel and A. L. Goodwin, *CrystEngComm*, 2021, **23**, 2915-2922.
153. A. W. Thornton, R. Babarao, A. Jain, F. Trousselet and F. X. Coudert, *Dalton Transactions*, 2016, **45**, 4352-4359.

154. S. Dissegna, P. Vervoorts, C. L. Hobday, T. Düren, D. Daisenberger, A. J. Smith, R. A. Fischer and G. Kieslich, *Journal of the American Chemical Society*, 2018, **140**, 11581-11584.
155. M. Mendt, F. Gutt, N. Kavoosi, V. Bon, I. Senkovska, S. Kaskel and A. Pöppl, *The Journal of Physical Chemistry C*, 2016, **120**, 14246-14259.
156. S. Ehrling, E. M. Reynolds, V. Bon, I. Senkovska, T. E. Gorelik, J. D. Evans, M. Rauche, M. Mendt, M. S. Weiss, A. Pöppl, E. Brunner, U. Kaiser, A. L. Goodwin and S. Kaskel, *Nature Chemistry*, 2021, **13**, 568-574.
157. S. Lowell, J. Shields, A. Thomas and M. Thommes, *Springer*, 2004.
158. M. Thommes, K. Kaneko, A. V. Neimark, J. P. Olivier, F. Rodriguez-Reinoso, J. Rouquerol and K. S. W. Sing, *Pure and Applied Chemistry*, 2015, **87**, 1051-1069.
159. M. J. Turner, J. J. McKinnon, D. Jayatilaka and M. A. Spackman, *CrystEngComm*, 2011, **13**, 1804-1813.
160. T. Düren, F. Millange, G. Férey, K. S. Walton and R. Q. Snurr, *The Journal of Physical Chemistry C*, 2007, **111**, 15350-15356.
161. K. S. W. Sing, *Pure and Applied Chemistry*, 1985, **57**, 603-619.
162. M. Thommes and K. A. Cychosz, *Adsorption*, 2014, **20**, 233-250.
163. J. Rouquerol, F. Rouquerol, P. Llewellyn, G. Maurin and K. S. W. Sing, *Academic Press, Oxford;* 2014.
164. I. Langmuir, *Journal of the American Chemical Society*, 1918, **40**, 1361-1403.
165. S. Brunauer, P. H. Emmett and E. Teller, *Journal of the American Chemical Society*, 1938, **60**, 309-319.
166. P. L. Llewellyn, F. Rodriquez-Reinoso, J. Rouqerol and N. Seaton, *Elsevier*, 2007.
167. O. M. Yaghi, M. J. Kalmutzki and C. S. Diercks, *Introduction to Reticular Chemistry: Metal-Organic Frameworks and Covalent Organic Frameworks*, Wiley, 2019.
168. D. A. Gómez-Gualdrón, P. Z. Moghadam, J. T. Hupp, O. K. Farha and R. Q. Snurr, *Journal of the American Chemical Society*, 2016, **138**, 215-224.
169. I. Senkovska and S. Kaskel, *Chemical Communications*, 2014, **50**, 7089-7098.
170. L. Sarkisov and A. Harrison, *Molecular Simulation*, 2011, **37**, 1248-1257.
171. E. First and C. Floudas, *Microporous and Mesoporous Materials*, 2013, **165**, 32–39.
172. R. L. Martin and M. Haranczyk, *Crystal Growth & Design*, 2014, **14**, 2431-2440.
173. S. Dantas, L. Sarkisov and A. V. Neimark, *Journal of the American Chemical Society*, 2019, **141**, 8397-8401.
174. I. Senkovska, K. A. Cychosz, P. Llewellyn, M. Thommes and S. Kaskel, in *The Chemistry of Metal–Organic Frameworks*, 2016, 575-605.
175. S. Dantas and A. V. Neimark, *ACS Applied Materials & Interfaces*, 2020, **12**, 15595-15605.
176. J. E. Mondloch, M. J. Katz, N. Planas, D. Semrouni, L. Gagliardi, J. T. Hupp and O. K. Farha, *Chemical Communications*, 2014, **50**, 8944-8946.
177. A. J. Howarth, A. W. Peters, N. A. Vermeulen, T. C. Wang, J. T. Hupp and O. K. Farha, *Chemistry of Materials*, 2017, **29**, 26-39.
178. A. P. Nelson, O. K. Farha, K. L. Mulfort and J. T. Hupp, *Journal of the American Chemical Society*, 2009, **131**, 458-460.
179. ImageJ, Image Processing and Analysis in Java, https://imagej.nih.gov/ij/, (accessed February 04, 2021).
180. U. Mueller, R. Förster, M. Hellmig, F. U. Huschmann, A. Kastner, P. Malecki, S. Pühringer, M. Röwer, K. Sparta, M. Steffien, M. Ühlein, P. Wilk and M. S. Weiss, *The European Physical Journal Plus*, 2015, **130**, 141.
181. T. G. G. Battye, L. Kontogiannis, O. Johnson, H. R. Powell and A. G. W. Leslie, *Acta Crystallographica Section D*, 2011, **67**, 271-281.
182. K. M. Sparta, M. Krug, U. Heinemann, U. Mueller and M. S. Weiss, *Journal of Applied Crystallography*, 2016, **49**, 1085-1092.
183. G. Sheldrick, *Acta Crystallographica Section C*, 2015, **71**, 3-8.
184. A. Spek, *Acta Crystallographica Section C*, 2015, **71**, 9-18.
185. V. Bon, N. Klein, I. Senkovska, A. Heerwig, J. Getzschmann, D. Wallacher, I. Zizak, M. Brzhezinskaya, U. Mueller and S. Kaskel, *Physical Chemistry Chemical Physics*, 2015, **17**, 17471-17479.
186. D. M. Többens and S. Zander, *Journal of large-scale research facilities JLSRF*, 2016, **2**.
187. M. Wojdyr, *Journal of Applied Crystallography*, 2010, **43**, 1126-1128.
188. J. VandeVondele, M. Krack, F. Mohamed, M. Parrinello, T. Chassaing and J. Hutter, *Computer Physics Communications*, 2005, **167**, 103-128.
189. B. G. Lippert, J. H. Parrinello and Michele, *Molecular Physics*, 1997, **92**, 477-488.

190. J. P. Perdew, K. Burke and M. Ernzerhof, *Physical Review Letters*, 1996, **77**, 3865-3868.
191. S. Goedecker, M. Teter and J. Hutter, *Physical Review B*, 1996, **54**, 1703-1710.
192. C. Hartwigsen, S. Goedecker and J. Hutter, *Physical Review B*, 1998, **58**, 3641-3662.
193. M. Krack, *Theoretical Chemistry Accounts*, 2005, **114**, 145-152.
194. J. VandeVondele and J. Hutter, *The Journal of Chemical Physics*, 2003, **118**, 4365-4369.
195. S. Grimme, J. Antony, S. Ehrlich and H. Krieg, *The Journal of Chemical Physics*, 2010, **132**, 154104.
196. M. Valiev, E. J. Bylaska, N. Govind, K. Kowalski, T. P. Straatsma, H. J. J. Van Dam, D. Wang, J. Nieplocha, E. Apra, T. L. Windus and W. A. de Jong, *Computer Physics Communications*, 2010, **181**, 1477-1489.
197. C. Adamo and V. Barone, *The Journal of Chemical Physics*, 1999, **110**, 6158-6170.
198. F. Weigend, *Phys. Chem. Chem. Phys.*, 2006, **8**, 1057-1065.
199. W. Zhang, Y. Hu, J. Ge, H.-L. Jiang and S.-H. Yu, *Journal of the American Chemical Society*, 2014, **136**, 16978-16981.
200. H. Wang, S. He, X. Qin, C. Li and T. Li, *Journal of the American Chemical Society*, 2018, **140**, 17203-17210.
201. L. Huelsenbeck, K. S. Westendorff, Y. Gu, S. Marino, S. Jung, W. S. Epling and G. Giri, *Crystals*, 2019, **9**, 20.
202. L. Abylgazina, I. Senkovska, R. Engemann, S. Ehrling, T. E. Gorelik, N. Kavoosi, U. Kaiser and S. Kaskel, *Frontiers in chemistry*, 2021, **9**, 674566.
203. R. S. Forgan, *Chemical Science*, 2020, **11**, 4546-4562.
204. T. Tsuruoka, S. Furukawa, Y. Takashima, K. Yoshida, S. Isoda and S. Kitagawa, *Angewandte Chemie International Edition*, 2009, **48**, 4739-4743.
205. M.-H. Pham, G.-T. Vuong, F.-G. Fontaine and T.-O. Do, *Crystal Growth & Design*, 2012, **12**, 3091-3095.
206. A. Krylov, I. Senkovska, S. Ehrling, M. Maliuta, S. Krylova, E. Slyusareva, A. Vtyurin and S. Kaskel, *Chemical Communications*, 2020, **56**, 8269-8272.
207. I. Mayergoyz, *Mathematical Models of Hysteresis and their Applications*, Academic Press., 2003.
208. M. J. Thompson, C. L. Hobday, I. Senkovska, V. Bon, S. Ehrling, M. Maliuta, S. Kaskel and T. Düren, *Journal of Materials Chemistry A*, 2020, **8**, 22703-22711.
209. N. Mehio, S. Dai and D.-e. Jiang, *The Journal of Physical Chemistry A*, 2014, **118**, 1150-1154.
210. S. Bureekaew, S. Amirjalayer and R. Schmid, *Journal of Materials Chemistry*, 2012, **22**, 10249-10254.
211. J. E. ten Elshof, C. R. Abadal, J. Sekulić, S. R. Chowdhury and D. H. A. Blank, *Microporous and Mesoporous Materials*, 2003, **65**, 197-208.
212. P. Melix and T. Heine, *The Journal of Physical Chemistry C*, 2020, **124**, 11985-11989.
213. G. A. Miller and R. B. Bernstein, *The Journal of Physical Chemistry*, 1959, **63**, 710-713.
214. D. Zahn and J. Anwar, *Chemistry – A European Journal*, 2011, **17**, 11186-11192.
215. A. Krylov, A. Vtyurin, P. Petkov, I. Senkovska, M. Maliuta, V. Bon, T. Heine, S. Kaskel and E. Slyusareva, *Phys Chem Chem Phys*, 2017, **19**, 32099-32104.
216. M. Rauche, S. Ehrling, S. Krause, I. Senkovska, S. Kaskel and E. Brunner, *Chemical Communications*, 2019, **55**, 9140-9143.
217. H. C. Hoffmann, B. Assfour, F. Epperlein, N. Klein, S. Paasch, I. Senkovska, S. Kaskel, G. Seifert and E. Brunner, *Journal of the American Chemical Society*, 2011, **133**, 8681-8690.
218. M. Rauche, S. Ehrling, L. Abylgazina, C. Bachetzky, I. Senkovska, S. Kaskel and E. Brunner, *Solid State Nuclear Magnetic Resonance*, 2022, **120**, 101809.
219. S. Ehrling, M. Mendt, I. Senkovska, J. D. Evans, V. Bon, P. Petkov, C. Ehrling, F. Walenszus, A. Pöppl and S. Kaskel, *Chemistry of Materials*, 2020, **32**, 5670-5681.
220. J. Pang, M. Wu, J.-S. Qin, C. Liu, C. T. Lollar, D. Yuan, M. Hong and H.-C. Zhou, *Chemistry of Materials*, 2019, **31**, 8787-8793.
221. W. Cai, T. Lee, M. Lee, W. Cho, D.-Y. Han, N. Choi, A. C. K. Yip and J. Choi, *Journal of the American Chemical Society*, 2014, **136**, 7961-7971.
222. J. Lyu, X. Gong, S.-J. Lee, K. Gnanasekaran, X. Zhang, M. C. Wasson, X. Wang, P. Bai, X. Guo, N. C. Gianneschi and O. K. Farha, *Journal of the American Chemical Society*, 2020, **142**, 4609-4615.
223. Y. Kim, R. Haldar, H. Kim, J. Koo and K. Kim, *Dalton Transactions*, 2016, **45**, 4187-4192.
224. S. Ehrling, I. Senkovska, A. Efimova, V. Bon, L. Abylgazina, P. Petkov, J. D. Evans, A. Gamal Attallah, M. T. Wharmby, M. Roslova, Z. Huang, H. Tanaka, A. Wagner, P. Schmidt and S. Kaskel, *Chemistry – A European Journal*, 2022, **28**, e2022012 .

225. J. D. Evans, J. P. Dürholt, S. Kaskel and R. Schmid, *Journal of Materials Chemistry A*, 2019, **7**, 24019-24026.
226. N. C. Burtch, S. J. Baxter, J. Heinen, A. Bird, A. Schneemann, D. Dubbeldam and A. P. Wilkinson, *Advanced Functional Materials*, 2019, **29**, 1904669.
227. M. J. Cliffe, J. A. Hill, C. A. Murray, F.-X. Coudert and A. L. Goodwin, *Physical Chemistry Chemical Physics*, 2015, **17**, 11586-11592.
228. H. Yang, T. X. Trieu, X. Zhao, Y. Wang, Y. Wang, P. Feng and X. Bu, *Angewandte Chemie International Edition*, 2019, **58**, 11757-11762.
229. G. A. Somorjai and Y. Li, *Proceedings of the National Academy of Sciences*, 2011, **108**, 917-924.
230. L. Heinke, Z. Gu and C. Wöll, *Nature Communications*, 2014, **5**, 4562.
231. Z. Ji, H. Wang, S. Canossa, S. Wuttke and O. M. Yaghi, *Advanced Functional Materials*, 2020, **30**, 2000238.
232. C. V. McGuire and R. S. Forgan, *Chemical Communications*, 2015, **51**, 5199-5217.
233. A. Umemura, S. Diring, S. Furukawa, H. Uehara, T. Tsuruoka and S. Kitagawa, *Journal of the American Chemical Society*, 2011, **133**, 15506-15513.
234. M. Kondo, S. Furukawa, K. Hirai and S. Kitagawa, *Angewandte Chemie International Edition*, 2010, **49**, 5327-5330.
235. B. V. K. J. Schmidt, *Macromolecular Rapid Communications*, 2020, **41**, 1900333.
236. L. Peng, S. Yang, D. T. Sun, M. Asgari and W. L. Queen, *Chemical Communications*, 2018, **54**, 10602-10605.
237. V. J. Pastore, T. R. Cook and J. Rzayev, *Chemistry of Materials*, 2018, **30**, 8639-8649.
238. J. Hwang, T. Heil, M. Antonietti and B. V. K. J. Schmidt, *Journal of the American Chemical Society*, 2018, **140**, 2947-2956.
239. S. Hiraide, H. Arima, H. Tanaka and M. T. Miyahara, *ACS Applied Materials & Interfaces*, 2021, **13**, 30213-30223.
240. H. Wang, J. Getzschmann, I. Senkovska and S. Kaskel, *Microporous and Mesoporous Materials*, 2008, **116**, 653–657.

List of publications and conferences

Publications

(i) **L. Abylgazina,** I. Senkovska, S. Ehrling, V. Bon, P. Petkov, J. D. Evans, S. Krylova, A.Krylov and S.Kaskel, "Tailoring adsorption induced switchability of a pillared layer MOF by crystal size engineering", *CrystEngComm,* 23**,** (2020) 538.

(ii) **L. Abylgazina,** I. Senkovska, R. Engemann, Sebastian Ehrling, T. E. Gorelik, N. Kavoosi, U. Kaiser, S. Kaskel,' "Impact of Crystal Size and Morphology on Switchability Characteristics in Pillared-Layer Metal-Organic Framework DUT-8(Ni)", *Fronties in Chemistry,* 9, (2021).

(iii) **S. Ehrling**, I. Senkovska, A. Efimova, V. Bon, L. Abylgazina, P. Petkov, J. D. Evans, A. G. Attallah, M. T. Wharmby, Maria Roslova, Z. Huang, H. Tanaka, A. Wagner, P. Schmidt, S. Kaskel, "Temperature Driven Transformation of the Flexible Metal-Organic Framework DUT-8(Ni)", *Chemistry - A European Journal,* 28, (2022).

(iv) M. Rauche, S. Ehrling, **L. Abylgazina**, C. Bachetzky, I. Senkovska, S. Kaskel, E. Brunner, "Solid-state NMR studies of metal ion and solvent influences upon the flexible metal-organic framework DUT-8", *Solid State Nuclear Magnetic Resonance Journal*, 120, (2022) 101809.

(v) **L. Abylgazina**, I. Senkovska, S. Kaskel, "Logic and Symbolism of Switchable Porous Framework Materials", *ChemRxiv.*

(vi) V. Bon, N. Busov, I. Senkovska, N. Bönisch, **L. Abylgazina**, A. Khadiev, D. Novikov, S. Kaskel, "The importance of crystal size for breathing kinetic in MIL-53 (Al)", *Chemical Communications,* 58**,** (2022) 10492-10495.

(vii) I. Senkovska, V. Bon, **L. Abylgazina**, M. Mendt, J. Berger, G. Kieslich, P. Petkov, J. L. Fiorio, J.-O. Joswig, T. Heine, L. Schaper, Rochus Schmid, Roland A. Fischer, Andreas Pöppl, Eike Brunner, Stefan Kaskel, "Understanding MOF flexibility: A model system focused analysis", *Angew. Chem. Int. Ed.,* (2023) e202218076.

Conferences

Conference	Presentation
12 September 2019, Bayreuth, 17. Mitteldeutsches Anorganiker Nachwuchssymposium	Oral
27 -31 October 2019, Paris, The 3rd European Conference on Metal Organic Frameworks and Porous Polymers	Poster
5 December, Dresden, FlexMOF symposium	Poster
23-24 July 2020, RCS twitter conference (digital)	Poster
12 January 2021, Webinar on Flexibility of pillared layer MOFs (digital)	Oral
10 -11 March 2021, The 32th German Zeolite Conference (digital)	Oral
21 -25 June 2021, The 2nd international School on Porous Materials (digital) *Poster Prize Award – the best poster №1*	Poster
11 -15 September 2021, The 4rd European Conference on Metal Organic Frameworks and Porous Polymers (digital)	Poster
2 February 2022, Symposium on the Influence of Crystal size and Morphology on Framework materials (digital)	Oral
5 May 2022, Dresden, The 1st chemTUgether conference	Poster
22 - 27 May 2022, Bloomfield, USA, The 14th International conference Fundamentals of Adsorption	Poster
04 - 07 September 2022, Dresden, The 8th International conference on Metal-Organic Frameworks and Open Frameworks Compounds	Poster
05 - 09 December 2022, The 3rd IAS Twitter Poster Conference (digital)	Poster

Workshops

26 - 27 November 2018, Munich, At the heart of MOF chemistry: Topology

26 - 31 March 2019, Stockholm, School on Reticular Chemistry

15 May 2019, Leipzig, Strategies and Practical Experiences for Characterizing Surfaces and Pore Structures

13 April 2021, Leipzig, Adsorption & Characterization of porous solids (digital)

Erklärung

Hiermit versichere ich, dass ich die vorliegende Arbeit ohne unzulässige Hilfe Dritter und ohne Benutzung anderer als der angegebenen Hilfsmittel angefertigt habe; die aus fremden Quellen direkt oder indirekt übernommenen Gedanken sind als solche kenntlich gemacht. Die Arbeit wurde bisher weder im Inland noch im Ausland in gleicher oder ähnlicher Form einer anderen Prüfungsbehörde vorgelegt.

Die vorliegende Arbeit wurde am Institut für Anorganische Chemie I der Technischen Universität Dresden in dem Zeitraum vom Oktober 2018 bis Dezember 2022 unter wissenschaftlicher Betreuung von Herrn Prof. Dr. Stefan Kaskel angefertigt.

03.04.23 Dresden Leila Abylgazina